Dilute Nitride Long Wavelength Semiconductor Diode Lasers

Xia Zhang

A Thesis submitted in Faculty of Graduate Studies and Postdoctoral Studies in partial fulfillment of the requirements for the Ph.D. degree in Electrical and Computer Engineering

April 2007

Ottawa-Carleton Institute for Electrical and Computer Engineering

School of Information Technology and Engineering

University of Ottawa

Ottawa, Ontario, Canada

Your file Votre référence
ISBN: 978-0-494-49405-9
Our file Notre référence
ISBN: 978-0-494-49405-9

uOttawa

L'Université canadienne
Canada's university

FACULTÉ DES ÉTUDES SUPÉRIEURES ET POSTOCTORALES

uOttawa

L'Université canadienne
Canada's university

FACULTY OF GRADUATE AND POSDOCTORAL STUDIES

Xia Zhang
AUTEUR DE LA THÈSE / AUTHOR OF THESIS

Ph.D. (Electrical Engineering)
GRADE / DEGREE

School of Information Technology and Engineering
FACULTÉ, ÉCOLE, DÉPARTEMENT / FACULTY, SCHOOL, DEPARTMENT

Dilute Nitride Long Wavelength Semiconductor Diode Lasers

TITRE DE LA THÈSE / TITLE OF THESIS

Henri Schriemer
DIRECTEUR (DIRECTRICE) DE LA THÈSE / THESIS SUPERVISOR

Trevor Hall
CO-DIRECTEUR (CO-DIRECTRICE) DE LA THÈSE / THESIS CO-SUPERVISOR

EXAMINATEURS (EXAMINATRICES) DE LA THÈSE / THESIS EXAMINERS

Peter Mascher

Pierre Berini

Robert Gauthier

Sergey Loyka

Gary W. Slater
Le Doyen de la Faculté des études supérieures et postdoctorales / Dean of the Faculty of Graduate and Postdoctoral Studies

Abstract

This thesis studies the novel dilute nitride semiconductor materials, GaInNAs and GaInNAsSb, and their usage in GaAs-based diode lasers emitting between 1.25 to 1.55 μm in wavelength. This work covers material physical modeling, laser simulations, design and the experimental work of device characterization.

The tabulated band anti-crossing theory of the quaternary GaInNAs is formulated. The resulting formulas are further corrected by our experimental observations. This modified band anti-crossing theory is implemented into the commercial laser simulator Las2D. Together with other electrical and optical models equipped with the unique GaInNAs parameters, Las2D becomes the first simulator that calculates the operational behavior of dilute nitride lasers.

A two-dimensional simulation algorithm is discovered using the samples of ridge waveguide GaInAs/GaAs lasers that emit at 1.0 μm in wavelength. This algorithm is used in the calibration of the Las2D simulator for dilute nitride lasers. Using the calibrated simulator, several optimized quantum well designs for high-speed, temperature-insensitive devices are suggested with special considerations on the carrier uneven distributions in quantum wells and the nitrogen-induced gain reduction that occurs in dilute nitride material.

Fabry-Perot cavity, ridge waveguide lasers emitting at 1275 nm were fabricated by molecular beam epitaxy using a double quantum well GaInNAs (well) – GaAs (barrier) structure. A complete set of static and dynamic characterizations were carried out on those lasers to evaluate dilute nitride material properties as an active media. The temperature dependent light-current (L-I) measurements demonstrated a temperature insensitive device with a characteristic temperature as high as 155 K. Although challenges in material quality remain, the lasers show lasing properties similar to conventional GaAs- and InP-based lasers with respect to the transparency current (6 mA), the material gain (1000 cm^{-1}), the optical loss (7 cm^{-1}), the beam quality (single transverse mode operation, 2.8 in linewidth enhancement factor, 0.55 nm/K in

the rate of spectral temperature shift), and the maximum modulation bandwidth (9.7 GHz).

The GaInNAsSb QW structure allows the further extension of the laser emitting wavelength to the desired 1.55 μm range. Although the quantum wells and the nitrogen-content barrier challenge the crystal growth, a room temperature, continuous-wave operating GaInNAsSb (quantum well) – GaNAs (barrier) laser was demonstrated for the first time with a record long operating wavelength (1553 nm) for GaAs-based lasers. L-I measurements were carried out on those lasers. The laser optical gain and loss properties were studied using the unique cavity loss dependent analysis.

To the people whom I am living for……

Acknowledgments

I owe my sincerest thanks to my supervisors, Dr. Trevor Hall and Dr. Henry Schriemer, for their guidance and generous support throughout this thesis work. Every graduate student needs supervisors who foster the interests of their students while allowing them to go on their own course. I am lucky to have both of those supervisors. I am grateful for the financial support provided by NSERC through the centre of research for photonics that enables me to complete my Ph.D. work.

I would like to thank Dr. James Gupta, a tremendous scientist in the National Research Council of Canada for the chance to work on this project, and his instruction and guidance in scientific research and writing. His enthusiasm, persistence and talent helped me go through difficulties along the way. His work on epitaxial growth is highly recognized.

I am grateful to Dr. Greg Pakulski for his expert advice and help in the labs. I thank Dr. Pedro Barrios for the laser processing and timely support on bar cleaving. I also appreciate Dr. Xiaohua Wu for the TEM micrographs essential for samples and Dr. Andre Delâge for his help with waveguide analysis. In the theoretical part of my work, I would like to thank Dr. Geof Aers for the in-depth discussion and his excellent work on the quantum calculation.

Dr. Karin Hinzer and Ron Millett in University of Ottawa deserve a special thank. They came to me in my thesis writing. The discussion, the advice and the correction on the draft rescued me from the embarrassment of errors. Their time and patience are highly appreciated.

There are many other colleagues in IMS-NRC and University of Ottawa who helped me in one way or another. I am grateful to Dr. Robin Williams and Dr Siegfried Janz for the management of resources and Dr. Marie D'Iorio and Dr. Sylvain Charbonneau for their encouragement. Also I want to thank CPFC for supporting my research in their facilities.

Thanks to the many graduate students whom I shared office with in the "gloomy" window-less CFPC basement, in particular Danny Kim and Sandy Ng, who made those dark days cheerful and meaningful.

Finally, I must thank the Cai family. A solid core formed of Xuefeng, Dominique and Cindy, for the immense understanding, support and love. I own them too much.

Statement of Thesis Contributions

Except where otherwise stated, the results presented in this thesis were obtained by the author during the period of her Ph. D. research project under the supervision of Dr. T.J. Hall and the co-supervision of Dr. H. Schriemer. They are to the best of her knowledge original. These include:

- Gain and wavelength tuning measurements of GaInNAs/GaAs double QW laser.
- Intrinsic dynamic measurements of GaInNAs/GaAs double QW laser including laser relative intensity noise and linewidth enhancement factor.
- Temperature dependent light-current measurements of 1.3 μm GaInNAs/GaAs and 1.55 μm GaInNAsSb/GaNAs lasers.
- Spectroscopy of CW GaInNAs/GaAs laser and pulsed GaInNAsSb/GaAs laser.
- GaInNAs QW e1-hh transition models based on the tabulated band anti-crossing theory.
- GaInNAs electron and hole mobility models based on the published results.
- GaInNAs affinity models based on the band anti-crossing theory.
- Lateral leakage analysis and suggested method of control for the ridge waveguide GaInNAs/GaAs and GaInNAsSb/GaAs lasers.
- Simulation methodology of ridge waveguide lasers using the laser simulator Las2D.
- Analysis of carrier uneven distribution in GaInNAs/GaAs lasers.
- Optimized structure of single QW GaInNAs/GaAs laser using the Las2D simulation.
- Optimized structure of DQW GaInNAs/GaAs laser using the Las2D simulation.
- Optimized structure of high-speed GaInNAs/GaAs laser using the Las2D simulation.

All epitaxial wafers were produced by Dr. J.A. Gupta at the Institute for Microstructural Sciences, National Research Council. All the laser samples were processed by Dr. P.J. Barrios, National Research Council. All the measurements were carried out on the test station that was organized by Dr. G. Pakulski, National Research Council. The cross-sectional TEM micrographs of GaInNAs/GaAs laser samples were produced by Dr. X. Wu, National Research Council. The modeling of the laser single mode condition was done by Dr. Andre Delâge, National Research Council. The $K \cdot P$ calculation of the band anti-crossing was published and updated by Dr. G. Aers, National Research Council.

The above work has led to the following papers:

- Xia Zhang, James A. Gupta, Pedro J. Barrios, Greg Pakulski, Trevor J. Hall, "Intrinsic Dynamic Properties of High-Characteristic Temperature GaInNAs Laser Diodes Operating at 1.3 μm", IEEE Photonics Technology Letters, Vol. 19, pp. 106-108, 2007.
- X. Zhang, J.A. Gupta, P.J. Barrios, G. Pakulski, X. Wu, T.J. Hall, "Analysis of gain in 1.3μm GaInNAs laser diodes", J. Vac. Sci. Technology, Vol. 24 A, pp 787-789, 2005.
- J.A. Gupta, P.J. Barrios, X. Zhang, J. Lapointe, D. Poitras, G. Pakulski, X. Wu and A. Delâge, "Room-temperature continuous-wave operation of GaInNAsSb laser diodes at 1.55|μm", Electronics Letters, Vol. 41 pp.1060-1061, 2005.
- J.A. Gupta, P.J. Barrios, X. Zhang, J. Lapointe, D. Poitras, G. Pakulski, X. Wu, Electronics Letters, Vol. 41, pp. 71-72, 2005.
- X. Zhang, J.A. Gupta, P.J. Barrios, G. Pakulski, T.J. Hall, "Linewidth Enhancement Factor of a 1.3μm GaInNAs/GaAs Laser by Optical Gain Analysis", LEOS Annual Meeting, 29 October-2 November, 2006, Montreal, Quebec, Canada, Proceeding pp. 60-61.
- X. Zhang, J.A. Gupta, P.J. Barrios, G. Pakulski, X. Wu, A. Delâge and T. J. Hall, "Properties of a High T_0 1.3μm GaInNAs/GaAs Quantum Well

Laser", Photonics West 2006, San Jose, CA, Proc SPIE 6133, 613301, February 2006.

Contributions not directly related to this thesis:

- Ronald Millett, Henry P. Schriemer and X. Zhang, "Irrelevance of bending angle in simple Y-branch power splitter design", Photonics North 2004, Proceedings of SPIE Vol. 5577, pp 503-510.

This work has been carried out in the Institute of Microstructural Science, National Research Council of Canada and supported by the Centre of Research for Photonics, University of Ottawa. I would like to thank NSERC for financial support.

Table of Contents

List of Figures

List of Tables

List of Abbreviations

AMQW	Asymmetric multiple quantum-well
ASE	Amplified spontaneous spectrum
BAC	Band Anti-crossing model
CW	Continuous wave
DFB	Distributed feedback
DQWs	Double quantum wells
DUT	Device under test
F-P	Fabry Perot
FWHM	Full width at half maximum
GRIN	Graded index
HCSEL	Horizontal cavity surface emitting laser
ICP-RIE	Inductively coupled plasma reactive ion etching
MBE	Molecular beam epitaxy
MOCVD	Metalorganic chemical vapor deposition
OSA	Optical spectrum analyzer
PECVD	Plasma enhanced chemical vapour deposition
PL	Photoluminescence
PM	Polarization maintaining
QW	Quantum well
RF	Radio frequency
RIN	Related intensity noise
RTA	Rapid temperature annealing
RWG	Ridge Waveguide
SCH	Separate confinement heterostructure
SEM	Secondary electron microscopy

SRH	Shockley-Read-Hall recombination
TEC	Temperature electronic controller
VCA	Virtual crystal approximation
VCSEL	Vertical cavity surface emitting lasers

Thesis Introduction

Semiconductor diode lasers are considered one of the most technologically critical inventions of the Twentieth Century. They are used in a wide variety of applications ranging from simple bar code readers to complex coherent light sources in precise instrumentation. Compared to solid-state lasers and gas lasers, diode lasers have the market share due to their considerably smaller size, higher energy efficiency and lower cost. Moreover, the unique ability of diode lasers to be modulated by the driving current enables fiber optical communications.

Diode lasers are categorized by their emission wavelength, and thus the semiconductor materials from which they are made. At this point of laser development, "short" wavelength (~0.7-0.9 μm) GaAs-based lasers and "long" wavelength (~1.3-1.65 μm) InP-based lasers have been in production. Shorter-wavelength visible range GaN based lasers and longer wavelength infrared range GaSb based lasers are being commercialized. As the fabrication techniques and device physics become more advanced, lasers made with new materials and principles are continuously under development for emerging applications. Research on novel materials, quantum dot lasers and cascade lasers are on going.

This thesis studies novel dilute nitride semiconductors and their usages in GaAs-based long-wavelength lasers. Traditionally, InGaAsP QWs grown on an InP substrate have been used to meet the wavelength requirements. However, those QWs are intrinsically sensitive to the temperature change. The lasers need complicated packages with electrical temperature controller. The cost of the lasers is not possible to reduce to the level for the applications such as fiber to home. Thus, material systems that can intrinsically give good performance at high temperature have been studied. Two examples are InGaAlAs/InP and GaInNAs/GaAs. After more than a decade's research, InGaAlAs/InP system has been used in industry to produce reliably laser. While GaInNAs/GaAs is more attractive in research communities due to it's unique band structure. By adding a few percents of nitrogen, or nitrogen and antimony, GaInAs alloys (dilute nitrides), the conduction band property of GaInAs changes dramatically. As the result, the band gap of dilute nitrides reaches the infrared range. On top of that, the smaller nitrogen atoms decrease the alloy's lattice constant, allowing device-quality materials to be grown lattice matched to GaAs substrates. Long-wavelength edge-emitting and surface-emitting lasers are both possible using dilute nitrides as quantum well materials. Furthermore, dilute nitride lasers feature superior temperature stability due to their unique band structures to other conventional semiconductors. These lasers are promising to operate uncooled at high driving speed, making them highly desired in local area networks and metropolitan networks.

The first chapter of the thesis briefly reviews the concepts of semiconductor laser physics and fabrication techniques that this work is been based on. It begins with the energy dispersion of semiconductors and band gap energy of III-V compounds. Then it follows with the formation of active media using heterojunction and quantum wells (QWs). The light-matter interaction is introduced within the recombination processes. As the light is generated by radiative recombination, the laser optical gain and the conditions of positive gain are discussed. Chapter 1 also reviews device fabrication techniques. Molecular beam epitaxy (MBE), which is an important method of growing laser structures, comprises the major part of the review. Ridge waveguide (RWG) laser processing is introduced in the last section of chapter 1.

With a better understanding of laser operational principles, chapter 2 introduces dilute nitride materials with an emphasis on material physics and QW design. At first, the uniqueness of dilute nitrides and the resulting advantages to device properties are introduced. Then the challenges and impact achievements in crystal growth and device process are summarized. Further, special considerations on QW structures are presented. The chapter finishes with the current status of dilute nitride laser development on edge-emitting lasers and on surface-emitting lasers.

Double QWs, RWG dilute nitride lasers were designed and fabricated. Chapter 3 presents the experimental characterization of these lasers. The measurement results enable a critical assessment of dilute nitride materials and fabrication process. Besides, the chapter describes some analytical methods and measurement techniques that are very useful in laser parametric tests. The measurement-based results demonstrated promising GaAs-based lasers emitting at 1.3 and 1.55 μm in wavelengths. Beside the superior temperature stability, the 1.3 μm GaInNAs/GaAs laser shows comparable lasing properties in thresholds, efficiency, beam quality and intrinsic dynamics.

The strong band bowing of dilute nitrides originates from the coupling between the localized nitrogen energy level and the conduction band of the host material. Chapter 4 presents the modeling of this novel material using the empirical band anti-crossing (BAC) theory. The chapter begins with the common considerations of material modeling in laser simulation. Then it discusses the classical BAC theory. By combining our experimental observations and the BAC theory, a model that describes GaInNAs energy dispersions is developed and implemented in the laser simulator Las2D. At last, other electrical and optical models that cannot be interpolated by the virtual crystal approximation (VCA) are empirically fitted to the experimental observations. With those models, Las2D becomes the first simulator that calculates the operational behavior of dilute nitride lasers.

Laser diodes represent a complicated interaction of electronic, thermal, and optical processes. Although most laser simulators employ self-consistent calculations, they require calibration to accurately represent the material systems and fabrication processes. Chapter 5 researches the calibration methodology for RWG lasers using the well-studied InGaAs/GaAs single QW lasers. The parameters that have profound influences on lasing threshold and efficiency have been determined by aligning the Las2D two-dimensional simulation results with the data from measurements. The values of those parameters are compared with references for realism. This calibration methodology is independent of the laser material systems and is applied to GaInNAs/GaAs lasers in chapter 6.

As mentioned above, broadband, uncooled dilute nitride lasers are highly desired in dispersion-free 1.3 μm fibre links. Chapter 6 studies the properties of 1.3 μm GaInNAs/GaAs RWG lasers using the calibrated simulator Las2D. The chapter is dedicated to exploring the design improvements with focus on the threshold current reduction and the differential gain enhancement, as those two factors play important roles in those lasers that operate at high-speed modulation. A careful analysis of band structure and gain reveals that the GaInNAs/GaAs heterojunction exhibits strong gain unevenness among spatially distributed QWs. A material combination of well and barrier is proposed to overcome the effect. Exhaustive, an optimized device structure is suggested by combining simulation results with a physical analysis.

Chapter 1 Introduction to Semiconductor Lasers

1.1 *Fundamental properties of III/V semiconductors*

1.1.1 Energy Dispersion of Semiconductors

Solid-state materials are basically divided into three forms based on their electrical conductivity: metals, semiconductors and insulators. Metals are excellent conductors. The large amount of free electrons forms current when an electrical field is applied. Dielectrics are good insulators that have few electrons in the conduction band that will react to the electrical field. Semiconductors have electrical properties between these two types. The conductivity of semiconductors varies with the temperature and material purity. Since the energy bandgap, E_g, of semiconductors is in the order of 1 eV, electrons can be excited to the conduction band by various means, leaving holes in the valence band. These free carriers allow electrical current to flow when an electrical field is applied.

The carrier concentration of a semiconductor depends on the density of electron states, $D(E)$, and the probability that an electron occupies a particular state. The probability of finding an electron at an energy, E, is given by the Fermi distribution function [1]:

$$f(E) = \frac{1}{1 + \exp((E - E_F)/k_B T)} \qquad 1\text{-}1$$

where E_F is the Fermi energy, k_B is the Boltzmann constant and T is the temperature in Kelvin. In intrinsic semiconductors, E_F is in the middle of the band gap, and the electron and hole concentrations are therefore balanced.

Semiconductors that are doped with either acceptor (p-type) impurity atoms or donor (n-type) impurity atoms have electron and hole concentrations that are no longer balanced. The Fermi energy will be either close to the valence band (p-type) or to the conduction band (n-type).

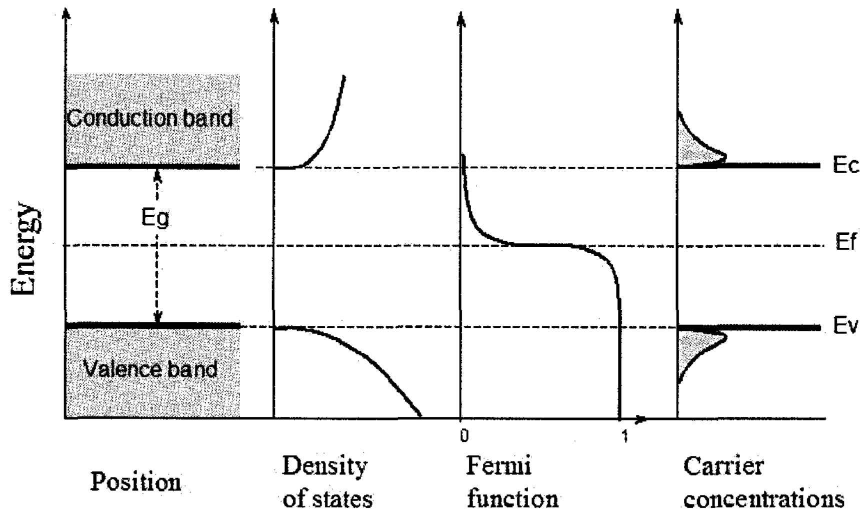

Fig. 1-1 The density of state of a semiconductor material, the carrier concentrations and Fermi function versus energy.

The density of electron states is determined by the energy dispersion function, $E(k)$. Fig. 1-1 illustrates $E(k)$ when electrons and holes are considered to be free particles. The solution of the wave-function results in a parabolic $E(k)$ function. The density of states as a function of energy is given by:

$$D_c(E) = \frac{1}{2\pi^2}\left(\frac{2m_c}{\hbar^2}\right)^{3/2}\sqrt{E - E_c} \qquad 1\text{-}2$$

and

$$D_v(E) = \frac{1}{2\pi^2}\left(\frac{2m_v}{\hbar^2}\right)^{3/2}\sqrt{E - E_v} \qquad 1\text{-}3$$

for the conduction band and the valence band, respectively, where m_c and m_v are the effective masses of electrons and holes. E_c and E_v are the energy of conduction and valence band edges. Integrating $D_c(E)f(E)$ over the energy from the band edges results in the total carrier concentrations:

$$n \approx N_c \exp\left(\frac{E_F - E_c}{k_B T}\right)$$
$$p \approx N_v \exp\left(\frac{E_F - E_v}{k_B T}\right) \qquad 1\text{-}4$$

where $N_c = 2\left(\frac{m_c k_B T}{2\pi\hbar^2}\right)^{3/2}$ and $N_v = 2\left(\frac{m_v k_B T}{2\pi\hbar^2}\right)^{3/2}$ are the effective density of states for the conduction and the valence band, respectively.

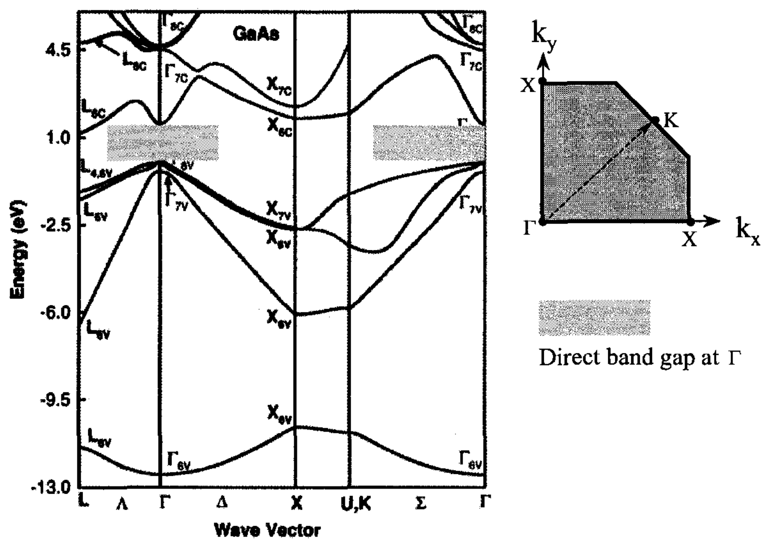

Fig. 1-2 Band dispersion diagram of GaAs throughout the first Brillouin zone. The left graph of the figure is adapted from M.L. Cohen and J.R. Chelikowsky [2]. The inset on the right indicates the definition of each point on the diagram using a quarter of the first Brillouin zone.

The energy dispersion relation of semiconductors is far more complicated than the one derived from the wave-function of free particles. The electrons in the semiconductors experience a periodic lattice potential that is built up by the atoms in the crystal lattice. Therefore the dispersion relations of semiconductors strongly depend on the crystal lattice structure. $E(k)$ deviates from a parabolic at large electron momentum values. The multi-band $K \cdot P$ method that uses a minimal set of empirical parameters can be applied to specific compounds for calculating energy dispersion. Fig. 1-2 shows the GaAs energy dispersion diagram at different lattice directions in the first Brillouin zone (where k is between $-\pi / a_0 < k_x < \pi / a_0$, and a_0 is the lattice constant). The band gap exists at the center of the first Brillouin zone Γ. As the diagram shows, $E(k)$ can be approximated by a parabolic function only at small electron momentum values. This approximation is sufficiently accurate for most of semiconductor calculations.

1.1.2 Band Gap of III/V Semiconductors and Alloys

III-V semiconductors are compounds of Group III and Group V elements. They normally have a zinc-blende crystal structure with two intertwined face-centered cubic sub-lattices of, for example, Ga and As atoms. Two properties have made III-V semiconductors important for optoelectronic applications. First, many of them are direct band gap materials. For direct band gap materials, carriers can transfer between the conduction and valence bands with no change in momentum, allowing light to be absorbed or generated efficiently. Second, it is possible to form alloys with more than two elements. By changing the alloy composition, the band gap and the lattice constant of III-V semiconductor alloys can be tailored to meet specified requirements, or to form heterojunctions where two materials with different band gap energy provide an extra potential barrier to carriers.

The circle points in Fig. 1-3 show the Γ-valley energy gaps as a function of the lattice constant for the zinc-blende forms of ten binary III-V semiconductors. The connecting curves represent the band gaps ternary alloys. The solid line indicates the Γ-valley direct gap. The dashed lines indicate several indirect gap materials where the Γ-valley is higher than the X and L conduction-band valleys. In terms of light-matter interaction, the band gap primarily determines the photon energy (or wavelength). The lattice constant confines ternary and quaternary alloys to certain binary compounds (substrates) in order to produce device quality materials. Reference [3] presents a comprehensive compilation of band parameters for most III-V compounds.

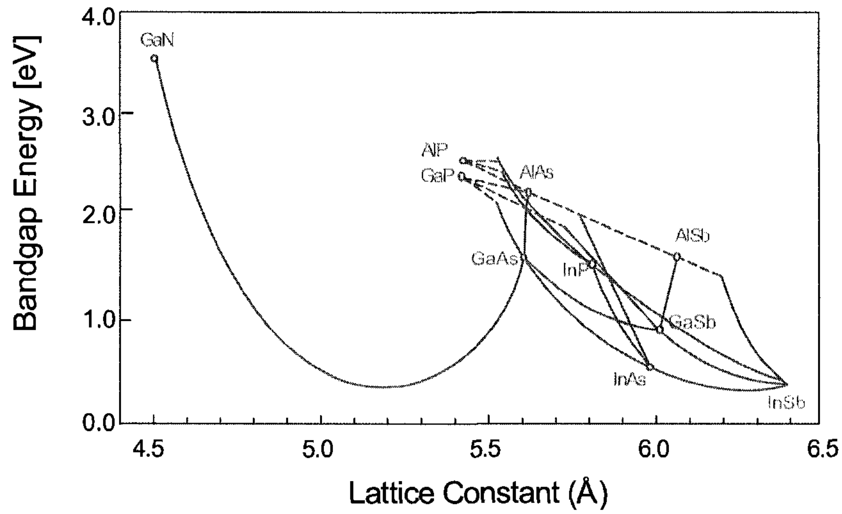

Fig. 1-3 The band gap energy and lattice constant for ten III-V compounds. The solid line indicates direct band gap alloys and the dashed line represents indirect band gap alloys.

1.1.3 The Linear Interpolation Approximation

The virtual crystal approximation (VCA) is the simplest treatment of the electronic structure of random semiconductor alloys. In this approximation, the electronic properties of the alloys are given by a linear interpolation between the properties of end-point materials. The alloy disorder effects are typically included through a bowing parameter. For example, the band gap of a ternary alloy can be interpolated as:

$$E_g(A_{1-x}B_x) = (1-x)E_g(A) + xE_g(B) - x(1-x)C \qquad 1\text{-}5$$

where the bowing parameter, C, accounts for the deviation from a linear interpolation between the two binaries A and B. This approximation is valid for most ternary and quaternary semiconductor alloys, in which there are only small differences between the properties of the end-point semiconductors. Composing the alloys in these cases, the bowing parameter is typically positive. That means the alloys parameters are normally smaller than the linearly interpolated value. The VCA approximation appears to be reliable for most alloys with small bowing effect. However, for the situation where one of the elements in the alloy is very different in atomic potential and dimension, a single bowing parameter is not sufficient for an accurate approximation due to the strong non-linear dependence on alloy composition. Other models must be applied instead.

1.1.4 Heterojunction and Quantum Wells

When layers of semiconductor materials of unequal band gaps are physically grown together, a semiconductor heterojunction is formed. As Fig. 1-4 illustrates, the carriers in the small band gap material will experience an additional potential beside the crystal lattice potential as the thickness of the small band gap material decreases to the atomic scale. At this scale, the potential confines the carriers and causes them to exhibit quantum effects. Solving the Schrödinger equation for a square well potential with thickness d_z gives

$$E_m = \frac{\hbar^2 k_{z,m}^2}{2m_n^z} = \frac{\hbar^2}{2m_n^z}\left(\frac{m\pi}{d_z}\right)^2 \qquad \text{1-6}$$

where E_m are the discrete sub-band energies, corresponding to the discrete wave numbers $k_{z,m}$. These solutions are plotted in Fig. 1-4. While only the discrete wave numbers $k_{z,m}$ are allowed in the z direction, the in-plane quantum well energy dispersion remains parabolic near the Γ point with the energy sub-bands as

$$E_m^t\left(k_x, k_y\right) = E_m + \frac{\hbar^2(k_x^2 + k_y^2)}{2m_{n,m}^t} \qquad \text{1-7}$$

The density of electron states of the QWs is a staircase function and it equals

$$D_m(E) = \frac{m_{n,m}^t}{\pi\hbar^2 d_z} \qquad \text{for } E > E_m \qquad \text{1-8}$$

within each sub-band m. The density of states decreases except at the step energies of the density of states compared to bulk materials.

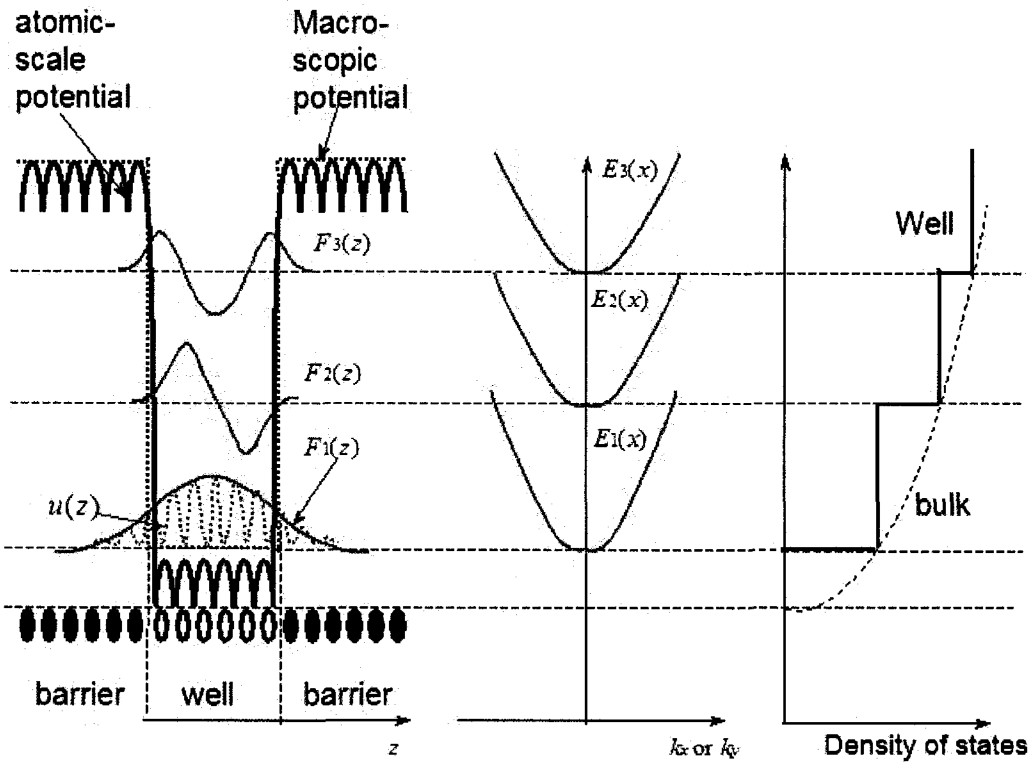

Fig. 1-4 Schematics of two-dimensional quantum confinement on the wave function, the energy dispersion and the density of states.

1.2 Semiconductor Laser Basics

1.2.1 Recombination Mechanisms

A variety of methods have been used for laser excitation, for example, optical pumping. However, carrier injection by means of a forward biased p-n junction is the only practical method. Photons are generated by the recombination of minority and majority carriers. Meanwhile, there exists a chance for injected carriers to recombine non-radiatively through either the recombination centers or the Auger recombination processes. The transition energy is transferred through phonons. The ratio of radiative to non-radiative recombination determines the light emission efficiency, and hence the threshold condition of the semiconductor lasers. In terms of band-to-band radiative transitions that are illustrated in Fig. 1-5, stimulated emission is the more important source of photons in laser operation, while spontaneous emission is a natural transition which dominants the carrier recombination paths in the absence of a classical field.

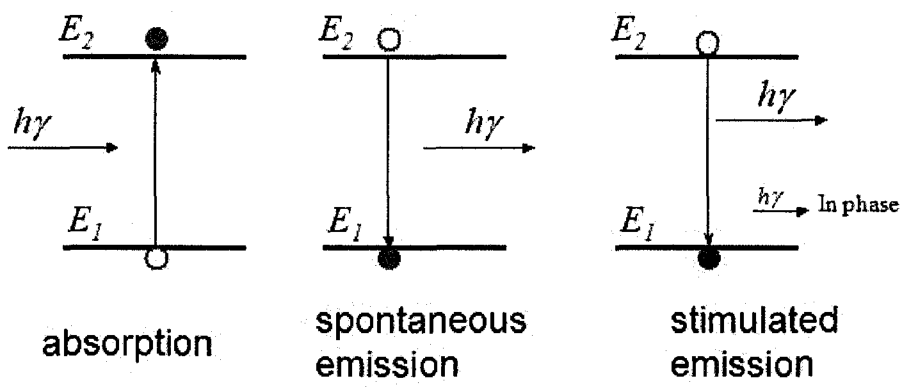

Fig. 1-5 Photon absorption and generation through the radiative recombination.

The rate of radiative processes depends primarily on the density of photons (field presented) and the density of the states pairs in materials. The latter is composed of two components: (1) the density of states in the conduction and valence bands, which is material dependent, and (2) the carrier injection that fills the available states. The net photon generation rate is:

$$R_{st} = R_{21} - R_{12} = R_r(f_2 - f_1) \qquad 1\text{-}9$$

where R_{st}, R_{21} are the recombination rates for stimulated and spontaneous emission, R_{12} is the rate of carrier generation, $f_1 = \frac{1}{e^{(E_1 - E_{Fv})/kT} + 1}$ and $f_2 = \frac{1}{e^{(E_2 - E_{Fc})/kT} + 1}$, where E_{Fc}, E_{Fv} are the conduction and valence band quasi-Fermi levels, and R_r is a general constant that relates to material. Under forward-bias, the quasi-Fermi levels are separated by a value that is slightly lower than the applied voltage across the junction. The net stimulated emission rate, and hence the optical gain, will become positive only when the separation of the quasi-Fermi levels is greater than the photon energy. Because the photon energy must at least be equal to the band gap energy, we must have

$$\Delta E_F = E_{Fc} - E_{Fv} > E_{21} = hv > E_g \qquad \text{1-10}$$

to achieve gain in semiconductors. This is the population inversion relation that must be satisfied to achieve a positive material gain.

1.2.2 Threshold Condition

For a laser to reach its threshold, the gain in the active region must compensate all loss mechamisms including propagation and mirror losses. The electric field exactly replicates itself after one round-trip in the cavity. The equivalent mathematical expression is $R_1 R_2 \exp\{(\Gamma g_{th} - \alpha_i)L\} = 1$, where g_{th} is the threshold gain, α_i is the propagation loss, Γ is the mode confinement factor, L is the cavity length and R_1, R_2 are the mirror reflectivities. Solving for the threshold gain, we obtain:

$$\Gamma g_{th} = \alpha_i + \frac{1}{L} \ln\left(\frac{1}{R_1 R_2}\right) \qquad \text{1-11}$$

When the laser is operating above the threshold, the steady-state gain in the laser cavity must be equal to its threshold value, $g = g_{th}$, due to gain saturation.

The gain of QW lasers can be modelled by a logarithmic relationship to the carrier density:

$$g = g_0 \ln \frac{N}{N_{tr}} \qquad \text{1-12}$$

where g_0 is an empirical gain coefficient and N_{tr} is the transparency carrier density. The threshold current density can be derived from 1-11:

$$\ln(J_{th}) = \ln(J_{tr} / \eta_i) + \left(\frac{\alpha_i + \alpha_m}{\Gamma g_0} \right) \qquad \text{1-13}$$

where η_i is the internal quantum efficiency and α_m is the mirror loss that equals the second term on the right side of equation 1-11.

1.2.3 Optical Gain

The material gain per unit length can be defined as the proportional growth of the photon density as it propagates along the laser cavity. Therefore the material gain per unit length becomes

$$g_{12} = g_{\max}(E_{21})(f_2 - f_1) \qquad \text{1-14}$$

where the maximum gain, $g_{\max}(E_{21})$, is determined by the density of states of the material. The Fermi factor $f_2 - f_1$ indicates the carrier injection level. The gain or absorption spectrum is bounded to a maximum value of $g_{\max}(E_{21})$. With no carrier injection, the material is strongly absorbing with an absorption spectrum equal to $-g_{\max}(E_{21})$. With sufficient carrier injection, we can invert the carrier population near the band edge and change the Fermi factor, $f_2 - f_1$, from –1 to +1, converting the absorption to gain. Since carrier inversion is highly concentrated near the band edge, $f_2 - f_1$ must steadily reduce back to –1 and the gain spectrum must become the absorption spectrum as the photon energy increases above the band edge. Fig. 1-6 depicts the conversion from absorption to gain for quantum-well materials with a step-like density of states. Many material properties can be obtained through gain spectral analysis.

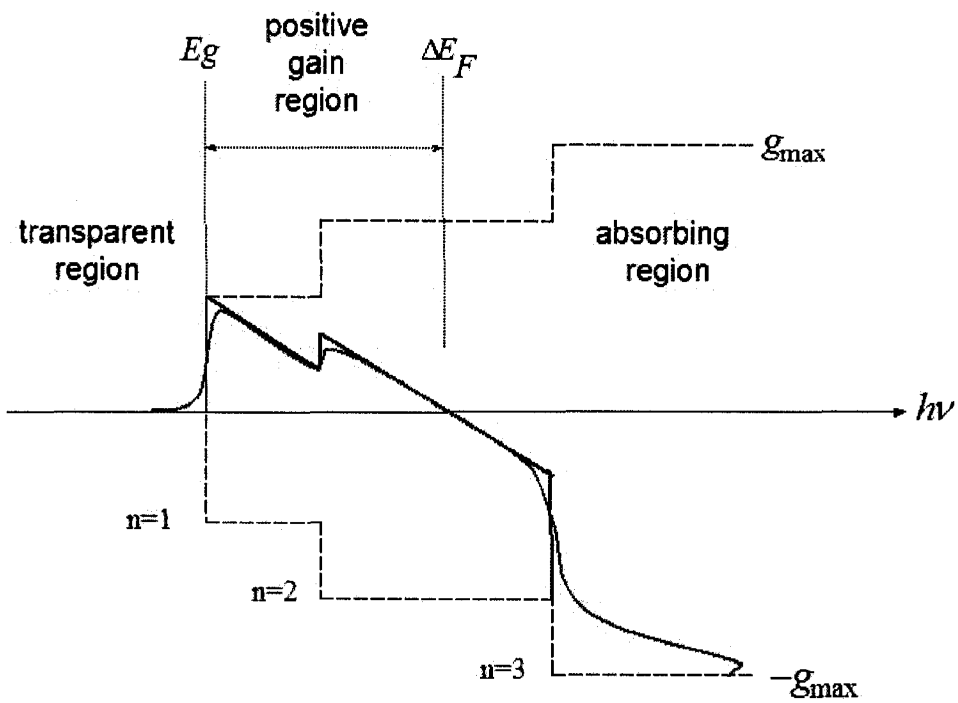

Fig. 1-6 Schematics of optical gain spectrum and the step-like density of electron energy states by quantum confinement. The separation of electron and hole quasi-Fermi levels is marked.

1.3 Semiconductor Laser Fabrication

1.3.1 Material Growth

To make multiple layer diode laser structures, it is necessary to grow single-crystal layers with precisely controlled thickness and composition over suitable substrates. Two important techniques in use today are molecular beam epitaxy (MBE) and metal-organic chemical vapour deposition (MOCVD). Both techniques have the capability to grow crystallized films as thin as a single atomic layer. However, as the name implies, they have different growth dynamics. In MOCVD, the growth is carried out with a moderate gas pressure. The chemical reaction happens near equilibrium conditions. The reaction can proceed in either the forward or the reverse direction to add or remove material. Therefore it can remove surface damage at onset growth. MOCVD tends to provide defect-free high quality interface materials, but MOCVD growth needs large amounts of toxic gases. The operation cost is high.

MBE, on the other hand, is a physical deposition process. It is carried out under ultra-high vacuum conditions. Beams of atoms evaporated from diffusion cells condense on a heated substrate. For stoichiometry control, MBE makes use of the fact that Group V elements are more volatile than Group III elements. Thus, if the substrate is sufficiently hot, Group V atoms will re-evaporate unless there is a Group III atom with which to form a compound. At the same time, the substrate must be sufficiently cool so that the Group III atoms will bond. Therefore, the growth rate is determined by the Group III flux. The Group V flux is typically set to several times higher than the level of Group III flux. This limits MBE to grow alloys that are composed of strongly volatile elements, for example, phosphor-content crystals. However, MBE's ultrahigh vacuum condition and precise flux control enables high purity materials and uniformly thin films.

1.3.2 Device Process

Practical diode lasers must emit light from a small aperture of a few microns to allow coupling to optical fibers and to support the fundamental mode of the optical waveguide. Lateral patterning of the active region is necessary. Beside its use in optical guiding, the laterally patterned narrow stripe plays an important role in current confinement so that as much current as possible is injected into the active region rather than finding some unproductive shunt path (leakage current).

Lateral confinement of carriers and photons has been accomplished in many ways, from simply using a narrow contact area to complicated buried-hetero-structure designs requiring multiple growth steps. Lasers with buried-hetero structures have lower threshold current and higher efficiency than other structures due to the superior electro and optical confinements. The processing, however, is more complicated, which normally means a low yield. Fig. 1-7 illustrates the process steps in constructing a ridge waveguide (RWG) lateral confinement structure. This process is standardized to produce the lasers in this work for process simplicity and reasonably good lateral confinement.

There are four steps in RWG laser processing. First, the ridge of the laser is defined by a photo-mask through lithography. After removal of SiO_2 but the region beneath the photo-resist, the wafer is dry etched by reactive ion etching (RIE) to a depth of ~200 nm above the laser active region. Second, the wafer is planarized to make electrical contacts. The whole wafer needs to be covered with SiO_2 and planarizing-coating (PC) photo-resist. RIE removes SiO_2, photo-resist and a thin layer of material on top of the ridges. Third, the wafer is covered with conducting metals. Ti/Pt/Au is e-beam evaporated on the wafer. Au plating finishes the formation of laser positive contacts. Then the wafer needs to be thinned mechanically. Au/Ge/Ni is e-beam evaporated on the backside of wafer to form laser negative contacts. Fourth, the processed wafer is diced to laser bars by mechanical cleaving. Laser bars are mounted p-side up on carriers.

1.4 Summary

This chapter reviewed the important aspects concerning semiconductor diode lasers, in particular the energy dispersion of semiconductors and the generation of optical gain in quantum wells. The fabrication techniques and lateral confinement structures have been introduced to prelude this thesis work.

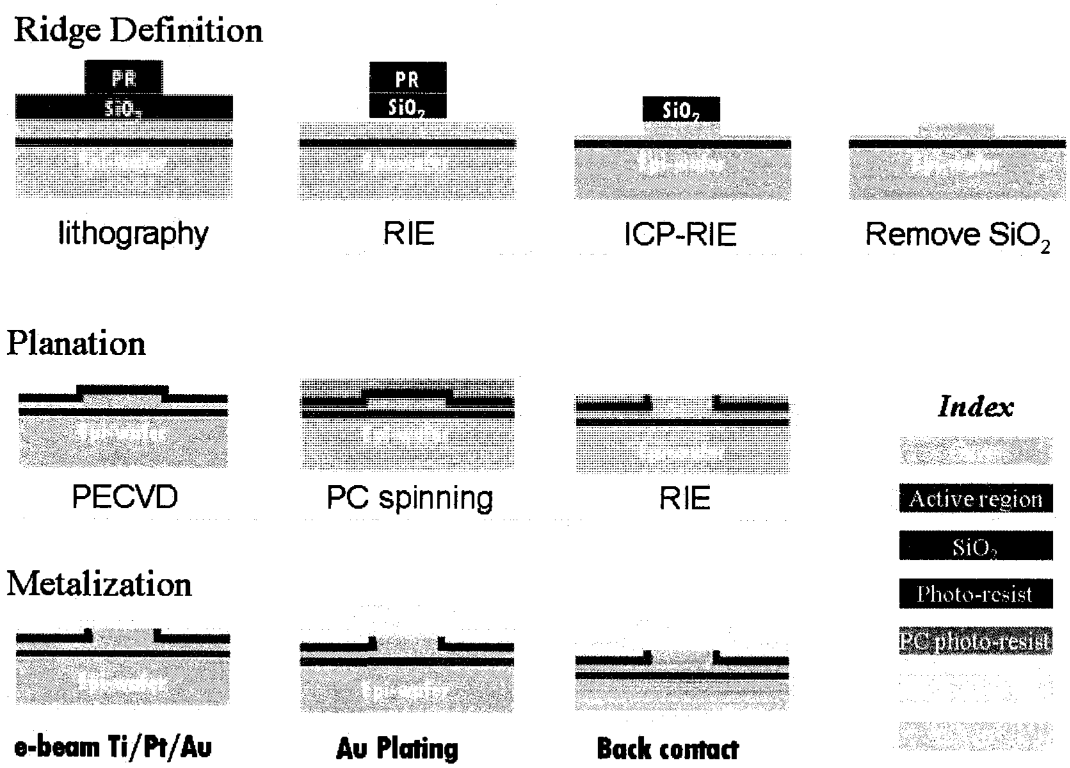

Fig. 1-7 Process flow for ridge waveguide (RWG) lasers.

Chapter 2 Background of Dilute Nitrides

2.1 *Introduction*

As communication networks evolve, data communication has generated an overwhelming demand for 1.31-1.55 μm laser diodes that can be modulated up to 10 Gbit/s ideally without temperature control. Traditionally, InGaAsP QWs grown on an InP substrate have been used to meet these wavelength requirements. However, those QWs are intrinsically sensitive to the temperature change due to a low conduction band offset and high non-radiative recombination rates. Tremendous efforts have been made to improve InGaAsP/InP laser performance [4, 5]. Nevertheless, it has been proved that there is no better way than adding electronics in the laser package to maintain temperature stability. Along with other reasons, such as the expense of InP substrates and processes, the cost of lasers in 1.3-1.55 μm range remains high.

Thus, other material systems have been intensively investigated. The candidates include AlInGaAs-InP [6, 7] and GaInNAs(Sb)/GaAs [8, 9]. While the dilute nitride system attracted more attention in the research community because of its unusual physical properties that challenge crystal growth, device process, modeling and characterization.

This chapter reviews the research work that has been carried out in the area of dilute nitrides, with an emphasis on material physics and QW design. At first, the uniqueness of dilute nitrides and the resulting advantages to device properties are introduced. Then the challenges and impact achievements in crystal growth and device process are summarized. Further, special considerations on QW structures are presented. The chapter finishes with the current status of dilute nitride laser development on edge-emitting lasers and on surface-emitting lasers.

2.2 Advantages of Dilute Nitride Materials

A number of articles have addressed the properties of diluted nitride material on GaAs, each with a slightly different focus. Ager III gave a comprehensive review of pioneering research works on the physical understandings and the material properties of dilute nitrides [10]. Lindsay and O'Reilly pioneered the use of the $K \cdot P$ Hamiltonian calculation to describe the conduction band dispersion of ordered GaInNAs with a small amount of nitrogen [11, 12]. Buyanova and Choulis provided the experimental support for the effects on band gap, the electron mass, as well as the recombination properties due to the incorporation of nitrogen [13, 14]. The most notable property of this material is its large observed band gap bowing. The band gap energy reduces dramatically with a small amount of nitrogen in the alloy. This enables the direct band gap of GaInNAs to access the near infrared, which is of great importance to the applications such as telecommunication and solar power conversion. At the same time, advances in thin-film deposition have allowed these materials to be grown with crystalline quality, allowing the development of dilute nitride lasers.

The advantages of dilute nitride lasers originate from the conduction band and the band alignment to GaAs. The large conduction band offset between GaInNAs QWs and GaAs barriers provides strong electron confinement that suppresses thermal-induced carrier leakage, enhances differential gain and reduces the temperature sensitivity of devices. Long-wavelength, uncooled lasers are possible. Further, GaInNAs QWs have a remarkably large effective electron mass compared to other conventional III-V compounds [15]. More efficient stimulated emission is expected from the similar effective masses for electrons and holes, because their densities of states will be similar and the pumping will produce more equal number of electrons and holes (see equation 1-8). Moreover, GaInNAs can be grown on GaAs substrates. The high refractive index contrast of the AlGaAs/GaAs Bragg reflectors forms an efficient mirror. Long wavelength vertical cavity surface emitting lasers (VCSELs) can be fabricated using GaInNAs as a quantum well material.

2.3 Challenges in Laser Fabrication

2.3.1 Crystal Growth

The growth of GaInNAs has proved to be substantially challenging compared to all earlier III-V systems. It is very difficult to incorporate sufficient nitrogen in a solid solution. Differences in the crystal structure between GaInN and GaInAs, the small size of nitrogen compared to As, and the high electro-negativity of nitrogen cause a large miscibility gap between GaInAs and GaInN. Device quality material must be grown at very low temperature, under metastable conditions, preferably by MBE. Only recently has MOCVD demonstrated device quality material.

The successful growths have taken placed in an MBE chamber with a reactive N_2/Ar RF plasma source [16]. The plasma source generates a variety of species at excited states. Which species are incorporated into the solid and the potential for ion damage is difficult to know. Also, phase segregation is hard to avoid, resulting in 3D epitaxial layers for the growth of a large number of QWs (more than 3).

Although it is challenging, many groups have achieved significant increases in photoluminescence (PL) intensity through growth optimization [17, 18, 19]. They have all drawn the conclusion that the RF source operating conditions and the substrate temperature are the most critical parameters for metastable growth of high quality materials. The growth temperature must be between 420°C and 450°C with the lower temperature favouring high nitrogen content alloys. The power of the RF nitrogen source must be optimized at the level that cracks the nitrogen source effectively while keeping the ion damage at the lowest.

In the recent effort to pursue long wavelength material beyond 1.3 μm, there have been two directions taken in crystal growth; both are trying to incorporate more nitrogen into the alloy. One approach is to use antimony surfactants to reduce the degree of phase segregation. Room temperature, continuous wave (CW) operation, 1.55 μm lasers have been demonstrated using this technique [20, 21]. The other approach focuses on modifying the growth dynamics to avoid the phase segregation and the strain relaxation. Groups from Infineon and the Paul-Drude Institute introduced extremely different growth conditions [22, 23]. Low V/III ratios of about 5 are used in the growth and the growth temperature is as low as 350°C. The extremely low growth temperature prevents strain relaxation, leading to an abrupt hetero-interface. The low As pressure increases the Group III diffusion length, and at the same time encourages more nitrogen into the layer by reducing the competition of Group V elements. Device quality material has been created using this technique.

2.3.2 Post-growth Treatment

Unlike conventional compounds, the GaInNAs alloy exhibits a metastable electronic band structure and unusual optical properties. During the growth, the chemical processes at the interface favour Ga-N bonds instead of In-N bonds. Such formations lead to ordered crystal structures with "small atom - small atom" and "large atom - large atom" bonds, which is less preferable to structural and optical properties. Therefore, post-growth treatment is needed to re-arrange the atoms and to change the nearest-neighbour environment of nitrogen.

Many experiments have been done to find the optimized conditions of post-growth annealing [24, 25]. Also, a number of measurement methods have been used to study the micro-structural change during annealing, and its influence on optical properties of GaInNAs [26, 27]. It is generally agreed that the reconfiguration of $N\text{-}Ga_4$ to $N\text{-}In_4$ leads to an effective blue-shift of the band gap energy at the same alloy composition [28]. Most importantly, the post-growth annealing process enhances the PL intensity and reduces the full width at half maximum (FWHM) of the epitaxial wafers [29].

2.4 Special Considerations on Laser Design

2.4.1 QW Compositions

The band structure of QWs largely determines the laser gain properties. Due to the band anti-crossing interaction between the nitrogen resonant states and the host conduction band edge, the band structure of GaInNAs/GaAs hetero structures changes greatly from GaInAs/GaAs . As a consequence, the dipole matrix elements, the electron effective mass and the gain versus the carrier concentration characteristics are modified. In addition to QW thickness and strain, the QW design must reflect those changes.

O'Reilly's group calculated the ideal InGaNAs QW laser gain characteristics using the 10-band $K \bullet P$ method. They have found that the peak gain and the differential gain at a fixed carrier density are decreased. The primary reasons are the reduced TE matrix element and the increased effective masses due to the addition of nitrogen [9]. The optimal GaInNAs QW should contain minimal nitrogen, ideally it should be nitrogen-free, if the alloy could emit at the required 1.3 μm wavelength without an excessively large strain.

There are particular trade-offs against the nitrogen content of the QWs. First, as indium reduces the band gap, we may reduce the amount of nitrogen in the alloy by maximizing the indium content. The maximum indium content can be estimated using the critical thickness of a GaInNAs/GaAs as a function of in-plane strain [30]. For pseudomorphic 7 nm-wide $Ga_{1-x}In_xN_yAs_{1-y}$ QW, we need $y > 1.5\%$ and $x < 39\%$ to achieve 1.3 μm emission. We can further reduce the nitrogen content by using narrower QWs or using a strain compensated structure. QW compositions ranging from $33\% < x < 40\%$ and $0.5 < y < 4\%$ have been reported.

2.4.2 Barrier Considerations

The temperature-insensitivity of the dilute nitrides originates from the large conduction band offset between the GaInNAs QW and the GaAs barrier. Therefore, GaAs is the natural choice for the barrier material. However, in seeking longer wavelength emission, more indium must be added to the QWs to keep the nitrogen content low. Since indium atoms are larger than gallium atoms, the $Ga_{1-x}In_xAs_{1-y}N_y$ QW is highly compressively strained. A structure that makes use of a tensile strained barrier to compensate for the compressively strained well is employed to keep the lattice un-relaxed.

In addition to strain compansition, the tensile GaAsN barrier extends emission wavelengths to longer wavelengths in two ways: First, the lower barrier reduces quantum confinement and thus the electron-hole transition energy. Second, the wavelength blue-shift resulting from the post-growth annealing is effectively suppressed compared to a conventional GaAs barrier [31]. This further increases the emission wavelength. Lasers with an emitting wavelength of over 1.4 μm have been demonstrated using conventional QW compositions with GaNAs barriers [32, 33].

GaAs is a substrate that can be lattice matched not only to GaInAs, but also to GaAsP and GaInP. This means that tensile-strained GaAsP can be used as a barrier material. Using tensile-strained GaAsP barrier layers allows a highly-compressively-strained $In_{0.4}Ga_{0.6}As_{0.995}N_{0.005}$ QW to be grown on a high-aluminium-content lower cladding layer. Devices of this type have achieved high current injection efficiencies[30]. Hitachi's group has also discovered that aluminium is an active impurity in GaInNAs QWs that results in three-dimensional growth of the QWs. Aluminium-free lasers using GaInP as the cladding layer have been suggested [34]. This device eliminates the use of active aluminium and enhances the PL intensity thought the smoother interfaces of epi-layers [35].

2.5 Recent Achievements

Ever since dilute nitride III-V compounds were proposed by Kondow for long-wavelength lasers on GaAs substrates [8], considerable effort has been expended on researching the material and device physics. Research teams from government laboratories, universities and industry slowly advanced the frontier until the industrial down turn in 2002. Up to that point, most theoretical models that described this novel material were developed with the support of experimental evidence. Experimentally, CW operation, long-wavelength VCSELs had been demonstrated for the first time [36]. Tansu *et al.* summarized the progress in edge-emitting lasers [37] and Pessa *et al.* reviewed the progress on VCSELs [38]. Although threshold currents of CW operation, edge emitting lasers were reduced to the levels comparable to lasers made from some conventional materials, they were still much higher than those of lasers made from InGaAs, the host material of GaInNAs.

After 2002, the research on dilute nitrides developed new directions. The objectives were to produce uncooled, high-speed, directly modulated lasers, targeted to short-reach optical links, and lasers of broad bandwidth. A group from Cielo demonstrated a 2.5 Gbit/s OC48 capable GaInNAs VCSEL [39]. Groups from France and Germany achieved small-signal modulation bandwidths of 9.7 GHz and 13.8 GHz, on Fabry-Parot (F-P) and distributed feedback (DFB) edge emitting lasers, respectively [40, 41]. Some groups are also seeking long-wavelength emission using GaInNAsSb QWs [20, 21].

A summary of the major research groups and their results on dilute nitride lasers is shown in Table 2-1. The summary focuses on the publications after 2004. From these results, we can conclude that GaInNAs lasers emitting at 1.3 μm may be suitable for an uncooled, 10 Gbit/s light source. Laser reliability studies will demonstrate the actual success or failure of this objective. Almost no experimental data are available to date, except for one MOCVD grown laser [42]. In particular, the reliability studies need to focus on nitrogen cluster evolution over time and their effects on non-radiative recombination centers. Note that research into dilute nitride lasers emitting at 1.55 μm is still in its infancy. The focus thus far has been on understanding material properties and advancing crystal growth, rather than on targeting applications. The research into such pentary materials is valuable in opening up a new area of metastable semiconductor alloys.

Table 2-1 Development of dilute nitride lasers since 2004.

Research group	λ (nm)	Active material	Structure	Epi-method	η_{ext}	I_{th} (mA)/J_{th} (Acm^{-2})*	T_0	T_1
Larsson, Chalmers, Sweden [43]	1280	GaInNAs/GaAs	RWG	MBE	0.46	22	180	-
Harris, Stanford, USA[17]	1500	GaInNAsSb/GaNAs	Broad area	MBE	0.49	450	73	125
Bonnefont, Alcatel, France [44]	1334	GaInNAs/GaAs	RWG	MBE	0.29	26	80	-
Gupta, NRC, Canada [21]	1553	GaInNAsSb/GaNAs	RWG	MBE	-	132	83	-
Gupta, NRC, Canada [45]	1280	GaInNAs/GaAs	RWG	MBE	0.46	34	155	218
Mitomo, Sony Material Lab, Japan [42]	1300	GaInNAs/GaAs	RWG	MOCVD	-	25	180	-
Riechert, Infineon, Germany [23]	1510	GaInNAs/GaAs	Broad area	MBE	0.35	780	40	-
Hierro, ISOM, Spain [46]	1435	GaInNAs/GaAs	Broad area	MBE	0.27	1755	78	-
Tansu, Wisconsin-Madison, USA [47]	1378	GaInNAs/GaNAs	Broad area	MOCVD	0.31	563	60	70
Nishida, Epson, Japan[48]	1262	GaInNAs/GaAs	VCSEL	MOCVD	0.55	-	-	-
Yamada, NEC, Japan[49]	1342	GaInNAs/GaAs	VCSEL	MOCVD	-	2.8	-	-

* Broad area lasers are evaluated by using threshold current density.

2.6 Summary

This chapter introduced dilute nitride alloys and the advantages in using them to make GaAs-based diode lasers. With their unique band gap bowing, dilute nitride QWs appear to address the long-wavelength challenge for surface emitting lasers due to the existence of highly AlAs/GaAs reflectors, which are not possible in InP-based system. The challenges that face fabrication of high-efficiency dilute nitride lasers are crystal growth, device processing and design. However, both edge emitting and surface emitting lasers have been reported. The chapter reviewed the impact of existing research in the field, as context to the present work.

Chapter 3 Dilute Nitride Laser Properties

3.1 Introduction

This chapter presents the experimental characterization of the dilute nitride lasers, with an emphasis on laser's static and dynamic properties. The measurement-based results enable a critical assessment of the material and the fabrication process. In addition, the chapter describes some analytical methods and measurement techniques used during the laser parametric tests.

The 1.3-μm GaInNAs laser's light-current (L-I) characteristics were measured for laser samples with different cavity lengths and ridge widths. This geometry-dependent L-I analysis is used to extract lateral leakage current and laser internal parameters. Laser temperature stability is studied by replicating the same measurements at various temperatures.

Optical spectroscopy was used to analyze laser beam properties. High-resolution spectra were taken at varying temperatures and bias currents. From the emission spectra, wavelength shift rates over temperature and current are determined.

High-resolution amplified spontaneous emission spectra (ASE) were taken to study the loss and gain properties of the 1.3 μm GaInNAs laser. The optical modal gain spectra were extracted using a computational algorithm. The modal gain spectra reveal the laser's transparency current, the internal loss and the differential gain. The values are compared with those in lasers made from conventional materials.

Laser noise analysis is used to determine laser intrinsic dynamics. The phase noise broadens the linewidth of the laser beam, which is described by the linewidth enhancement factor (α-factor). Moreover, the spectral broadening of a directly modulated laser is proportional to laser's α-factor. Determination of laser's α-factor is one of the important parts of laser dynamics. A unique method was found to exclude the junction-temperature-induced refractive index change. The α-factor of GaInNAs laser was measured, and compared with that of conventional lasers.

The modulation bandwidth of lasers was studied by analyzing and measuring the power-dependent laser relative intensity noise (RIN). The resonance frequency and damping factor are extracted from the measurements. The relationship between these parameters results in a figure of merit for high-speed lasers. Measurement-based calculation is applied to estimate the laser maximum modulation bandwidth.

3.1.1 Device Description

The 1.3 μm GaInNAs lasers were grown on an n-type GaAs (100) substrate in a custom VG V90 MBE system using conventional effusion cells for Ga, In and Al with As_2 generated by a valved cracker cell. A VEECO UniBulb radio-frequency plasma cell was used to produce active nitrogen using Ar/N_2 dynamic gas [50]. The laser active region is composed of two 6.7-nm-thick $Ga_{0.67}In_{0.33}N_{0.015}As_{0.985}$ quantum wells separated by a 20-nm-thick GaAs barrier. Two additional 148 nm thick GaAs layers, one above and one below the QWs, complete the waveguide. The n-type and p-type cladding layers are 1.8-μm-thick n-$Al_{0.33}Ga_{0.67}As$:Si and 1.5-μm-thick p-$Al_{0.33}Ga_{0.67}As$:Be, doped at 2.0×10^{18} cm^{-3} and $1.0\times10^{18}cm^{-3}$, respectively. A 200-nm-thick heavily-doped (1.0×10^{19} cm^{-3}) p-GaAs:Be layer was grown as the top contact layer. Detailed layer structure is shown in Table 3.1.

The transition energy versus the nitrogen content y for the $Ga_xIn_{1-x}N_yAs_{1-y}$ QW was systematically studied using photoluminescence and absorption spectroscopy [51]. Type I band alignment lines up the band structure of GaInNAs QWs and the GaAs barriers. The transition energy between electrons and heavy holes was calculated as 988 meV (1255 nm) for the 6.7-nm-thick QWs containing 67 percent of gallium and 1.5 percent of nitrogen. The conduction band offset for the above QW was found to be as high as 441 meV.

Table 3-1 The epitaxial structure of the 1.3 μm DQWs GaInNAs/GaAs laser.

	Material	Doping (cm^{-3})	Thickness (nm)	Composition	Layer description
11	GaAs:Be	1.00E+19	200		p-contact
10	$Al_xGa_{1-x}As$:Be	1.00E+18	1500	x=0.33	p-cladding
9	GaAs	n/a	148		SCH layer
7	$Ga_xIn_{1-x}N_yAs_{1-y}$	n/a	6.7	x=0.67, y=0.015	Well
6	GaAs	n/a	20		Barrier
5	$Ga_xIn_{1-x}N_yAs_{1-y}$	n/a	6.7	x=0.67, y=0.015	Well
3	GaAs	n/a	148		SCH layer
2	$Al_xGa_{1-x}As$:Si	2.00E+18	1800	x=0.33	n-cladding
1	GaAs:Si	2.00E+18	200		n-buffer
	(100)-GaAs:Si	2.00E+18			Substrate

After epitaxy, the wafer was annealed in an oven at 775°C for 5 minutes. N_2 flows into the oven to provide an inert ambient. The epitaxial wafer was capped with a GaAs substrate to avoid out-diffusion of As. RWG lasers were fabricated using inductively coupled plasma reactive ion etching (ICP-RIE). The ridge widths of the lasers were defined by contacting mask ranging from 2 to 10 μm. TiPtAu and NiGeAu metallizations were applied to the p and n sides of the wafer, respectively, for contacts. The lasers were cleaved to form Fabry-Perot (F-P) cavities at lengths of 450, 600, 900 and 1200 μm. The facets are as cleaved. The laser bars were mounted p-side up onto alumina carriers.

One processed laser bar is shown in Fig. 3-1. The secondary electron microscope (SEM) picture shows the cross-section of a typical ridge structure. The mask used to fabricate these devices was designed for the purpose of screening lasers. Bars produced with this mask contain 18 devices, consisting of 9 pairs of devices with ridge widths from 2 to 10 μm.

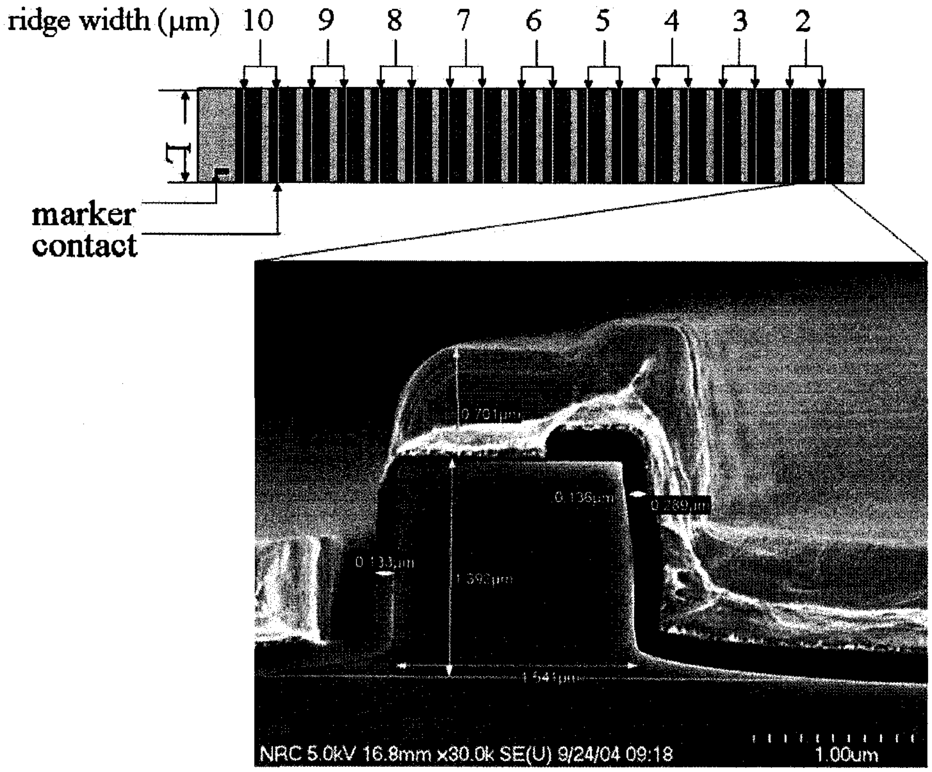

Fig. 3-1 Schematic of a processed bar. The cross-sectional SEM was taken for a 2 μm wide ridge device. The actural ridge width is marked.

There are three advantages of this mask: (1) The duplication of devices on each ridge width provides an easy method to verify the device properties, as each pair should be identical. (2) The threshold current should have a linear dependence on ridge width for devices wider than the carrier diffusion length, estimated to be between 3 and 4 μm. (deviation from linearity is an indication of improperly functioning devices). (3) The slope efficiency should exhibit a small, smooth variation with device width, tending towards lower efficiencies for wider devices. Deviations from this trend, or large scatter in the data, may indicate substandard devices. For devices with two cleaved facets, the scatter in the data could also be an indication of uneven mirror reflectivity, which would preclude an analysis of the internal laser parameters based on the external differential efficiency.

3.2 *Light Current Characteristics*

3.2.1 Distribution of Laser Light Current Characteristics

L-I measurements were performed on devices with different ridge widths and cavity lengths, with current injection provided by an ILX lightwave LDP-3811 precision pulsed current source (1 μs pulse width, 1% duty cycle). The pulse measurement permitted the elimination of obviously suspect devices without over heating the junction and keeping the L-I analysis accurate. Laser temperature was maintained at 20°C during measurement through active control of alumina carriers by an ILX lightwave LDC-3722 laser diode controller. A calibrated large-area Ge detector collected light from the laser's front facet. A Keithley 199 multi-meter measured the voltage across the laser diodes and an HP 3440A multi-meter measured the photocurrent generated by the Ge detector. After acquiring basic information of the lasers, selected devices were further characterized by other measurements.

Equipment described above and those used for other measurements in following text were calibrated regularly. Sensitivity of equipment was kept within instrument's specs through maintenance. Furthermore, either Labview or C was programmed for data acquisition. Small increment of injection current further improved measurement accuracy. Therefore the instrumental uncertainty in this work was small.

On the other hand, temporal effects due to device aging were significant. Threshold current of the devices in this work are relatively high. The heat produced by high injection current increases junction temperature, thus degrades devices as time goes. The phenomenon is more pronounced in InGaNAsSb 1.55μm devices. Measurements under pulsed current injection were performed to keep the measurement uncertainty as small as possible, unless measurements require CW current injection. Nevertheless, temporal effects dominate measurement uncertainty.

As we gained more understanding of dilute nitride, improvements on laser structure, MBE growth and device process had been on-going during the period of this thesis work. For each processed wafer, only selected parts were cleaved into laser bars. Lasers on those bars were screened using pulsed L-I measurement. Other measurements were performed only on selected lasers. The results reported here were mainly for process feasibility study, as those selected lasers were very representive to a particular process, and the results of measurements were sensitive to changes.

Three apparent trends are discussed below, for representative L-I measurements, as presented in Fig. 3-2 through Fig.3-7

(1) All lasers from this batch show a change in L-I characteristics after they have been biased once. This change is shown in Fig. 3-2 for a 4 μm x 448 μm (W, L) device. The device was measured three times under pulsed mode. The first scan exhibits a delayed threshold onset, and a typical L-I curve, as compared to the later two, which show very similar characteristics. The reason for this, while not definitively known, may relate to the residue of SiO_2 during the process of opening the ridge. This residue may migrate after the annealing of metal-semiconductor interface by a surge of current. Good Ohmic conduction then is estiblished since.

(2) The laser's L-I characteristics show a uniform distribution over laser geometry. The threshold current increases linearly with ridge width (Fig. 3-5). The slope efficiency varies monotonically with cavity length

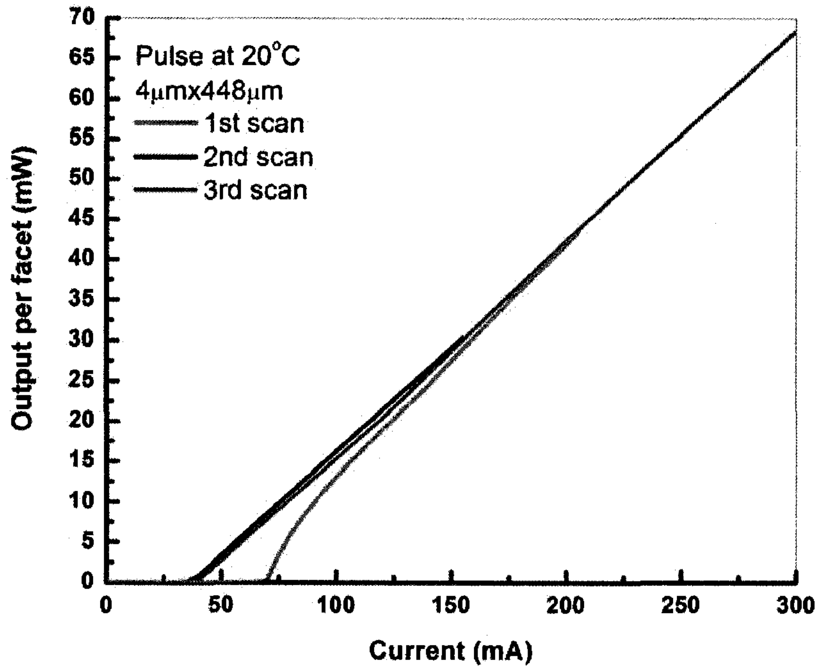

Fig. 3-2 L-I characteristics of one device measured under three sequenced scan. The changes in the characteristics shows that the device needs a surge of current to behave normally.

(Fig. 3-6) up to the highest of ridge width. Note that a plot like Fig. 3-3 reveals a typical data, indicative of a suspect device (3 μm ridge device in this bar).

(3) The lasers also operate in CW current injection mode. Selected devices were measured with CW current injection. Fig. 3-4 is a representative result for a 3 μm x 450 μm device. This device shows a threshold current of 36 mA. The slope efficiency of one facet is 0.216 mW/mA considering both facets. This value corresponds to an external quantum efficiency of 0.453. The wall plug efficiency is calculated to be 16%, using the ratio of total optical power over the electrical power. A separate measurement shows that the laser has a turn-on voltage between 0.8 and 0.9 V. The value is slightly smaller than the band gap energy and it agrees well with the theory. The series resistance, evaluated over the region from 50 to 150 mA, is 4.5 Ω.

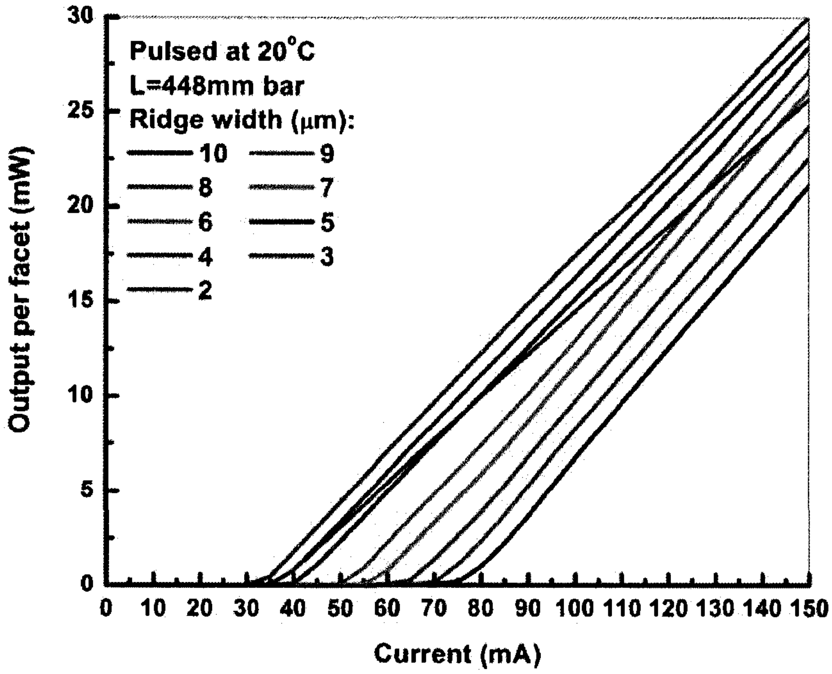

Fig. 3-3 L-I characteristics measured at pulsed current injection mode for the lasers on a 448 μm long bar. The curves are from the second scan.

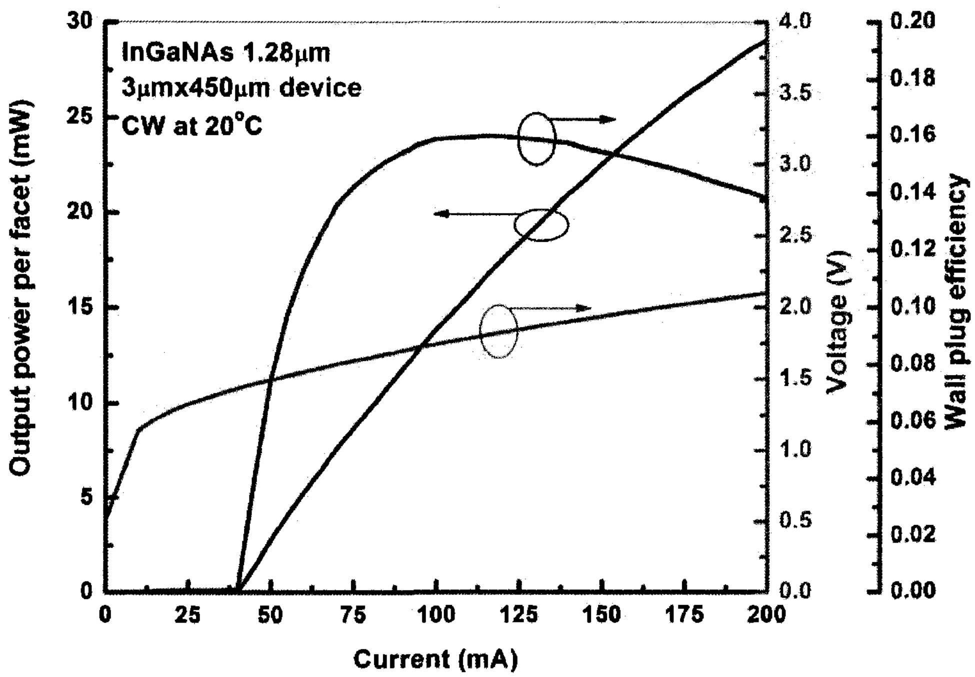

Fig. 3-4 L-I-V characteristics measured at CW current injection mode for a 3 μm x 450 μm device. The wall plug efficiency takes both facets into account.

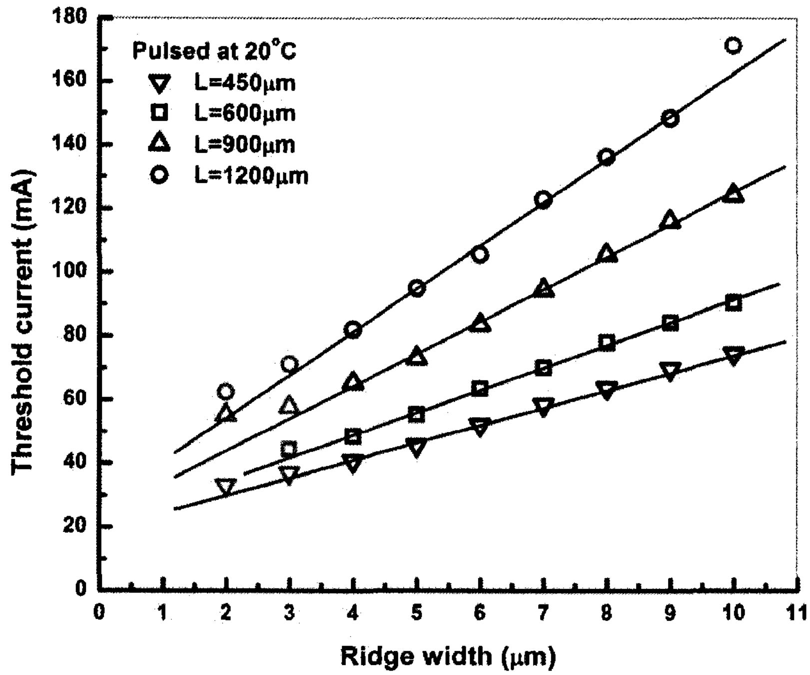

Fig. 3-5 Threshold currents as a function of the laser ridge width. The laser cavity length is indicated. Data in red are excluded from the linear fit.

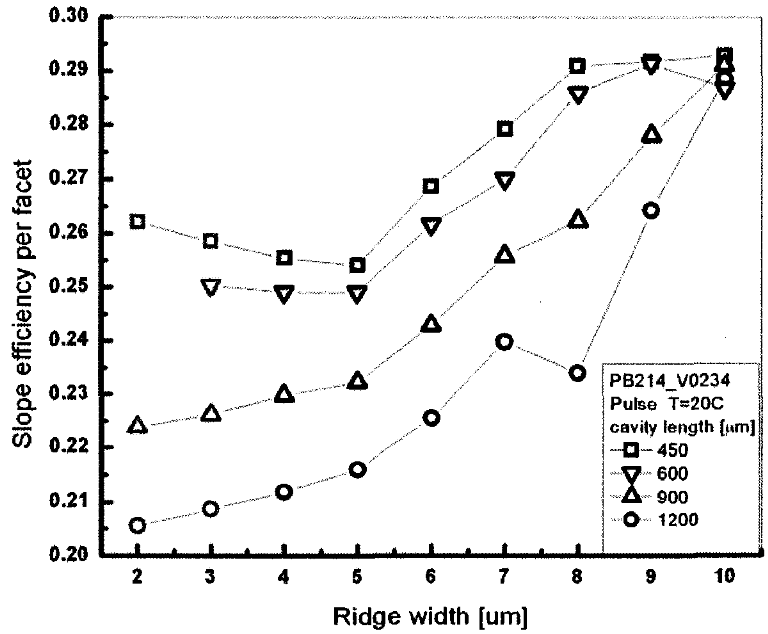

Fig. 3-6 The slope efficiency as a function of ridge width for the lasers of varying cavity lengths measured with pulsed mode. The cavity lengths are indicated. Data in red are excluded from the linear fit.

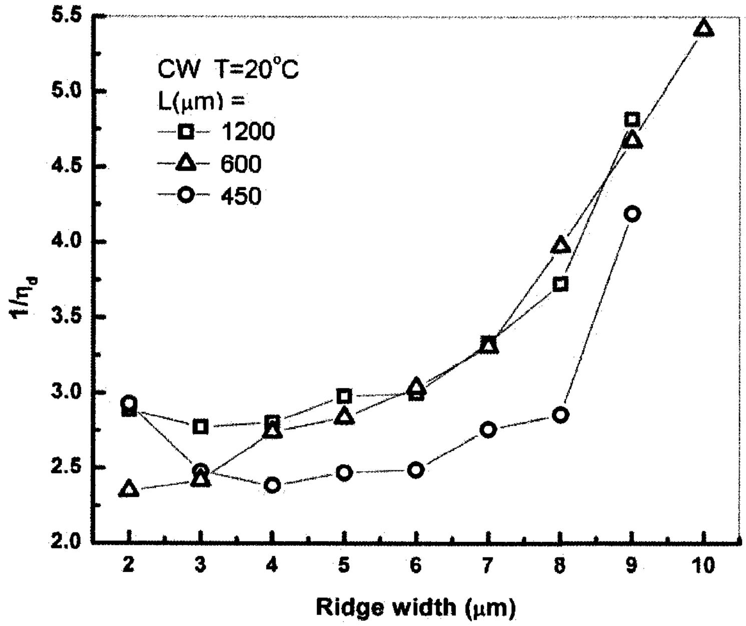

Fig. 3-7 The reciprocal external quantum efficiency as a function of ridge width for lasers with varying cavity lengths. The measurements were carried out with CW mode. The significant reduction of laser efficiency for the wide-ridge devices indicates strong junction self-heating.

3.2.2 Lateral Leakage Estimation

The cavity-length-dependent pulsed L-I measurement technique is used because it is an easy method for estimating laser properties such as gain and loss. Strictly speaking, this technique yields accurate results only for broad-area lasers. Applying the same analysis to ridge waveguide lasers will cause considerable error due to lateral current confinement. The accuracy of this method as applied to RWG lasers is determined by the amount and treatment of lateral leakage current.

Hu *et al.* have suggested a simple method to determine the lateral leakage current in a RWG laser [52]. As Fig. 3-5 indicates, the threshold current of RWG lasers is linearly dependent on the laser ridge width, with only small deviation from linearity of the narrowest ridge devices. The threshold current can be approximated as the sum of two parts, as:

$$I_{th} = I_{leak} + (L_c J_{th}) \cdot W \qquad 3\text{-}1$$

where I_{leak} is the lateral leakage current, L_c is the laser cavity length, W is the ridge width of the RWG laser and J_{th} is the threshold current density. This implies that the intercept of the linear fit in Fig. 3-5 yields the lateral leakage current. The slope of the linear fit gives the threshold current density for devices of that cavity length. Table 3-2 lists the estimated lateral leakage currents, and the threshold current densities with leakage exclusion. The lateral leakage current takes as much as half of the threshold current in short-cavity devices. This will increase the threshold current, and thus the heat during laser operation.

Table 3-2 The estimated lateral leakage current and the threshold current density for varying cavity lengths.

L (μm)	J_{th} (Acm^{-2})	I_{leak} (mA)
450	1295	17.4
600	1182	20.5
900	1136	23.5
1200	1123	27.1

Fig. 3-6 plots the slope efficiency as a function of ridge width measured for pulsed current injection. The wide-ridge lasers show a high slope efficiency of about 0.29mW/mA. However, under CW current injection, the slope efficiency undergoes a significant reduction. Fig. 3-7 shows that the reciprocal quantum efficiency increased rapidly for ~9 μm or wider ridges. The difference in laser efficiency for the two current injection modes, particularly for large threshold current devices, indicates strong junction self-heating. The laser performance can be improved by reducing the lateral leakage current through structural optimization.

3.2.3 Internal Parameter Extraction

The drive to lower threshold currents in laser diodes requires accurate assessment of the active material. This information is used when modeling and optimizing the device structure. Although dilute nitride materials have been intensively studied for a decade, device quality materials have been produced only recently. These quality materials make it possible to investigate GaInNAs material parameters using measurable device characteristics.

Cavity-dependent pulsed L-I measurements are used to determine the laser internal loss, internal quantum efficiency, optical gain factor and transparency current. These parameters are related in a QW laser in the context of the following two assumptions: (1) the material gain produced by current injection is logarithmically related to current density (cf. Equation 1-13). (2) the laser reaches its threshold when net modal gain equals net optical loss (cf. Equation 1-11). Thus, a linear fit of threshold current density versus reciprocal cavity length gives the gain factor, g_0, via the slope and the transparency current density, J_{tr} via the intercept. Similarly, a linear fit of reciprocal external quantum efficiency versus cavity length results in the laser internal quantum efficiency, η_i, via the reciprocal slope and internal loss, α_i, via the intercept.

Accurate parameter extraction is possible only if junction self-heating is avoided, as suggested by the different L-I characteristcs in pulsed mode and CW mode discussed above. This requires pulsed L-I measurements at a fixed ambient temperature (20 °C here) with a small duty cycle (1%) and pulse width (1 μs).

Care must also be taken when calculating the laser external quantum efficiency from the slope efficiency, $\Delta P / \Delta I$, as obtained from the pulsed L-I measurements. For the as cleaved facets, the reflectivities of both facets are presumed identical. The external quantum efficiency is equal to:

$$\eta_d = 2\frac{q\lambda}{hc}\frac{\Delta P}{\Delta I} \qquad 3\text{-}2$$

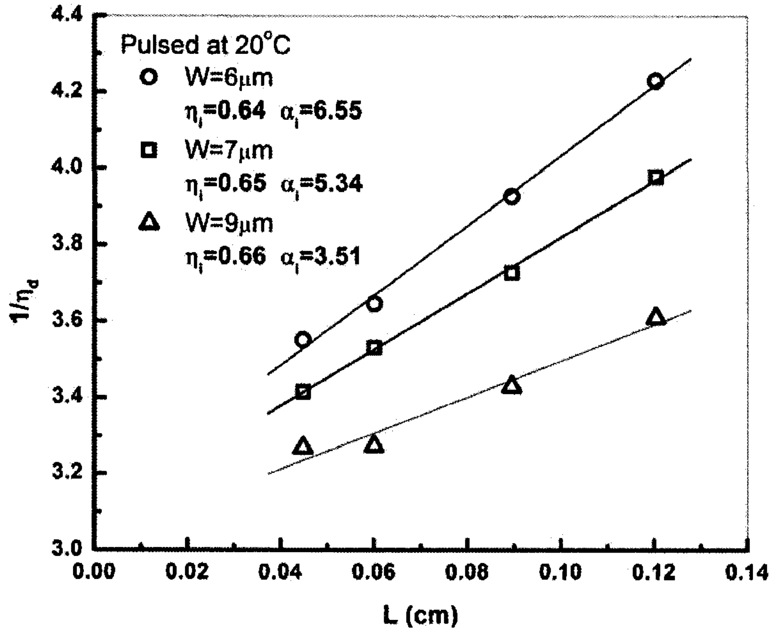

Fig. 3-8 The reciprocal external quantum efficiency as a function of cavity length. The internal loss and the internal quantum efficiency are extracted using the linear regressions. The ridge widths are indicated.

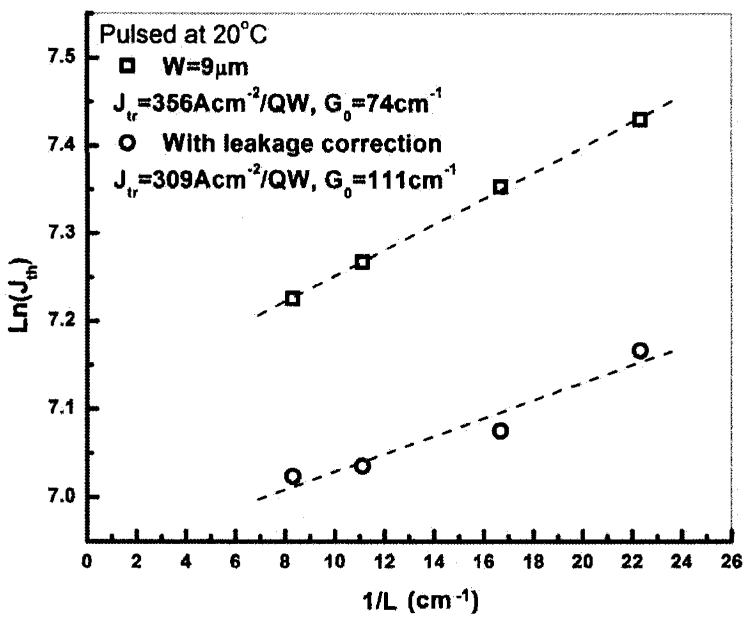

Fig. 3-9 The threshold current density as a function of the reciprocal cavity length. The gain factor and the transparency current density per QW are extracted, with and without the leakage current correction.

In the case of coated facets, the reflectivity is not same for the front and the rear mirrors. The output power is unevenly distributed between facets. A laser normally emits more power from the front facet. To correlate the external quantum efficiency to the slope efficiency, a factor smaller than two must be applied to Equation 3-2. This factor is related to the facet reflectivity [53] as:

$$F = \frac{1 - R_f^2}{\left(1 - R_f^2\right) + \frac{R_f}{R_r}\left(1 - R_r^2\right)} \qquad 3\text{-}3$$

Fig. 3-8 plots the inverse external quantum efficiency as a function of the laser cavity length. The linear fit to the data gives an internal quantum efficiency of 0.65. The divergence in internal loss values (3.5 - 6.5 cm^{-1}) reflects the carrier density effects on the active region. The narrow ridge devices have higher internal absorption due to higher carrier densities. Using an internal quantum efficiency of 0.65 and an internal loss of 5 cm^{-1}, the gain factor and transparency current density are deduced from linear fits in Fig. 3-9. Two sets of data are presented in Fig. 3-9. One has a leakage current correction, meaning the threshold current density in Fig. 3-9 is the difference between the measured value and the lateral leakage current density in Table 3-2. This set of data gives a transparency current density of 618 Acm^{-2} and a gain factor of 111 cm^{-1}. These results agree well with values obtained from subsequent measurements presented later. These results are also equivalent to those of broad-area lasers used as test samples. Parameters extracted without lateral leakage correction clearly understate the gain factor and overstate the transparency current density. This demonstrates that lateral leakage correction must be applied to the cavity dependent L-I analysis for RWG lasers.

3.2.4 Temperature Characteristics

One of the reasons that a laser degrades when operating at high ambient temperatures is that thermally excited electrons can surmount the barriers. This effect, however, is weak in the QW/barrier combination formed by GaInNAs QWs and GaAs since the potential barrier is quite high. Devices that are stable in temperature are expected.

The physics involved in extracting the influence of temperature on laser behaviour is challenging. It requires knowledge of the band structure and recombination mechanisms, both of which vary with material and device structure. However, for the purpose of a laser temperature sensitivity assessment, two figures of merit suffice, T_0 and T_1. These are defined based on the variation of laser threshold current and slope efficiency over temperature, respectively. The rate of increase is typically similar for lasers made from material systems that have similar recombination mechanisms for a given temperature range.

The characteristic temperature, T_0, is defined by the Arrhenius relationship of a diode laser:

$$I_{th}(T) = I_0 e^{T/T_0} \qquad \text{3-4}$$

where I_0 is the threshold current at absolute zero degree and T_0 is the characteristic temperature. As equation 3-4 indicates, for the same amount of temperature increase, threshold current increaseas less for devices with larger T_0. In other words, device performance would not degrade much as temperature increase, making uncooled operation possibly for large T_0 lasers.

T_0 can be extracted from the inverse slope of a linear fit to the natural log of the threshold current over the specified temperature range. T_0 is largely determined by the dominant recombination mechanism, which varies greatly with temperature. Fig. 3-10 shows pulsed L-I measurements across the temperature range from 20 to 75°C at intervals of 10°C (except the last one). This temperature range is limited by the capacity of the test station's Peltier thermoelectric cooler (TEC). A characteristic temperature of T_0 =155 K is estimated for a 3 μm x 1204 μm device as seen in Fig. 3-10. The same figure shows another device (3 μm x 1196 μm) with T_0 =132 K. Devices of other geometries were measured to obtain statistical information on T_0. The average T_0 of the GaInNAs laser devices is about 130 K. This value is far higher than those of AlGaInAs-InP (T_0=84 K) [54] and InGaAsP-InP (typical T_0 is 60 K) lasers [55] in the 1.3 μm wavelength range, explaining the observed superior temperature stability of the dilute nitride lasers.

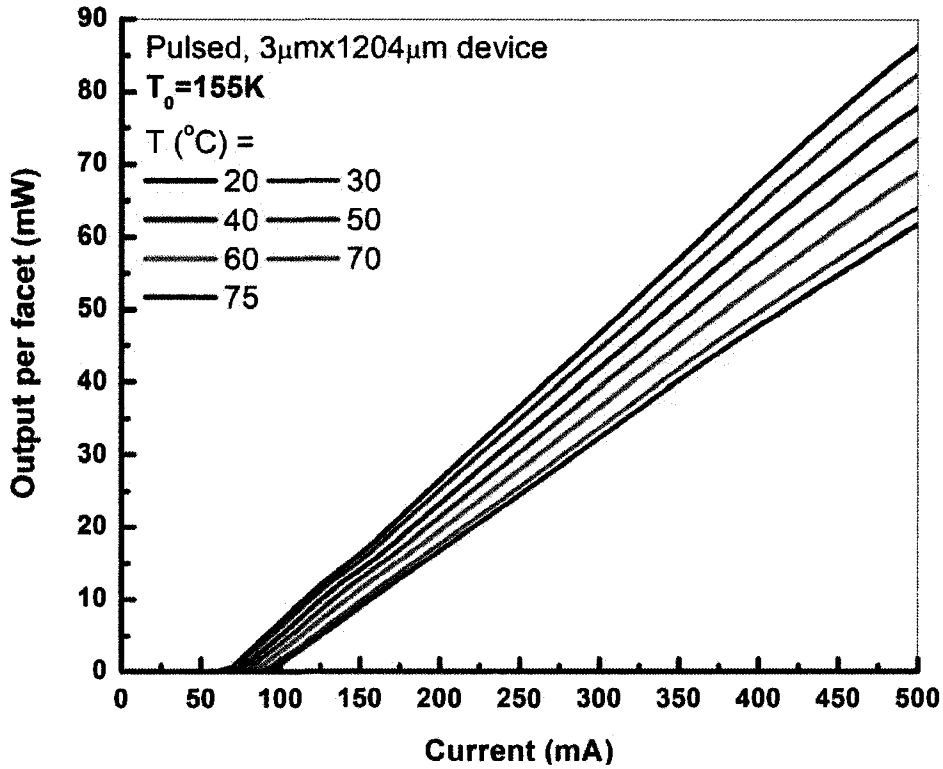

Fig. 3-10 Pulsed mode L-I characteristics measured at varying temperature for a 3 μmx1204 μm device.

The other figure of merit, T_1, is extracted from:

$$\frac{1}{T_1} = -\frac{1}{\eta_d}\frac{d\eta_d}{dT} \qquad \text{3-5}$$

assuming the external quantum efficiency, η_d, decreases linearly with increasing temperature. T_1 was found to be 228 K using the same device that gave a T_0 = 155 K. Fig. 3-11 shows typical results for T_0 and T_1.

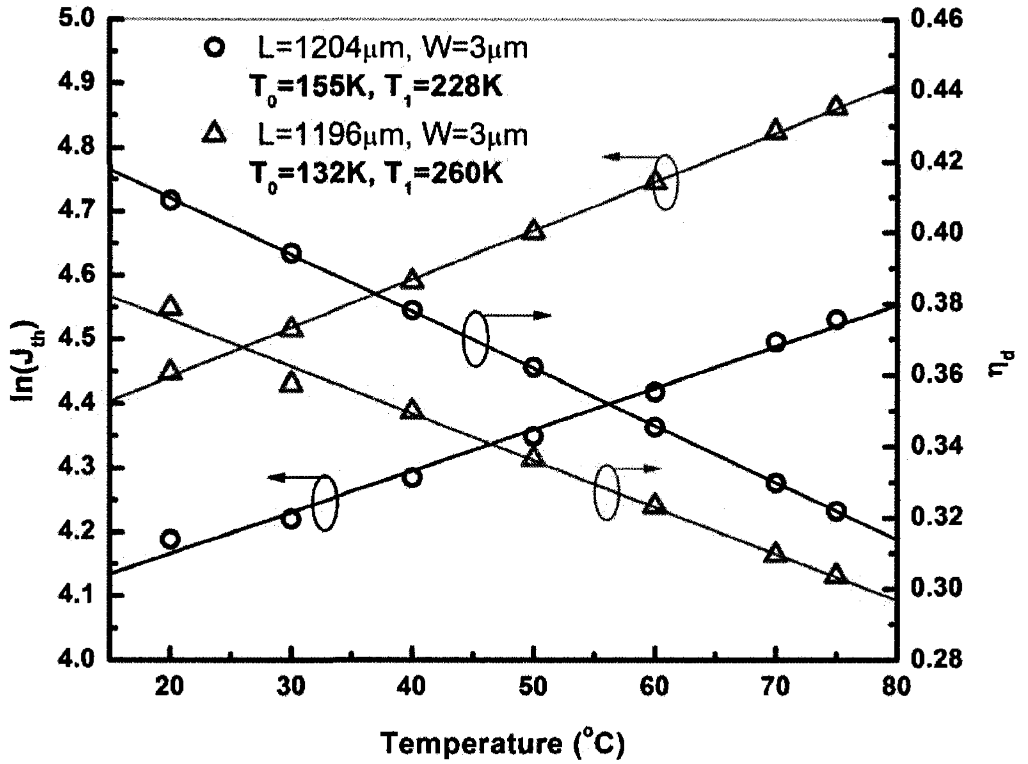

Fig. 3-11 The threshold current density and external quantum efficiency as a function of temperature for two devices with a similar geometry. T_0 is 132 K and 155 K, and T_1 is 260 K and 228 K, respectively, evaluated from 20°C to 75°C.

3.3 *Optical Characteristics*

3.3.1 Optical Loss

In Section 3.2.3, the internal optical loss of the laser was estimated using geometry dependent analysis. This section describes an optical measurement method for determining the laser's internal loss. This measurement is based on the principles of F–P cavity resonance.

In a F-P resonant cavity, the steady-state output intensity at the end of a laser may be approximated as [57]

$$I_{\pm}(v) = \frac{B(1+R_{\mp}G_S)(1-R_{\pm})}{(1+RG_s)^2 - 4RG_s\sin^2(\theta)} \qquad \text{3-6}$$

where $R_{\pm}$ are the reflectivities of the mirrors, G_s is the single-pass intensity gain, and B is the total amount of spontaneous light at frequency v coupled into the laser mode. The "positive" superscript refers to the right-hand end of the laser, while the "negative" superscript refers to the left-hand end.

For a symmetrical laser cavity, $R^2 = R_+R_-$, and $\theta = 2\pi Lv/c$, where $c/2L$ is the free spectral range of the resonator. At $\theta = 0$ and $\theta = \pi/2$, the intensity of the output reaches its minimum and maximum, respectively. The intensity ratio between the adjacent peak and valley can be calculated as [57]:

$$r = \frac{I_p}{I_v} = (\frac{1+G_sR}{1-G_sR})^2 \qquad \text{3-7}$$

At transparency, the single pass gain relates to the internal loss by

$$G_s = e^{-\alpha_i L} \qquad \text{3-8}$$

where L is the cavity length. The internal loss, α_i, can be found using equations 3-7 and 3-8 once the intensity ratio r is determined.

The facet reflectivity can be calculated using the laser's effective index of reflection, n_{eff}, in Fresnel's reflectivity formula (see equation 3-16 below). n_{eff} can be estimated by measuring the longitudinal mode spacing in the F-P cavity using

$$\Delta\lambda = \frac{\lambda^2}{2Ln_{eff}} \qquad \text{3-9}$$

where λ is the lasing wavelength and $\Delta\lambda$ is the mode spacing.

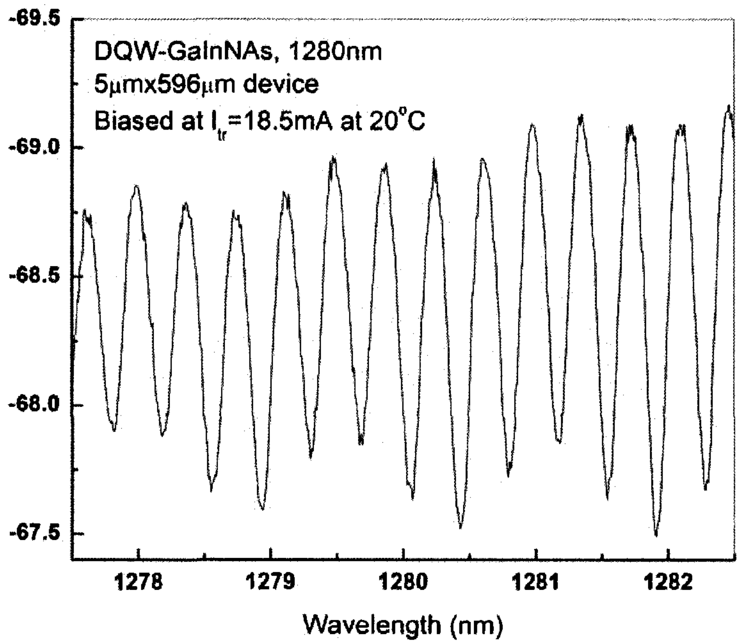

Fig. 3-12 The Fabry-Perot resonance of the spontaneous emission from a GaInNAs laser taken by a high resolution OSA at 20°C. The laser was biased at its transparency current of 18.5 mA. The vertical axis is in dBm.

A tapered polarization-maintaining (PM) fiber is used to couple the spontaneous emission from the laser facet to an ANDO 6317B optical spectrum analyser (OSA). Coupling efficiencies as high as 20% can be achieved by carefully adjusting the position of PM fiber using a three-dimensional micro stage. Fig. 3-12 is the spontaneous emission spectrum near the emission wavelength. During this measurement, the laser was biased at the transparency current. To compensate for the asymmetric intensity of the resonance waveform, ten data points of r were determined. The internal loss was calculated as 22.8 cm^{-1} and 13.5 cm^{-1} for the GaInNAs and the InGaAsP lasers, respectively, using the average value of r.

3.3.2 Optical Gain

Similar to the optical loss measurement, the optical gain may be determined by considering the multiple reflection of a photon in a laser cavity at a sub-threshold current. Assuming that only the fundamental mode is excited in the laser cavity, the electric field at facet one is F_1, where F_1 is the fundamental mode field. The reflected field is $\sqrt{R_1}F_1$. The field travels back along the cavity and experiences reflection at facet two. When the field returns to facet one, the electric field is $\sqrt{R_1 R_2}F_1 \exp(-2\alpha(\lambda)L)$, where $\alpha(\lambda)$ is the mode propagation gain (or loss) in the cavity. Considering multiple reflections of this field by both facets, the total field of the constructive wave at facet one is [56]:

$$F_1^+ = F_1 \sum_{n=0}^{\infty} \left(\sqrt{R_1 R_2}\right)^n \exp(-n\alpha L) = \frac{F_1}{1-\sqrt{R_1 R_2}\exp(-\alpha L)} \qquad 3\text{-}10$$

and the total field of the destructive wave at the same facet is:

$$F_1^- = \frac{F_1}{1+\sqrt{R_1 R_2}\exp(-\alpha L)} \qquad 3\text{-}11$$

The constructive and destructive waves can be measured outside of the laser cavity by means of intensity variation. The ratio of the maximum and minimum intensities P_+ and P_- respectively is:

$$r(\lambda) = \frac{P^+}{P^-} = \left(\frac{1+\sqrt{R_1 R_2}\exp(-\alpha(\lambda)L)}{1-\sqrt{R_1 R_2}\exp(-\alpha(\lambda)L)}\right)^2 \qquad 3\text{-}12$$

Hence, the modal gain or loss may be calculated as:

$$\alpha(\lambda) = \frac{1}{L}\ln\left(\frac{\sqrt{r(\lambda)}+1}{\sqrt{r(\lambda)}-1}\right) + \frac{1}{2L}\ln R_1 R_2 \qquad 3\text{-}13$$

The material gain, $G(\lambda)$, is related to $\alpha(\lambda)$ by:

$$\Gamma G(\lambda) = \alpha(\lambda) \qquad 3\text{-}14$$

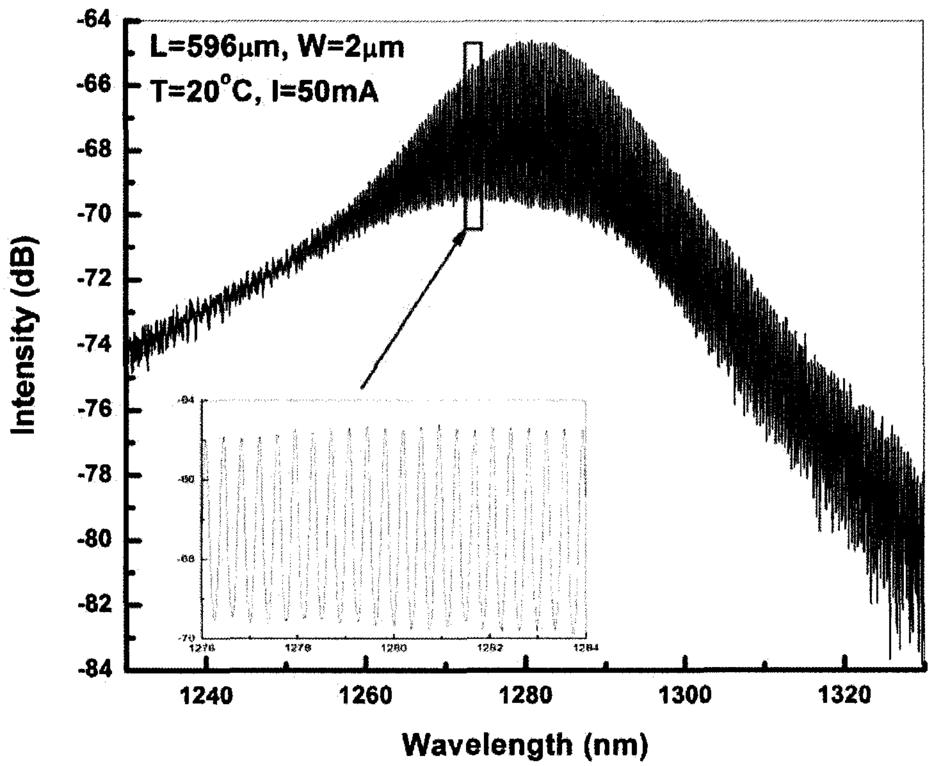

Fig. 3-13 The sub-threshold spontaneous emission spectrum of a 1280 nm GaInNAs laser. The insert displays a section of the spectrum near the lasing wavelength.

During the gain spectra measurement, the device under test (DUT) was temperature controlled and biased at sub-threshold. The laser output was coupled into a PM fiber in the same manner as for the loss measurement. The OSA recorded the spectra over a 100 nm span with a high sensitivity. The resolution bandwidth was 0.1 nm. The intensity of the spontaneous emission was measured five times at each measurement point and the average value was taken. TE and TM polarized spectra may be distinguished using a high extinction ratio (over 25 dB) polarizer between the PM fiber and the OSA.

Fig. 3-13 displays the spontaneous emission spectrum below threshold, from 1230 nm to 1330 nm. The insert more clearly shows the F-P resonance mode across an 8-nm-wide spectral range. A noise elimination algorithm was implemented to locate the peaks and valleys. The program also read the maximum and minimum intensities. To increase the accuracy of gain extraction, algorithms such as the mode sum minimum method [57] and the nonlinear least-squares fitting method [58] were exploited. An averaging method was used to compute the intensity contrast, $r(\lambda)$, at any wavelength by first averaging the intensities of each adjacent peak, $\frac{1}{2}(P_i + P_{i+1})$, and then dividing by the intensity of the intermediate valley, V_i [59]:

$$r_i = \frac{P_i + P_{i+1}}{2V_i} \tag{3-15}$$

This algorithm allows accurate gain extraction down to -60cm^{-1} and effectively extends the modal gain acquisition to the long-wavelength side of the spontaneous spectrum where the white noise is strong. However, single transverse mode, short cavity lasers yield excellent data. These devices have a "clean" spectrum and the intensity contrast can be read more accurately.

The 2 μm × 450 μm and 2 μm × 600 μm devices were selected for the gain spectra measurements. The mode spacings, $\Delta\lambda$, are 0.50 nm and 0.38 nm, respectively, at a lasing wavelength of 1280 nm. The calculated effective indexes n_{eff} are 3.657 and 3.593, respectively. The mirror reflectivities are then calculated using Fresnel's reflectivity formula:

$$R = \left(\frac{n_{eff} - 1}{n_{eff} + 1}\right)^2 \tag{3-16}$$

as 0.326 and 0.319, respectively.

The observed mode spacing varies slightly over the 100 nm wavelength span due to the dependence of n_{eff} on wavelength. However, this effect is negligible in the calculation of the facet reflectivity and the modal gain.

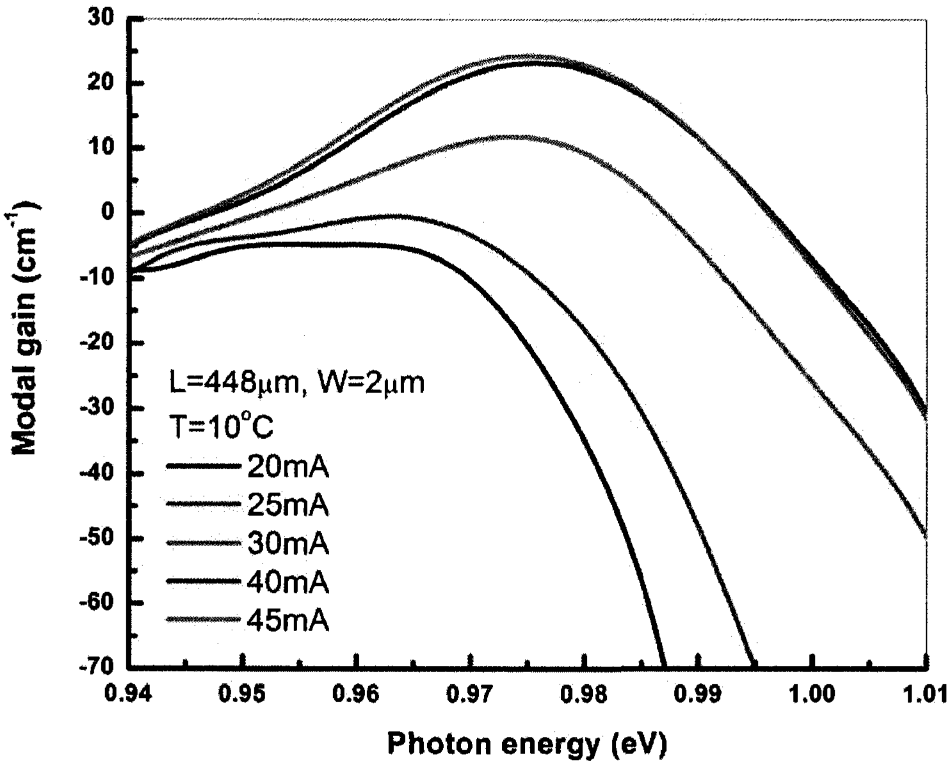

Fig. 3-14 Modal gain spectra measured at 10°C for a 2 μm x 448 μm GaInNAs laser. The bias currents are indicated in the figure.

Fig. 3-14 shows the modal gain spectra as a function of photon energy, in electron-volts (eV), measured at 10°C for increasing bias currents. The gain spectra reveal the following features of the GaInNAs lasers:

(1) Internal loss

When the photon energy is below the band gap, the material is transparent to light. This is seen in Fig. 3-14 where the modal gain converges to a single absorption value on the low photon energy side of the spectra. Since the material does not absorb light, the absorption at these values indicates a loss from the laser waveguide, that is the internal loss, α_i. For 450 and 600-μm-long devices, the internal losses are about 10 and 5 cm^{-1}, respectively. This agrees well with the internal loss estimated by laser geometry dependent analysis.

(2) Material gain

At threshold of 44mA, the amplitude of the modal gain peak is equal to the mirror loss. This amplitude is 24.4 cm^{-1} for the 450 μm long device at gain saturation. This value is in good agreement with the calculated mirror loss of 25.1 cm^{-1}, using $\alpha_m = (1/L) \times Ln(1/R)$, and the facet reflectivity of 0.326. The net material gain is found to be about 1000 cm^{-1}, using an internal loss of α_i=7cm^{-1}, and a confinement factor of $\Gamma = 0.032$ (calculated using a mode solver).

(3) Transparency current

The transparency current can also be estimated from Fig. 3-14. It equals the bias current at the lasing wavelength that gives zero net modal gain. At 10°C, the laser experiences stimulated emission at 1276 nm (972 meV). Linear interpolation between the 20 and 25 mA data yields a transparency current of 24 mA. This value over estimates the transparency current by including the lateral leakage current, which equals 17.4 mA for the 450 μm long devices (Fig. 3-5). Subtracting the leakage current, the transparency current was estimated to be between 6 and 7 mA. This corresponds to a transparency current density of ~350 A-cm^{-2} per QW. This value is in good agreement with the transparency current density extracted from Fig. 3-9 (356 A-cm^{-2} for 9μm ridge width) using the cavity length dependence analysis.

The modal gain temperature dependence is shown in Fig. 3-15 for gain spectra obtained at 10, 30 and 50°C. Temperature induced band gap shrinkage is demonstrated by the strong red shift in gain peak as the temperature increases. The average rate of increase is 0.58 nm/°C over a 20 °C interval. This value is similar to both InP-based materials and highly-strained InGaAs-GaAs materials, whose reported rates range from 0.3 to 0.5 nm/°C [60, 61].

Gain reduction at higher operating temperatures leads to temperature sensitive devices. The average gain reduction rate of GaInNAs is –0.15 cm^{-1}/°C over a 20°C interval. The magnitude of this reduction is less than that found for 1.3 μm AlGaInAs-InP and InGaAsP-InP QW structures (about –0.3 cm^{-1}/°C) [54, 60].

In Fig. 3-16, the peak intensity and peak wavelength of the net modal gain are plotted as a function of bias current for measurements taken at 10°C and 30°C. Due to stimulated emission carrier recombination, the modal gain is clamped at the threshold value of 31.4 cm^{-1}. The differential modal gain $d\Gamma g/dI$ was 1.25 cm^{-1}/mA from 20 to 40 mA at 10°C. This is lower than the typical value of 5 cm^{-1}/mA for InGaAs(P)/InP lasers [60]. However, it is comparable to a value of 1.9 cm^{-1}/mA reported for lasers made from AlGaInAs/InP [54].

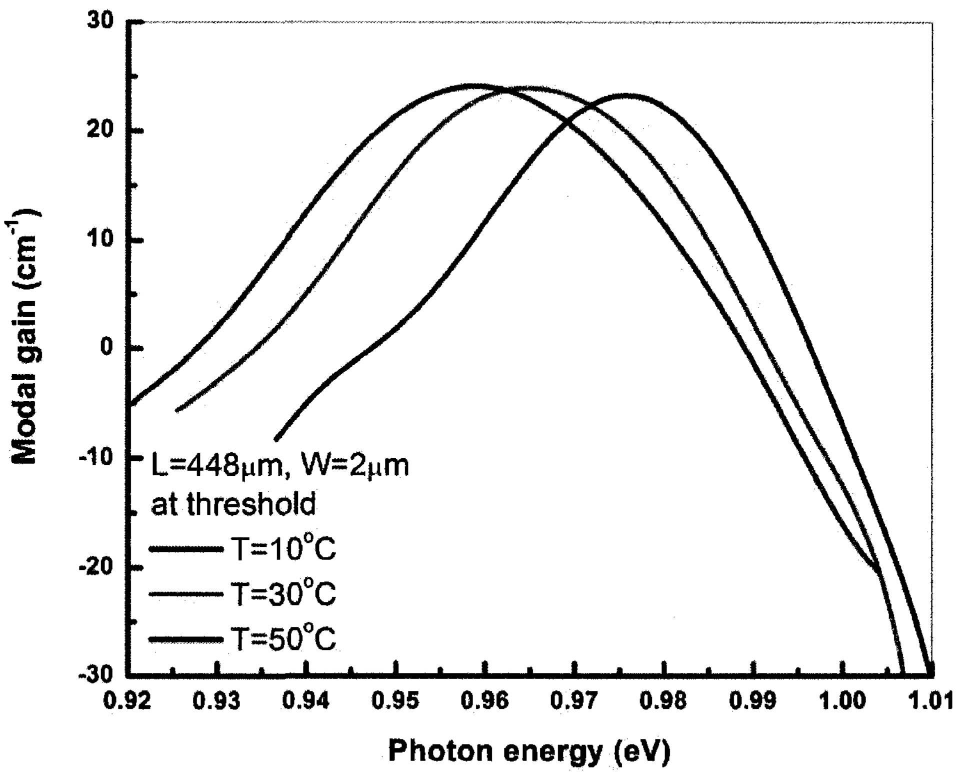

Fig. 3-15 Modal gain spectra taken at different temperatures for the 450 μm long device. The bias currents are set to the laser threshold.

Since differential gain is related to the variation in carrier density, the net modal gain may be represnted against its dependence on carrier density rather than current. The carrier density below the threshold can be approximated by:

$$n = \frac{I\tau_d}{eV} \quad 3\text{-}17$$

where V is the volume of quantum wells, e the carrier charge, and τ_d the carrier life time. For the 600 μm long device, the ratio of the carrier density to the injection current is 2.0×10^{17} cm^{-3}/mA, given the following assumptions: (1) there is no carrier leakage at sub-threshold currents, (2) for small injection currents, the carrier lifetime follows a $1/n$ dependence, and it asymptotically decreases to a limiting value. (3) the limiting carrier lifetime in GaInAsN QWs is 0.5 ns. This value of carrier life time has been measured for both 1.3 μm InGaAsP and AlGaInAs QWs [54, 60, 62]. (4) the carrier life time of GaInNAs is of the same magnitude as InGaAsP and AlGaInAs materials.

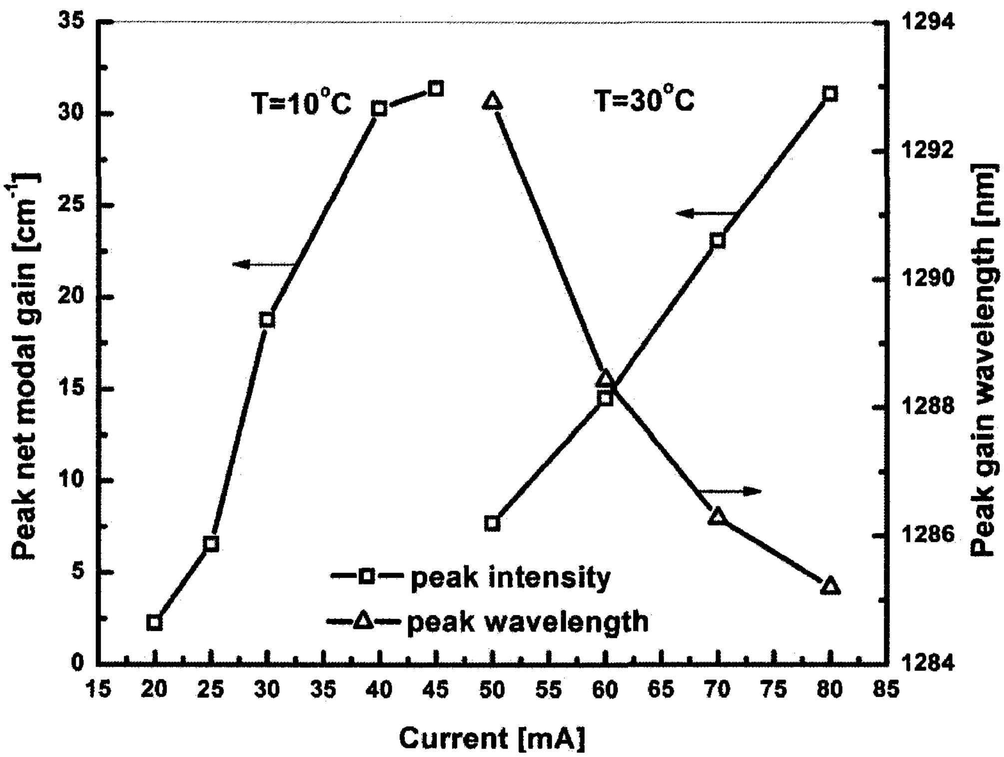

Fig. 3-16 Peak net modal gain and wavelength as a function of the sub-threshold current, measured at 10 and 30°C.

Peak modal gain against carrier density is plotted in Fig. 3-17 for the 600 μm-long device. It increases monotonically to the threshold value and saturates as stimulated emission recombination dominates. This laser exhibits the highest differential modal gain among the lasers that have been tested. The value is 13.6 $cm^2/10^{18}$ at a carrier density of $5\times10^{18}\,cm^{-3}$.

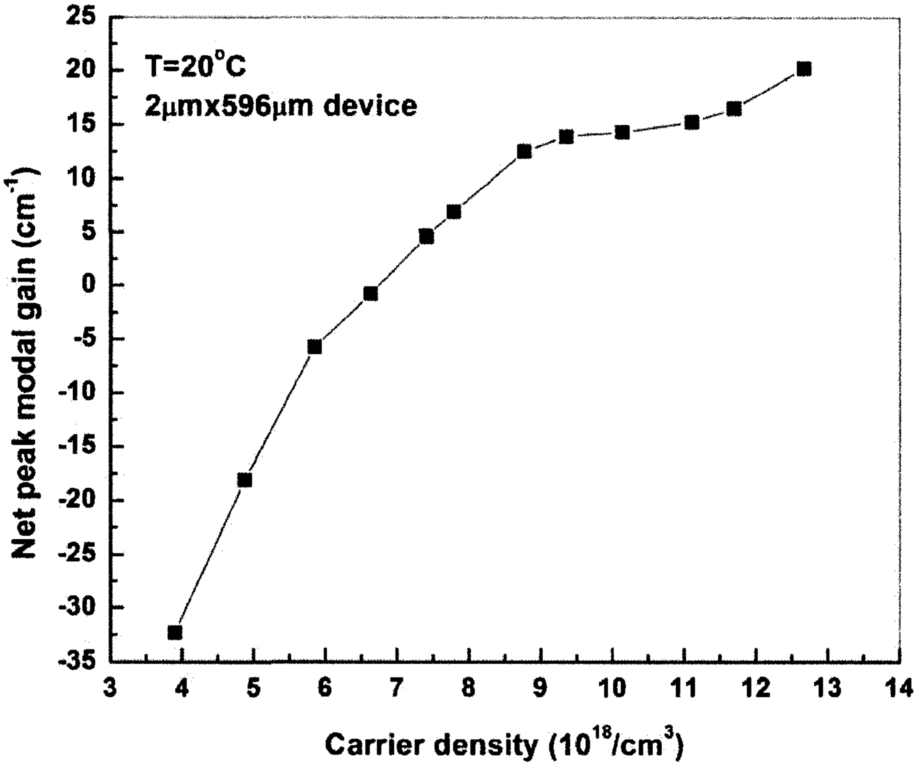

Fig. 3-17 The peak modal gain as a function of the carrier density for the 596 μm long device.

In Fig. 3-16, the gain peak blue-shifts on average at the rate of -0.25 nm/mA as the current increases across its range. This rate is unusually low compared to the blue shift rates of 1 to 3 nm/mA that have been measured in 1.3μm AlGaInAs/InP, InGaAsP/InP and in highly strained InGaAs/GaAs QW structures [54, 60, 61]. Two mechanisms may cause the weak blue shift: one is the weak band-filling effect resulting from the non-parabolic conduction band of GaInNAs; the other is the strong red shift originating from the junction temperature rising. The first possibility will be discussed below, while discussion of the second is deferred until the next section.

Further insight into the weak blue shift in the gain peak may be obtained by analyzing the FWHM of the gain spectra. In Fig. 3-18, the linear dependence of the FWHM on current can be approximated to be 0.42 meV/mA for the measurements taken at 30°C and 50°C. The FWHM at 30°C saturates at a threshold value of approximately 41.1 meV. A similar FWHM (about 40 meV at 25°C) is reported for a 1.3 μm GaInAsP/InP MQW laser [60]. However, the FWHM increases at a much larger rate (from 2 to 3 meV/mA) in the InGaAsP/InP QWs. The small gain spectral broadening observed as the current increases supports the hypothesis that there is a small band-filling effect, and therefore a large density of states in the GaInNAs QWs. The large density of states can be explained by the strong non-parabolic energy dispersion of the GaInNAs conduction band, where the effective electron mass increases dramatically with the energy state. See, however, the next section.

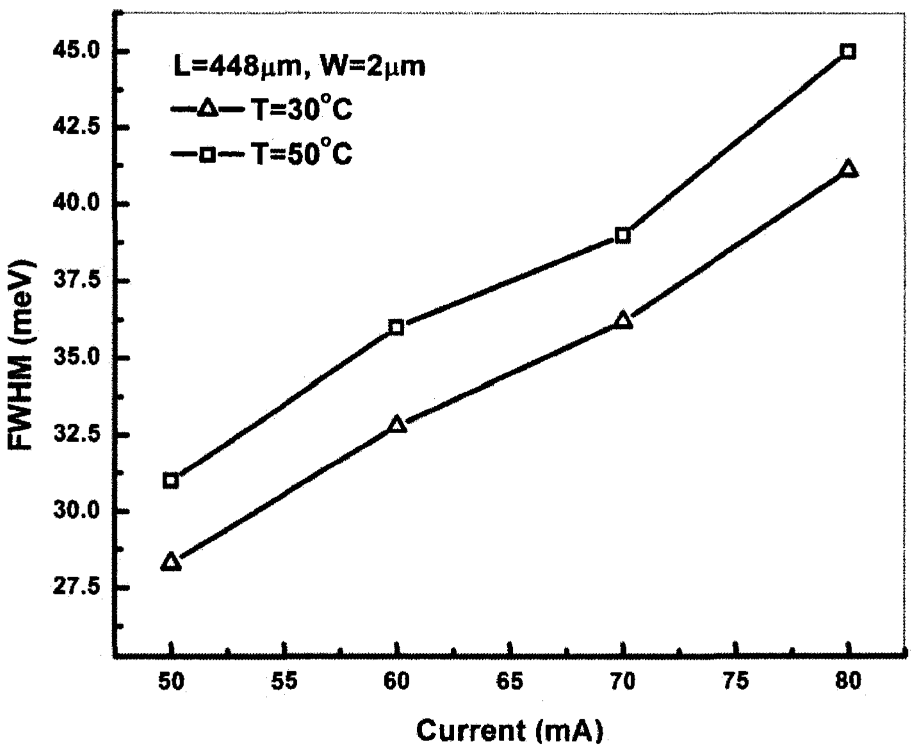

Fig. 3-18 FWHM of the gain spectra as a function of sub-threshold current measured at 30 and 50°C.

3.3.3 Optical Spectrum

The spectral properties of a 3 μm-ridge laser are discussed below. Fig. 3-19 shows the emission spectra as the current increases. It demonstrates that the laser is excited by a single transverse mode. Mode competition clearly exists with increasing current.

Temperature dependent spectroscopy is reported in Fig. 3-20 for current values of 1.05 times the threshold current at four different temperatures. The laser wavelength increases with temperature at an average rate of 0.55 nm/C°. This value is very close to the red shift of the gain peak, which is 0.58 nm/C°. Clearly, a rising junction temperature may also contribute a red shift to the gain peak that might partially compensate a blue shift at increasing sub-threshold current. However, at these low currents, the junction temperatures are likely to be quite modest, implying a small band-filling effect as the dominant cause of the slighly blue shift with increasing sub-threshold currents.

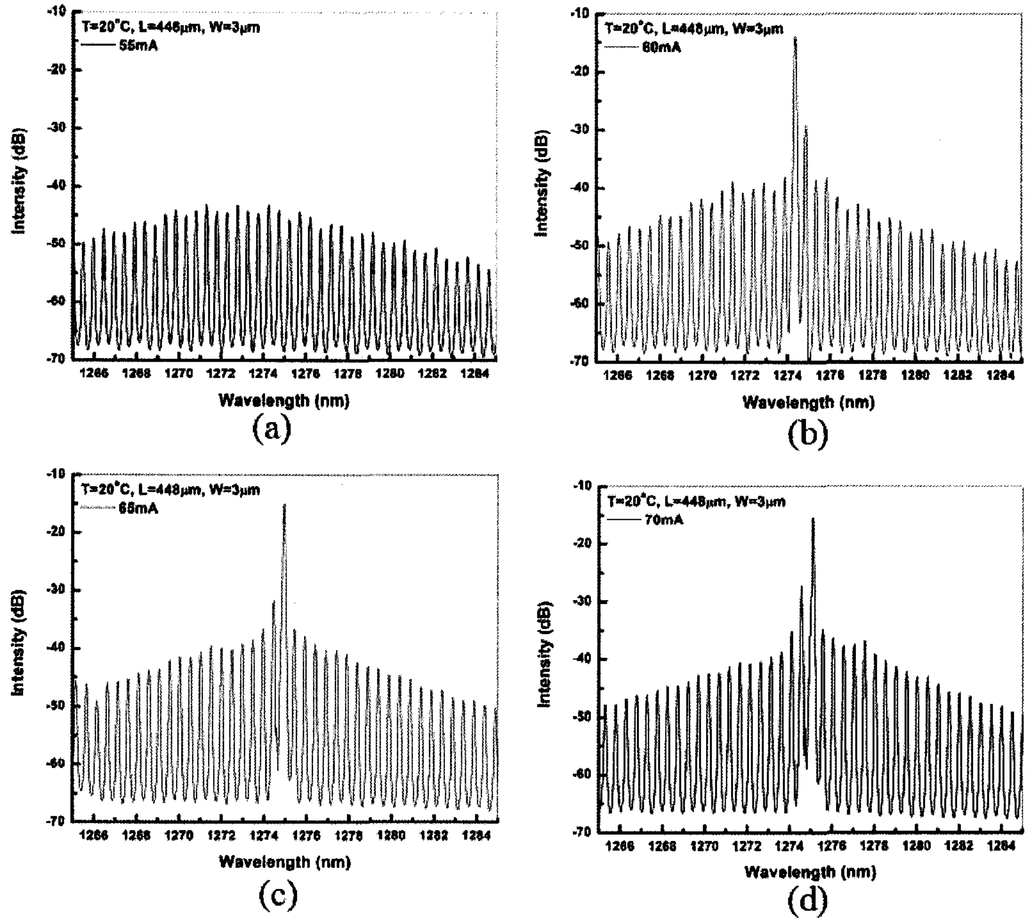

Fig. 3-19 High resolution emission spectra from a 3 μm x 448 μm laser at (a) 55 mA, (b) 60 mA, (c) 65 mA, and (d) 70 mA.

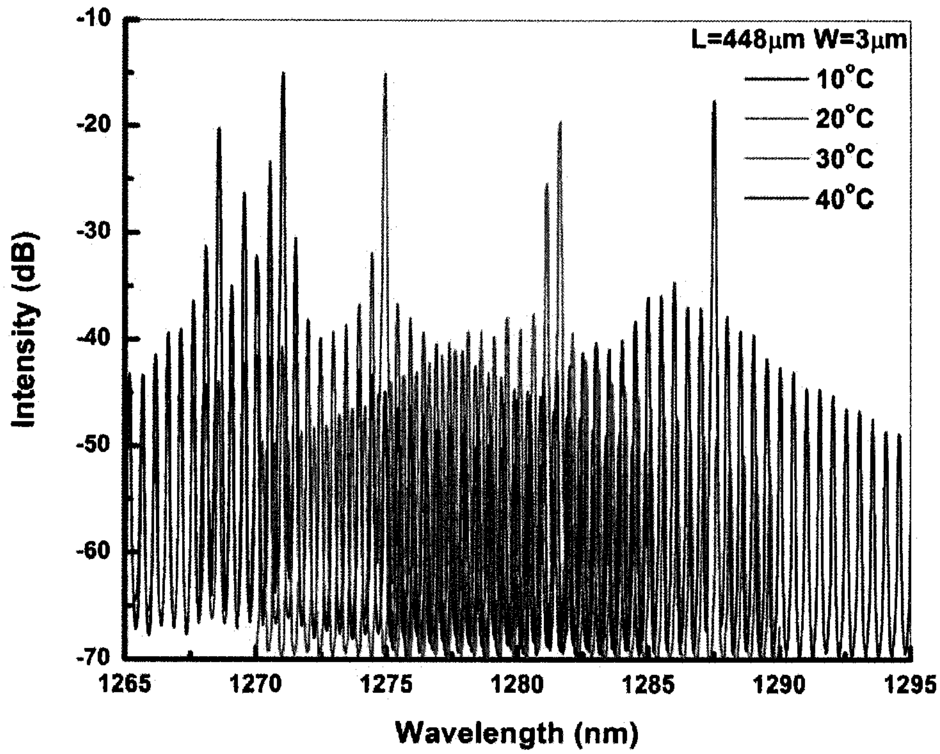

Fig. 3-20 The high resolution emission spectra of a GaInNAs laser taken at different temperatures. The bias current is controlled at $1.05xI_{th}$, where I_{th} varies with temperature.

3.4 *Intrinsic Dynamics*

3.4.1 Laser Noise

Diode laser operation involves carrier and photon dynamics even when there is no variation in the applied current. The recombination and generation events that occur within a laser cavity produce variations in the carrier and photon concentrations. These variations can be described by three quantities: the amplitude $a_n(t)$ and phase $\varphi_n(t)$ of the electric field, and the carrier density $n(t)$. Considerable theoretical work has been directed towards finding the physical origin of AM/FM noise. A few of the more important works are referenced here [63, 64, 65, 66].

Since the amplitude of the photon density changes with output power level, a normalized noise spectral density, or the relative intensity noise (RIN), is introduced to quantify the noise of the laser.

The laser RIN is defined by

$$RIN = \frac{\langle |\Delta P(\omega)| \rangle^2}{\langle P \rangle^2} \tag{3-18}$$

where $\langle P \rangle$ is the mean optical power and $\langle |\Delta P(\omega)| \rangle$ is the noise power spectral density. Using the photon and carrier density rate equations, a simple and intuitive formulation may be derived. By applying the linear approximation in gain (neglecting gain compression), the fluctuation of photon density and carrier density can be related by the following equations [67, 68]

$$\frac{ds}{dt} = \left(\Gamma v_g g(n,s) - \frac{1}{\tau_{ph}} \right) s + \frac{\Gamma R_{sp}}{V} + F_s(t) \tag{3-19}$$

$$\frac{d(n)}{dt} = \frac{I}{qV} - \frac{n}{\tau_n} - v_g g(n,s) s + F_n(t) \tag{3-20}$$

In the above equations, s and n are the photon and carrier densities in the active region; $g(n,s)$ is the gain; R_{sp} is spontaneous emission rate; $\Gamma R_{sp} / V$ is the spontaneous emission rate coupled into the laser mode; I is the injection current; V is the volume of the active region; Γ is the confinement factor; v_g is the group velocity; τ_{ph} and τ_n are the photon and electron decay times, and F_s and F_n are Langevin noise terms, originating from spontaneous emission.

By using standard small-signal analysis, and the diffusion relations for the noise terms, the RIN is found to be of the form [53]:

$$RIN = \frac{A + B\omega^2}{\left(\omega^2 - \omega_r^2\right)^2 + \omega^2 \gamma^2} \tag{3-21}$$

where

$$\omega_r = \sqrt{\frac{(v_g g_n / X)s}{\tau_{ph}}} = D\sqrt{P} \qquad 3\text{-}22$$

is the resonance frequency, P is the light output power from one facet, and

$$\gamma = (v_g g_s / X)s + \frac{1}{X\tau_n} = \frac{K\omega_r^2}{4\pi^2} + \frac{1}{X\tau_n} \qquad 3\text{-}23$$

is the damping factor linearized in ω_r^2, and $X = (1 + \tau_{ph}/\tau_n)$ is a transport factor.

FM noise is strongly affected by fluctuations in the carrier density, as is the spectral density. The relaxation resonance will thus also appear in FM noise. The FM noise spectral density has the form:

$$S_F(f) = C\delta\omega_{st}\left[1 + \frac{\alpha^2 f_R{}^4}{(\omega^2 - \omega_r^2)^2 + \gamma^2\omega^2}\right] \qquad 3\text{-}24$$

where $\delta\omega_{st}$ is the linewidth, C is a constant , and f_R is the resonence frequency. The linewidth enhancement factor α is expressed as:

$$\alpha = 2\frac{\partial\omega_{st}/\partial n}{\partial g/\partial n} = \frac{4\pi}{\lambda_0}\frac{\partial n_{eff}/\partial n}{\partial g/\partial n} \qquad 3\text{-}25$$

where n_{eff}, n, and g are the refractive index, the carrier density and the gain, respectively, and λ_0 is the lasing wavelength.

The physical meaning of the linewidth enhancement factor is given by the Schawlow-Townes formula [53]. It states that the linewidth of the excited emission mode increases by an amount equal to $\alpha^2\omega_{st}$ during laser operation due to carrier density fluctuation [53]. Significantly, the linewidth enhancement factor determines the frequency chirp when the laser is directly modulated. It may therefore limit the operation of high-speed laser in networks with dispersive optical fibers.

3.4.2 Intrinsic Frequency Response

The modulation speed of a laser is determined by its frequency response as noted by the 3dB bandwidth. The frequency response can further be characterized by a resonance frequency and a damping factor, and their variations with laser power.

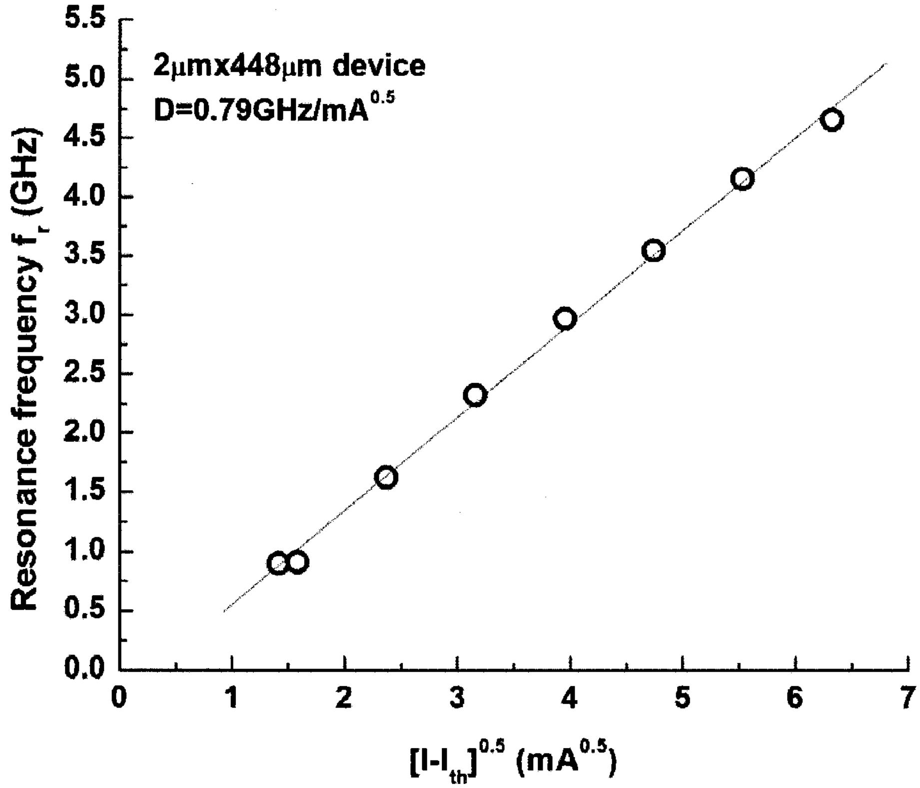

Fig. 3-21 The relaxation resonance frequency as a function of the bias current for a 448 μm device.

Noise power was measured by coupling the light output from the sample laser to a photodetector, with any necessary optical isolation and attenuation. A HP7140C Lightwave Signal Analyzer was used to detect the noise spectral density of the photocurrent. The measured electrical noise power has three components: (1) the thermal noise from the detection circuit; (2) the shot noise generated by the photon detection process in the photo detector; and (3) the current generated by the laser RIN. Ideally, RIN is found by subtracting the thermal noise and the shot noise from the measured noise current. First, the light-current characteristics were obtained using the power meter function of the HP7140C light-wave spectrum analyzer. After acquiring the laser threshold current and the thermal roll-over current, the noise density spectrum of the background thermal noise was obtained by biasing the laser below its threshold. Eight spectra were then taken at biasing currents between threshold and the thermal roll-over. The biasing currents were chosen to be evenly distributed along $(I-I_{th})^{1/2}$. The RIN spectra were calculated as the difference between these spectra and the thermal background spectrum, under the assumption of minimal shot noise (see below for a discussion of this point). The resonance frequency, $f_r = \omega/2\pi$, and damping factor, γ, are the variables fitted to the RIN spectra of equation 3-21, using the least-squares algorithm.

Fig. 3-21 shows the resonance frequency, f_r, as a function of the square root of the injection current above threshold, since f_r increases linearly with the square root of laser output power. The slope of the linear fit, D, acts as a figure of merit to characterize laser frequency response. High-speed performance is expected from a device with a high value of D. This laser shows D=0.79 GHz/mA$^{1/2}$ and f_r=4.7 GHz at current equal to 72 mA. The resonance frequency tends to saturate at larger currents due to thermal roll-over.

Fig. 3-22 displays the dependence of the damping factor on the square of the resonance frequency for the device of Fig. 3-21. As equation 3-23 indicates, it is a linear relationship in ω^2, and the slope K acts as another figure of merit characterizing laser frequency response. A lower value of K gives a higher speed laser. An unweighted linear fit yields a K factor of 0.85 ns and $1/(\chi\tau_n)$=2.67x10^9. In the absence of an extrinsic limit, the maximum intrinsic modulation bandwidth is determined by $f_{max} = 2\pi\sqrt{2}/K$ [69]. A f_{max} value of 9.7 GHz is found. This value demonstrates GaInNAs's potential for 10 Gbit/s direct modulations. Further-more, the spontaneous recombination lifetime, τ_n is estimated to be 375 ps, neglecting carrier transport effects ($\chi = 1$).

The meaurements discussed above include the contribution of shot noise from the photodetector. Since the shot noise rises with increased photocurrent, the thermally-corrected measured spectra may increasingly diverge from the true RIN spectra at large bias currents. Tatham *et. al.* have proposed the "white" shot noise spectrum method to correct the measured response [70]. The accuracy of the above results may be improved by applying this method.

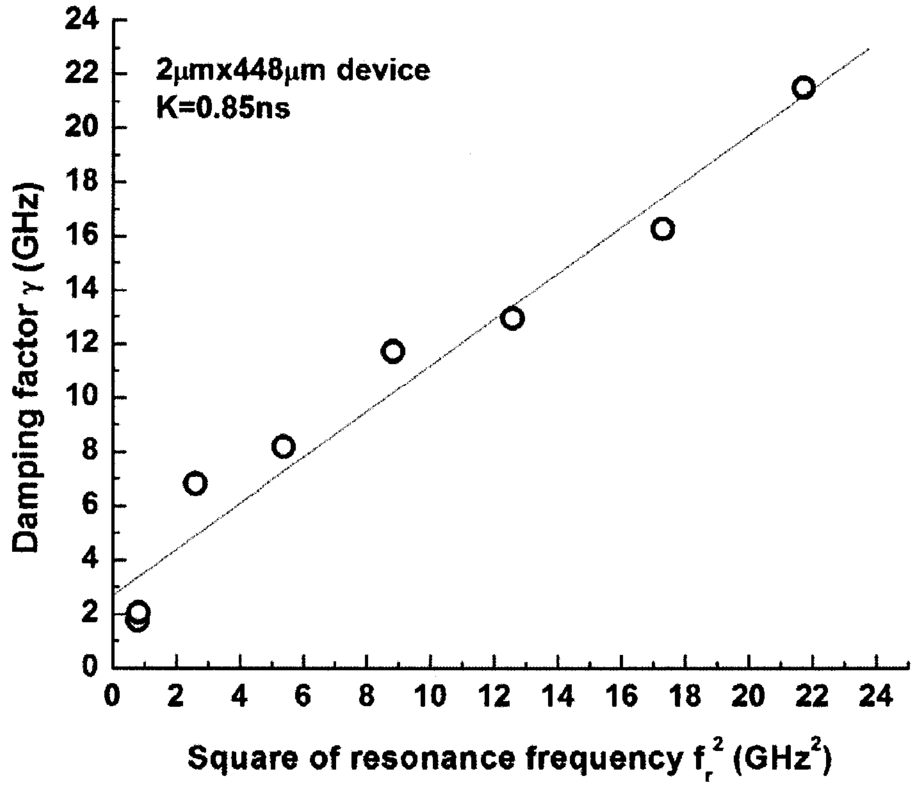

Fig. 3-22 The damping factor as a function of relaxation resonance frequency for the 448 μm device.

It is instructive to compare this laser frequency response with published results from other groups. To date, there has been only one report of a GaInNAs laser[71] - this one with three QWs (as opposed to two in the present study). The parameters found for this 270-μm-long device were D=0.92 $GHz/mA^{1/2}$ and K=0.44 ns. While this suggests a laser with better high-speed performance than the one in the present study, such may be attributed to the differences in device size and QW number, since both systems show very similar intrinsic dynamics.

The QW number in the GaInNAs/GaAs material system is restricted by the large strain between the GaInNAs and GaAs substrate. Practical limitations are about 5QWs, setting a limitation to high-speed performence. The intrinsic bandwidth of GaInNAs/GaAs lasers is not likely to go beyond 20 GHz using current design.

3.4.3 Linewidth Enhancement Factor

The α-factor will determine the degree of frequency chirp when the laser is directly modulated. Much early work was devoted to the physical determination of the α-factor. However, there are few reports on the α-factor of GaInNAs lasers. Seo *et. al.* calculated a low α-factor using a microscopic model [72]. More recently, experimental measurements have revealed a reduced α-factor due to nitrogen incorporation [73].

The α-factor is determined by equation 3-25 above. The carrier density increases linearly with the applied current when the laser is biased at small sub-threshold currents. The ratio of refractive index change over carrier density, and the differential gain as a function of carrier density, can both be determined by varying the applied current. It is then possible to extract the values of dg/dI and dn_r/dI individually from the high-resolution emission spectra. Although this method seems straight forward, accurate measurement requires careful control of applied currents. The current should be low enough to maintain the linear relation to carrier density, while high enough for the OSA to detect the F-P resonance. Fig. 3-23 displays the laser modal gain spectra at 15, 20 and 25 mA, as determined by the Cassidy method [57]. The threshold of this device is 35 mA. The gain spectra allow for the calculation of the differential gain spectra dg/dI.

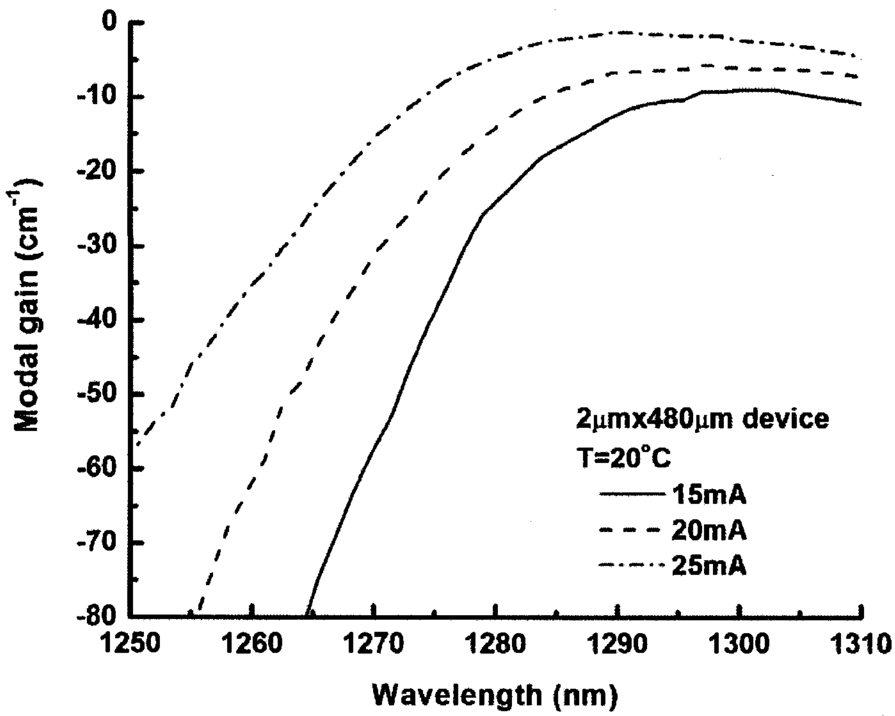

Fig. 3-23 20°C sub-threshold modal gain spectra measured at low bias currents.

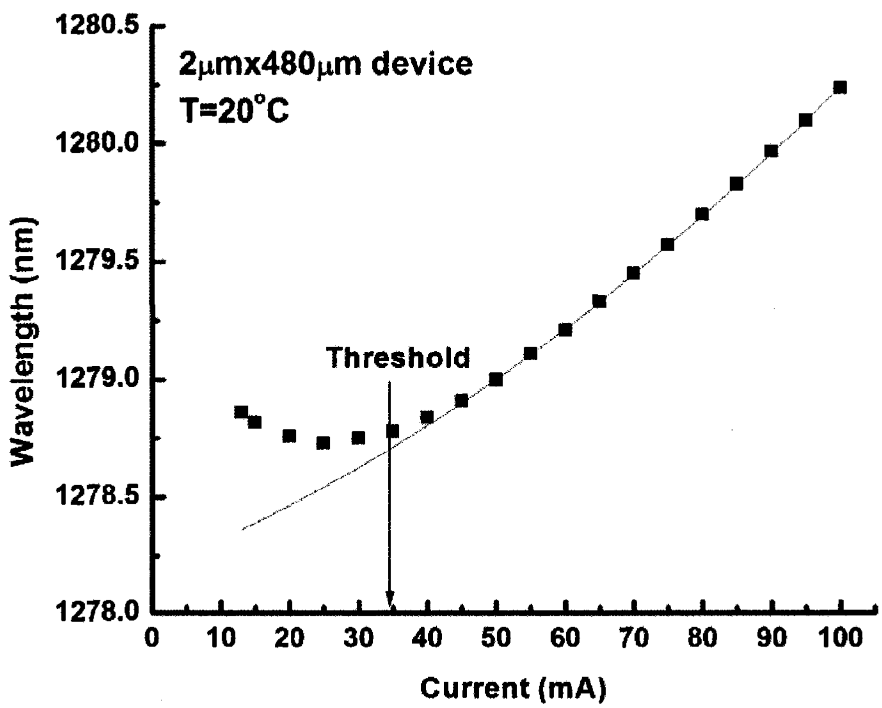

Fig. 3-24 The F-P mode spectral position as a function of current. The solid line is the quadratic fit to the data above threshold.

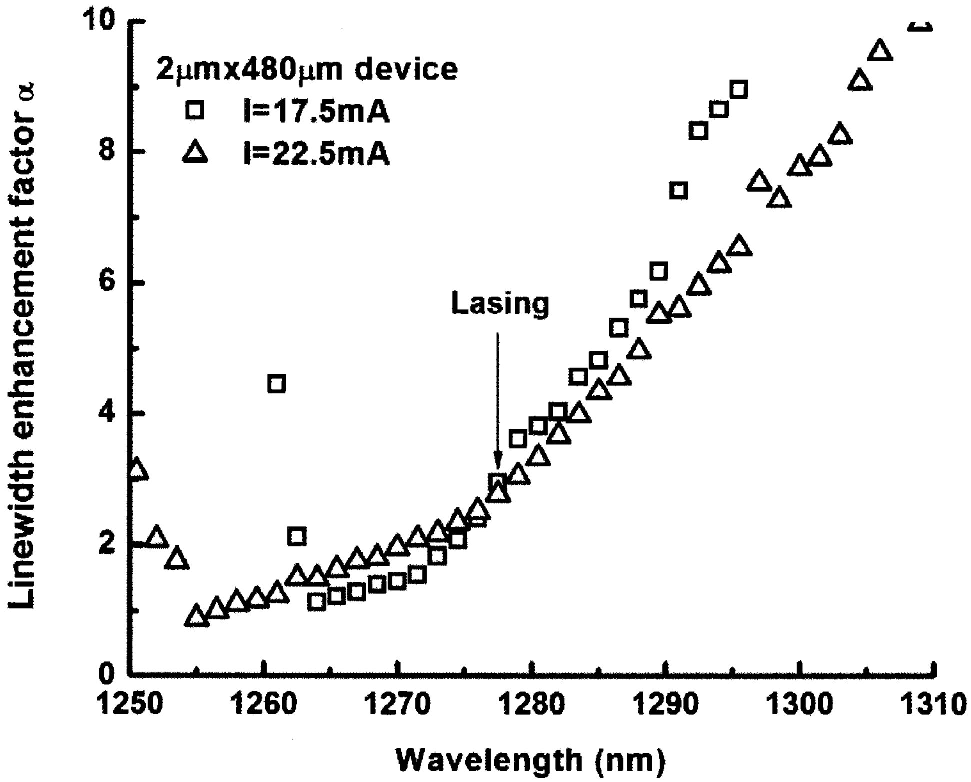

Fig. 3-25 The spectra of the linewidth enhancement factor. The laser emission wavelength is indicated.

The rate of change in refractive index with injection current, dn_r/dI, is obtained from the local slope of the F-P mode spectral position versus current, $d\lambda/dI$, using $dn_r/dI = -(n_r/\lambda)\times(d\lambda/dI)$. The data are shown in Fig. 3-24. A careful analysis of $d\lambda/dI$ reveals two effects: (1) The blue shift in the spectral position of the F-P resonance below threshold requires the refractive index to decrease with increasing carrier density. This blue shift terminates at the threshold current due to carrier clamping. (2) The F-P resonance mode red shifts above the threshold because the junction temperature rises with increasing current. Since this effect is also present below threshold, it must be removed in order to determine the pure carrier density-induced dn_r/dI. This is accomplished by subtracting the contribution due to junction heating, as determined by a quadratic fit to the data above threshold, (where $d\lambda/dI$ is influenced only by the junction temperature rising).

Fig. 3-25 shows the wavelength dependence of the α-factor at two injection levels. An α-factor of 2.8 at the emission wavelength is determined. This value is slightly higher than the value reported in [73], where they failed to exclude the temperature-induced refractive index change.

3.5 1.55 μm GaInNAsSb Laser

3.5.1 Antimony in Dilute Nitrides

In principle, with quaternary $Ga_xIn_{1-x}N_yAs_{1-y}$ alloys as an active material, a wide spectral range from 1.2 to1.6 μm can be covered. In practice, however, it has proved to be very difficult to reduce the band gap energy of $Ga_xIn_{1-x}N_yAs_{1-y}$ below 0.95 eV (1.3 μm). Decreasing the $Ga_xIn_{1-x}N_yAs_{1-y}$ band gap requires alloys with high indium and high nitrogen contents. These alloys deteriorate the optical quality of the epitaxial layers due to the increased larger strain. A high nitrogen-content alloy increases the number of non-radiative recombination centers. On the crystal growth side, the epitaxy of high indium and nitrogen content alloys on GaAs substrates is constrained by the intrinsic thermodynamic instability of $Ga_xIn_{1-x}N_yAs_{1-y}$. A strong phase separation occurs at even low growth temperatures, leaving a very narrow growth window for high quality material.

In researching long wavelength emission from systems on GaAs substrates, a number of groups found that adding a small amount of antimony to the alloys dramatically improved the quality of the material. Strong luminescence has been demonstrated at wavelengths beyond 1.5 μm[74, 75]. Although several measurement methods have been applied to antimony-containing dilute nitrides[76, 77], the importance of antimony and its proper use as a reactive surfactant has only recently been proposed. Yuen *et. al.* concluded from their composition- dependent optical and structural studies that antimony can improve or deteriorate material properties depending on how much indium is in the alloy[78]. The addition of antimony to high indium (high strain) GaInNAs leads to a dramatic improvement in optical quality, and to a widening of the growth window. Regrettably, antimony degrades GaInNAs of low indium (low strain) composition because indium and antimony are both large-atomic-radii atoms that compete for incorporation into GaInNAsSb alloy. While local strain inhibits the simultaneous incorporation of both atoms, antimony in high strain layers works as a surfactant to improve the structural quality of QWs via the reduction in local indium compositional fluctuations.

Using this new understanding of the role of antimony, we designed and fabricated a GaInNAsSb/GaAs laser with highly-strained QWs [79]. This laser features double $Ga_xIn_{1-x}N_yAs_{1-y-z}Sb_z$ QWs and a $Ga_xN_yAs_{1-y}$ barrier. The 39% molar fraction of indium in the QWs increases compressive strain to 2.3%. Indium also assists nitrogen in reducing the band gap energy of the QWs to 0.797 eV. The GaInNAsSb laser described herein holds the record to date, at 1532nm, for long wavelength lasers on GaAs substrates. Room temperature CW operation reveals a threshold current of 105 mA.

Table 3-3 lists the epitaxial layers of the laser. The transmission electron microscope image in Fig. 3-26 shows flat interfaces between the QWs and the barriers. Planar growth is clearly encouraged by the addition of antimony.

Table 3-3 Epitaxial structure of the 1.55 μm DQWs GaInNAsSb/GaAs lasers.

	Material	Doping (cm^{-3})	Thickness (nm)	Composition	Layer description
11	GaAs:Be	1.00E+19	100		p-contact
10	$Al_xGa_{1-x}As$:Be	1.00E+18	1500	x=0.33	p-cladding
9	GaAs	n/a	148		SCH layer
8	GaN_yAs_{1-y}	n/a	20	y=0.044	Barrier
7	$Ga_xIn_{1-x}N_yAs_{1-y-z}Sb_z$	n/a	7	x=0.61, y=0.027, z=0.011	Well
6	GaN_yAs_{1-y}	n/a	20	y=0.044	Barrier
5	$Ga_xIn_{1-x}N_yAs_{1-y-z}Sb_z$	n/a	7	x=0.61, y=0.027, z=0.011	Well
4	GaN_yAs_{1-y}	n/a	20	y=0.01	Barrier
3	GaAs	n/a	148		SCH layer
2	$Al_xGa_{1-x}As$:Si	2.00E+18	97	x=0.33	n-cladding
	GaAs:Si	3.00E+18	3		repeat 18 time
1	GaAs:Si	2.00E+18	200		n-buffer
	(100)-GaAs:Si	2.00E+18			Substrate

The standard process is applied to these epi-wafers. Since there is no etch stop layer, the ridges are formed by timed dry etching. The lasers are cleaved into different cavity lengths and mounted p-side up on alumina carriers. The laser facets are left as cleaved or with a highly reflective coating either on the rear facet or on both facets.

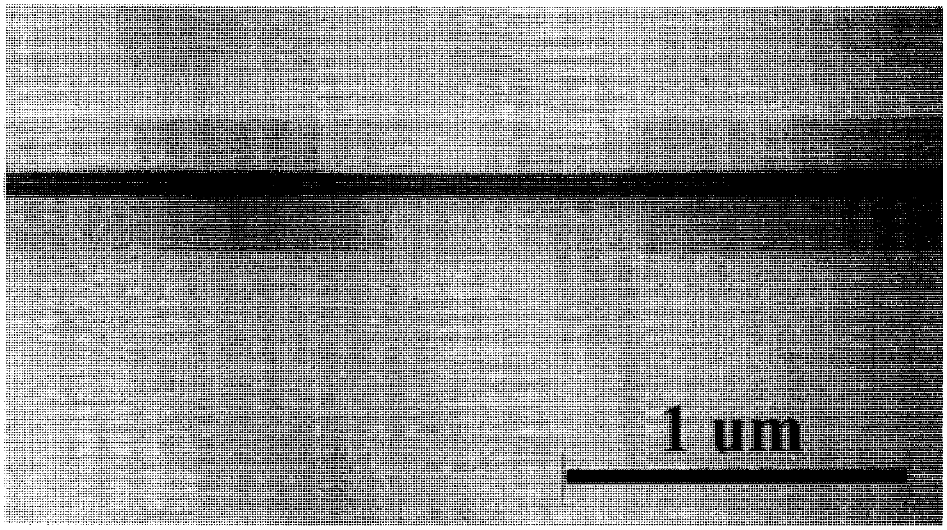

Fig. 3-26 A cross sectional TEM image of the 1.55 μm GaInNAsSb/GaAs DQWs laser. The picture shows no surface fluctuation at well-barrier interfaces.

3.5.2 Light Current Characteristics

Pulsed L-I measurements were carried out at a 1% duty cycle and a pulse width of 1.0 μs. To avoid unreliable measurements due to overshoot pulses generated by the precision-pulsed current source (ILX-Lightwave LDP-3811), a 43 Ω resistor was placed in series with the laser diode.

Fig. 3-27 shows the threshold current as a function of laser ridge width for pulsed current measurements on lasers of different cavity lengths. The laser facets are uncoated. A geometry-dependent analysis yields an estimated value of ~100 mA for the lateral leakage current. The lowest threshold current density is 4100 Acm^{-2} for 1202 μm long devices.

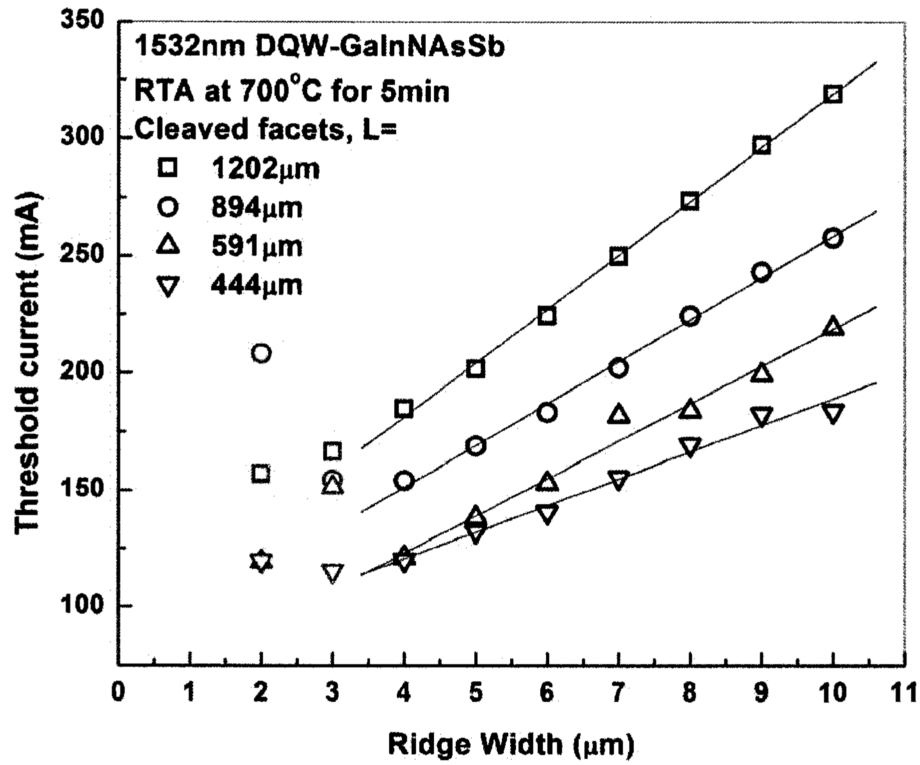

Fig. 3-27 Threshold current as a function of ridge width for lasers of different cavity lengths. The measurements were carried out at 20°C with pulsed current injection. The epi-wafer was annealed at 700°C for 5 minutes. The laser facets were left as-cleaved. Data in red are excluded from linear fit.

Due to excessive heating in the active region, the devices do not operate in CW mode at room temperature. However, some of the lasers did exhibit CW operation at 0°C (as shown in Fig. 3-28), or pulsed operation with a 20% duty cycle at 20°C. These results indicate that a small improvement in design or material quality should be sufficient to bring down the junction temperature and therefore enable CW room temperature operation.

A series of deep-etched lasers were processed using the same epi-wafer to reduce the lateral leakage current. To further reduce the optical loss, laser bars were coated with multiple SiO_2/Si layers either on the rear facet only (98% in reflectivity) or on both facets (98% in rear and 80% in front). Several lasers having both facets coated exhibit room temperature CW operation, as is shown in Fig. 3-29. Due to large current density in laser active region, which causes defect migration, those lasers can only last a few hours under CW operation.

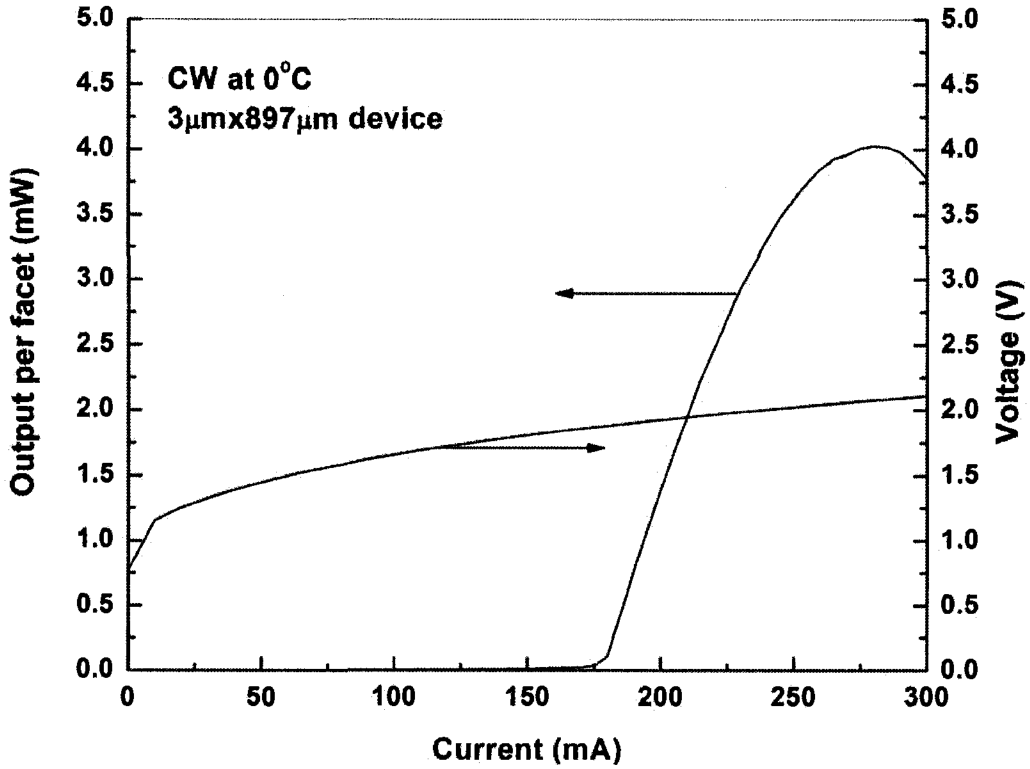

Fig. 3-28 The CW output power and voltage as a function of injection current at 0°C. The threshold current is about 180 mA, while thermal roll-over occurs at 250 mA.

The internal parameters of the GaInNAsSb lasers were extracted using cavity length dependent analysis. These data are shown in Fig. 3-30 and Fig. 3-31. The internal quantum efficiency and the internal loss are estimated to be 62% and 27 cm^{-1}, respectively, for lasers with 9 μm ridges. The gain factor and transparency current density are estimated to be 1360 cm^{-1} and 480 A/cm^2, respectively.

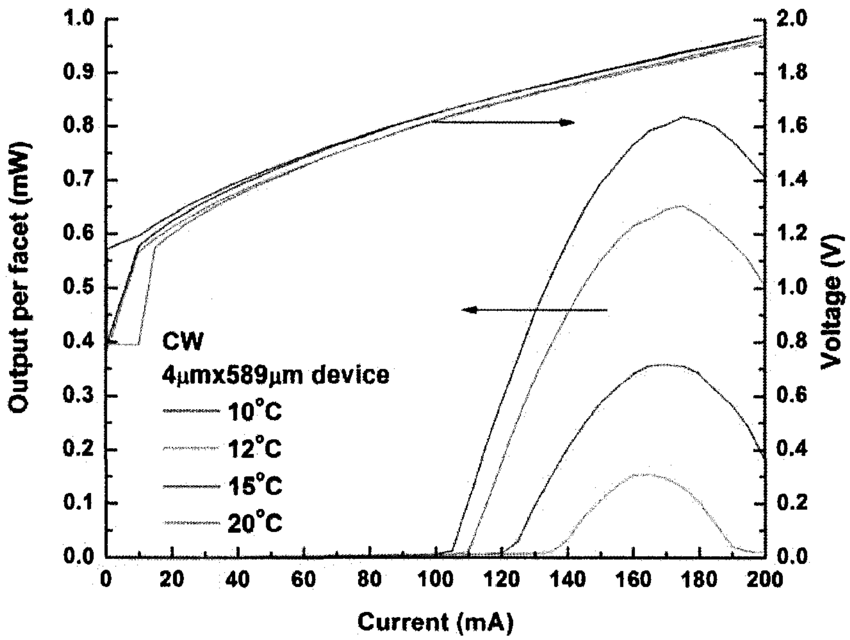

Fig. 3-29 The first room temperature, continuous wave operation GaAs-based laser with 1550 nm wavelength emission.

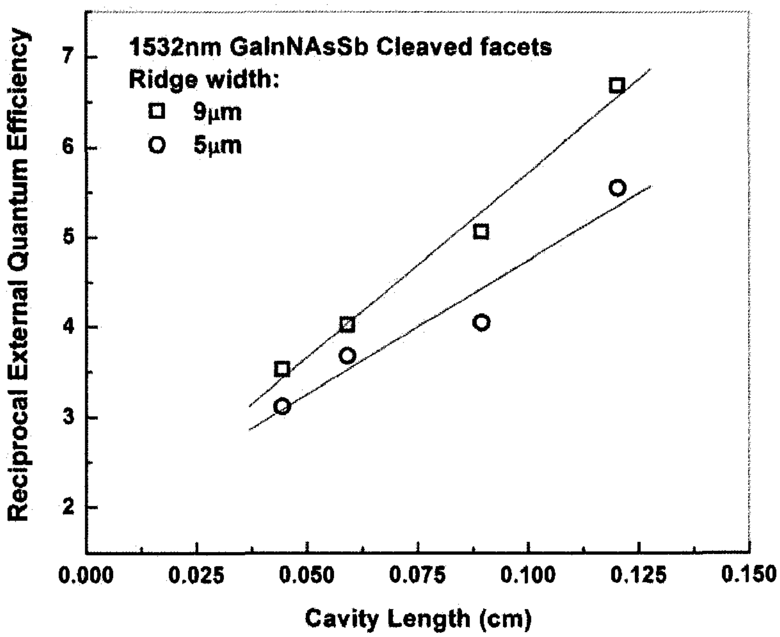

Fig. 3-30 The inverse external quantum efficiency as a function of cavity length. The wide ridge device gives more reliable results.

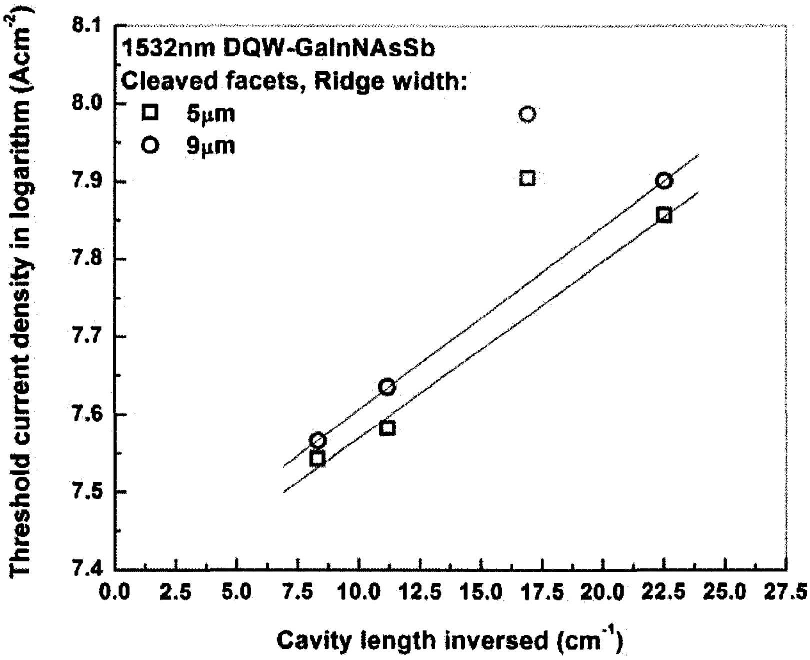

Fig. 3-31 The threshold current density as a function of inverse cavity length. The 600-μm-long devices have abnormally high threshold currents and are excluded from the linear fits.

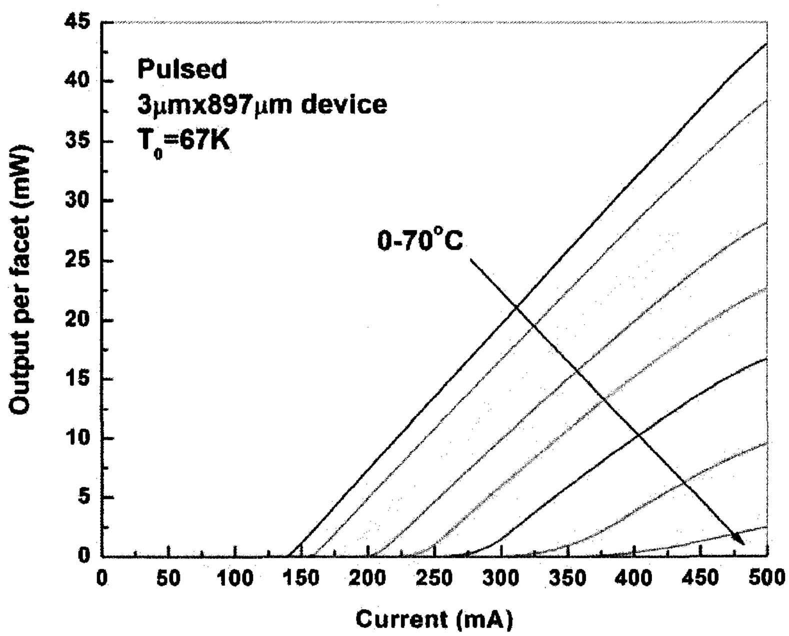

Fig. 3-32 Pulsed L-I measurements for a 3 μm x 897 μm device. The characteristic temperature is calculated.

Temperature dependent L-I measurements were carried out to determine the characteristic temperature of these lasers. The result for a 3 μm x 897 μm device is shown in Fig. 3-32. The curves shown are for data in 10°C increments from 10°C to 70°C. A value of T_0=67 K was found using data from 10°C to 70°C. Normally, long devices with narrow ridges have higher characteristic temperatures since their geometry confers better thermal dissipation and lower injection current. The same measurement was applied to other lasers, including those with facet coatings. The characteristic temperatures were found to be between 60 K and 85 K. The devices with facet coatings were found to have the higher T_0 values, while devices with untreated facets have lower T_0 values (due to the higher threshold currents).

3.5.3 Gain and Loss

To understand the high optical absorption observed in GaInNAsSb lasers, the optical field intensity was calculated using the refractive index profile of the layer structure in Table 3-3. As Fig. 3-33 indicates, significant portions of the field are located outside the waveguide (approximately 21% both above and below), where the material is highly doped with Be (1×10^{18} cm^{-3}) and Si (2×10^{18} cm^{-3}). At this level of impurity concentration, the free carrier absorption factors can be as high as 30 cm^{-1} for p-type AlGaAs and 10 cm^{-1} for n-type AlGaAs [80]. The structure thus likely suffers a large optical loss. This suggests that the doping profile, particularly the p-type doping profile, should be carefully tailored in next-generation devices. The thickness of separate confinement hetero-structure (SCH) waveguide should also be increased to improve optical confinement and to reduce the field intensity outside the waveguide region.

It is very important to know the material gain properties of GaInNAsSb QWs. However, the direct measurement of laser gain under pulse mode has proved to not be feasible. An alternative method is applied. It is well known that the optical gain equals the total optical loss at the laser threshold. Hence, the optical gain profile can be acquired through an exponential fit to the threshold current versus optical loss. This method only requires simple pulsed L-I measurements. The laser cavity length and facet reflectivity are the variables used to tailor the optical loss. The internal loss is assumed to be a constant among lasers from the same epi-wafer and it is estimated to be 27 cm^{-1} for the 9 μm-wide ridge devices.

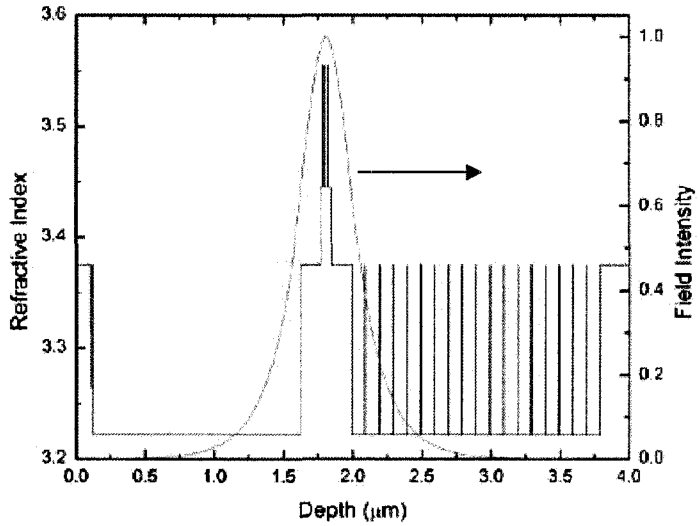

Fig. 3-33 The refractive index profile (black) and the calculated optical field intensity (red) for the GaInNAsSb laser. The layer structure is given in Table 3-3. The refractive index of GaInNAsSb is assumed to be 3.55. The data for this figure was provided courtesy of A. Delage, IMS-NRC.

Fig. 3-34 displays the optical gain as a function of injection current density. The data points for low optical loss are from lasers with coated facets. These data improves the standard deviation of the exponential fit. The transparency current density of ~700 Acm^{-2}/QW is obtained from Fig. 3-34 when optical net loss is zero. For the purpose of comparison, Fig. 3-34 also shows the gain profile of the 1.28 μm GaInNAs laser. Its differential gain is about four times larger than that of the GaInNAsSb laser.

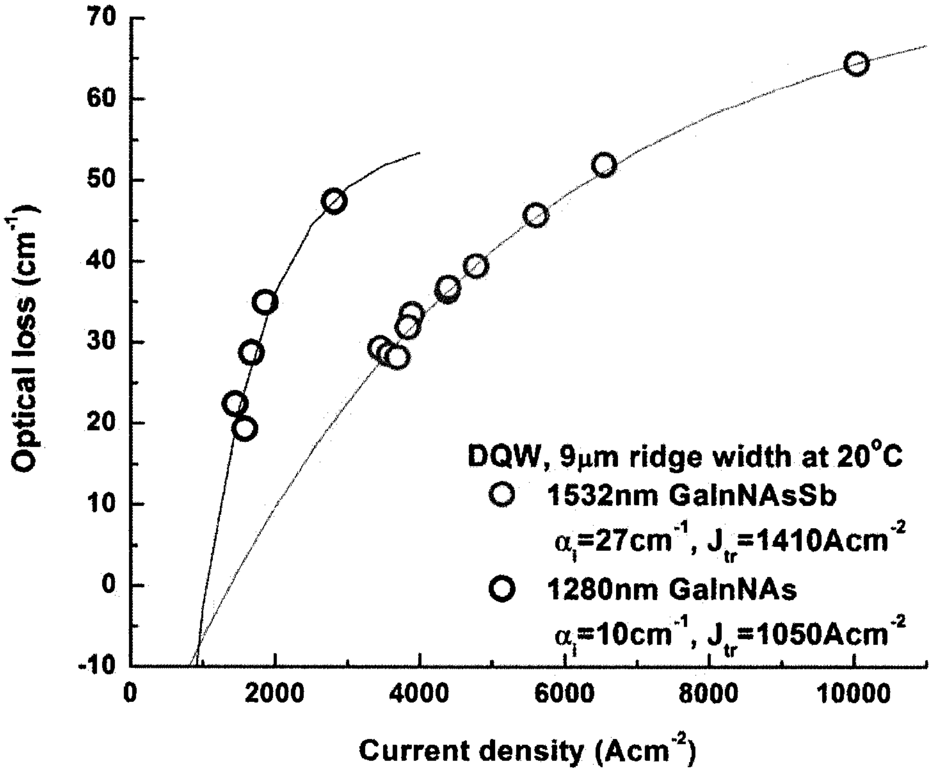

Fig. 3-34 The optical gain or loss as a function of injection current density for the GaInNAsSb and GaInNAs lasers emitting at 1.55 and 1.28 μm, respectively.

3.5.4 Spectral Properties

The optical spectra of the lasers were acquired using a high resolution OSA, with the laser driven by a pulsed current. The duty cycle was increased to 20% to afford the collection of sufficient light. Fig. 3-35 shows spectra for a 2 μm x 900 μm device, measured at 20°C, for three currents just above threshold. The spectra indicate a wavelength of 1536 nm. Strong mode hopping to the long-wavelength side is observed due to the carrier injection.

Temperature dependent spectroscopy was performed on the same device. During the measurement, the bias current was adjusted to 110% of the threshold current for each temperature. Fig. 3-36 shows the increase in emission wavelength from 1536 nm at 20°C to 1557 nm at 60°C. The temperature-tuning rate is 0.52 nm/K.

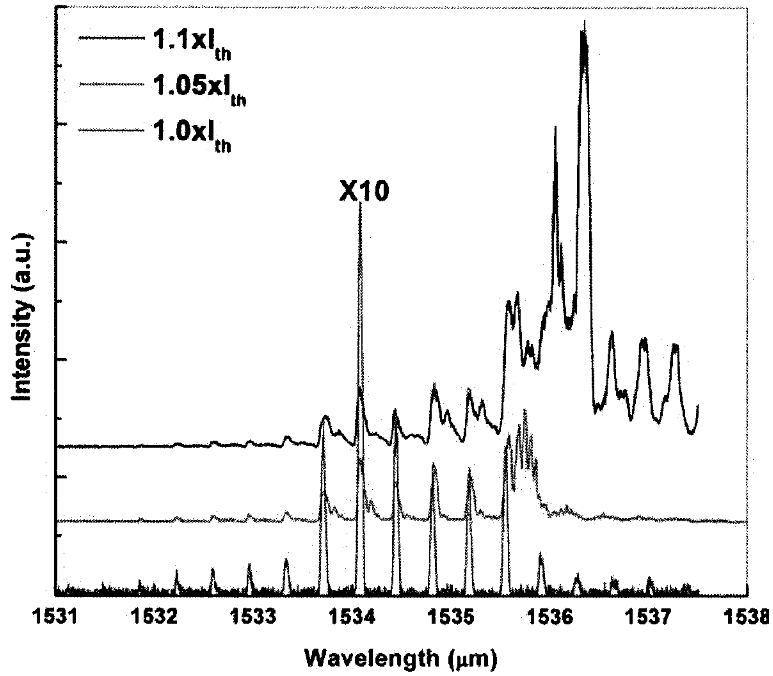

Fig. 3-35 The spectra of a 2 μm x 900 μm device near the laser threshold at 20°C. Vertical axis is in linear scale.

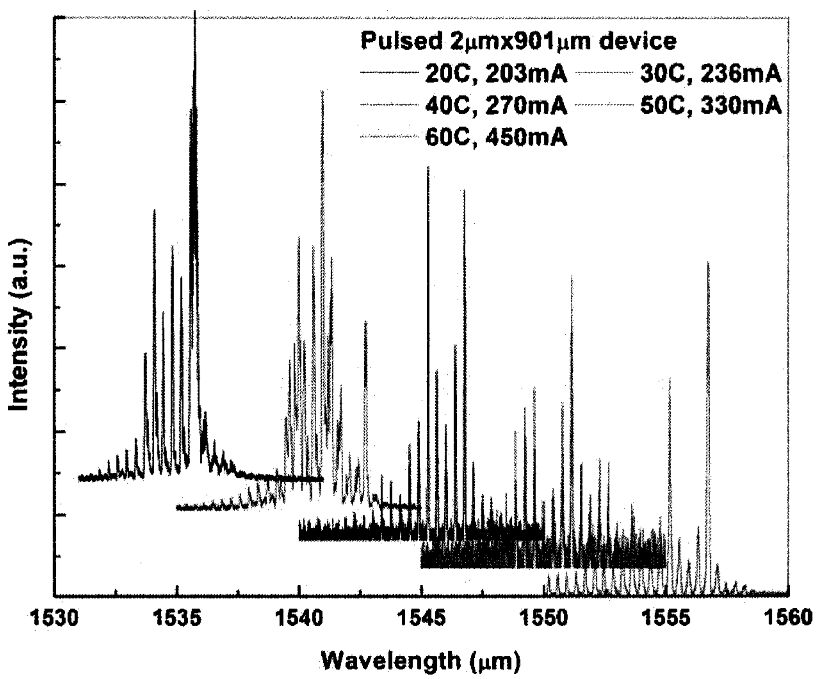

Fig. 3-36 The spectra of a 2 μm x 900 μm device at the $1.1xI_{th}$ measured from 20 to 60°C. Vertical axis is in linear scale.

3.6 Conclusions

In this chapter, the properties of GaInNAs/GaAs and GaInNAsSb/GaAs were studied by various measurements. L-I measurement of a 3 μm x 450 μm device showed continuous wave (CW) operation at room temperature with threshold current of 34 mA. A geometry-dependent threshold current analysis estimated that the laser suffers from a large lateral current leakage. The leakage may be reduced by a deeper ridge etching, leaving considerable room for improving the laser threshold. The temperature-dependent L-I measurement of a 3 μm x 1200 μm device exhibited a characteristic temperature of T_0=155 K. The high T_0 indicates that these lasers are less sensitive to temperature changes.

Optical loss and gain properties of the 1.3 μm GaInNAs laser were studied using high resolution amplified spontaneous spectrum (ASE) measurements. The internal loss and differential gain were determined as 7 cm^{-1} and 1.25 $cm^{-1}mA^{-1}$, respectively. A unique method, able to exclude junction-temperature-induced refractive index change, was used to determine the linewidth enhancement factor (α-factor). A value of 2.8 is in general agreement with such values found for QW lasers made from other material systems. The RIN measurements showed a 4.7 GHz resonance frequency and a 0.79 $GHz/mA^{1/2}$ damping factor. The measurement-based calculation revealed that the laser has a maximum modulation bandwidth of 9.7 GHz, indicating the potential of this laser in 10 Gbit/s applications.

In seeking long wavelength 1.55 μm emission, GaInNAsSb lasers were studied in this chapter. Initial results show that antimony's incorporation into the matrix enables long wavelength emission. The first 1.55 μm, room temperature, CW operation laser on a GaAs substrate was demonstrated.

Finally, although dilute nitride materials are expected to give a high material gain due to a band structure favourable to stimulated emission, it does exhibit a high concentration of non-radiative recombination centers. Advances in material quality, however, will lead to improved laser performance. This will require breakthroughs in epitaxy, lattice thermal re-arranging and the concise comprehension of nitrogen's incorporation effects on the electrical, optical and thermal properties of the materials. The laser performance can also be improved through structural and compositional optimization.

Chapter 4 GaInNAs Material Modeling

4.1 Introduction

This chapter aims to connect fundamental theories in semiconductor physics to laser design and performance analysis by establishing the models that precisely describe GaInNAs quantum wells. Since the 1970's, a large amount of work has been carried out to understand the properties of conventional III-V compounds. As a result of this research, various simulation packages have been developed to predict device behaviour by applying physical theory to the determination of material properties. Although each package has its own characteristics, the physical models and computational algorithms are similar [81].

Dilute nitrides have exceptional material properties. The incorporation of nitrogen dramatically changes the electronic properties of the host materials. In contrast to typical applications of the virtual crystal approximation (VCA) to conventional semiconductor alloys, many dilute nitride material parameters cannot accurately be determined by simple interpolation. New models need to be established to accommodate the changes.

This chapter presents the author's work on dilute nitride material modeling. Author studied the generally accepted energy dispersion theory of dilute nitrides, the band anti-crossing theory (BAC). Based on BAC model, and used 10 band $K \bullet P$ computation tool, a Γ band gap model and electron effective mass model were established. These models were further modified by our experimental results. Author also analyzed the mobility theory of dilute nitride and acquired the low field mobility model using the published Hall measurement. Optical function and affinite of dilute nitride were also discussed. These models then were implemeneted in laser simulator LAS2D. With the reasonable device structure and calibrated physical parameters, which will be presented in latter chapters, LAS2D is able to calculate GaInNAs laser performance. To date, no commercial laser simulator includes dilute nitride material. Since material properties are independent of simulation platforms, the knowledge presented in this chapter can be implemented in any other software tools.

The chapter begins with general considerations common to material modeling. The purpose is getting to know the essential parts of material properties for laser simulation. Then BAC theory and its issues of usage are discussed. The center part of the chapter describes the details on how author set up the models. At last, the electrical and optical characteristic parameters that cannot be accurately interpolated within the virtual crystal approximation are empirically determined.

4.2 Aspects in Material Modeling

Over the last four decades, a comprehensive theory for describing the physical properties of semiconductor has developed. It includes (1) the determination of electron energy bands with temperature and doping; (2) the electrical conductivity at applied electrical field as characterized by carrier transport, carrier generation and recombination; (3) the optical properties as extracted from absorption spectra; (4) thermal and mechanical properties. Quantitative exploitation of these theories generally requires the input of sophisticated physical parameters that are only available for the most widely studied materials, such as Si and GaAs. *Ab initio* approaches are too mathematically involved and time consuming to implement directly into device simulation packages.

Empirical modeling is an effective approach to the simplification of multi-factor phenomena that retains all essential physics at the parameter level. Normally, a model is suggested using the variables from theory. Algorithmic description permits the variables to be fitted to experimental observations. The fitting results form a parameter set for each material, allowing the construction of input matrix as a lookup or interpolation table. Such matrices may either be directly embedded in computation packages, or declared as user-defined values during the simulation. This section introduces the most common parameters and models in laser simulators.

4.2.1 Material Parameters for III-V Semiconductors

Table 4-1 lists the basic physical parameters for III-V binary compounds. The parameters for ternary and quaternary alloys follow the VCA law, and hence can be constructed using the data from binary materials. Beside E_g^{Γ}, a_0, σ_T and ε (with the later two representing the reciprocal of thermal conductivity and the permittivity), respectively, the rest of the parameters in table 4-1 are briefly introduced here.

(1) Varshni Temperature Effect.

In a bulk semiconductor, both direct and indirect energy gaps are temperature-dependent quantities with the functional form often fitted to the empirical Varshni equation [82],

$$E_g(T) = E_g(T=0) - \frac{\alpha T^2}{T+\beta} \qquad \text{4-1}$$

where α and β are adjustable parameters. In particular, Varshni parameters for the Γ band, α^{Γ} and β^{Γ}, are given in Table 4-1 for the calculation of direct band gap energies over various temperatures. These parameters can be found in Vurgaftman's publication [3]. Bands other than the Γ band, illustrated in Fig. 1-2, have different Varshni parameters. These latter bands are not generally involved in carrier transitions and hence are not of concern here.

Table 4-1 Material parameters for III-V binary compounds [3, 83, 84]

	Unit	InAs	GaAs	AlAs	InP	GaP	AlP	GaN	InN
E_g^{Γ}	eV	0.354	1.414	3.099	1.424	2.886	3.63	3.299	1.94
α^{Γ}	meV/K	0.276	0.541	0.885	0.363	----	0.577	0.593	0.245
β^{Γ}	K	93	204	530	162	----	372	600	624
Δ_{so}	eV	0.39	0.341	0.28	0.108	0.08	0.07	0.07	0.006
m_c	m_0	0.023	0.067	0.15	0.08	0.13	0.22	0.2	0.2
E_p	eV	21.5	28.8	21.1	20.7	31.4	17.7	14.0	14.6
F	-----	-2.9	-1.94	-0.48	-1.31	-2.04	-0.65	----	----
γ_1	-----	20	6.98	3.76	5.08	4.05	3.35	2.67	3.72
γ_2	-----	8.5	2.06	0.82	1.6	0.49	0.71	0.75	1.26
γ_3	-----	9.2	2.93	1.42	2.10	2.93	1.23	1.1	1.63
a_c	eV	-5.08	-7.17	-5.64	-6.0	-8.2	-5.7	-2.2	-1.85
a_v	eV	1.0	1.16	-2.47	-0.6	-1.7	-3.0	5.2	1.5
b	eV	-1.8	-2.0	-2.3	-2.0	-1.6	-1.5	-2.2	-1.2
c_{11}	GPa	832.9	1221	1250	1011	1405	1330	293	187
c_{12}	GPa	452.6	566	534	561	620.3	630	159	125
σ_T	cmK/W	3.7	2.27	1.1	1.47	1.3	0.77	0.7	0.07
ε	-----	14.6	13.1	10.06	12.56	11.1	9.8	9	15
a_0	Å	6.058	5.653	5.661	5.870	5.451	5.467	4.50	4.98

(2) Effective Mass

The energy dispersion illustrated in Fig. 1-2 defines a band edge effective mass whose characteristic parameters are available through calculation of the dispersion. The conduction band effective mass m_c is given in terms of the band parameters as

$$\frac{m_0}{m_c} = (1+2F) + \frac{E_P(E_g + 2\Delta_{so}/3)}{E_g(E_g + \Delta_{so})} \qquad 4\text{-}2$$

where m_0 is the electron rest mass; E_p is the matrix element that accounts for the interaction between s-like conduction bands and p-like valence bands; F is the matrix element that accounts for higher band contributions to the conduction band; and Δ_{so} is the spin-orbit split off energy. E_p and F are usually taken to be independent of temperature. This means that the temperature variation of the effective mass arises only through the temperature dependencies of the energy band gaps, as in equation 4-1.

At the valence band edge, the heavy hole and light hole masses in the z crystallographic direction are given by

$$\left(\frac{m_0}{m_{hh}}\right)^z = \gamma_1 - 2\gamma_2 \text{ and } \left(\frac{m_0}{m_{lh}}\right)^z = \gamma_1 + 2\gamma_2 \qquad 4\text{-}3$$

where γ_1 and γ_2 are Luttinger parameters. Note that z is not a power in equations 4-3, but a superscript denoting crystallographic direction <100>. The effective hole mass in other crystallographic directions, and the split-off hole mass, have different values. They are normally not involved in light-matter transitions.

(3) Strain Effect on Bands

Stress deforms the crystal lattice, producing a strain. The strain magnitude ε_{ij} is proportional to the relative change in the lattice period $\varepsilon_{ij} = \Delta a_i / a_j$, and it may depend on crystallographic direction. For a cubic crystal, $\varepsilon_{xx} = \varepsilon_{yy} = \Delta a_0 / a_0 \neq \varepsilon_{zz}$, where the strain components are related by parametric elastic stiffness constants c_{11} and c_{12} as $\varepsilon_{zz} = 2c_{12}\varepsilon_{xx}/c_{11}$. The effect of strain may be treated as a perturbation to the Hamiltonian that governs the unstrained case, yielding energy shifts in both conduction and valence band edges. The shifts are related to hydrostatic deformation potentials a_c and a_v and to the shear deformation potential b as

$$E_{hh}(0) = E_v^0 + a_v\left(\varepsilon_{xx} + \varepsilon_{yy} + \varepsilon_{zz}\right) + \frac{b}{2}\left(\varepsilon_{xx} + \varepsilon_{yy} - 2\varepsilon_{zz}\right) \qquad 4\text{-}4$$

$$E_{lh}(0) = E_v^0 + a_v\left(\varepsilon_{xx} + \varepsilon_{yy} + \varepsilon_{zz}\right) - \frac{b}{2}\left(\varepsilon_{xx} + \varepsilon_{yy} - 2\varepsilon_{zz}\right) \qquad 4\text{-}5$$

in valence bands, and

$$E_c(0) = E_c^0 = E_v^0 + E_g + a_c\left(\varepsilon_{xx} + \varepsilon_{yy} + \varepsilon_{zz}\right) \qquad 4\text{-}6$$

in the conduction band.

4.2.2 Carrier Dynamics

Electrons and holes are the two species of charge carriers that yield current in semiconductor devices. The flow of electrons and holes are described by the drift-diffusion model. The drift current is generated by an electric field, $\vec{E}$. The respective current magnitudes are proportional to electron and hole conductivities. The latter are related to the carrier concentration in materials by $\sigma_n = q\mu_n n$ and $\sigma_p = q\mu_p p$, where μ_n and μ_p are the electron and hole mobilities, q is the charge, n and p represent the concentration of electrons and holes.

The diffusion currents are driven by the electron and hole concentration gradients. Their magnitudes are proportional to their respective diffusion coefficients D_n and D_p. In a uniform semiconductor, assuming Boltzman carrier distributions, the total current densities of electrons and holes are expressed by carrier transport equations as

$$\vec{j}_n = q\mu_n n\vec{E} + qD_n\nabla n \text{ and } \vec{j}_p = q\mu_p n\vec{E} + qD_p\nabla p \qquad 4\text{-}7$$

These current densities are governed by the charge continuity equation. In any finite region, the changes are driven by the spatial change in current flow and by the electron-hole pairs generated or recombined in that space and time. The respective continuity equations are

$$q\frac{\partial n}{\partial t} = \nabla \bullet \vec{j}_n - q(R - \mathrm{G}) \quad \text{4-8}$$

$$q\frac{\partial p}{\partial t} = -\nabla \bullet \vec{j}_p - q(R - \mathrm{G}) \quad \text{4-9}$$

where G and R are carrier generation and recombination rates for either electrons or holes, and R-G is the net recombination rate of electron-hole pairs.

The electric field $\vec{E}$ is affected by the charge distribution, which includes the mobile electron and hole carriers (of concentrations n and p, respectively), the fixed charges of donor and acceptor dopant ions (of concentrations N_D^+ and N_A, respectively), and deep trap level charges (of concentration $N_{trap}(f_{T_j})$, where f_{T_j} is the distribution function for the trap of type j). The steady-state Poisson equation describes the relationshop between the field and the charge concentrations as:

$$\vec{\nabla}\left(\varepsilon\vec{E}\right) = q(p - n + N_D^+ - N_A + \sum_j N_{trap}(f_{Tj})) \quad \text{4-10}$$

The laser simulation software determines the self-consistent solution to the three equations described above, given material and structural properties as inputs. It yields the required carrier transport behaviour (current).

4.2.3 Mobility Model

Electron and hole mobiliies, μ_n and μ_p, are important input parameters to carrier transport computation. Over the years, the subject of carrier mobility has been studied extensively, both experimentally and theoretically. Various scattering mechanisms have been invoked to accurately determine mobility variation with carrier concentration and temperature. Most of the theories, however, require the input of sophisticated physical parameters, such as deformation potentials and alloy scattering potentials. As yet, these parameters are only available for the well-characterized Si and GaAs material systems. Empirical mobility models have therefore been developed by combining these theories with experimental observation of mobilities measured by the Hall Effect. An accurate model suited to III-V materials is the low-field Caughey-Thomas-like mobility model [85]. In this model, carrier mobility is a function of both temperature and doping, expressed as

$$\mu(N,T) = \mu_{\min} + \frac{\mu_{\max}(300K)(300/T)^{\theta_1} - \mu_{\min}}{1+\left(\dfrac{N}{N_{ref}(300K)(T/300)^{\theta_2}}\right)^{\lambda}} \qquad \text{4-11}$$

where N and T are the carrier concentration and temperature, respectively. The sensitivity of the electron and hole mobilities to N and T is measured by the factors $\theta_1, \theta_2, N_{ref}, \lambda$, and $\mu_{\max}$ is the maximum mobility that is normally measured in un-doped materials, while $\mu_{\min}$ is the minimal mobility, normally refered as the mobility of heavily doped materials. These six parameters were fitted to the available Hall measurement data across a large range of carrier concentrations and temperatures, using a least-squares method. Reference 2 lists them for common III-V binary and ternary materials. The VCA law is commonly used for ternary and quaternary alloys.

4.2.4 Recombination Model

Electron-hole recombination includes various physical mechanisms that are categorized either as radiative recombination (spontaneous and stimulated) or non-radiative recombination (mainly from Auger and Shockley-Read-Hall recombination). The total recombination rate is the sum of all recombination rates in which the carriers are involved.

In bulk materials under external stimulus, the spontaneous rate is characterized by a material coefficient, B. Since two particles are involved in the recombination event, the spontaneous recombination rate can be written as

$$R_{spon} = B(np - n_0 p_0) \qquad \text{4-12}$$

where $np - n_0 p_0$ reflects the excess carrier concentration (the subscript denotes the thermal equilibrium value). Clearly, R_{spon} vanishes in thermal equilibrium. B is normally experimentally obtained as the second order coefficient in a polynomial fit to the recombination rate measurements as a function of carrier concentration. For GaAs and InP materials, there is an order of magnitude spread in B over the range from 1×10^{-10} to 1×10^{-9} cm^3/s.

The radiative event that is triggered by an optical field is stimulated emission. This recombination rate is related to the intensity of the optical field by

$$R_{stim} = v_g g(n,p) \bullet S \bullet I(x,y) \qquad \text{4-13}$$

where $g(n,p)$ is the material gain, S is the photon density, $I(x,y)$ is the optical field, and v_g is the group velocity.

Auger recombination is a nonradiative process whereby excess carriers recombine in a band-to-band transition that transfers energy to another charge carrier. The rate is parameterized by c_n and c_p reflecting energy transfers to the valence and conduction bands, respectively. Since three particles are involved in an Auger event, the Auger recombination rate is determined by a third-order polynomial fit to the recombination rate measurements. It is a function of carrier concentration, and is expressed as

$$R_{Aug} = (c_n n + c_p p) \bullet (np - n_0 p_0) \qquad \text{4-14}$$

The last recombination process normally considered in carrier dynamics is Shockley-Read-Hall (SRH) recombination. It concerns the deep traps near the middle of the band gap and is normally significant only in low quality crystals and in semi-insulating materials. Unlike the other recombination processes, the SRH process is the interaction between carriers and ionized energy levels deep inside the semiconductor band gap. These energy levels are normally generated by crystal defects (deep traps). The recombination rate is proportional to trap density and is parameterized by electron and hole carrier life times τ_n and τ_p, respectively. Trap properties are very strongly dependent on their local environment, and calculation of SRH recombination rates are therefore generally a very complicated process. However, in good quality crystals, where the deep trap density is much less than the doping concentration, the SRH recombination rate can be approximated by:

$$R_{SRH} = \frac{np - n_0 p_0}{\tau_p (n + n_1) + \tau_n (p + p_1)} \qquad \text{4-15}$$

where n_1 and p_1 depend on the intrinsic carrier density and the energy level of the trap acting as a recombination center.

4.2.5 Optical Gain Model

The optical gain is proportional to the probability that a given photon triggers an electron transition from a higher energy level j to a lower energy level i. Quantum mechanical calculation for this probability is well established. The simple gain function is found to be [86]:

$$g_{ij}(h\nu) = \frac{q^2 h}{2 m_0^2 \varepsilon_0 n_r c} \bullet \frac{1}{h\nu} \bullet \left|M(E_{ij})\right|^2 \bullet D_r(E_{ij})(f_j - f_i) \qquad \text{4-16}$$

where $M(E_{ij})$ is the transition matrix element. $M(E_{ij})$ determines the transition strength between energy levels in a given material. The density of allowed transitions between the two bands is given by $D_r(E_{ij})$, the reduced density of electronic states. The Fermi function f_j gives the probability that carrier occupies an energy level of E_j. The total optical gain will be the integral of all transitions to heavy and light holes, respectively, within the k-selection rule.

Although simulators usually evaluate each variable in a self-consistent calculation, two items are worth mentioning in greater detail: the transition matrix element and the relaxation time.

(1) Transition Matrix Element

The transition matrix element $M(E_{ij})$ depends on the angle between the electron wave vector $\vec{k}$ and the optical field vector $\vec{E}$. The optical transition requires averaging over all electron vectors encountered by the field at the given photon energy. For bulk zinc blende semiconductors, averaging over all possible $\vec{k}$ vectors results in an isotropic transition matrix element given by

$$|M|^2 = \frac{m_0}{6m_c}\frac{E_g(E_g + \Delta_{so})}{(E_g + 2\Delta_{so}/3)} \qquad \text{4-17}$$

where Δ_{so} is the energy gap between valence band (heavy and light hole) and the split-off valence band. E_g, Δ_{so} and m_c are calculated assuming a parabolic energy dispersion. The strain effects are incorporated in the calculation of the electron effective mass, m_c. Obviously, this model over-simplifies the sophisticated gain physics by ignoring details such as band mixing and many body effects. However, with the incorporation of a user-defined scaling factor, this simple model does match experimental results. More physically rigorous models are available, but they are much more challenging to implement numerically. Their implementation in device computation packages is unreasonable due to time and numerical solver constraints.

For quantum well structures, the transition matrix elements are highly anisotropic, and the gain depends on the polarization of the optical field, whether transverse electric (TE) or transverse magnetic (TM). Rather than the single isotropic transition matrix element M of the bulk material, there are now four such elements, one for each of the combinations of heavy hole, light hole and polarization state. These are modified by factors that depend on the direction of optical field, and expressed as

$$\left|M_{hh}^{TE}\right|^2 = \frac{3}{2} O_{ij} \frac{3 + 3\cos^2(\theta_e)}{4} M^2 \qquad \text{4-18}$$

$$\left|M_{lh}^{TE}\right|^2 = \frac{3}{2} O_{ij} \frac{5 - 3\cos^2(\theta_e)}{4} M^2 \qquad \text{4-19}$$

$$\left|M_{hh}^{TM}\right|^2 = \frac{3}{2} O_{ij} \frac{3 - 3\cos^2(\theta_e)}{2} M^2 \qquad \text{4-20}$$

$$\left|M_{lh}^{TE}\right|^2 = \frac{3}{2} O_{ij} \frac{1 + 3\cos^2(\theta_e)}{2} M^2 \qquad \text{4-21}$$

where O_{ij} is the overlap integral of the electron and hole wavefunctions, and θ_e is the angle to determine the polarisation factor.

(2) Relaxation Time

In semiconductors, an electron or hole will frequently interact with other carriers and with phonons. As a result, the electron and hole energies form sub-bands. This energy uncertainty will cause a symmetrical linewidth broadening to the transitions. The actual gain is then a convolution integral over the linewidth broadening function

$$g(hv) = \int dE_{ij} g_{ij}(hv) L(hv - E_{ij}) \qquad \text{4-22}$$

where $L(hv - E_{ij})$ is a weighting factor. Asada *et. al.* report the electron scattering processes in detail and suggest this broadening function have a Lorentzian line shape governed by a single parameter: [87, 88] the electron scattering time (or in some references, the electron relaxation time). This model is referred to as the Asada model. It is implemented in Las2D as the default model for the gain calculation of quantum well structures.

4.2.6 Temperature Model

Band gap shrinkage with increasing temperature is the intrinsic cause of the temperature dependence of many semiconductor parameters. There are two approaches to implement temperature models: the complete model, where each parameter is explicitly based on a temperature-dependent derivation; and the generic temperature model, where the temperature dependence is based on simple scaling projection of the temperature independent values. Las2D applies the latter approach. The user provides the temperature dependence of the parameters based on one of two generic temperature models.

The first generic temperature model uses a power law form as

$$P_i(T) = P_i(300)(\frac{T}{300})^{\alpha} \qquad 4\text{-}23$$

where P_i is a known parameter, $P_i(300)$ at the canonical temperature of 300K, and α is the power law exponent. This generic model is suitable for parameters that exhibit strong temperature dependence such as the radiative recombination constant, the intra-band relaxation time and the carrier mobility.

The second generic temperature model uses an exponential form as

$$P_i(T) = P_i(300)\exp(\frac{T - 300}{\beta}) \qquad 4\text{-}24$$

where β is the critical temperature. For a critical temperature not too far from 300 K, the exponential form approximates linear behaviour. The exponential law is thus suitable for parameters that show weak temperature dependence. Many temperature-dependent parameters can be modeled by this exponential law. Among them, the Auger coefficients and the optical absorption coefficients are typical examples.

4.3 GaInNAs Band Models

4.3.1 Band Anti-Crossing Theory

It is well known that the incorporation of isoelectronic impurities into a semiconductor will result in highly localized impurity states. The energies of these states depend on the electro-negativities of the substitution impurities. In the case of a highly electronegative impurity like nitrogen as a substituting anion in GaAs or InGaAs, the energy levels are located close to the conduction band edges. For example, in GaAs, nitrogen generates an energy level at about 0.23 eV above the conduction band edge. With increasing nitrogen concentration, the interaction between this localized nitrogen level and the GaAs (host material) band states changes the electronic structure of the resulting GaAsN system. The band Anti-Crossing (BAC) theory of dilute nitride alloys is found on this phenomenon and is expressed via a band gap $K \bullet P$ calculation.

Shan *et al.* introduced an extra interaction term in the Hamiltonian of two-band $K \bullet P$ calculation to include the coupling effects between the localized nitrogen level and the extended state of the GaInAs matrix. The 2×2 determinant is of the form [89]:

$$\begin{vmatrix} E - E_C & V_{NC} \\ V_{NC} & E - E_N \end{vmatrix} \qquad \text{4-25}$$

Where E_C is the conduction band edge energy of the nitrogen-free GaInAs matrix, E_N is the N level relative to the valence band edge of the host material, and V_{NC} is the matrix element describing the interaction between those two types of states. The interaction leads to a splitting of the conduction band. The dispersion relations of the reconstructed conduction sub-bands are expressed by

$$E_{\pm}(k)=\frac{1}{2}\left\{[E_C(k)+E_N]\pm\sqrt{[E_C(k)-E_N]^2+4V_{NC}^2}\right\} \qquad 4\text{-}26$$

Fig. 4-1 illustrates the dispersion relations of equation 4-26. The flattened and downshifted lower sub-band is responsible for most of the unusual effects demonstrated by nitrogen-content materials, such as the dramatic band gap reduction and the increase in electron effective mass.

Although the above description gives an exact relationship between the interacting energy levels, the dependence of the energy levels on alloy composition cannot be so determined. Using a tight-binding Hamiltonian, Lindsay *et al.* extended the BAC model. They determined empirically the dependence of the energy band gap and inter-band momentum matrix element on alloy composition and strain for GaNAs with up to 10 percent of nitrogen [11]. These key results enable simple analytical calculations of band gap dispersion, effective mass and optical functions of nitrogen content alloys.

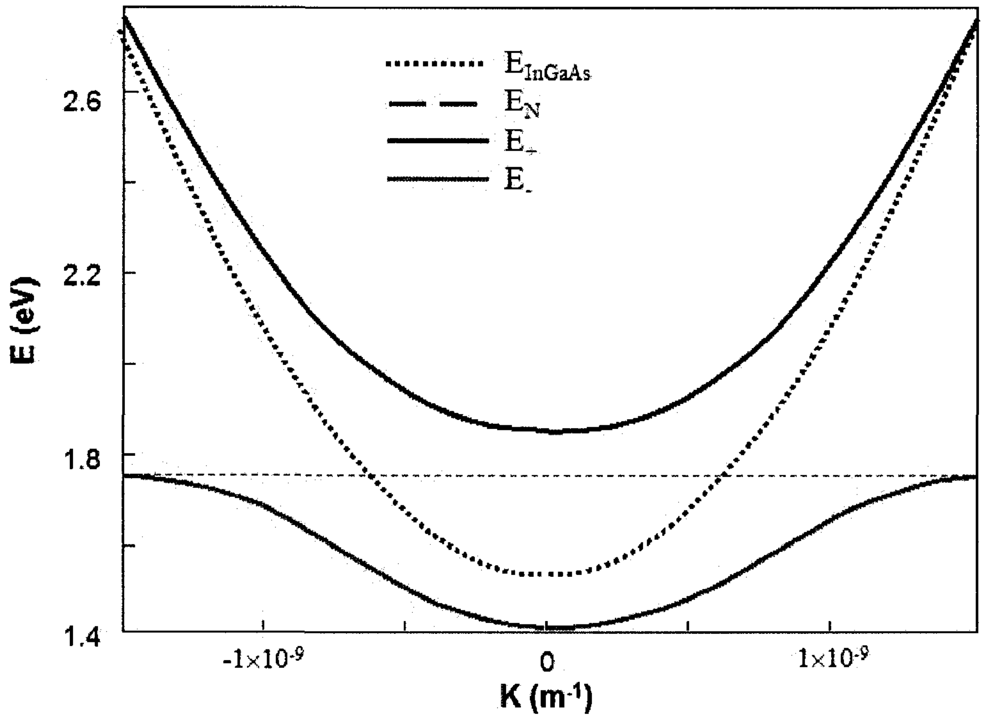

Fig. 4-1 Schematics of the conduction band reconstruction by localized nitrogen energy level in diluted nitride alloys.

Lindsay's empirical BAC model has been validated by photo-modulation spectroscopy, where electron transition behaviour under applied hydrostatic pressure was studied [89]. However, as noted in the following four points, some simplifying assumptions limit the accuracy of Lindsay's BAC model in practical thin film structures. Empirical modification is required for accurate implementation of the theory within simulation packages.

(1) Single Nitrogen Energy State

In the BAC model, the spatial distribution of nitrogen atoms is assumed random and homogeneous. The nitrogen is treated as a single, spatially-defined energy level underlying the non-nitride hosts, such as GaAs, InGaAs, and GaP. This assumption is not valid when nitrogen clusters exist in crystals. It has been shown that there is a tendency to form N-In_4 and N-In_3Ga_1 clusters in strained layers [90]. Those clusters can lead to multiple nitrogen energy levels that make the conduction band re-construction more complex than expressed in the BAC model. Therefore, the BAC model is limited to nitrogen concentrations for which the distance between neighbouring nitrogen atoms is much larger than the spatial extension of atom wave function. That means the nitrogen content in the alloy should not exceed about five percent.

(2) Un-deformed Valence Band

The BAC model considers an un-shifted valence band when adding nitrogen due to the relatively large energy separation between the nitrogen energy level and the valence band states. However, there is evidence of heavy/light-hole splitting in GaNAs even with a few percent of nitrogen [91]. The valence band splitting by the nitrogen incorporation implies that the valence-band deformation potential does not follow the linear interpolation of binary ends in nitrogen containing strained layers. This inconsistency is around 40 meV [91, 92]. If the bilinear interpolation is still applied to calculations of deformation potentials, the proper treatment is to add an empirical parameter that takes the extra valence band up-shift into account.

(3) Strain-induced Band Deformation

The conclusions of the BAC model were made in the absence of strain and quantum confinement. The native (unstrained) lattice constants of GaInNAs are, however, lattice mismatched to the GaAs substrate. O'Reilly accounts for the strain-induced band shifts using an 10×10 empirical Hamiltonian for GaNAs to GaAs [11, 12]. For InGaNAs gaps, the unstrained gap and the hydrostatic shift due to finite indium content must also be added to O'Reilly's theory.

(4) Temperature Effect

The dependence of the band gap on temperature is assumed from the conduction band dispersion $E_C(k)$, which follows from the Varshni formula. The nitrogen energy level E_N is considered independent of temperature. It implies an unchanged nitrogen energy level with temperature. One consequence of this assumption is a considerable weakening on the variation of fundamental energy gap with temperature in dilute nitride alloys.

4.3.2 Modified BAC Band Gaps

The Γ point is the normal reference in transition energy calculations. For strained layer quantum wells, the transition energy is determined by the material band gap, the hydrostatic shift and the quantum effect shift. Of these quantities, the quantum effect is the only one that can reasonably be treated separately.

To calculate the transition energy without the quantum effect, we must add two shifts into O'Reilly's GaNAs 10×10 $K \bullet P$ model. One is the unstrained gap, which is a chemical-induced shift. The other is the hydrostatic shift due to the finite indium content in the GaInNAs thin layer. The resulting Hamiltonian is [93]:

$$H = \begin{vmatrix} E_N & V_{CN} & 0 & 0 & 0 \\ V_{CN} & E_C - P(x) & 0 & 0 & 0 \\ 0 & 0 & E_V + Q(x,y) & 0 & 0 \\ 0 & 0 & 0 & E_V - Q(x,y) & -2^{1/2}Q(x,y) \\ 0 & 0 & 0 & -2^{1/2}Q(x,y) & E_V - \Delta(x,y) \end{vmatrix} \qquad \text{4-27}$$

where

$E_N = E_N^0 + \gamma y$, $E_N^0 = 1.61eV$ and $\gamma = 3.89eV$

$E_C = E_C^0 + \alpha y + \alpha_2 y^2$, $E_C^0 = E_g(x,0,T) = 1.414x + 0.354(1-x) - 0.477x(1-x)$

$\alpha = 1.55eV$, $\alpha_2 = 50.0eV$

$V_{CN} = \beta\sqrt{y}$, $\beta = 2.40eV$

$E_V = E_v^0 + \kappa y$, $E_v^0 = 0eV$, $\kappa = 3.88eV$

$P(x) = (a_v - a_c)(2\varepsilon_{xx} + \varepsilon_{zz})$, calculated for $In_{1-x}Ga_xAs$

$Q(x,y) = -b_v(2\varepsilon_{zz} - \varepsilon_{xx})$, calculated for $In_{1-x}Ga_xAs_{1-y}N_y$

The total transition energy is calculated by adding the quantum shifts. Using these equations, the calculated electron-to-heavy hole transition energy at 300 K is in good agreement with the experimental emission spectroscopy from the 7 nm InGaNAs/GaAs quantum well structure grown by MBE [94].

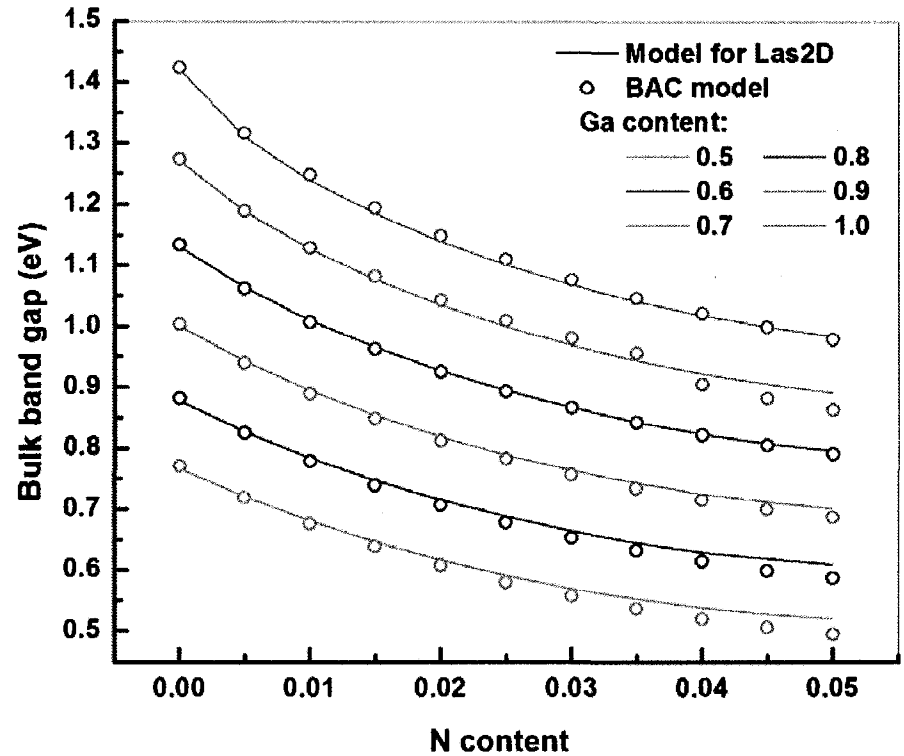

Fig. 4-2 The comparison in Γ band gaps as a function of nitrogen content between modified BAC model that is used in Las2D and the multi-band $K \cdot P$ calculation.

There are two practical problems in implementing the above 10×10 $K \cdot P$ calculation within laser simulators. First, the simulator cannot handle matrix calculation in material input files. Only simple analytical expressions are accepted. Second, in these software packages, the hydrostatic shift is calculated separately from the lattice matched band gap (chemical shift in band gap) using linear interpolation of related deformation parameters. Directly formulating equations 4-26 and 4-27 into simulation packages will double the hydrostatic shift. Moreover, as described in the last section, the simple linear interpolation of the deformation potential results in about 40 meV errors in the valence band shift.

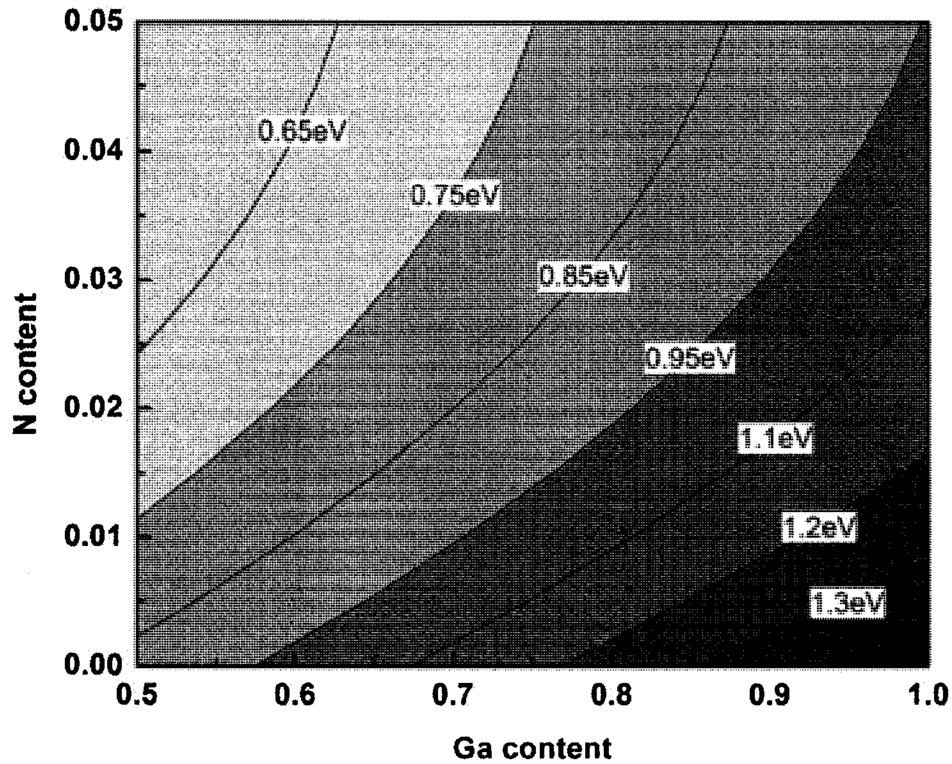

Fig. 4-3 Contour plot of Γ band gap of GaInNAs alloy with its composition of Gallium (0.5 ~ 1) and nitrogen (0~5%)

To solve the numerical application issue in a simple and straight forward way, equation 4-26 is implemented in a laser simulator with the corresponding parameters as determined by the 10×10 $K \bullet P$ calculation. All possible discrepency will be corrected by a variable valence band edge energy to the nitrogen composition by fitting the transition energy from equation 4-27 to the computation results from the 10×10 $K \bullet P$ calculation. Hence, instead of $E_V = E_v^0 + \kappa y$ with $E_v^0 = 0\,eV$ and $\kappa = 3.88\,eV$, the valence band edge is fitted as $E_V = E_v^0 + \kappa y + \zeta y^2$ with $E_v^0 = 0.037\,eV$, (that is an ~40 meV shift), with $\kappa = 4.5\,eV$ and $\zeta =$ 16.1eV. Fig. 4-2 compares the e1-hh1 transition energy at 300 K, calculated by the 10×10 $K \bullet P$, with the one calculated by the modified equation 4-26. The result agrees well within the interesting indium composition region for nitrogen contents of less than 5 percent. Fig. 4-3 is the GaInNAs's phase diagram using the modified BAC band gap as inputs.

4.3.3 Modified Electron Effective Mass

The effective mass approximation in semiconductors is valid only for the parabolic energy dispersion at small wave vectors $\vec{k}$, and for small electron energies near the minimal Γ point. However, due to N incorporation, the conduction band energy saturates at relatively low $\vec{k}$ magnitude, resulting in a heavy effective electron mass at higher energy levels in the InGaNAs alloys. The bending E_- band in Fig. 4-1 illustrates the effect.

To include the non-parabolic conduction band, the approach developed by Zawadzki is used. It calculates non-parabolic dispersion in small band gap semiconductors [95]. The electron effective mass m_c is energy dependent and its inverse is given by

$$\frac{1}{m_c(k)} = \frac{1}{\hbar^2 k}\left|\frac{dE(k)}{dk}\right| \qquad \text{4-28}$$

Replacing $E(k)$ by equation 4-26, the analytic expression for k-dependent inverse electron effective masses of nitrogen containing alloys is

$$\frac{1}{m_{c\pm}(k)} = \frac{1}{2m_c^0(k)}\left(1 \pm \frac{E_C(k) - E_N}{\sqrt{(E_C(k) - E_N)^2 + 4V_{CN}^2}}\right) \qquad \text{4-29}$$

where $m_c^0(k)$ is the electron effective mass of the host material, such as $Ga_xIn_{1-x}As$ in the case of $Ga_xIn_{1-x}N_yAs_{1-y}$. It can be taken as constant for a specific composition of x at small electron energy levels, which is the case of non-degenerated n-type $Ga_xIn_{1-x}As$.

The electron effective mass in $Ga_xIn_{1-x}As$ has been well studied, both theoretically and experimentally. However, the most reliable data is obtained for $Ga_{0.47}In_{0.53}As$, which is the composition that is lattice matched to InP. The data reveals the presence of a 0.0091 bowing factor in the VCA law. For the Ga composition of interest here, which is from 0.5 to 1, we ignore this bowing factor. The electron effective mass of $Ga_xIn_{1-x}As$ as a function of x is

$$m_c^0(In_{1-x}Ga_xAs) = 0.067x + 0.023(1-x) \qquad \text{4-30}$$

Fig. 4-4 gives a comparison between the 10×10 $K \bullet P$ calculation and the modified BAC model of equation 4-29 and equation 4-30 for the un-split electron effective mass (no quantum shifts).

As equation 4-29 indicates, the electron effective mass at higher energy levels is solely determined by the energy dispersion of the host material $E_c^0(k)$, for a given alloy composition. Hence, even though the energy dispersion of nitrogen content alloys is not parabolic, the effective mass, either of quantum-confinement-induced splitting or of degenerate electrons due to heavy impurity doping, can be calculated using the well-known host material energy dispersion. However, every laser simulation package assumes a parabolic dispersion and embeds this assumption in their computational algorithms. They calculate the electron effective mass at high energy levels based on the un-split mass using the parabolic approximation. Therefore, the split effective mass calculated by the simulator is smaller than the one calculated from the modified BAC model. The difference can induce errors on other entities such as the density of states.

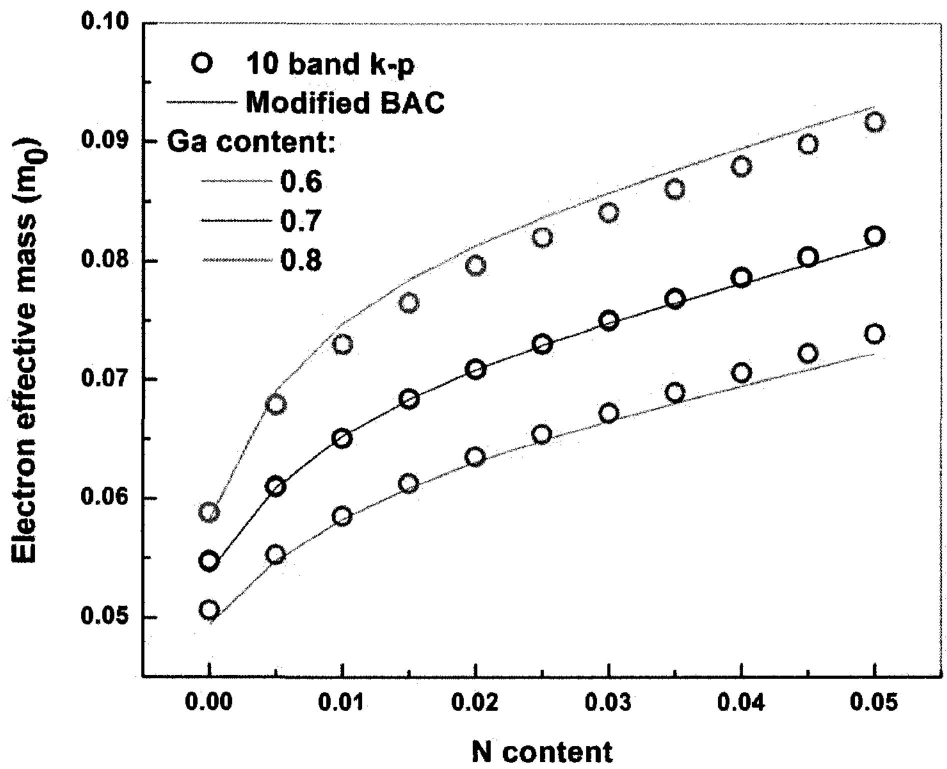

Fig. 4-4 The comparison in un-split electron effective mass as a function of nitrogen content between modified BAC model that is used in Las2D and the multi-band $K \cdot P$ calculation.

4.3.4 Band Alignment to GaAs

The formation of a dilute nitride alloy with the GaAs material system increases its laser wavelength into the fiber communication range of 1.3 to 1.6 μm. GaInAs QWs grown on GaAs cannot reach this wavelength range without over-straining the lattice. As a result, GaInNAs is of interest mainly as an active material in lasers. Therefore, the nature and magnitude of the GaInNAs/GaAs hetero-junction is important. A straightforward interpretation of the BAC model implies that the GaInNAs conduction band minimum must lie below that of GaAs. In term of valence band maxima, the relative energy position is less clear. Studies yield controversial results of type I and type II GaNAs/GaAs heterojunctions, indicating a nearly- vanished valence band offset [13, 96, 97].

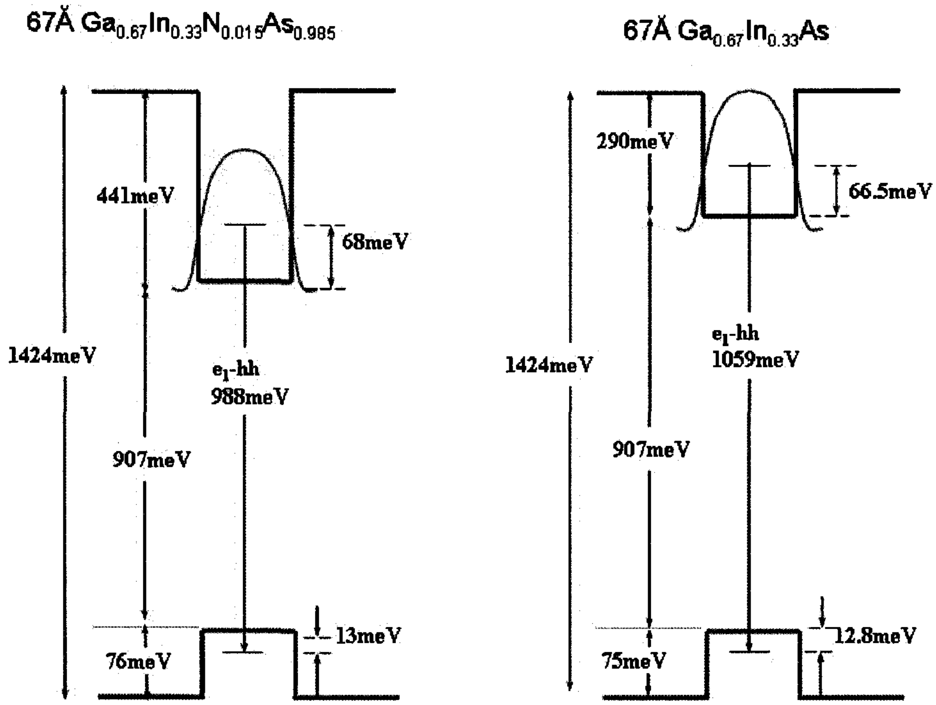

Fig. 4-5 Band alignment of GaInAs/GaAs and GaInNAs/GaAs at the same Ga/In ratio calculated by the multi-band $K \cdot P$ method. The valence band alignment remains same.

We assume that the heavy hole valence band does not shift much with the addition of nitrogen. The valence band offset (VBO) of a GaInNAs/GaAs hetero-junction equals that of GaInAs/GaAs hetero-junctions. This assumption implies a type I band alignment for GaInNAs/GaAs. Fig. 4-5 is an example of the band alignment from the 10×10 $K \bullet P$ calculation for both GaInNAs and GaInAs quantum well structures. The 1 meV difference in VBO at 1.5% nitrogen supports this assumption. The calculation is for a gallium content of x=0.67 with the hydrostatic shift included.

A large number of experimental and theoretical findings have been published over the years for the band alignment of GaInAs/GaAs hetero-junctions. However, the results are widely-spread due to the high degree of strain, which prevents the direct measurement of the VBO. Vurgaftman [3] did a comprehensive summary. He suggested that the VBO equals 0.21 eV for InAs/GaAs and 0.56 eV for $Ga_{0.47}In_{0.53}As$ excluding hydrostatic shift. The no-strain VBO as a function of gallium content can be obtained using the VCA law with a bowing factor of 0.477:

VBO ($Ga_xIn_{1-x}As$/GaAs) =

$$0.21(1-x)+0.477x(1-x)=0.21+0.267x-0.477x^2 \qquad \text{4-31}$$

The VBO of the GaInAs layer with respect to the GaAs substrate will decrease under compressive strain. The multiple band $K \bullet P$ calculation gives an approximately linear VBO as a function of gallium content x. The VBO with and without hydrostatic shift is plotted in Fig. 4-6. It agrees well with published data [2].

Fig. 4-7 is a schematic of the energy levels with respect to the vacuum energy E_0 for GaAs, GaInAs and GaInNAs. Detailed information on electron affinity is available for GaAs and InGaAs [98]. The electron affinity of GaInNAs can be calculated by aligning its conduction band edge with respect to the vacuum energy as

$$\chi = 4.07 + E_g(GaAs) - E_g(GaInNAs) - VBO(GaInAs) \qquad \text{4-32}$$

where $E_g(GaInNAs)$ and $VBO(GaInAs)$ are calculated using equation 4-26 and 4-31, respectively. The temperature effect of the affinity is included in the temperature-dependent band gaps of GaAs and GaInNAs, assuming the ratio of band discontinuity of conduction and valence band remains same.

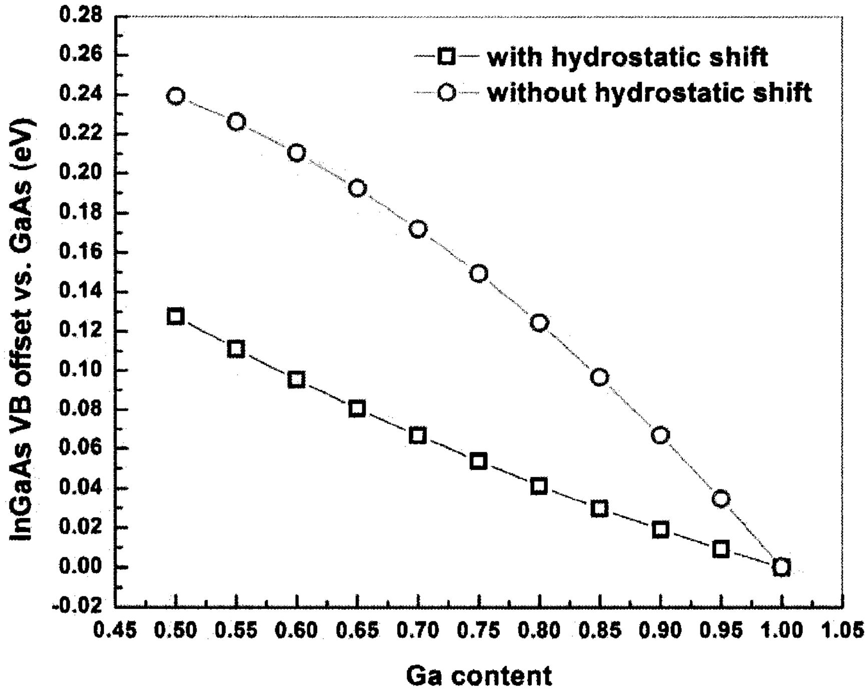

Fig. 4-6 Valence band offset with and without hydrostatic shift at the InGaAs/GaAs interface. The GaInNAs/GaAs interface presents a very similar valence band offset at the same gallium content.

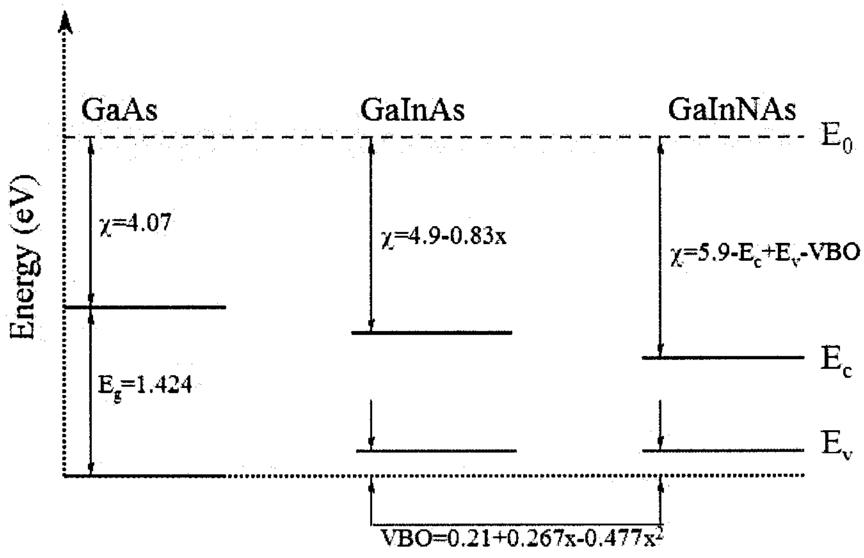

Fig. 4-7 GaInNAs affinity under the assumption of un-shifted valence bands by the nitrogen addition. The data in the schematics are at 300 K.

4.4 Electrical and Optical Properties of GaInNAs

4.4.1 Modified Caughey-Thomas-like Low-field Mobility Model

The Caughey-Thomas-like low-field mobility model is commonly used in calculating electron and hole mobilities for III-V semiconductors. Las2D simplifies the model with two modifications of equation 4-11. First, it separates the temperature and carrier density effects by first calculating room temperature mobility assuming that N_{ref} is close to N. Second, it uses a user-adjustable variable in the input file to include the temperature effect. This approach has two effects. The adjustable variable increases the calculation flexibility, but a simulation calibration is needed for each material system. In addition, a user defined mobility factor is used for adjusting the magnitude of mobility. These modifications eliminate three out of six fitting parameters in equation 4-11, leading to two simplified equations:

$$\mu(300K) = f_\mu \bullet \frac{\mu_{max}(300K)}{1+(N/N_{ref})^{\lambda}} \qquad 4\text{-}33$$

and

$$\mu(T) = \mu_{max}(300)\ \{\frac{T}{300}\}^{\theta} \qquad 4\text{-}34$$

where θ represents the temperature dependence of the mobility, and f_μ is the user adjustable mobility factor. Other parameters are defined in equation 4-11. The values can be found in Sotoodeh's publication [85] for the common binary and ternary materials.

4.4.2 Effective Electron Mobility

Before applying the model to dilute nitride alloys, reasonably accurate fitting parameters to the Hall mobility must be found, either directly for quaternary

GaInNAs or indirectly for ternary GaNAs and InNAs. Although transport properties for nitrogen-free GaInAs, GaAs and InAs are well established, any interpolation directly involving them will over-estimate the mobility of dilute nitrides. Ironically, beside the nitrogen clusters increasing the carrier scattering, the reason for low mobility in GaInNAs alloy is the intrinsic strong band gap bowing that makes it attractive for applications in lasers and solar cells.

There are a few theoretical analyses that estimate the mobility of dilute nitrides. Fahy et. al. [99] uses scattering theory to examine the dependence of electron mobility in GaNAs on temperature and nitrogen concentration. The mobility is predicted as no more than 2000 cm^2/Vs in intrinsic GaNAs. Moreover, the mobility has very weak temperature dependence in the temperature range from 100 to 300 K.

Experimentally, there are few data on Hall mobilities for dilute nitrides. Volz et. al.[100] has reported, for thick doped $Ga_{0.934}In_{0.066}N_{0.023}As_{0.977}$ layers on a GaAs substrate, the Hall mobility as a function of carrier concentration. Mobility values of 2000 cm^2/Vs for electrons and 200 cm^2/Vs for holes are achieved at low carrier concentrations. This result agrees well with Fahy's theoretical prediction. Moreover, the close Hall mobility values at 77 K and 300 K at all levels of hole concentrations provide evidence of the weak temperature dependence.

Based on the conclusions of the above references, the following strategy is used to obtain the electron mobility of GaInNAs and its dependence on electron concentration. The maximum mobility of GaNAs in Ref. [99] is curve-fitted for nitrogen contents up to two percent. It is the maximum mobility due to the fact that the theoretical analysis is dealing with intrinsic material and the doping is the major reason for mobility reduction. The finite indium effect on the maximum mobility is then added up using the interpolation between GaN, InN and GaAsN, taking advantage of the well-known properties of Wurtzite GaN and InN

$$Ga_xIn_{1-x}N_yAs_{1-y} = Ga_xN + In_{1-x}N + Ga_1AsN - Ga_1N \qquad 4\text{-}35$$

This results in the maximum electron mobility as a function of nitrogen content as shown in Fig. 4-8. The addition of indium shifts the mobility up slightly. However, as the figure shows, μ_{max} = 2000 cm^2/Vs is still a good estimate for the compositions of interest.

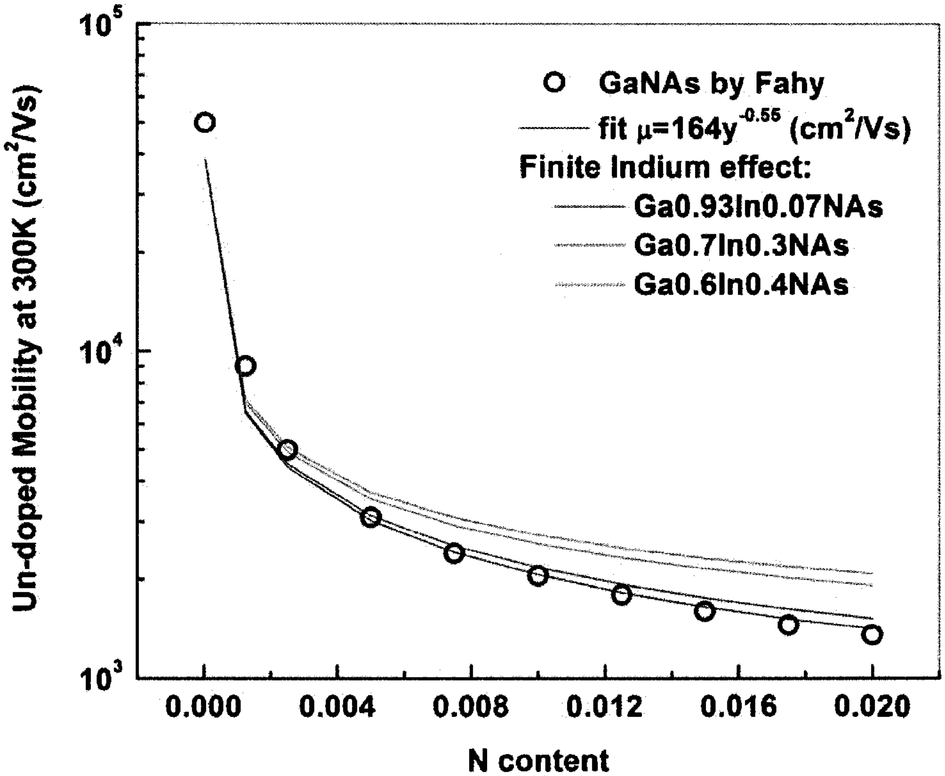

Fig. 4-8 The maximum electron mobility of GaInNAs. The finite indium effect is added into the GaNAs electron mobility theory proposed by Fahy et. al. by bilinear interpolation.

The doping effect is found by fitting the Hall mobility data provided in Ref. [100] using equation 4-34. The maximum mobility value was found to be 1300 cm^2/Vs for the composition of $Ga_{0.93}In_{0.07}N_{0.023}As_{0.977}$. This value is in excellent agreement with the theoretical estimation (Fig. 4-8) at the specified composition. N_{ref} and λ were found to be $5x10^{16}$ cm^{-3} and 0.4, respectively. Using the two step bilinear interpolation between GaNAs(GaAs-NAs) and InNAs(InN-InAs), with the respective data in Table 4-1, the calculated GaInNAs electron effective mobility agrees with the fitted model.

Putting the above analyse together, the electron mobility is modeled as

$$\mu_{max}(300K) = f_{\mu n} \bullet \frac{164y^{-0.55}}{1+(N/5x10^{16})^{0.4}} \qquad \text{4-36}$$

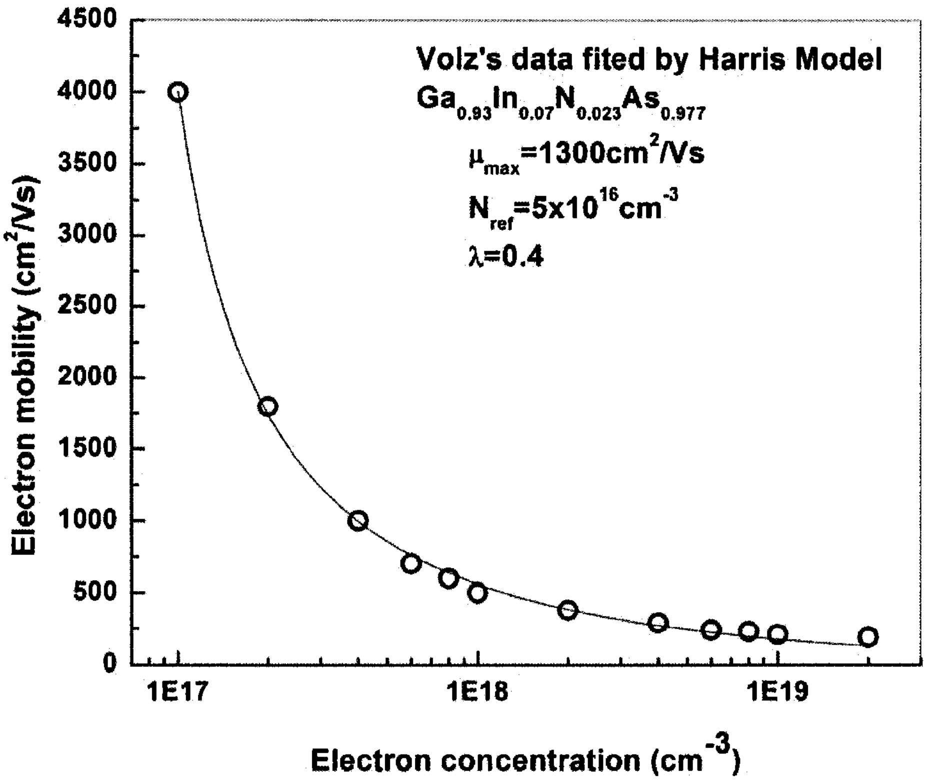

Fig. 4-9 Hall electron mobility of GaInNAs at the composition that lattice matches GaAs. The modified low-field Caughey-Thomas-like mobility model is achieved by fitting the Hall mobility.

with the temperature-dependent factor $\theta = 1$. Fig. 4-9 compares the electron mobility from equation 4-36 with Volz's Hall data in reference [100].

4.4.3 Effective Hole Mobility

There is even less information on hole mobilities in dilute nitride. Volz has grown Mg-doped p-type $Ga_{0.93}In_{0.07}N_{0.023}As_{0.977}$ layers on GaAs substrates. Hole mobility was shown to be smaller than 200 cm^2/Vs [100]. Like its electron counter parts, the hole mobility is also a weak function of temperature. Its carrier concentration dependence is fitted in the same manner as for electrons, resulting in a hole mobility of the form

$$\mu_{max}(300K) = f_{\mu p} \bullet \frac{85}{1+\left(N/1\times10^{19}\right)^{0.64}} \quad \text{4-37}$$

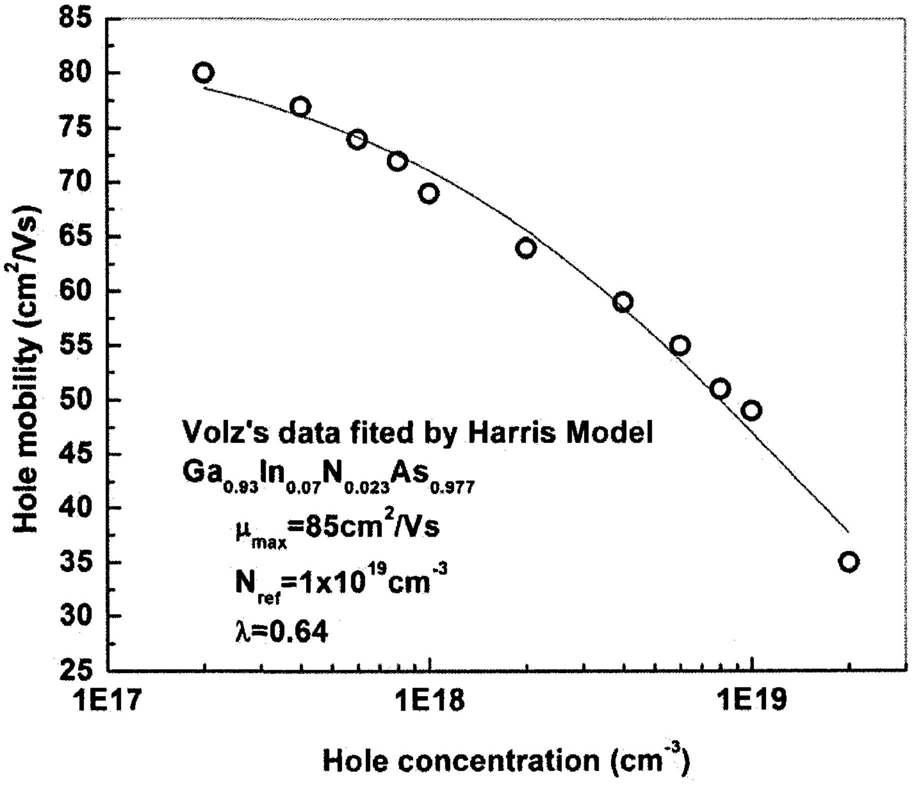

Fig. 4-10 The Hall mobility of p-GaInNAs at the composition that lattice matches to GaAs. The modified low-field Caughey-Thomas-like mobility model is achieved by fitting the Hall mobility in reference [100].

Fig. 4-10 compares the calculated hole mobility from equation 4-37 with Volz's Hall data in reference [100]. A good agreement has been achieved in the hole concentration of $1x10^{17}$ to $1x10^{19}$ cm^{-3}. Table 4-2 summaries the parameters in the Caughey-Thomas-like low-field mobility model for the alloys related to this work.

Table 4-2 Empirical parameters for low-field Caughey-Thomas-like mobility.

	Electron/ Hole	$\mu_{max}(300K)$ (cm^2/Vs)	$\mu_{min}(300K)$ (cm^2/Vs)	$N_{ref}(300K)$ (cm^3)	λ	θ_1	θ_2
GaAs	Electron	9400	500	$6.0x10^{16}$	0.394	2.1	3.0
	Hole	491.5	20	$1.48x10^{17}$	0.38	2.2	3.0
InAs	Electron	34000	1000	$1.1x10^{18}$	0.32	1.57	3.0
	Hole	530	20	$1.1x10^{17}$	0.46	2.3	3.0
GaN*	Electron	1461	295	$1.0x10^{17}$	0.66	----	1.02
	Hole	-----	-----	----	----	----	----
InN*	Electron	3138	774	$1.1x10^{17}$	0.68	----	6.39
	Hole	-----	-----	----	----	----	----
GaInNAs	Electron	$165/y^{0.55}$	-----	$5.0x10^{16}$	0.4	1.0	----
	Hole	85	-----	$1.0x10^{19}$	0.64	1.0	----

* Wurtzite crystals

4.4.4 Optical Function

Semiconductor lasers present both electrical and optical phenomena in one entity. The laser cavity is the active medium generating photons as well as confining generated electromagnetic waves to the waveguide. Two material parameters fully describe the interaction between optical radiation and semiconductor materials. They are the index of refraction $n_r(\lambda)$ and the optical absorption coefficient $\alpha_0(\lambda)$. These two physical parameters are inter-related.

Knowledge of the absorption spectrum will enable the calculation of the refractive index spectrum.

Absorption spectra have three distinguishable regimes: (1) The valence to conduction band transition where the photon energy is above the band gap. In this region, the absorption coefficient is related to frequency (and hence wavelength) as $\alpha_0 \propto \sqrt{\hbar\omega - E_g}$. (2) As photon energy decreases to levels that are slightly below the band gap, the absorption coefficient decays exponentially. These two mechanisms are normally included in laser gain and loss models and will be calculated in a self-consistent way by laser simulators. (3) Further decreasing the photon energy, the transitions within conduction band and valence band emerge as the dominant absorption mechanism. Those inter-band transitions are referred to as free-carrier absorption. The optical absorption coefficient is a function of the carrier concentration as

$$\alpha_0 = k_n n + k_p p \qquad 4\text{-}38$$

where k_n and k_p are the free-carrier absorption coefficients for n-type and p-type materials, respectively. Many types of transitions can be involved. However, inter-valence band absorption is of special importance as the energy separation between valence bands matches the photon energy generated by the device. The free-carrier absorption coefficients are found to be very similar among InP, GaAs and InGaAs. At 1.3μm, k_n=2x10^{-18} cm^2 and k_p=1.3x10^{-17} cm^2. Since the addition of nitrogen does not change the valence band structure much, the same values for inter-band free-carrier absorption coefficients are used in Las2D.

Regarding the other aspect of optical function, modeling the wavelength dependence of the index of refraction takes many forms. The most widely used one is the empirical second-order Sellmeier model

$$n_r^2(\lambda) = s_0 + \frac{s_1\lambda^2}{\lambda^2 - \lambda_1^2} + \frac{s_2\lambda^2}{\lambda^2 - \lambda_2^2} \qquad 4\text{-}39$$

where s_i and λ_i are fitted Sellmeier coefficients. Table 4-3 provides a list of values for the related binaries and their valid wavelength range. These coefficients can be interpolated directly to obtain the coefficients of ternary and quaternary alloys.

Table 4-3 Emperical parameters of Sellmeier model for some binary compounds[101].

	S_0	S_1	λ_1 (μm)	S_2	λ_2 (μm)	*Range* (μm)
GaAs	3.5	7.4969	0.4082	1.9347	37.175	1.4-11
InAs	11.1	0.71	2.551	2.75	45.662	3.7-31.3
GaN*	3.6	1.75	0.256	4.1	17.861	<10
InN*	----	----	----	----	----	----

* Wurtzite crystals

Table 4-4 Sellmeier parameters of GaInNAs alloys derived by bilinear interpolation for the binary end materials

$(Ga_xAs_{1-y}\text{-}In_{1-x}As_{1-y})\text{-}Ga_xN_y$	$(Ga_xAs_{1-y}\text{-}Ga_xN_y)\text{-}In_{1-x}As_{1-y}$
$s_0 = 3.5 + 22.9y - 22.8y^2$	$s_0 = 3.5 + 22.9y - 0.3y^2$
$s_1 = 7.5 - 26.1y + 20.4y^2$	$s_1 = 7.5 - 26.1y + 17.3y^2$
$\lambda_1 = 0.41 + 6.3y - 6.4y^2$	$\lambda_1 = 0.41 + 6.3y - 0.5y^2$

In Las2D, the first-order Sellmeier model is implemented for most III-V binaries and ternary alloys. However, as Table 4-3 implies, there is no information on InN. Interpolation must be made, either among $(Ga_xAs_y\text{-}In_{1-x}As_{1-y})\text{-}Ga_xN_y$ or among $(Ga_xAs_{1-y}\text{-}Ga_xN_y)\text{-}In_{1-x}As_{1-y}$. Using the lattice matching condition for $Ga_xIn_{1-x}As_{1-y}N_y$ on GaAs substrate (x=1-2.8y), the dependence of the Sellmeier parameters on nitrogen composition is summarized below. Table 4-4 indicates that the disagreement for different interpolating sequences is as small as a few percent. The quadratic terms for the equations in table 4-4 can be ignored, resulting in the same relationship to nitrogen composition of y.

4.5 Conclusions

This chapter presented the modeling of quaternary GaInNAs materials for laser simulation. The tabulated band gap energy and effective electron mass of the quaternary GaInNAs was formulated based on the BAC theory. The resulting formulas were further corrected based on experimental observations. This modified band anti-crossing theory was incorporated into the commercial laser simulator Las2D.

The characteristic parameters in the Caughey-Thomas-like low-field mobility model were found by fitting the Hall mobilities of electrons and holes that were reported in the literature. The mobilities for GaInNAs as a function of doping concentrations and temperature were implemented in Las2D. Similar methods were applied to optical functions. Other material parameters that follow the VCA law were put together into Las2D's look-up table.

The accomplishment of this material modeling was based on author's careful researches and investigations on: 1. BAC theory published on literatures, its applications and its limitations; 2. Empirical models of common physical identities in semiconductor material; 3. Multiple band $K \bullet P$ calculation tools, the origin of its discrepancy with BAC model; 4. LAS2D's computation principle in using its material models. As the results of this work, LAS2D is equipped with a new semiconductor alloy system. Together with other existing material systems (any combinations of Al, In, Ga, As, P), LAS2D becomes the first laser simulator to calculate the operational behavior of dilute nitrides.

Chapter 5 Simulation of Ridge Waveguide Lasers

5.1 *Introduction*

This chapter describes the two dimensional laser simulation methodology and analysis using the computational software package Las2D.

Although small in size, diode laser is a complicated micro system. Its operation involves electrical, optical, and electro-optical interaction. LAS2D simulates laser performance by self-consistent calculation among its physical models, namely, carrier transport model, gain model, heat flues model and optical mode model. Self-consistent calculation is often engaged to solve complicated systems which were governed by multiple models. Before simulation, a parameter set, a few hundred in LAS2D's case, in reasonable range of value, must be given in order to initialize calculations. The convergence criterion such as boundary conditions must be in place. During computation, numerical iteration adjusts those parameters continuously until unique values have been achieved. Those unique values satisfy the same initial models and the convergence criterion. Computation then terminates with solution. If by all means the unique value set are not found, the computation terminates without convergence (no solution to the initial model).

Traditionally, simulator calibrations are carried out one-dimensionally using broad-area laser samples. Broad-area lasers have ridge widths larger than 10 μm, which allows one to disregard any lateral current as it will account for less than 10% of the total current. One dimensional calibration is an efficient way to determine the value of each physical variable because it makes prominent important factors in sophisticated physical phenomenon. However, this method has difficulties in GaInNAs due to the fact that such broad-area lasers cannot achieve stimulated emission under the given current constraint of measurement equipment. An alternative is to calibrate the model with RWG devices in which the lateral current is of the same order of magnitude as the total current [102]. A methodology that is suitable for two-dimensional calibration must therefore be investigated.

The calibration methodology is researched using the well-studied InGaAs/GaAs single QW RWG laser. These lasers emit at a wavelength of 1.0 μm and exhibit high external quantum efficiency. First, laser emission theory is studied to find the parameters with dominant influence on laser threshold and efficiency. The values of these parameters for the InGaAs/GaAs lasers are extracted by combining two-dimensional calculation with experimental observations. The results are compared with references in the literature. The paramount importance of this work is that the methodology developed here is independent of laser material systems. To this extent, we can estimate the unknown parameter values of novel materials by combining results from simulation and simple experimental observation (L-I characteristics and their temperature dependencies). This estimation method avoids the need of advanced measurements, such as the carrier lifetime [103] and Auger recombination rate measurements [104] before proceeding to the simulation of dilute nitride lasers. This calibration methodology will be applied in chapter 6 to the GaInNAs lasers.

5.1.1 Las2D Simulator

Las2D is an integrated non-isothermal Fabry-Perot laser simulator developed by the scientists in the optoelectronics laboratory at the Polytechnique University of Montreal. During the past fifteen years, the models and functionality have been upgraded according to the requirements from the laser designers at Nortel Networks (formerly Bell Northern Research). It can calculate strained-layer quantum well lasers and semiconductor amplifiers, made on GaAs and InP, with arbitrary alloy compositions. The self-consistent calculation is based on classical models of carrier transport, optical gain, heat flux and mode profile. The major advantages of Las2D simulator are as follows: (1) The physical models are kept simple. Users with a background in physics or electrical engineering can understand the models and the computational algorithm. (2) Users have control of simulation results through user-defined parameters. This makes for easy calibration of Las2D using the fabricated laser samples of the specified process. The simulator has been fully calibrated with Nortel's 1.3 μm and 1.55 μm InGaAsP/InP lasers. (3) New material systems can be added in the simulator using stand-alone material simulators, which can calculate even the more complex properties of semiconductors. (4) The interface is user-friendly. It uses read-in input files to define the device structure and it can easily be modified to any structural change.

Las2D has not previously been calibrated for GaAs-based materials. Although Las2D employs a self-consistent calculation, it may not faithfully represent the materials and fabrication processes. By aligning the simulation result with measured InGaAs/GaAs laser characteristics, the values of parameters for GaAs material systems can be found.

5.1.2 InGaAs/GaAs Lasers

InGaAs on GaAs quantum wells are the most technologically mature III-V material systems. InGaAs alloys are used as gain media for high-speed electronic devices, infrared lasers and long wavelength quantum cascade lasers. The most important optoelectronic application of InGaAs/GaAs devices is for high-power 980 nm pump lasers, one of the key devices in submarine fiber communication systems. InGaAs is valuable for advanced research because it retains a direct-gap material over its entire composition range. Its band structure is known with great precision and its quantum well exhibits the highest optical gain [53]. However, as its indium composition increases, the increased lattice mismatch to GaAs limits the increase of InGaAs emission to 1.2μm. This explains the use of GaInAsP/InP lasers in fiber communications since it requires laser emission in the 1.3 to 1.65 μm wavelength range.

Table 5-1 Layer structure of the strained-layer single quantum well GaInAs/GaAs laser emitting at 1.0μm.

layer	thickness (nm)	dopant (cm^{-3})
p-GaAs (contact)	100	Zn: 1.0×10^{19}
p-$Al_{0.22}Ga_{0.78}As$ (cladding)	870	Zn: 1.0×10^{18}
AlAs (etch stop)	3	Zn: 1.0×10^{18}
p-$Al_{0.22}Ga_{0.78}As$ (cladding)	130	Zn: 1.0×10^{18}
GaAs (SCL)	200	intrinsic
$In_{0.2}Ga_{0.8}As$ (QW)	7.5	intrinsic
GaAs (SCL)	200	intrinsic
n-$Al_{0.22}Ga_{0.78}As$ (cladding)	3000	Si: 1.0×10^{18}
n-GaAs (Substrate)	5000	Si: 2.0×10^{18}

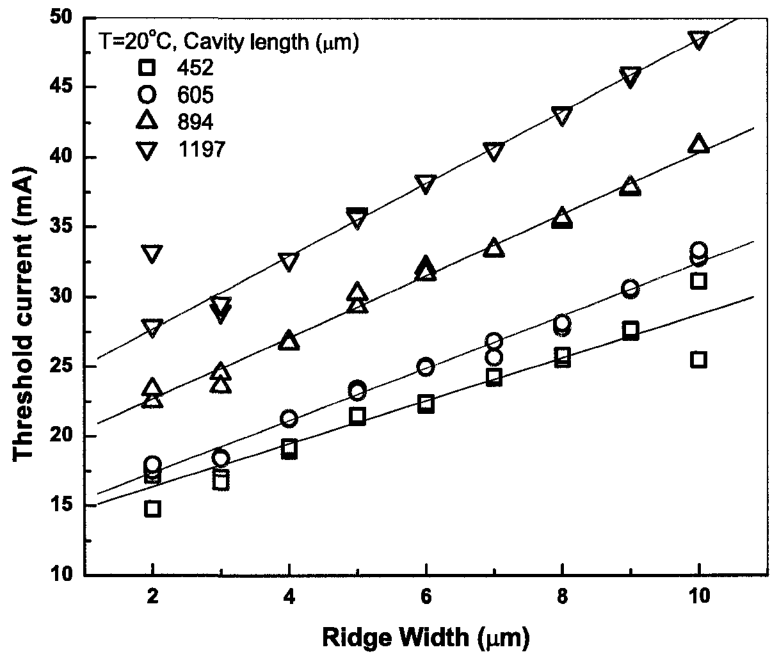

Fig. 5-1 The threshold current as a function of ridge width for lasers made by etch stop process. The data from 2 and 3 μm ridge devices (in red) are not included in the linear fits.

The GaInAs/GaAs material system is also very important for this study, as the GaInNAs/GaAs is no more than a study of GaInAs/GaAs with the nitrogen as an additional substituting anion. Chapter 4 exclusively studied the nitrogen's effect on band gap, electron effective mass and carrier mobility. In this chapter, the focus is on the simulation of GaInAs/GaAs 1.0 μm lasers.

Table 5-1 lists the layer structure of the MBE-grown single QW InGaAs/GaAs laser. The standard process introduced in Chapter 1 was applied to make RWG lasers with one small change: rather than dry etching all the way through the active region, the mesa was formed by first dry etching, followed by selective wet etching. The thin 3 nm AlAs layer acts as an etch stop and therefore prevents further penetration of the etching solvent. This process leaves a uniform p-cladding layer over the wafer. Lasers with ridge widths ranging from 2 to 10 μm in increments of 1 μm were fabricated. The lasers were cleaved into cavity lengths ranging from approximately 450 to 1200 μm. The facets were left as cleaved without passivation and coating. Fig. 5-1 plots the threshold current for each laser sample, measured at 20°C. The linear fit to the data reveal some of the important laser internal parameters.

5.2 Laser Geometry Dependent Simulation

5.2.1 Analysis of Carrier Consumption at Threshold

The diode laser threshold carrier density, N_{th}, is determined via the threshold current

$$I_{th} = I_{SRH} + I_{spon} + I_{Auger} + I_{vleak} + I_{lleak} \qquad 5\text{-}1$$

where the subscripts refer to Shockley-Read-Hall (SRH) recombination, spontaneous emission (spon), Auger recombination (Auger), vertical leakage (vleak), and the lateral leakage (lleak). SRH and Auger recombination are weak because the material is of high quality and the InGaAs/AlGaAs/GaAs hetero-junctions has a relatively wide band gap. Moreover, the deep QW created by a InGaAs and GaAs hetero-junction greatly suppresses vertical carrier leakage. As a result, lateral leakage and spontaneous emission consume most of the injected carriers below threshold. Although the etch stop process of these InGaAs/GaAs lasers effectively improves the uniformity in threshold current over devices, the geometry-dependent L-I measurements show only a marginal decrease in lateral leakage current, remaining about half the threshold current for all lasers with cavity lengths ranging from 600 to 1200 μm (Fig. 5-1). To simulate laser behaviour appropriately, the first step is to evaluate the lateral leakage current accurately.

The lateral leakage current is mainly caused by diffusion and the drift of holes through the remainder of the heavily p-doped ($1\times10^{18}cm^{-3}$) AlGaAs cladding layer under the ridge. Hence one can write the threshold current as

$$I_{th} = J_{th}L_cW + I_{lleak} = J_{th}L_c \bullet W + J_{lleak}t \bullet L_c \qquad 5\text{-}2$$

where J_{lleak} is the lateral leakage current density, L_c is the cavity length, W is the ridge width and t is the thickness that the lateral leakage current passes through. Note that t may not equal the thickness of the remaining p-cladding. Nevertheless, it is safe to assume that t is the same for all lasers under this study due to the etch stop process. I_{lleak} is obtained from the intercepts of the linear fits in Fig. 5-1. Applying a linear fit of I_{lleak} to cavity length L_c, the lateral leakage current density can be estimated as $J_{lleak}t = 150\, mA \bullet cm^{-1}$, as is shown in Fig. 5-2.

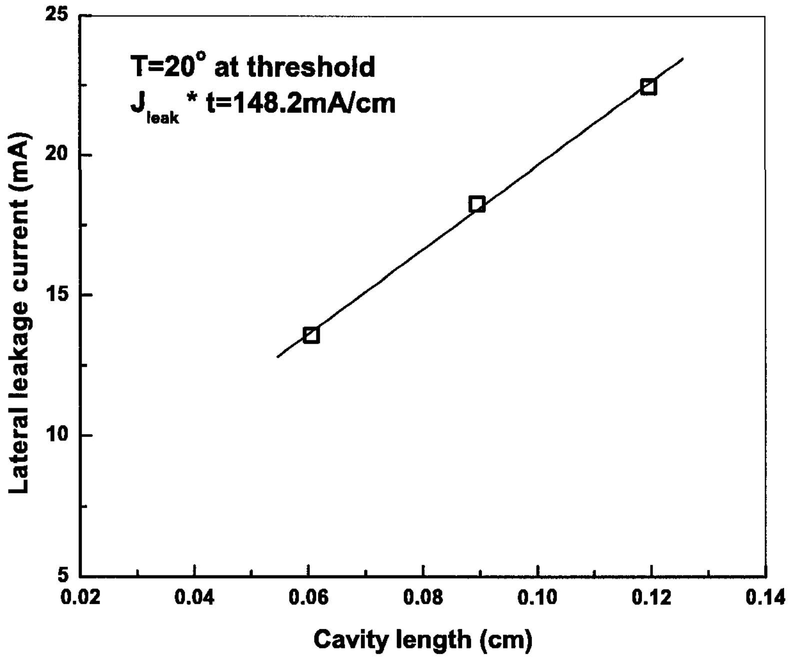

Fig. 5-2 Lateral leakage current as a function of cavity length. The linear fitting gives the integral of leakage current density over the vertical direction (along the growth direction).

The current density in a p-type semiconductor can be described by the one-dimensional charge continuity equation derived from equation 4-9, as

$$\frac{\partial p}{\partial t} = -p\mu_p \frac{\partial \varepsilon}{\partial y} - \mu_p \varepsilon \frac{\partial p}{\partial y} + D_p \frac{\partial^2 p}{\partial y^2} + G - R + \frac{j_p}{qd} \qquad 5\text{-}3$$

where j_p is the injection current into a volume of thickness d. μ_p and D_p are the hole effective mobility and effective diffusion coefficient. These two relate to each other through the Einstein relation, $D_p = B\mu_p kT / q$, where B is a material-related factor.

Laterally, carrier generation and recombination are unlikely underneath the ridge, and the injection current density, j_p, is small as well. Therefore the last three terms in equation 5-3 above can be neglected. The lateral leakage current density strongly depends on the effective hole mobility, which is the dominant parameter in the first three terms in equation 5-3. Other parameters, particularly the spontaneous emission rate, play a second-order role through the hole spatial distribution. Applying this analysis to equation 5-1, we conclude that the effective hole mobility largely determines the intercepts of the linear fit in Fig. 5-1. This is the lateral leakage current at threshold as the laser ridge width goes to zero.

Vertically, equation 5-3 describes the hole dynamics. An analogous equation exists for electrons. Carrier generation and recombination is the force driving the laser to reach threshold. All effects contribute either to gain or loss until the carrier density reaches the threshold level. Hence, the slopes of the linear fits in Fig. 5-1 are determined by gain, spontaneous emission rate, and mobility (lateral leakage), under the assumption that all other recombination mechanisms and vertical carrier leakage are minimal.

The above analysis, although qualitative, is helpful in determining the starting point of the simulations, namely finding an appropriate effective hole mobility factor for the heavily doped $Al_{0.22}Ga_{0.78}As$ layer. The analysis simplifies the two-dimensional problem by de-correlating lateral and vertical axis. A rigid analysis using carrier transport and continuity theories proves that, rather than a constant, the lateral leakage current is a function of laser ridge width, W, as [105]

$$I_{lleak}(W) = \frac{J_{th}L_cL_D\left(1-e^{-W/L_D}\right)}{1-\frac{L_D}{W}\left(1-e^{-W/L_D}\right)} \qquad \text{5-4}$$

where L_D is the hole effective diffusion length.

Varying the ratio of ridge width to hole effective diffusion length permits an intuitive understanding of the lateral leakage current density. As W/L_D approaches zero, $I_{lleak}(W \to 0) = 2J_{th}L_cL_D$. As W/L_D gets large, $I_{lleak}(W \to \infty) = J_{th}L_cL_D$. Combining the slopes of Fig. 5-1's linear fits, which equals $J_{th}L_c$, the hole effective diffusion length is estimated as $L_D \approx 4\ \mu m$. This is the reason why the threshold current departs from the linear trend at ridge widths narrower than 4 μm.

5.2.2 Hole Effective Mobility

In Las2D, the "field" mobility model is the default in two-dimensional calculations. The low field hole mobility of $Al_xGa_{1-x}As$ is modeled as:

$$\mu_p = \frac{\left(0.04 - 0.048x + 0.02x^2\right)\times 10^4}{\left(1 + N_p / 2.75 \times 10^{17}\right)^{0.4}} f_{up} \qquad \text{5-5}$$

where N_p is the doping concentration and f_{up} is a global rescaling factor for users to arbitrarily change the mobility value. A two dimensional simulation is conducted for the 4 μm ridge width device for a range of f_{up} and spontaneous emission rates. Other parameters remain at default values in the simulations. An example of calculated results on lateral leakage current densities is shown in Fig. 5-3 for both electrons and holes. The lateral leakage current density increases asymptotically as injection current is increased. The holes strongly spread out around 8.5 μm, which is the position of the active region and the heavily p-doped $Al_{0.22}Ga_{0.78}As$ region under the AlAs etch stop layer.

To determine the mobility factor, f_{up}, the lateral hole current density in Fig. 5-3 is integrated over the vertical direction (the growth direction). By comparing with the experimental data, found as $J_{lleak}t = 150\, mA \cdot cm^{\ 1}$, an effective hole mobility factor between 0.65 and 0.85 covers the range of most probable spontaneous emission rate of 0.5 to $2.5\text{x}10^{-10}$ $cm^{-3}s^{-1}$ (Fig. 5-4). The best fit value is found later as $f_{up} = 0.65$, corresponding to a hole effective mobility of $\mu_p = 107 cm^2 / Vs$ using equation 5-5. This value agrees well with the published hole mobility of heavily-doped AlGaAs [98].

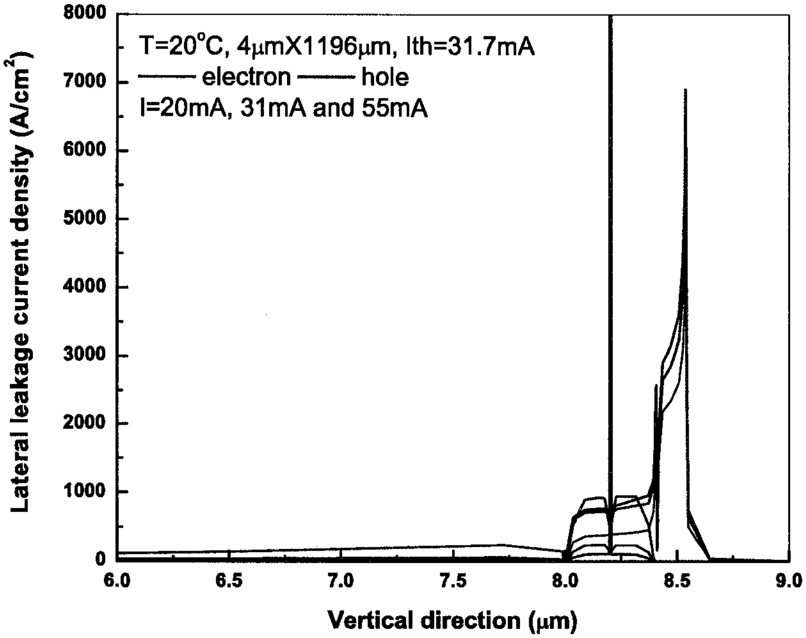

Fig. 5-3 Lateral current density along the growth direction. The figure shows that the primary lateral leakage is from hole diffusion through the heavily doped upper cladding layer.

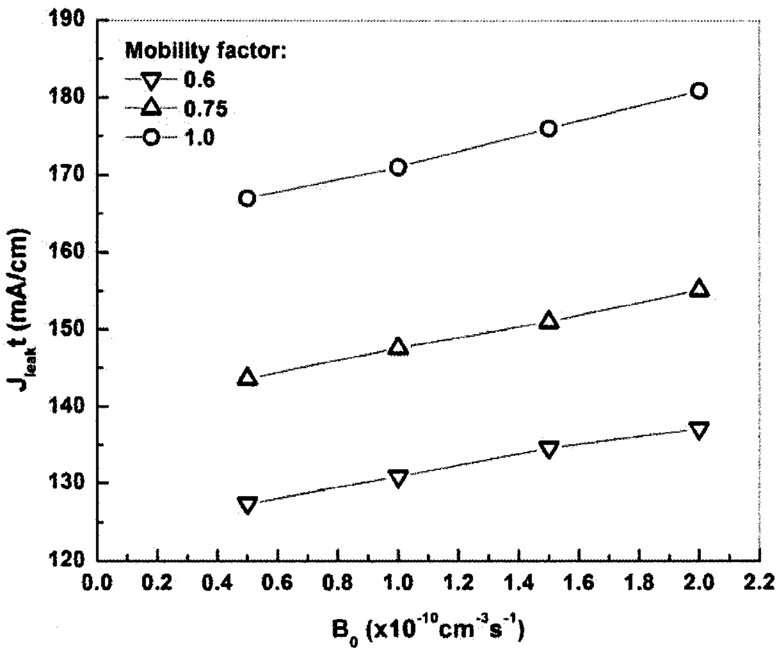

Fig. 5-4 The integral of leakage current over the growth direction as a function of spontaneous emission rate for a set of hole mobilities of the p-AlGaAs upper cladding layer. A mobility factor of 0.65 is estimated.

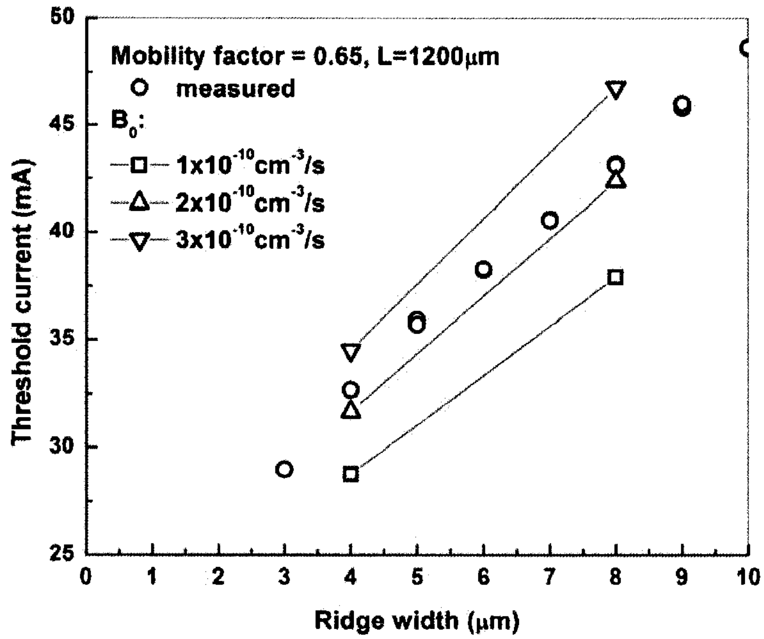

Fig. 5-5 Threshold current of 4 and 8 μm devices with a set of spontaneous emission rate calculated at fixed mobility factor of 0.65 and optical absorption coefficient of 2 cm^{-1}. $B_0 = 2x10^{-10}$ cm^{-3}/s is estimated.

5.2.3 Spontaneous Emission Rate

After excluding the lateral leakage from equation 5-1, the spontaneous emission becomes the major carrier consumer below threshold. Effectively, it is the sole factor that determines the slope of the linear fit in Fig. 5-1. The spontaneous emission rate of photons is characterized by a material coefficient, the spontaneous emission recombination constant, B_0. B_0 is around $1.0x10^{-10}$ cm^3/s for lightly doped (~10^{14} cm^{-3}) $Ga_{0.47}In_{0.53}As$ (band gap energy equal to 0.8 eV) and $7.2x10^{-10}$ cm^3/s for n-GaAs [106]. Information on B_0 for $In_{0.2}Ga_{0.8}As$ (band gap energy ~ 0.95 eV) could not be found. However, B_0 tends to increase with larger band gap values.

Las2D specifies B_0 as a variable in the input file. Calculating the threshold current as a function of ridge width for 4 and 8 μm wide devices at a set of B_0, the best B_0 that fits the slope of experimental data is found to be B_0=$2.0x10^{-10}$ cm^3/s (Fig. 5-5).

5.2.4 Optical Absorption Coefficients

Beside threshold current, L-I measurements provide another important performance parameter, namely, the slope efficiency. The slope efficiency is defined as $\eta_s = dP/dI$ above threshold and is related to cavity loss

$$\eta_s = dP/dI = \eta_i \frac{\alpha_m}{\alpha_m + \alpha_i} \frac{\hbar\omega}{q} \qquad \text{5-6}$$

The internal quantum efficiency η_i can be understood as the probability of an additional electron, injected above threshold, contributing to the stimulated recombination. At this stage of simulation, it is taken as a constant. α_i is the optical absorption factor determined by the integral of the local absorption coefficient α_0 over the cavity dimension, weighted by the intensity of optical field. Micro-analysis of the local absorption coefficient reveals that

$$\alpha_0 = \alpha_b + k_n n + k_p p + k_{ivb} p \qquad \text{5-7}$$

where α_b represents carrier-density-independent mechanisms such as photon scattering at defects. k_n, k_p are the free carrier absorption coefficients for electrons and holes, respectively, and k_{ivb} is the inter-valence band absorption coefficient. These absorption mechanisms, as well as α_i, are carrier density dependent.

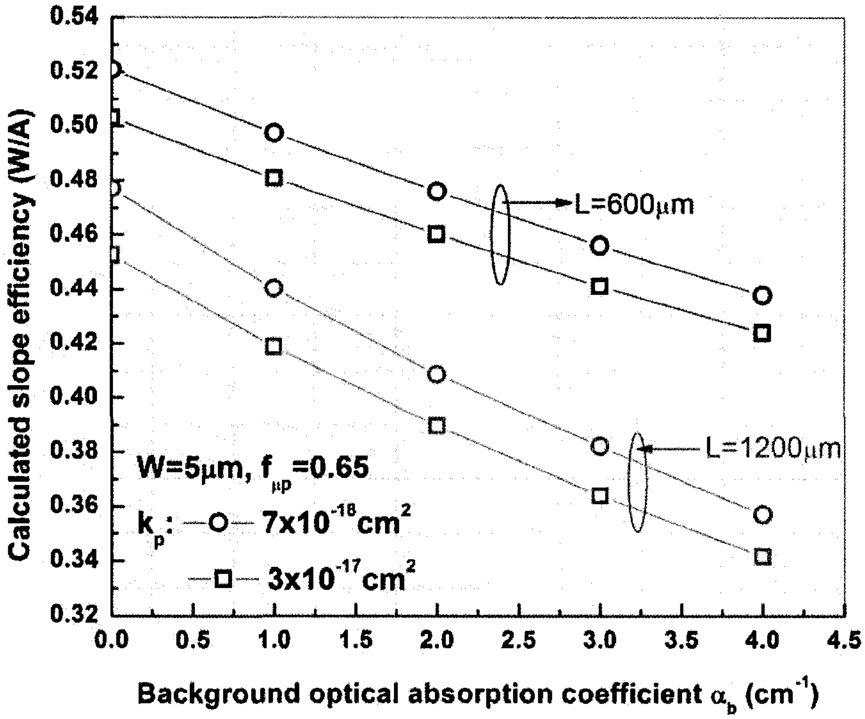

Fig. 5-6 Slope efficiency as a function of background optical absorption coefficient at different values of free hole absorption coefficient assuming free electron absorption is insignificant.

It is very difficult to accurately measure the free carrier absorption coefficients in quantum wells. However, band analysis points to a small free electron absorption coefficient of $k_n \sim 10^{-18}$ cm^2 [106]. Inter-band absorption is proportional to hole concentration. Employing compressive strain in QWs can reduce the inter-band absorption through the deformed valence bands, which can be expressed as $k_p >> k_n \approx k_{ivb}$. Free hole absorption dominates the carrier dependent absorption mechanisms.

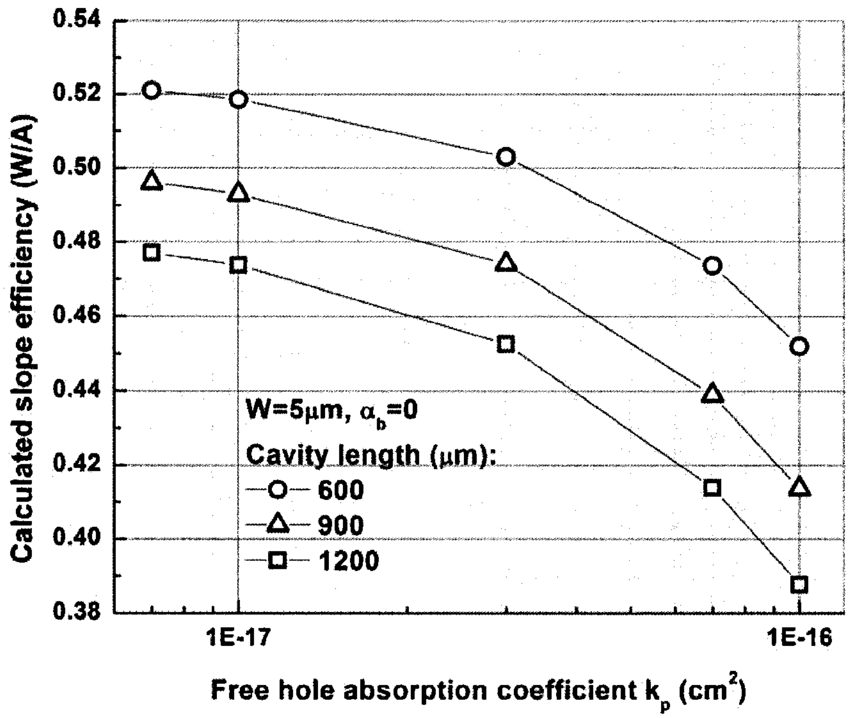

Fig. 5-7 The slope efficiency as a function of free hole absorption coefficient at different cavity length as the background absorption factor vanishes. The slope efficiencies from the common factor of $k_p = 7\text{x}10^{-17}$ cm^2 provides the best fit.

Using Las2D's default values of $k_n = k_{ivb}$=3x10^{-18} cm^2, Fig. 5-6 shows an attempt to find a common set of α_b and k_p for the 600 and 1200 μm long devices by fitting the calculated slope efficiency to the L-I results. The slope efficiencies are 0.47 and 0.42 W/A for 600 and 1200 μm devices, respectively. Unfortunately, no overlapping k_p values are achieved for $\alpha_b > 0$. Nevertheless, Fig. 5-6 indicates that as α_b vanishes, a common k_p may exist for devices with different cavity lengths. A similar simulation is carried out at $\alpha_b = 0$, for cavity lengths of 600, 900 and 1200 μm, respectively, using k_p as the variable. As Fig. 5-7 shows, a common k_p value of 7x10^{-17} cm^2 is found. This value is ten times larger than Las2D's default k_p value. It lies between the measured values of strongly strained (3.5×10^{-17} cm^2) [80] and unstrained (1.4×10^{-16} cm^2) quantum wells [107].

5.2.5 Intra-band Relaxation Time

The interaction of electrons and holes with other carriers and photons leads to an energy uncertainty that broadens the transition energy in carrier recombination. Modelling the effect with a Lorentzian line shape is a good approximation, as was found by Asada [88]. This is because the occupation probability of an electron state decays exponentially, with a scattering time constant called the intra-band relaxation time. The intra-band relaxation time varies as a function of temperature and carrier density. Since the carrier density increases as the laser dimension decreases, the intra-band relaxation time will be longer for shorter devices.

Las2D incorporates Asada's Lorentzian line shape model for the calculation of gain broadening. The intra-band relaxation time is an adjustable constant in the input files. Given a set of intra-band relaxation times, a series of simulations may be carried out for different laser cavity lengths. Fig. 5-8 plots the calculated threshold current as a function of intra-band relaxation time. The intra-band relaxation time can be estimated by aligning the calculated threshold current with the experimental one. It varies with cavity length and the values are found to be 210, 150, 120 and 100 fs for the cavity lengths of 450, 600, 900 and 1200 μm, respectively. As later simulation demonstrates, the intra-band relaxation time is the only parameter that varies with device length.

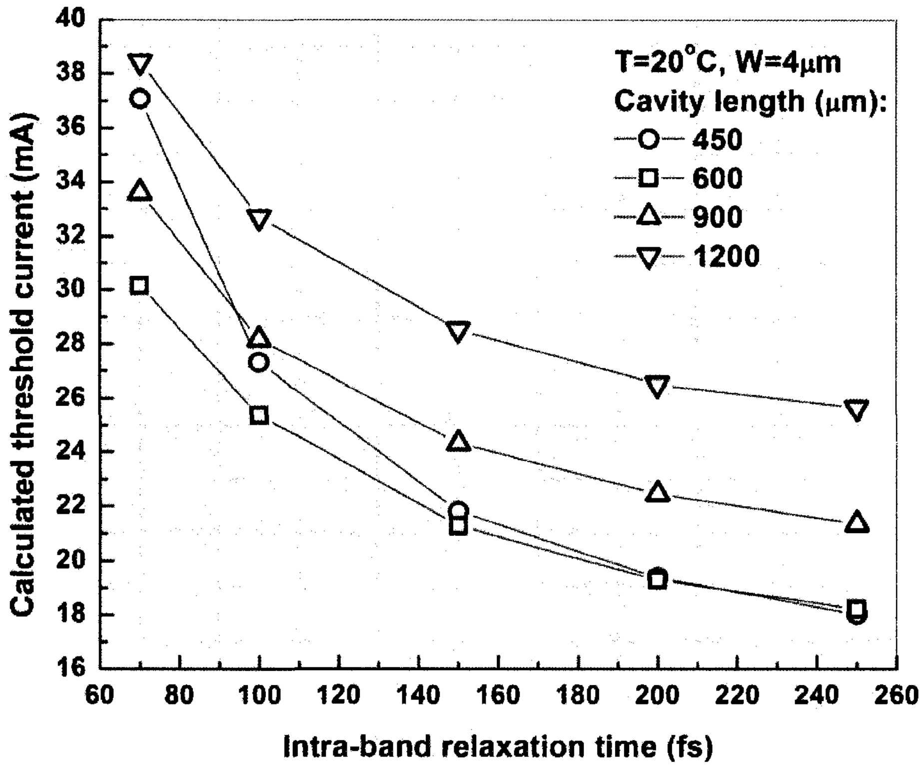

Fig. 5-8 The calculated threshold current as a function of intra-band relaxation time for the 4 μm width devices at different cavity lengths. For 1196 μm devices, a default value of 100fs is used.

5.2.6 Geometry Dependent Simulation

Using the parameters discussed in sections 5.2.1 through 5.2.5 as input, and simulating the devices with various geometrical sizes, the threshold current and slope efficiency are calculated. The results are plotted in Fig. 5-9 and Fig. 5-10. The experimental values obtained from the L-I measurement are plotted as well. The excellent fit of the threshold current for all devices implies the internal physical parameters were correctly approximated. Moreover, it demonstrates an effective method of calibrating a laser simulator for the two-dimensional ridge waveguide structure.

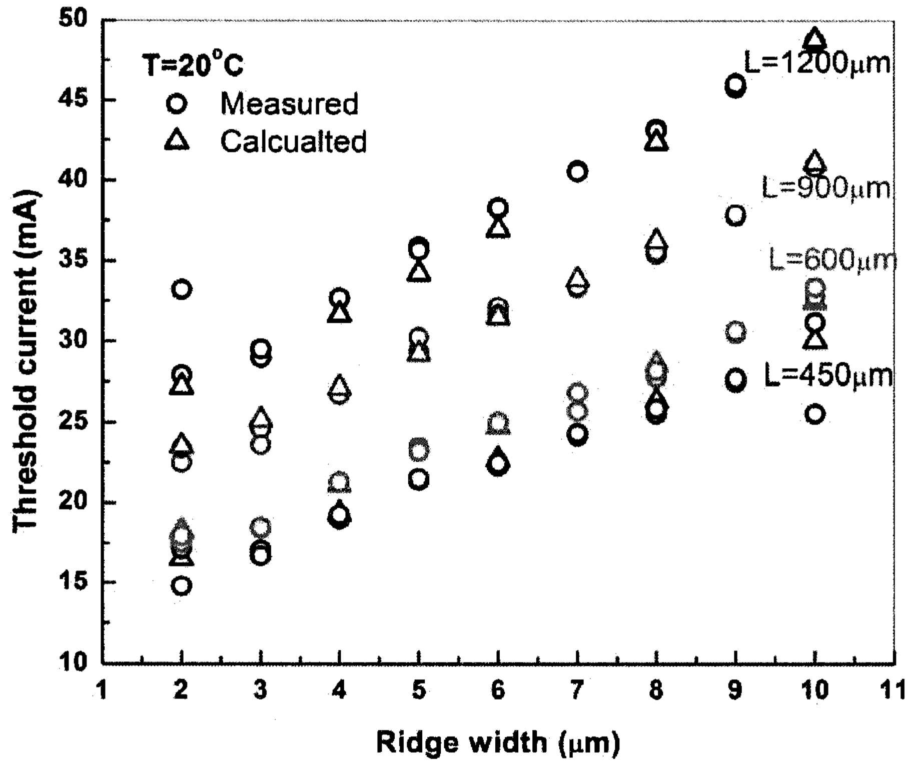

Fig. 5-9 The simulated and experimental threshold currents using the calibrated Las2D simulator. The experimental data is reproduced from Fig.4-1.

As Fig. 5-10 indicates, the calculated and measured slope efficiencies reveal deeper physics. The calculated slope efficiency agrees well with the experimental results for ridge widths larger than 5 μm. For the 2 to 5 μm ridge widths, the measured values diverge from the calculated ones by up to 20% for the narrowest ridges. This disagreement in narrow devices is due to a more pronounced scattering loss in narrow devices. The increased scattering loss is not taken into account by the simulator, and optical absorption increases at higher carrier densities. Las2D does include the effect in its self-consistent calculation by using adjustable free carrier absorption coefficients. However, the linear model of equation 5-7 under-estimates the carrier density effect on optical absorption. A non-linear optical absorption model would remedy the problem.

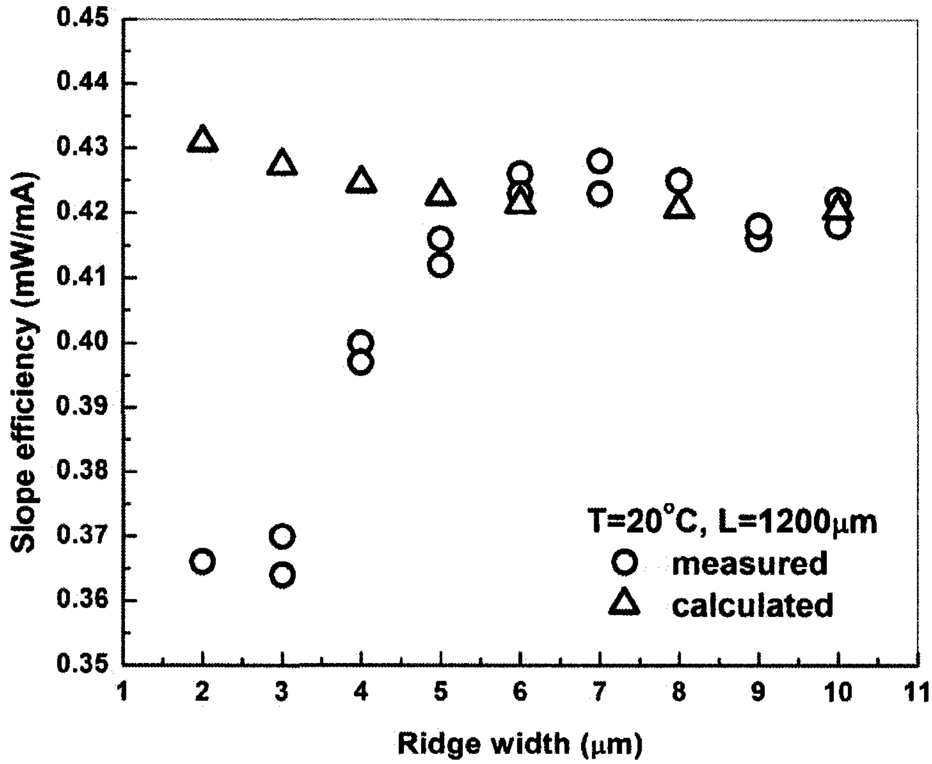

Fig. 5-10 The simulated and measured slope efficiency for various ridge widths.

5.3 Simulation Results of GaInAs/GaAs Laser

5.3.1 Band Structure

Stimulated emission in diode lasers can only occur in p-n junctions when more electrons are present in the conduction band than in the valence band. The external electrical field allows carriers to stay in energy inversion by injecting current into the junction. This equilibrium between carrier injection and carrier consumption is sustained in the nearby junction region. One of the major concerns in laser design is to optimize band structures for efficient carrier injection and better carrier confinement. Although band structure is grossly determined by the material combination of quantum wells and barriers, fine tuning of the layer thickness and doping levels can tailor laser performance for specified requirements, such as ultra-low threshold operation, high modulation speed operation, or large output power.

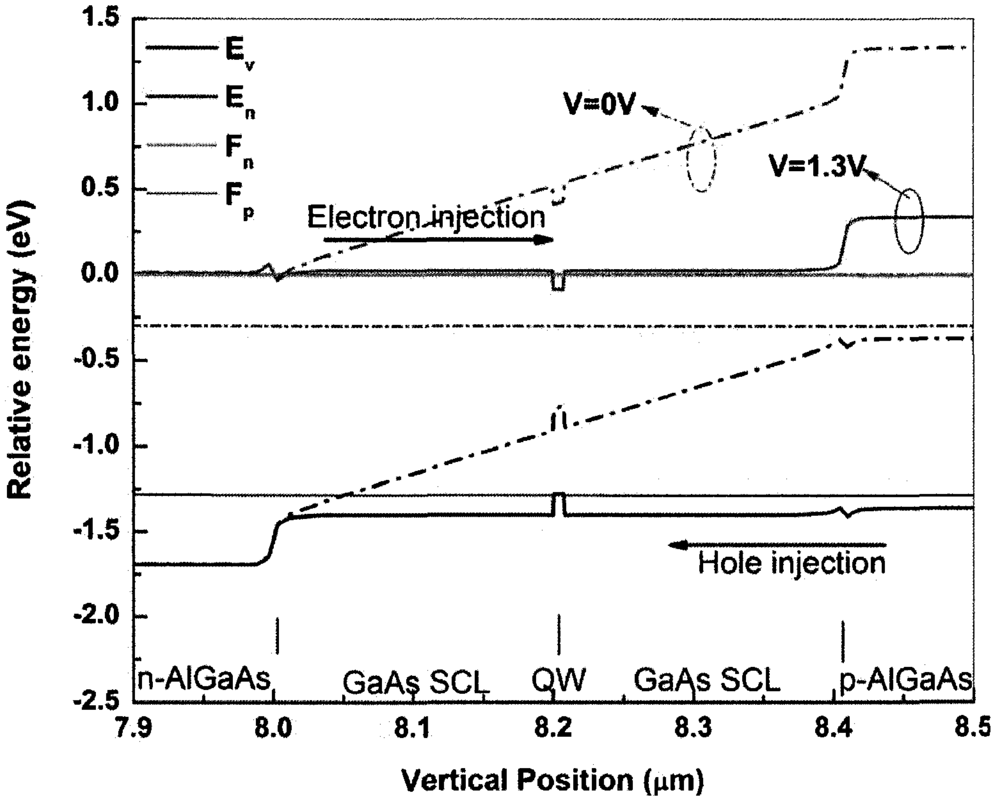

Fig. 5-11 The conduction bands, the valence bands and the Fermi levels calculated by Las2D. The plot shows the change from zero bias (V=0 V) to the bias at threshold (V=1.3 V).

A self-consistent simulation calculates the bands and the carrier distribution for different applied electrical fields using the drift-diffusion model. Fig. 5-11 illustrates the change in conduction and valence bands for the InGaAs/GaAs single QW laser from zero bias to 1.3 V, the value at which the device reaches lasing threshold. The figure also indicates the Fermi levels of the electrons and holes. The deep entrapped electron Fermi level in the QW indicates the carrier inversion at that voltage. However, the shallow and thin QW is not efficient to capture carriers. The large potential steps provided by the AlGaAs cladding and GaAs separate confinement layers ensure the carrier confinement.

5.3.2 Optical Gain

The choice of proper model and input values is supported by the excellent agreement of the calculated gain peak, the calculated e1-hh transition energy by the $K \bullet P$ method, and the peak of the emission spectrum. They are at 0.993, 0.990 and 0.998 μm, respectively. The first two values are from a calculation based on the parabolic band approximation for InGaAs. In addition to the strain incorporation method, Las2D's simulation approach differs from the $K \bullet P$ band calculation. It does this by taking into account carrier dynamics over the applied voltage using a self-consistent carrier drift-diffusion model and an optical model. The result agrees more closely with the sophisticated physical interaction inside a laser cavity. Therefore Las2D's calculation gives a better match to the experimental wavelength than the $K \bullet P$ band calculation [108].

Fig. 5-12 displays the optical modal gain spectra at different levels of bias current. At low current, the second electron excitation level is clearly observed (at 0.925 μm). As the current increases, the e2-hh transition gets harder to observe due to band filling of electrons. The gain experiences a step like non-linear increase. The maximum differential modal gain is calculated as 4.9×10^{-17} cm^2, corresponding to a material gain of 1530 cm^{-1} per 1×10^{18} cm^{-3} carrier density (1.5×10^{-15} cm^2 differential material gain).

Fig. 5-12 also demonstrates the blue shift of the gain peak with increasing bias current due to carrier occupancy of higher energy states. The wavelength-current shift is calculated to be -0.39nm/mA.

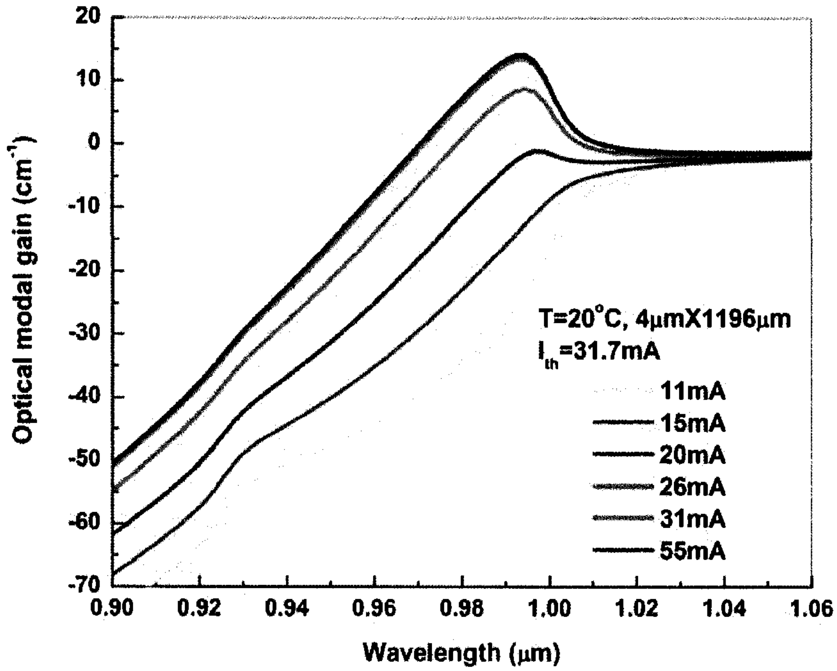

Fig. 5-12 Room temperature modal gain spectra calculated by Las2D. Gain saturation is clearly observed above the threshold current.

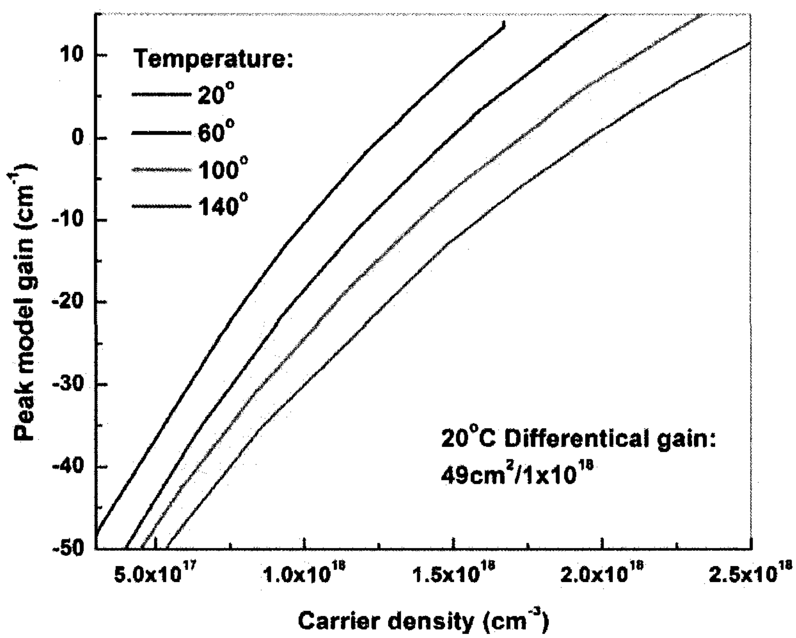

Fig. 5-13 The peak modal gain as a function of carrier density in the QW. The differential gain decreases as the temperature increases.

One of the major reasons for diode laser performance degradation at high ambient temperature is the reduction in material gain caused by the wider spreading of the carrier Fermi distribution at higher temperatures. In Fig. 5-13, the peak modal gain at different temperatures is plotted. Not only does it decrease with increasing in temperature, the differential gain also reduces at a rate of 1.4×10^{-19} $cm^2/°C$. The reduction in differential gain indicates an increase in non-radiative carrier recombination at high temperature. The spreading of electron energy also reduces the band gap. This thermal band gap shrinkage is observed as the modal gain peak shifts to the low energy side of the spectra with increasing temperature. GaInAs/GaAs lasers exhibit a rate of -0.37 meV/K. That is equivalent to 0.29 nm/K in the wavelength-temperature coefficient.

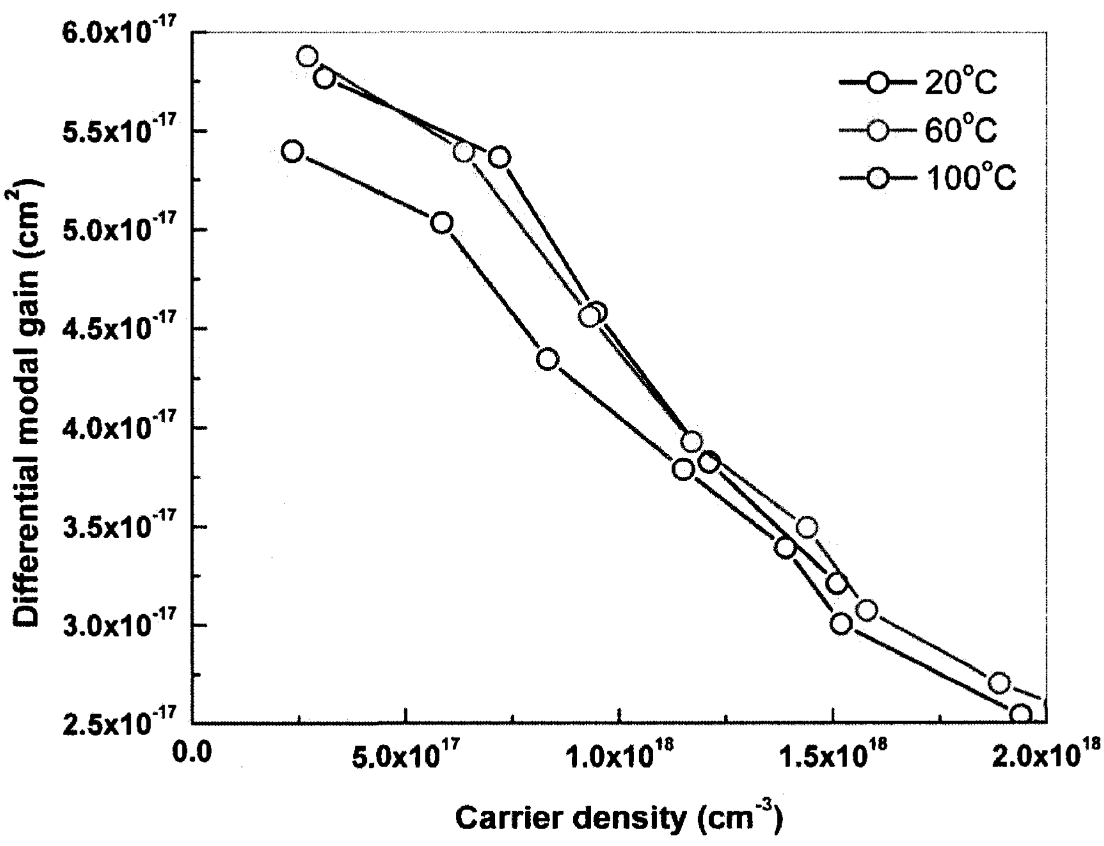

Fig. 5-14 The differential gain versus carrier density for three operating temperatures. The step-like decrease of the differential gain is observed at the carrier density levels of $5 \times 10^{17} cm^{-3}$, $7 \times 10^{17} cm^{-3}$ and $1.4 \times 10^{18} cm^{-3}$.

5.3.3 Optical Loss

Once a photon is generated by an electron-hole recombination, it either stimulates another radiative recombination or is absorbed by exciting an electron-hole pair. This competition is always present during the laser operation, and it determines the laser efficiency. Two loss factors are required to quantify the amount of absorption. They are the mirror loss α_m and the internal loss α_i. The former one can be easily calculated using facet reflectivity and cavity length. The latter one depends on many factors such as the carrier density, optical field intensity and cavity imperfection. Modeling-wise, the value of the internal loss can only be determined by self-consistent simulation.

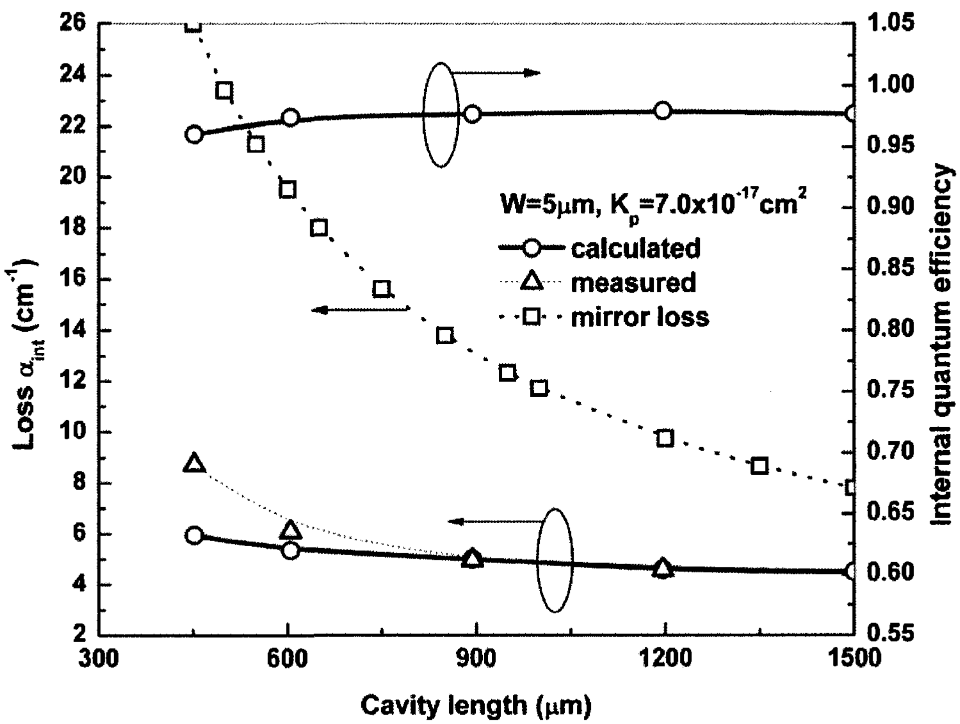

Fig. 5-15 Internal loss and internal quantum efficient as a function of cavity length calculated by the calibrated simulator. The exponentially increasing mirror loss at short cavity length explains the strong dependence of optical absorption to the carrier density. Experimental results on optical loss are plotted for comparison.

Las2D calculates the internal loss α_i through integration of the local absorption coefficient weighted by the optical intensity. The conventional way to acquire α_i uses a linear fit of cavity-length-dependent L-I measurements. This method is valid only for long cavity devices, since it is based on the assumption that the internal quantum efficiency and internal loss are independent of the cavity length. In fact, the internal loss is proportional to the carrier density in the laser cavity. Therefore, shorter devices have larger internal loss and lower internal quantum efficiency.

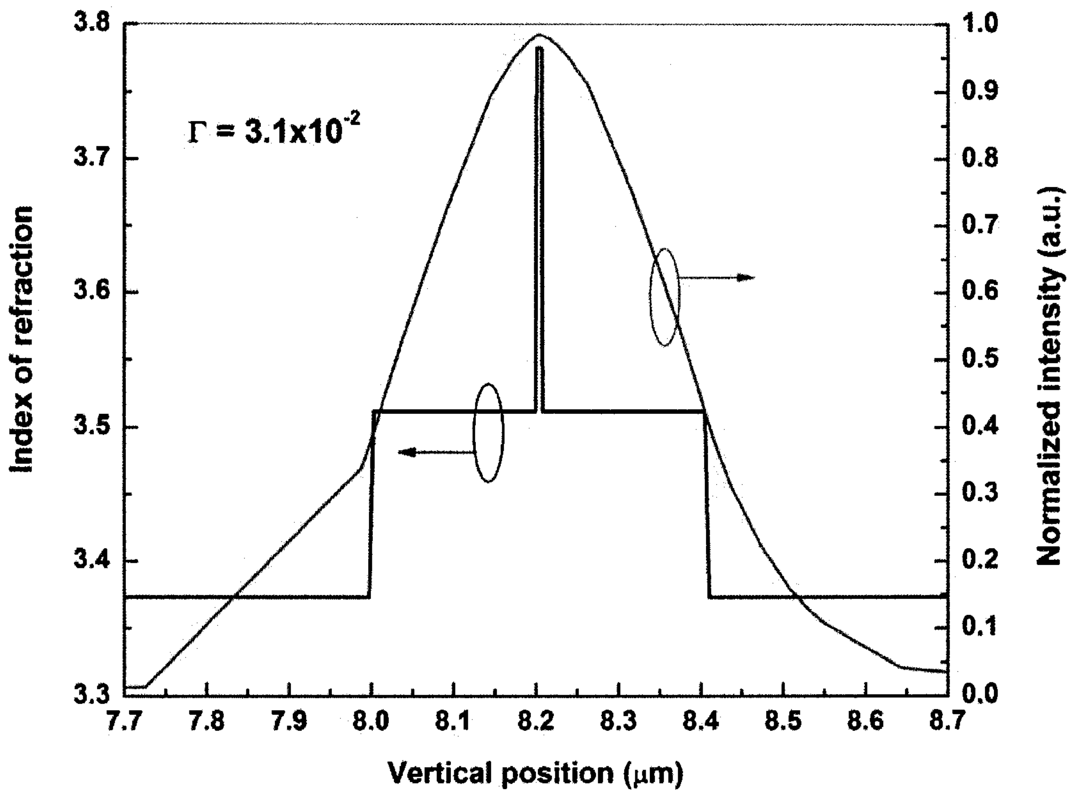

Fig. 5-16 The calculated refractive index profile and optical intensity along the growth direction in laser active region. As carrier saturates beyond threshold, the refractive index profile reminds the same at higher current injection.

Fig. 5-15 reveals the cavity length effect on the internal parameters. The calculated internal quantum efficiency decreases slightly for cavity lengths shorter than 600 μm, while the internal loss increases strongly for cavity lengths less than 900 μm. The same trend is predicted by the simulated internal loss. However, the simulator underestimates the internal loss for the shorter cavities. This divergence between simulation and experiments is correlated with the mismatched slope efficiency in the 450-μm-long devices, using the same K_p value as in the longer cavity devices. Two points can be drawn here. First, the simple linear absorption model underestimates the effect of carrier density on optical absorption. Second, the linear fit to extract internal parameters is valid only for devices with cavity lengths longer than 900 μm. In those long devices, the mirror loss has only a weak dependence on cavity length, as does the transparent carrier density. This observation sets a practical guideline for the experimental analysis of laser internal parameters.

Of primary importance for proper laser operation is the calculation of the refractive index profile and hence the optical mode in the laser cavity. Fig. 5-16 plots the optical intensity along the growth direction in a laser cavity at a bias current slightly above laser threshold. The optical confinement factor Γ, that is defined as the ratio of the optical volume in the active layer to the volume of the total optical mode, is calculated as 0.031. This factor is determined by the refractive index profile near the active region at the biasing carrier density. This "hot" refractive index profile is therefore used for optical mode calculations. A simulation that does not involve carrier dynamics could result in a faulty optical profile, with very negative impact on ridge width design close to the single mode operation limit (usually around 2 to 4 μm).

5.3.4 Carrier Consumption

As described in the previous section, once a carrier is injected, it has a chance to vanish via non-radiative or radiative recombination, with the probability depending on the band structure, material quality, and operating temperature. By integrating the recombination rates over the volume of the active region, the carrier consumption for each recombination mechanism can be calculated as a function of current. The carrier leakage, either vertically over the confinement layers or laterally spreading out of the active region, can be quantified as a function of current by integrating the current density over the corresponding cross section.

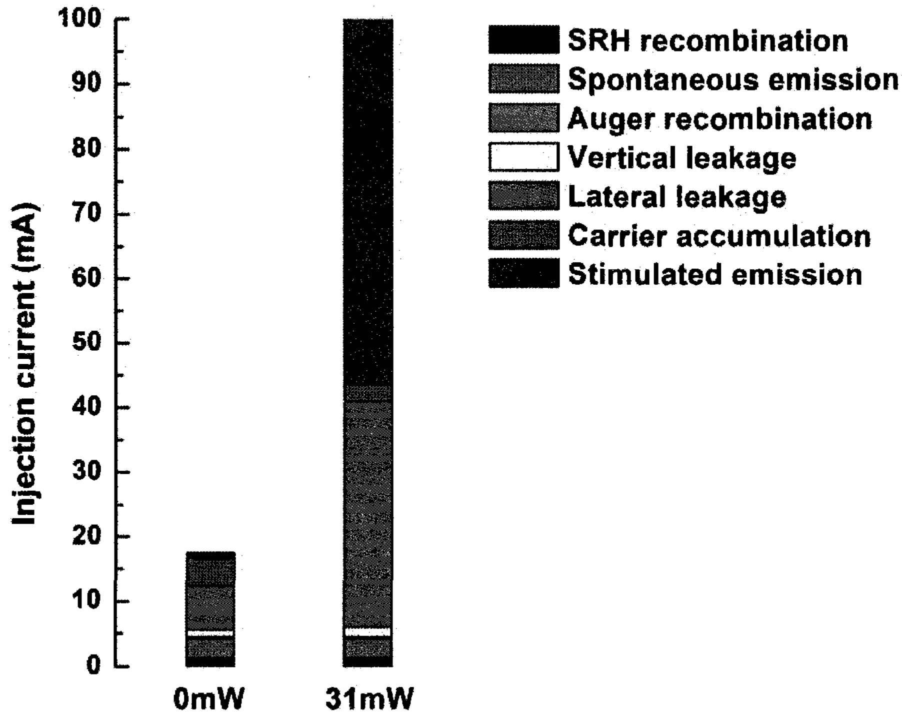

Fig. 5-17 The chart of carrier consumption below threshold and at 100 mA biasing current, which gives an output of 31 mW.

Fig. 5-17 shows the proportion of each carrier consumption mechanism by a chart. The height of each colored bar represents the equivalent amount of injection current for a particular way of carrier consumption. The height of the bars is in scale. At transparency current of 18mA, there is no optical output. Around 40% of injected carriers spread out laterally, while the Auger recombination, the SRH recombination and the vertical leakage are relatively small. At 100 mA injection current, more than half of the carriers are recombined as stimulated emission. Other recombination processes increase marginally, apart from the lateral leakage, which increases about five times. A structure that can effectively control lateral leakage is thus important in improving laser performance. The structure optimization will be discussed in Chapter 6.

5.4 Conclusions

This chapter described the two-dimensional simulation methodology used for GaInAs/GaAs single QW RWG lasers. It was found that the hole mobility of the p-AlGaAs upper cladding layer (~100 cm^2/Vs) has a predominant influence on fitting the threshold current to the experimental data. On the other hand, an appropriate setting of the spontaneous recombination coefficient (B_0 = 2x10^{-10} cm^{-3}/s) aligns the slope efficiency of laser. This alignment is improved after fine-tuning of optical absorption coefficients, in particular the coefficients for background scattering absorption (α_0 = 0 cm^{-1}) and free hole absorption (k_p=7x10^{-17} cm^2). Adjustment of intra-band relaxation time yielded perfect matching of the L-I characteristics between the simulation and experiment.

Self-consistent calculation using a calibrated Las2D simulator indicated that about 40 percent of injected carriers spread out laterally in this RWG laser. The internal loss, hence the internal quantum efficiency, varies with laser cavity length. The simulator is accurate in optical modal gain estimation. However, it needs improvement in calculating the optical scattering loss.

Chapter 6 Simulation of 1.3 μm GaInNAs/GaAs Lasers

6.1 Introduction

This chapter reports the properties and optimized structures of 1.3 μm GaInNAs/GaAs RWG lasers using the calibrated simulator Las2D.

Geometry dependent calculations of GaInNAs lasers achieve agreement with experiment, after the adjustment of a few parameters. The GaInNAs model is used to analyze nitrogen incorporation effects on bands, gain, carrier distribution and carrier consumption. The analysis demonstrates that the large threshold current of GaInNAs laser is caused for the most part by the unusually large electron mass and conduction band offset, rather than (as initially suspected) the material quality.

The second part of the chapter is dedicated to the exploration of design improvements with a focus on the reduction of threshold current and the enhancement of differential gain. These two factors play important roles in laser high-speed modulation. A careful analysis of band structure and gain reveals that GaInNAs/GaAs heterojunctions exhibit strong gain unevenness among spatially distributed QWs. A material combination of wells and barriers is proposed to overcome the effect. Finally, an optimized device structure is suggested by combining the simulation with the physical analysis.

6.2 *Simulator Calibration for GaInNAs QWs*

6.2.1 Geometry Dependent Simulation

Chapter 3 introduced the structure and process of the MBE grown, 1.3 μm GaInNAs/GaAs double QW RWG laser. L-I measurements were carried out on lasers with different cavity lengths and ridge widths. The threshold current of these lasers is about three times larger than that of InGaAs/GaAs lasers. Moreover, the laser quantum efficiency is only about 0.4, compared to 0.75 for the InGaAs/GaAs lasers. Although lateral leakage current still forms a large component of the threshold current, its ratio to the total current is reduced to around 30%. On the other hand, the low quantum efficiency indicates increasing non-radiative recombination and optical absorption. The degradation of quantum efficiency is most likely due to the nitrogen incorporation.

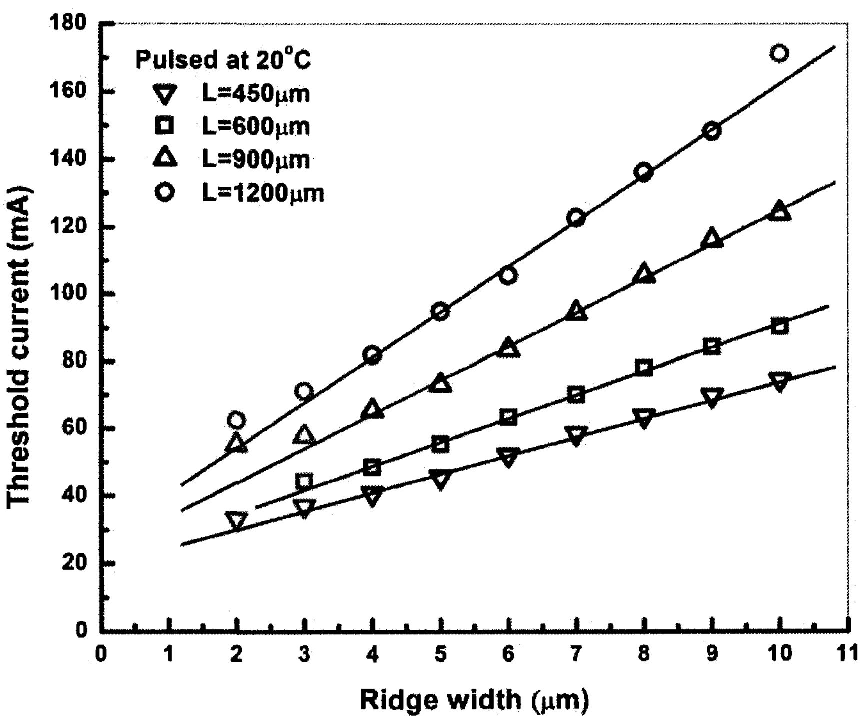

Fig. 6-1 Measured threshold current as a function of ridge width for the GaInNAs lasers in various cavity length. Data is red are excluded in linear fit.

To fit the geometry-dependent L-I measurements, the values of defect-related material parameters must be increased. Las2D provides two directly related parameters: the SRH carrier life-time of electrons and holes, and the background absorption factor. After reducing the SRH carrier life-time from $3x10^{-8}$ s to $4x10^{-9}$ s, and increasing the background absorption factor from zero to 5 cm^{-1}, the simulation gives reasonable good fit to the experimental results. As before, slightly higher slope efficiency is calculated comparing with the measurements. The results are shown in Fig. 6-2.

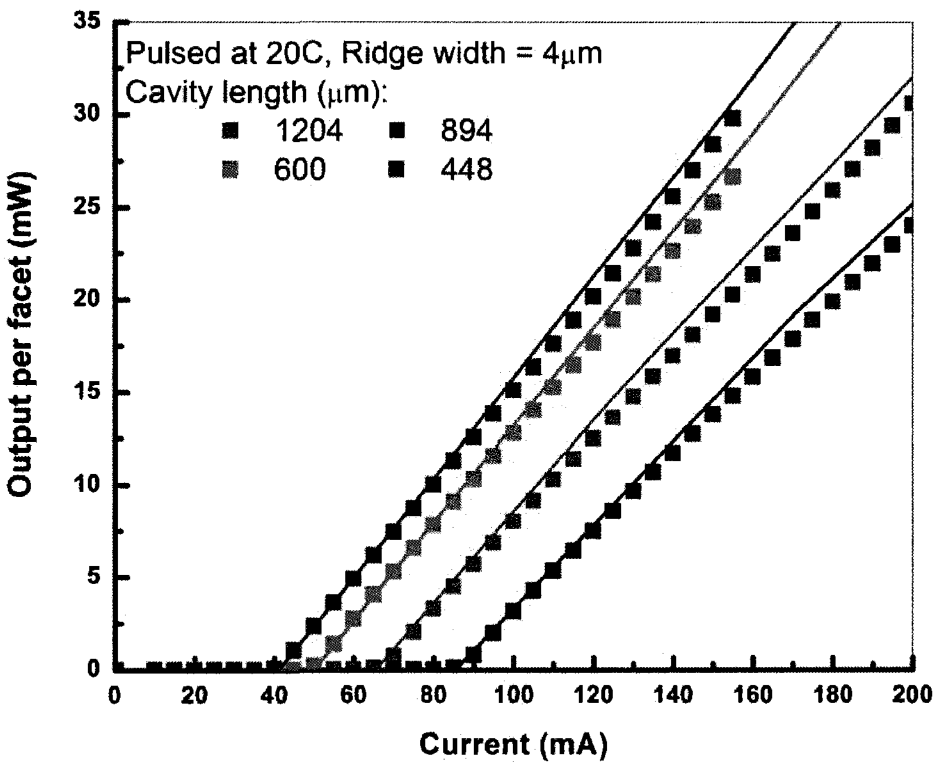

Fig. 6-2 The L-I characteristics for the 4 μm wide devices at different cavity lengths measured (dots) and simulated (line).

6.2.2 Temperature Dependent Simulation

GaInNAs lasers are less temperature sensitive than devices of other material systems due to the large conduction band offset between the GaInNAs quantum well and the GaAs barrier. The large energy discontinuity prevents the "hot" electrons from escaping the quantum wells. The 155 K characteristic temperature indicates the superior temperature stability of GaInNAs lasers.

Las2D simulation supports the temperature insensitivity of these lasers. Simulations were carried out for a 4 μm x 900 μm device from 20 to 70 °C using the default values of Las2D's temperature models. The threshold current shows a stronger increase than the measured one at high temperature. It indicates that the default temperature model over-predicts the temperature influence on laser performance.

A series of simulation were carried out using different characteristic temperatures in Las2D's temperature models. The best fit is shown in Fig. 6-3. The relaxation time turns out to be temperature independent. The exponential dependence factor of spontaneous emission is reduced from 1.5 to 0.5. The characteristic temperature of free electron absorption is reduced from 350 K to 150 K.

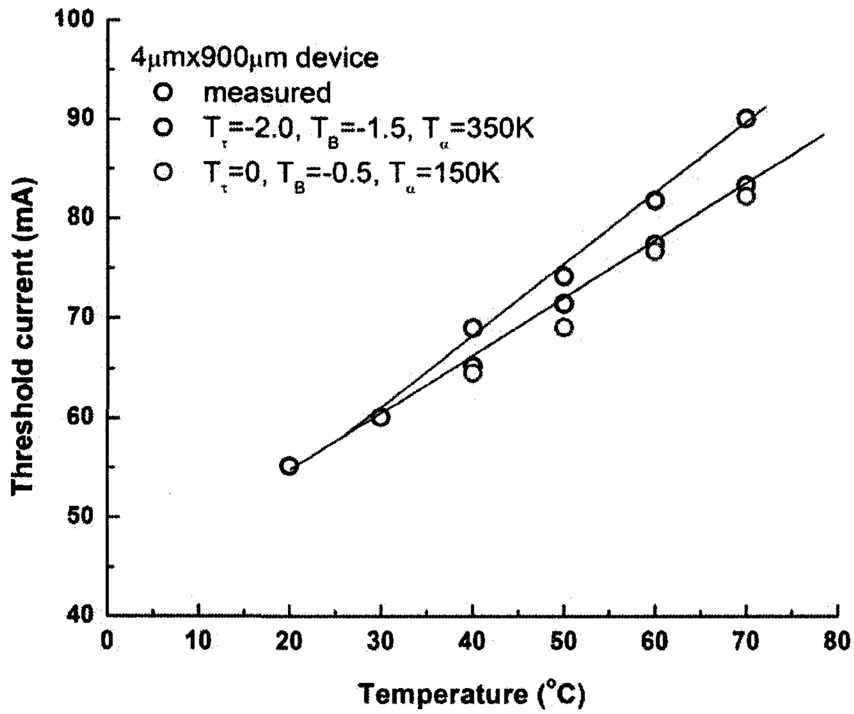

Fig. 6-3 Temperature dependent threshold current of GaInNAs laser measured and simulated for a 4 μm x 900 μm device. The weaker temperature models fit the experimental results.

6.3 *Simulation Results*

6.3.1 Carrier Consumption

Carrier consumption analysis is very useful in understanding the internal carrier dynamics in GaInNAs lasers. The same method as described in section 5.4.4 is applied to a 4 μm x 1200 μm GaInNAs laser. The distribution of carrier consumption changes dramatically in comparison to the GaInAs laser. Although lateral leakage still takes a large portion of injected carriers, the ratio is reduced. Auger recombination becomes one of the major carrier-consuming mechanisms. GaInNAs lasers emit lower-energy photons (1.3 μm in wavelength) than in InGaAs lasers (1.0 μm in wavelength). The probability of losing photon energy to the transitions between valence bands hence increases. Moreover, the highly localized hole concentration in GaInNAs QWs (3.5×10^{18} cm^{-3} vs. 2.0×10^{18} cm^{-3} in GaInNAs and GaAs QWs for the same sized devices) further increases the Auger recombination. Fig. 6-4 illustrates the carrier distribution for an injection current below laser threshold and at 100 mA, respectively. The distribution of carrier consumption is partitioned between Auger recombination, lateral leakage and spontaneous emission.

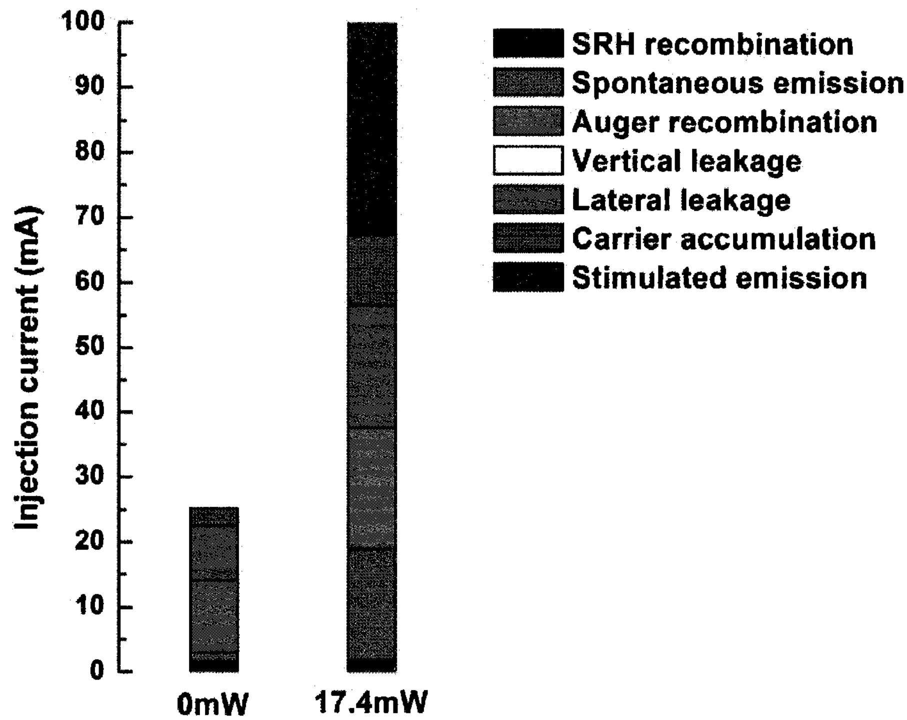

Fig. 6-4 The distribution of carrier consumption for a 4 μm x 1200 μm GaInNAs/GaAs laser at the injection current below threshold and at 100 mA (17.4mW).

6.3.2 Optical Gain and Loss

Fig. 6-5 plots the gain spectra of a GaInNAs laser at different bias currents. The gain peak is at 1250 nm. This value agrees well with the heavy hole transition wavelength of 1255 nm calculated by the $K \cdot P$ method. The emission peak was measured at 1276 nm at 20°C by a high-resolution spectrum analyzer. The ~20 nm difference between the calculated gain wavelength and the actual laser emission wavelength is due to the band filling effect. This effect is commonly observed in the two-dimensional active region of III-V semiconductor lasers [109].

The differential material gain was calculated as 1x10^{15} cm^{2} at 20°C. Compared to InGaAs/GaAs laser, where a value of 1.5x10^{15} cm^{2} was determined at the same temperature, the differential material gain of GaInNAs laser is 30% lower. This can be explained by the high non-radiative recombination rate shown in Fig. 6-4. However, the differential gain reduces more slowly with temperature in GaInNAs lasers. Fig. 6-7 plots the gain spectra evolution for various temperatures. In the same temperature range from 20 to 150 °C, the calculated differential gain reduction rates are 4.4x10^{17} cm^{2}/°C and 2.3x10^{-18} cm^{2}/°C for the InGaAs/GaAs laser and the GaInNAs/GaAs laser, respectively. The result reinforces the superior temperature stability of GaInNAs laser over those of other conventional III-V compounds.

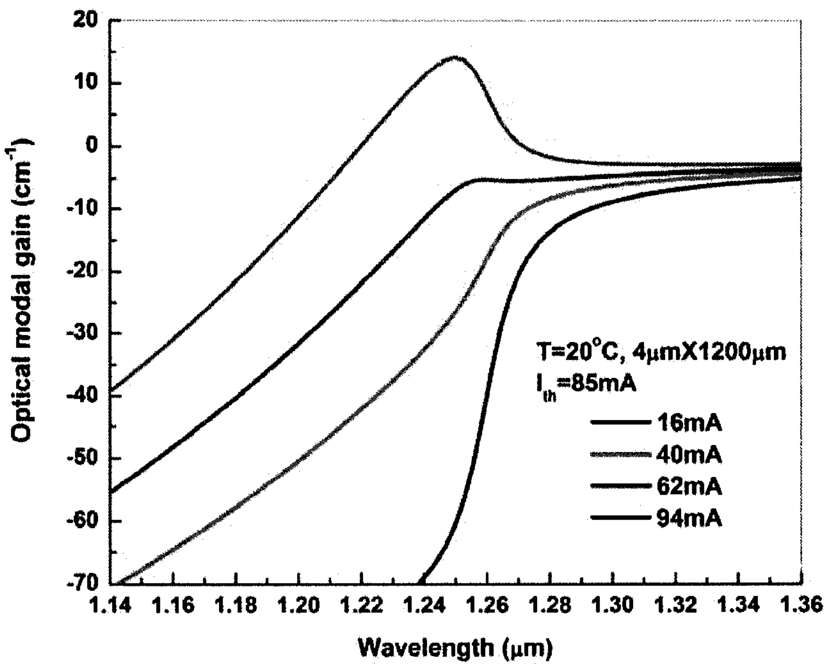

Fig. 6-5 Calculated gain spectra at a set of injection current of a 4μm x 1200 μm GaInNAs laser.

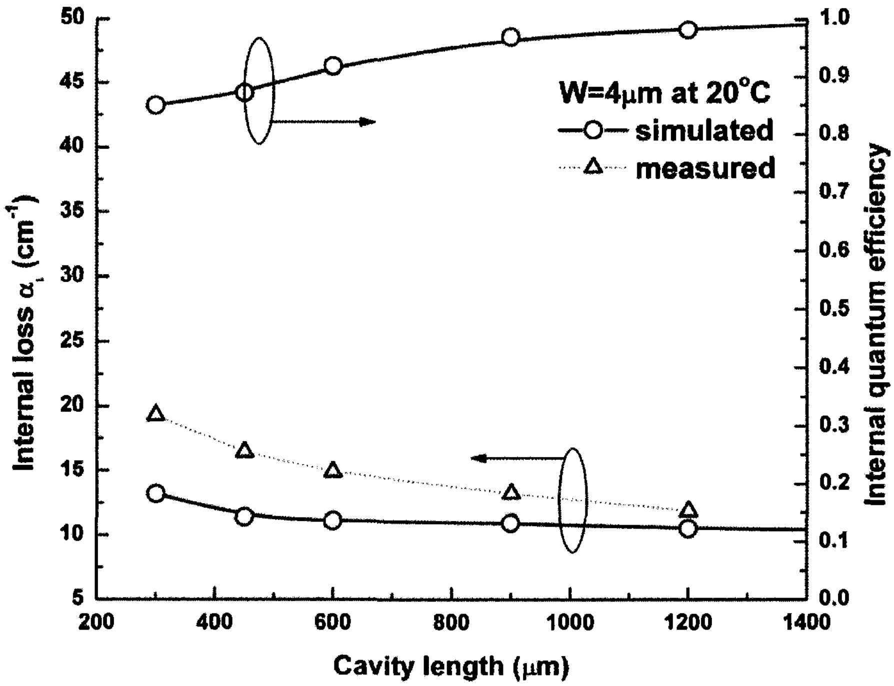

Fig. 6-6 The internal loss and internal quantum efficiency as a function of laser cavity length.

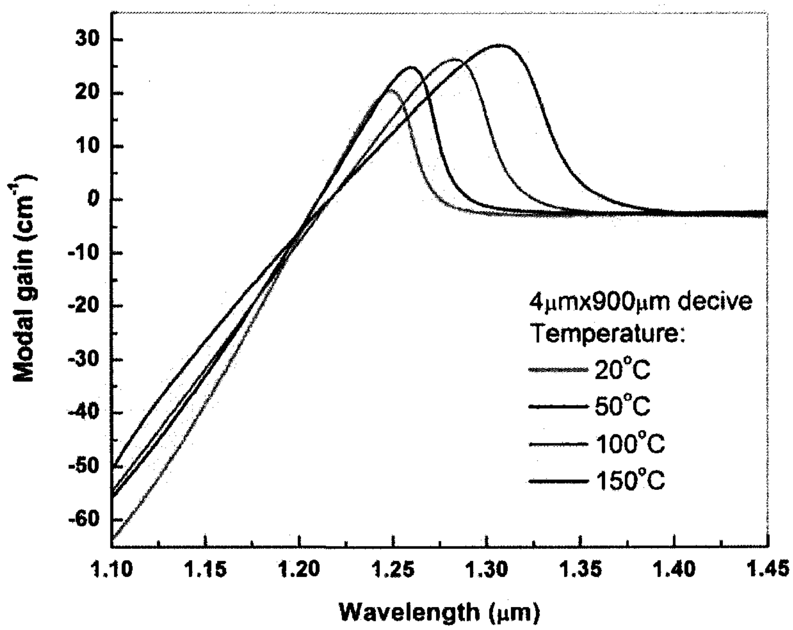

Fig. 6-7 The calculated modal gain spectra at a series of temperature. The temperature tuning efficiency is 0.48 nm/°C.

Fig. 6-6 shows the internal loss and the internal quantum efficiency, as calculated by the Las2D simulation. The internal loss as estimated from the measurements increases rapidly with decreasing of cavity length. The disagreement in internal loss values between simulation and experiment is more pronounced for the GaInNAs laser than for the GaInAs laser. This can be explained as follows. To reach the same level of mirror loss, GaInNAs QWs need more carriers. The extremely high carrier density results in strong carrier dependent optical loss. As was concluded in chapter 5, this dependence is not modeled appropriately in Las2D.

Fig. 6-7 displays calculated gain spectra at different temperatures for a 4 μm x 900 μm device. The gain peak shift rate over temperature was calculated as 0.48 nm/K. This temperature-tuning rate is slightly lower than the experimental data of 0.58 nm/K measured by gain spectra. In fact, the lower shift rate of the peak wavelength over temperature could call into question the accuracy of the thermal model of GaInNAs band structure. In gain measurements, the laser was biased at different currents. The current-induced junction heating clearly cannot be excluded experimentally, whereas in Las2D, the junction self-heating effect is not taken into account. This results a weaker gain peak shift over temperature. From other las2D users, same phenomenon has been observed in InGaAsP/InP and AlInGaAs/InP lasers. [110]

6.4 *Carrier Distribution in Multiple QWs*

6.4.1 Uneven Carrier Distribution in Multiple QWs

In seeking high performance and high-speed lasers, multiple-quantum-well (MQW) active regions have been widely employed in lasers made from various barrier/well III-V compound combinations. Although MQW features many advantages over single QW, in particular higher differential gain, it can suffer from non-uniform carrier distribution across the active region. The uneven distribution of carriers results in an uneven gain from the QWs in different spatial positions. Rather than improving gain, adding more QWs beyond a certain number can actually degrade device performance.

A great deal of work has been done to investigate this carrier nonuniformity effect. Tessler *et. al.* presented a carrier dynamic model where the electron-hole interaction was considered [111-112]. Their model yielded a non-uniform carrier distribution along the crystal growth axis. Hangleiter *et. al.* further improved the understanding of carrier dynamics in QWs [113]. They pointed out that the slow transport of holes between individual QW leads to a strong inhomogeneous carrier distribution. More importantly, they compared the carrier unevenness in InGaAsP and InGaAs QWs and suggested that the improved performance of InGaAs/InGaAlAs QWs arises from the favouriable band discontinuity that could speed up hole transport.

Experiments have demonstrated an uneven carrier distribution in GaInAsP QWs. Hamp *et. al.* designed and grew mirror-imaged asymmetric multiple quantum-well (AMQW) lasers [114]. They pointed out that the uneven carrier distribution has a substantial effect on devices with more than four QWs [115]. Since the degree of carrier unevenness varies with QW material, its impact on device performance must be analyzed independently.

In simulation of 1.3 μm GaInNAs double QW laser using Las2D, a strong uneven carrier distribution was found from self-consistent calculations. As a result, the gain was unevenly distributed between the two QWs. This unusually strong effect compared to other conventional material systems is caused by the unique band structure of GaInNAs.

6.4.2 Analysis of Uneven Gain in Multiple QWs

Fig. 6-8 to Fig. 6-10 are the band structures and carrier densities in the active region of the 1.3 μm GaInNAs/GaAs double QW laser calculated by two-dimensional simulations. At zero bias (Fig. 6-8), the GaInNAs bands agree well with our previous QW calculations [93]. When the laser is forward biased, electrons are injected from the n-cladding layer and holes from p-cladding layer. Carriers drift/diffuse across the bulk 3D separate confinement hetero-structure (SCH) region are then captured by the 2D QWs. Neglecting other second order factors, equilibrium is established among three processes: injection, drift/diffusion and capture. They determine the spatial distribution of electrons and holes. The delay times of electrons and holes quantify carrier transport processes. In SCH layers, they depend on electric field and mobility. As the SCH layers are made from GaAs, the time delays would be similar to other devices. It is of the order of a few picoseconds.

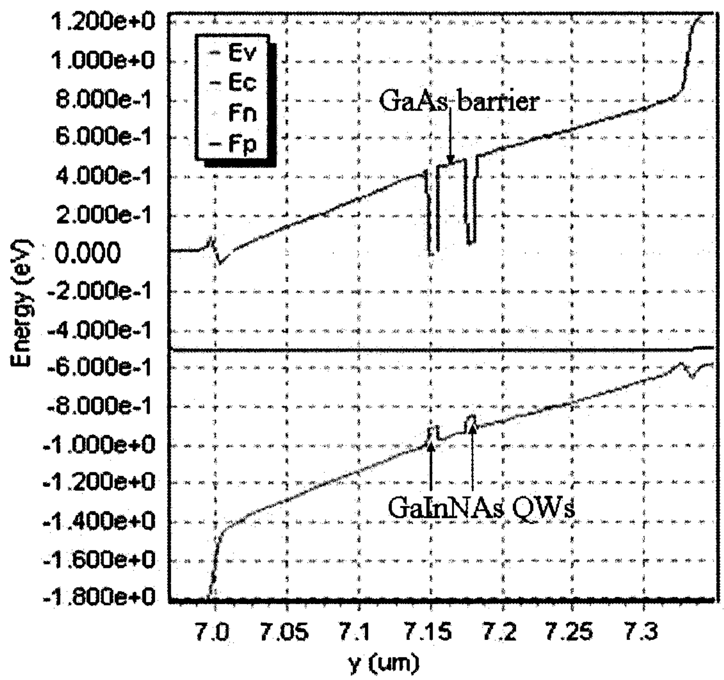

Fig. 6-8 Energy bands and Fermi levels of GaInNAs/GaAs double QWs at zero bias.

As carriers approach the QWs, quantum effects must be taken into account in describing carrier dynamics. The capture rates of electrons and holes are proportional to the densities of states in the conduction and valence bands [116]. As indicated by modal gain measurements, GaInNAs lasers show an unusually large density of states in the conduction band [45]. Hence, the electron capture rate increases substantially in GaInNAs QWs. Unlike QWs from InP-based III-V material systems where the slow transport of holes induces carrier inhomogeneity, GaInNAs QWs may feature electron-dominated carrier unevenness.

Table 6-1 The ratio of conduction band offset to the band gap difference for commonly used III-V heterojunctions.

Heterojunction	ΔEc/ΔEg
AlGaAs/GaAs	0.65
GaInAsP/InP	0.4
AlGaInAs/InP	0.7
AlGaInN/GaN	0.7
GaInNAs/GaAs	0.85
GaInAs/GaAs	0.8

The carrier escape process further enhances the electron dominated carrier unevenness. The escape rate is directly related to the band alignment between QWs and barriers. Table 6-1 Lists the ratio of conduction band discontinuity to the band gap difference, $\Delta E_c / \Delta E_g$, for commonly used QW/barrier combinations. For the combination of $Ga_{0.67}In_{0.33}N_{0.015}As_{0.985}$/GaAs, $\Delta E_c / \Delta E_g$ ~ 0.85, while $\Delta E_c / \Delta E_g$ ~ 0.4 and $\Delta E_c / \Delta E_g$ ~ 0.7 for GaInAsP/InP and GaAlInAs/InP, respectively. The strong electron confinement by the high GaAs barrier prevents electrons from reaching the second well. At the same time, a strong built-in field is created. These two effects are evidenced by the Fermi energy change across the QW region. In addition, the unchanged valence band of GaInNAs (comparing to GaInAs) results in shallow wells for holes. Eventually, the well that is closest to the p-cladding layer cannot reach the threshold for population reversion. That QW shows a negative gain.

Fig. 6-9 visualizes the uneven band and carrier density under forward bias.

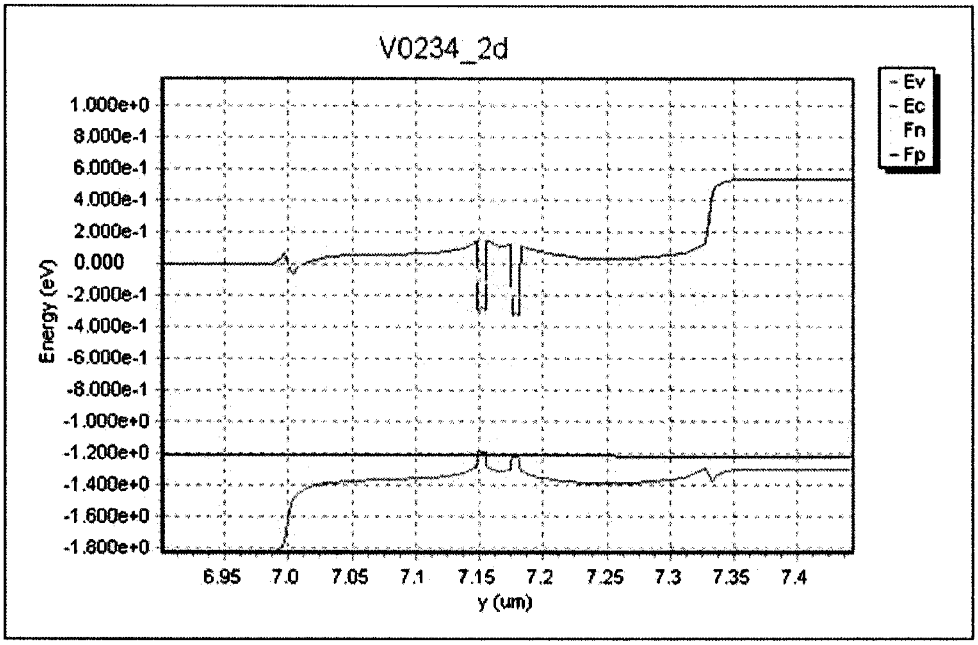

(a)

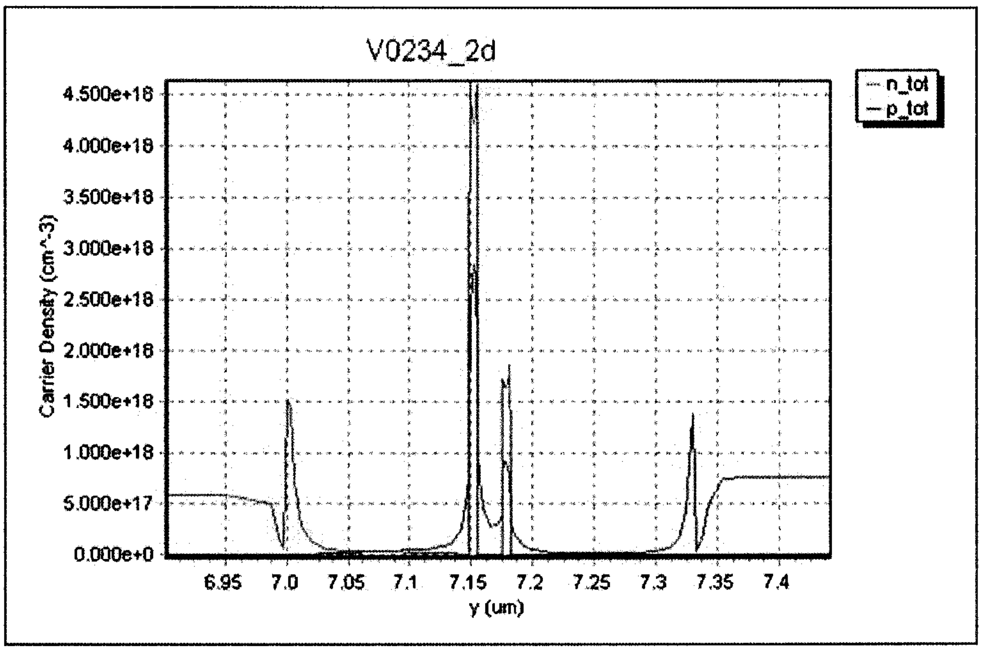

(b)

Fig. 6-9 Forward biased energy bands, Fermi levels and carrier densities of the naturally aligned GaInNAs/GaAs heterojunctions. (a) The energy bands of the GaInNAs/GaAs double QWs at a current of 23 mA. (b) The carrier density in the QW at current of 23 mA. The carrier density in the right QW is lower by half than that in the left QW for $\Delta E_c / \Delta E_g = 0.85$.

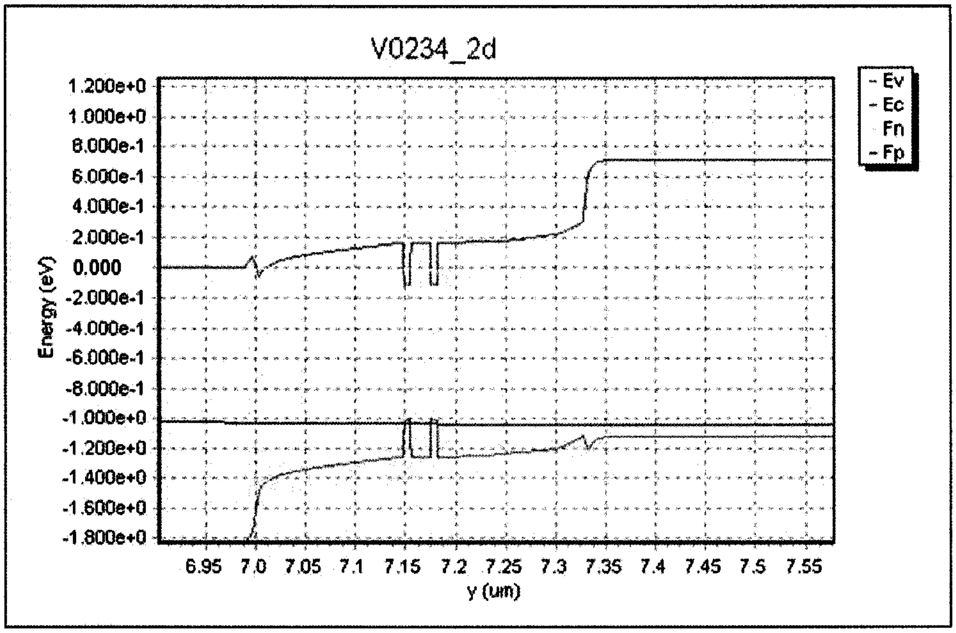

(a)

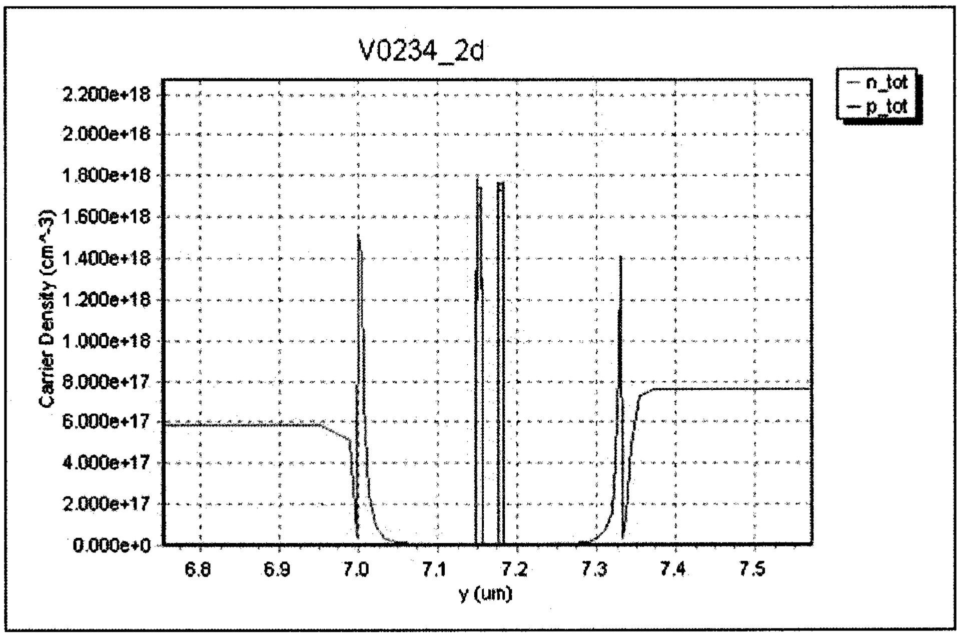

(b)

Fig. 6-10 Forward biased energy bands, Fermi levels and carrier densities at the affinity of GaInNAs was decreased by 100 meV. (a) The energy bands of the GaInNAs/GaAs double QWs at a current of 23 mA. (b) The carrier density in the QWs at a current of 23 mA. The carriers are evenly distributed between the two QWs for $\Delta E_c / \Delta E_g = 0.61$.

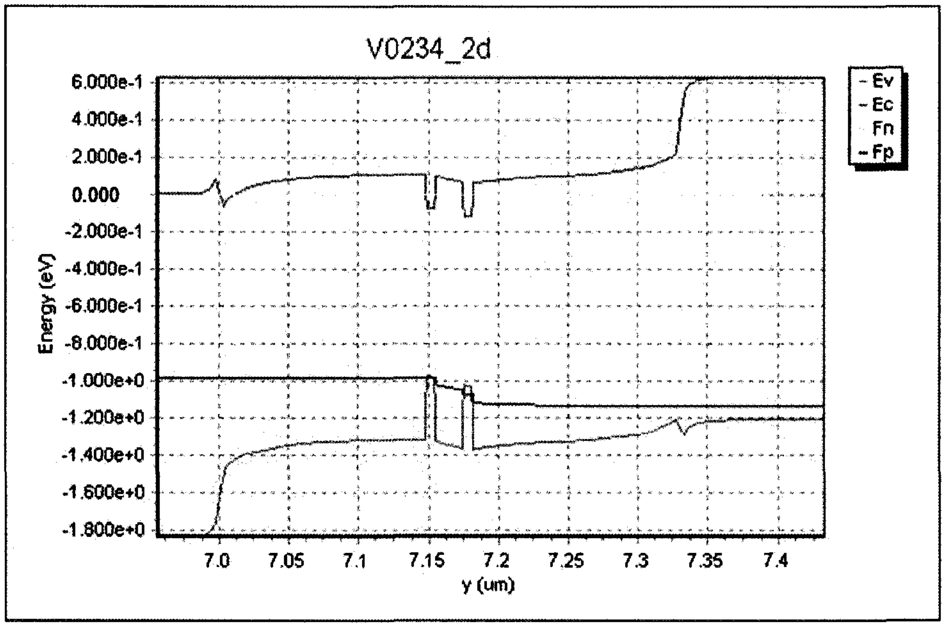

(a)

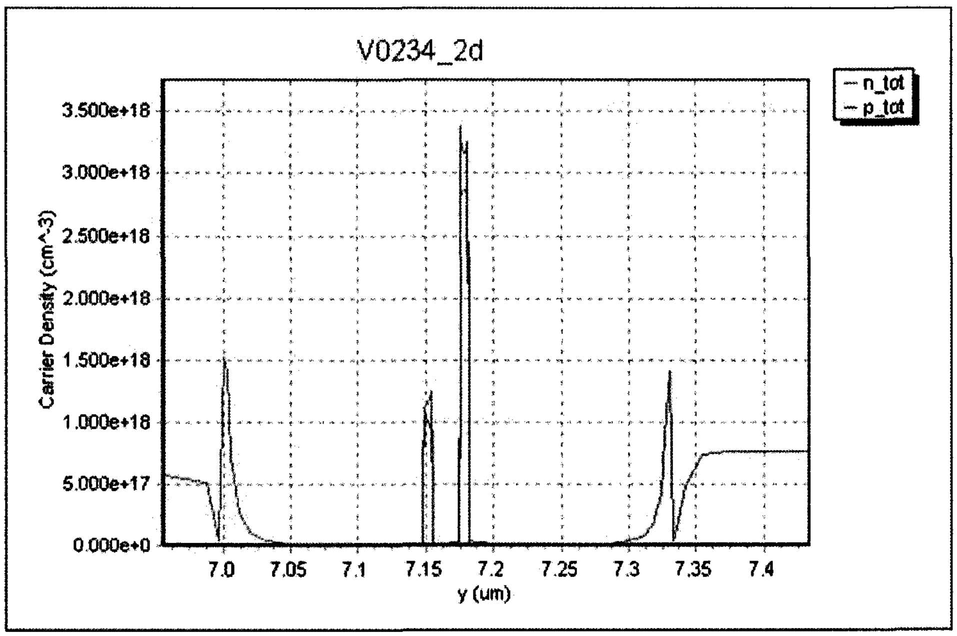

(b)

Fig. 6-11 Forward biased energy bands, Fermi levels and carrier densities at the affinity of GaInNAs was decreased by 200 meV. (a) The energy bands of GaInNAs/GaAs double QWs at a current of 23 mA. (b) The carrier density in QW at a current of 23 mA. The carrier density in the right QW is higher by half than that in the left QW at $\Delta E_c / \Delta E_g = 0.43$.

6.4.3 Simulation and Experimental Observations

To firm up the above hypothesis that the large conduction band discontinuity causes uneven gain, two additional simulations were performed. The GaInNAs affinity is reduced artificially. The band gap of GaInNAs with respect to that of GaAs was shifted downward by 100 and 200 meV. The forward biased band alignment and carrier densities are shown in Fig. 6-10 and Fig. 6-11, respectively. The carriers are evenly distributed between two QWs in the case of 100 meV down shift. However, the uneven distribution of holes is demonstrated by Fig. 6-11, which is the result for 200 meV down shift. The models used in the simulator may not exactly represent the complicated carrier dynamics in the active region. However, simulation results agree with reference [113] in that there is a prefered band discontinuity between conduction band and valence band for high performance MQW lasers. In other words, unevenness in carrier distribution must be taken into account when designing MQW structures. This is particularly important for MQWs with large uneven band offsets such as demonstrated by GaInNAs/GaAs (electron transport limited) and InGaAsP/InP (hole transport limited).

The gain unevenness was noticed experimentally in the early 1990's during the development of MQW GaInAsP/InP lasers. Two experimental methods are quoted here. Hamp *et. al.* designed the mirror image AMQW technique to provide quantitative information regarding the degree to which the carrier distribution affects the gain of QWs in the active region [114]. Smowton *et. al.* deployed a segmented contact method to measure the gain unevenness using the normal laser samples [117]. These two methods can be extended to study the gain unevenness in GaInNAs lasers. Considering current stage of material quality, Hamp's method will give more reliable results.

Gollub *et. al.* observed the gain unevenness in their study of GaInNAs/GaNAs/GaAs MQW lasers [118]. The results provided the evidence of the strong gain unevenness in GaInNA material system. They estimated the average gain per QW using a linear fit of cavity dependent L-I measurements for lasers with two, three and five QWs. They have found that the average modal gain per

QW in the five QW structure is only about one third of that in the two QW structure. Furthermore, they concluded that the difference in average gain per QW is the result of the high conduction-band offset and the increased electron effective mass in GaInNAs QWs. Their experimental observations support the simulation results of this work.

6.5 GaInNAs/GaAs Laser Design Improvement

6.5.1 Lateral Leakage Control Structure

The analysis of carrier consumption indicates that the lateral leakage takes about one third of threshold current in GaInNA/GaAs lasers. Electrons and holes can both diffuse/drift laterally away from the active region. However, since the current confinement provided by the ridge is on the p-side of the junction, hole diffusion is the major cause of the lateral leakage current.

To reduce the lateral leakage current, the one option is to increase the series resistance of the hole diffusion path. There are two ways to do this. First, the thickness of the p-cladding layer under the ridge can be reduced by a deeper etch during ridge formation. However, the corner of the air/semiconductor interface will be close to the active region. The optical field may be disturbed. Calculation shows that the p-cladding layer underneath the ridge must be thicker than 150 nm to maintain single transverse mode operation.

The other method is to reduce the p-doping just for the cladding layer underneath the ridge while leaving the p-cladding of the ridge heavily doped. Since the layer is around 150 nm thick, carriers are able to inject into the active region effectively. At same time, the lateral series resistance can be reduced.

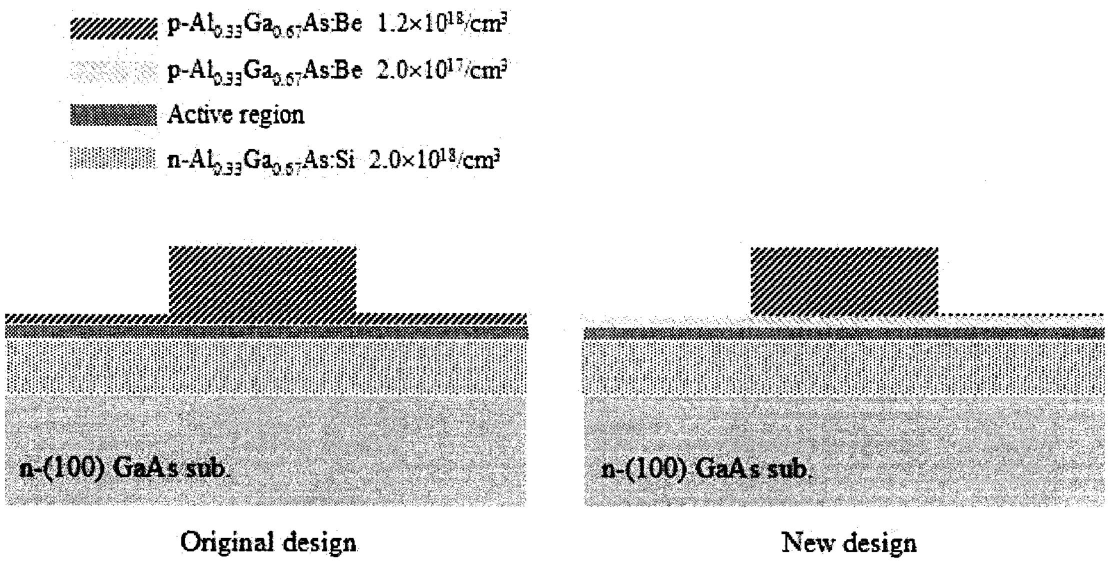

Fig. 6-12 The suggested RWG laser structure for lateral leakage control. Modelling shows that this structure would reduce the threshold current from 65 mA to 42 mA without reduction on slope efficiency.

Fig. 6-12 shows the suggested RWG structure for lateral leakage control. During epitaxy, a low p-cladding layer will be grown prior to the AlAs etch stop layer. Simulations are carried out with the layer thickness of 150 nm at doping levels from 2.0×10^{17} - 1.0×10^{18} cm^{-3} to optimize the p-type doping level. Fig. 6-13 is the calculated lateral current density along the growth direction at the side of the ridge. The calculation shows a reduced lateral leakage current, with respect to the original, of 17.1 mA versus 9.7 mA. Fig. 6-14 plots the threshold current and slope efficiency as a function of doping concentration for 4 μm x 900 μm lasers. As Fig. 6-14 indicates, there is a trade-off between threshold current and slope efficiency in chosing of the doping level. The optimized value is 2.0×10^{17} cm^{-3}.

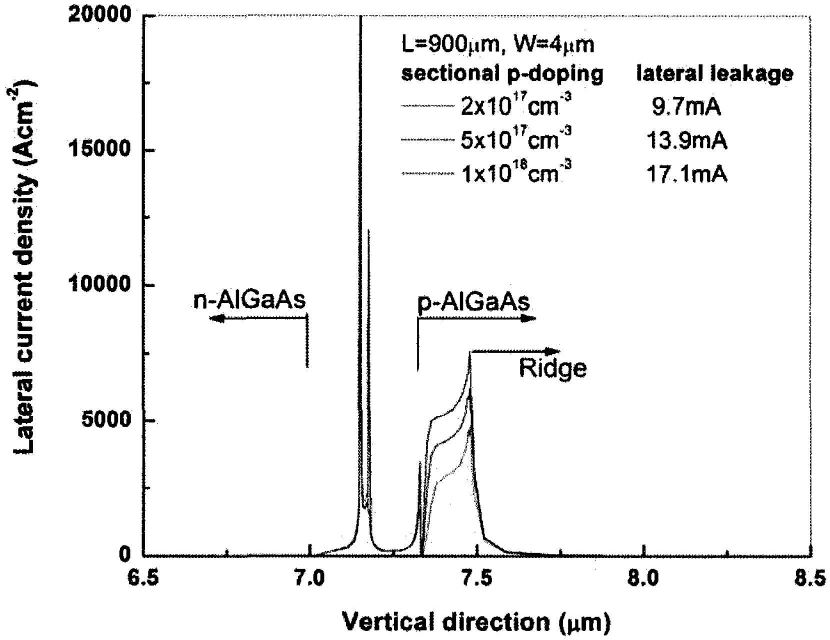

Fig. 6-13 Lateral current density long growth direction. Lateral leakage current is calculated at varies doping levels in the p-cladding layer underneath the ridge.

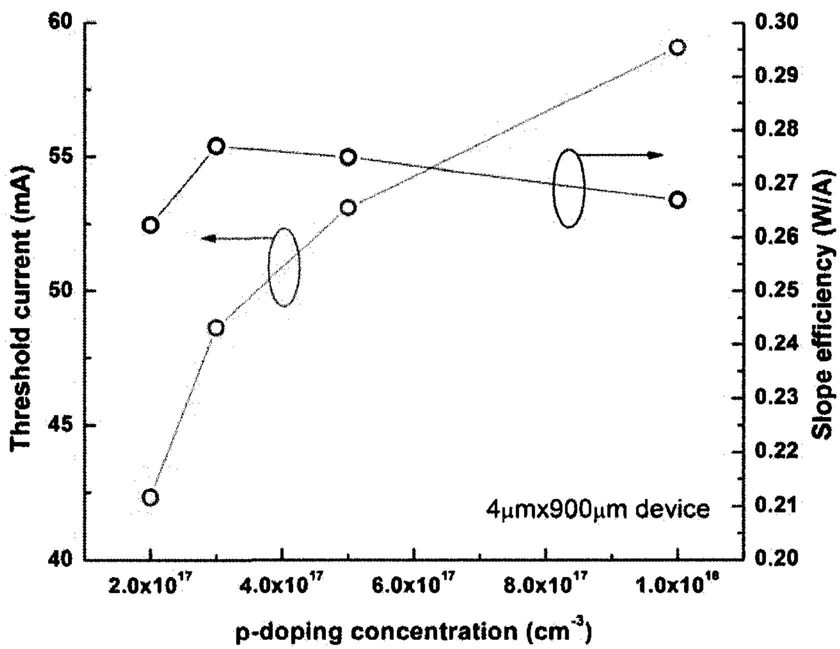

Fig. 6-14 Threshold current and slope efficiency as a function of the doping levels in the p-cladding layer underneath the ridge.

6.5.2 GaInNAs 1.3μm Single QW Laser

As described in previous sections, gain unevenness limits GaInNAs/GaAs QWs to three for GaInNAs/GaAs well/barrier combinations. This small number of QWs confines the use of GaInNAs/GaAs lasers to high power applications. However, this material system features superior temperature stability, making it useful for applications requiring low threshold, low power dissipation, uncooled applications. This makes the design of single QW structure of critical importance because the single QW laser normally exhibits the lowest threshold current and a small temperature-induced carrier leakage. For appropriate cavity lengths, a single QW laser is more immune to temperature variations than are a MQW lasers in the same material system.

The other important consideration in pursuing single QW design is to improve laser performance by increasing the hole barrier in the GaInNAs/GaAs hetero-junction. The simulation on double QWs reveals that a deeper hole barrier in the GaInNAs/GaAs hetero-junction will favour laser operation. However, to increase valence band discontinuity of GaInNAs/GaAs, one needs to incorporate more indium in the QW. This will increase the lattice mismatch of GaInNAs to GaAs. As a single QW has one thin layer, the increased strain will not exceed the strain relaxation limit for the crystal, and high indium content QW is therefore feasible.

Table 6-2 GaInNAs composition for single QW SCH structure with the QW thickness of 7.5 nm. The strain is limited to –2.6% to avoid difficulties in crystal growth and device reliability. The predicted operation performance is evaluated by the threshold current (Ith), slope efficiency (η_s), emission wavelength (λ), and internal loss (α_i).

	Gallium	Nitrogen	VBO	strain	Ith	η_s	λ	α_i
	(%)	(%)	(meV)	(%)	(mA)	(%)	(nm)	cm^{-1}
A	67	1.5	75	-2.0	34.54	25.5	1264	8.96
B	60	1	96	-2.6	24.72	26.2	1282	8.56
C	60	1.2	96	-2.5	23.80	25.7	1305	8.60
D	62	1.2	90	-2.4	26.78	25.8	1283	8.63

Table 6-2 lists the possible GaInNAs QW compositions, including the valence band offset (VBO) and the strain relative to GaAs. Composition A is from the original design. To keep strain within –2.6% of the relaxation limit, the maximum indium composition is limited to 40%. Nitrogen composition is varied accordingly to keep the desired bandgap energy (emission wavelength of 1.3 μm). Simulations for lateral leakage control are carried out using the improved structure. The calculated threshold current, slope efficiency, emission wavelength and internal loss are listed in Table 6-2. Fig. 6-15 shows the results of threshold current and slope efficiency together. Composition C leads to the best lasing performance at its longest emission wavelength and for the lowest threshold current.

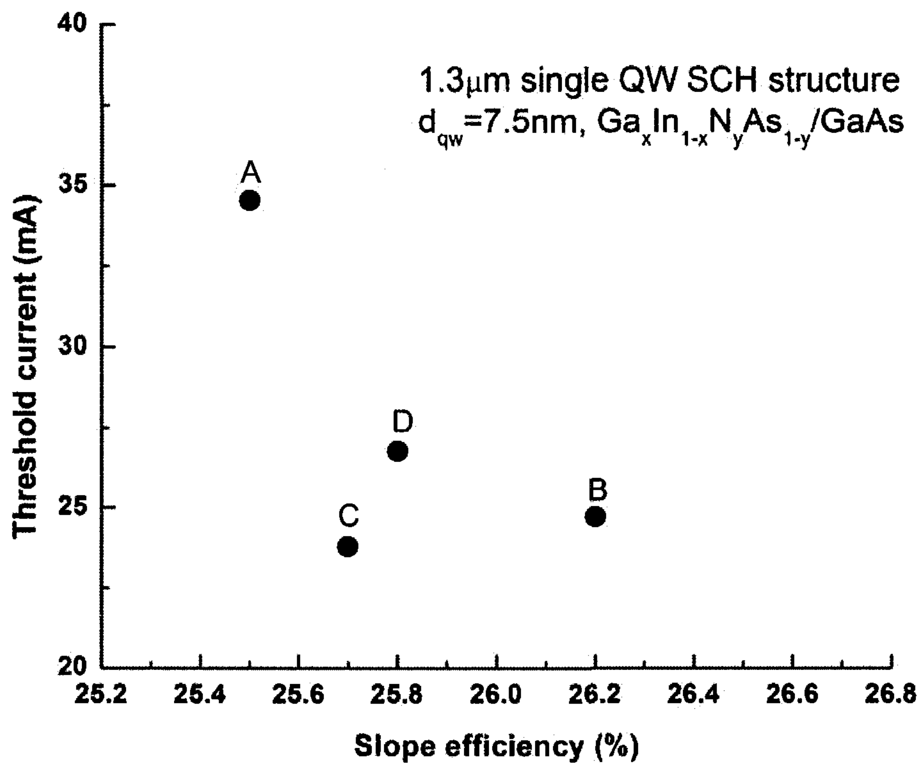

Fig. 6-15 Threshold current and slope efficiency calculated for single QW laser with composition displayed in Table 5.2. The device dimension is 4 μm x 900 μm.

The feasibility of growing highly-strained GaInNAs layers is beyond the scope of this work. However, there is evidence that GaInNAs thin layers with –2.5% strains can be grown by MBE. Wei *et al.* report a 7 nm double QW structure with compressive strain as high as –2.5% ($Ga_{0.613}In_{0.387}N_{0.012}As_{0.988}$) using GaAs barriers [119]. They have achieved a record low laser threshold density of 150 A/cm^2 per QW for a broad area laser. The threshold current density of the RWG laser that is made of composition C is calculated as 660 A/cm^2 for the 4 μm x 900 μm device. The threshold current density agrees with Wei's experimental value, assuming the application of a scaling factor of about 5 when comparing a broad area laser to a 4 μm wide RWG laser, as justified by the weak current confinement of a RWG lasers for ridge widths larger than 20 μm.

6.5.3 GaInNAs Multiple QWs with GaAs Barriers

High power and high-speed lasers depend on the realization of multiple QWs, because MQWs provides large differential gain, which means fewer carriers are modulated to generate the same amount of variation in light. This property is highly desired for high speed (>2.5 Gb/s) modulated lasers.

However, the strong gain unevenness in the GaInNAs/GaAs QW/barrier combination prevents each QW giving similar amounts of gain. Nevertheless, since much of effort has been made in material grown and fabrication for this QW/barrier combination, it is worthwhile to study the device performance using simulation and find the optimized solution for this design.

Table 6-3 lists seven double QW structures for which device performance was simulated using Las2D. The difference is in device size and optical confinement. In addition to threshold current and slope efficiency, lasing properties are evaluated using an additional parameter, the gain inhomogeneity factor.

The gain inhomogeneity factor is defined as the ratio of gain in the QW close to the p-cladding layer (QW1) to that of the QW close to the n-cladding layer (QW2). The value is between –1 and +1 with +1 indicating an equal gain in each

QW. Fig. 6-16 shows the threshold current and gain inhomogeneity factor for the structures. Two conclusions may be drawn from the calculations. First, reduced size devices decrease gain unevenness. Larger transparency carrier densities increase the likehood of carriers to populate the second QW. Second, the graded index (GRIN) structure has a more even gain from the QWs comparing with SCH structures due to the tighter carrier confinement, although the improvement is marginal. As the result, the calculation for a 2 μm x 200 μm device with high indium content in the QWs gives the largest gain inhomogeneity factor of 0.46. Since devices shorter than 200 μm do not reach stimulated emission, further decreasing cavity length for a more even gain is not possible. Thus the maximum number of QWs for this QW/barrier combination is limited to two.

Table 6-3 Simulation structures for obtaining the most even gain between two QWs in the GaInNAs/GaAs double QWs structure.

	Structure			Quantum well			Properties		
		L (μm)	W (μm)	Ga	N	Strain	Ith (mA)	η_s	g_2/g_1
A	SCH	900	4	0.67	0.015	-0.02	42.3	0.262	-0.57
B	GRIN	900	4	0.67	0.015	-0.02	63.3	0.263	-0.23
C	SCH	300	2	0.67	0.015	-0.02	37.9	0.35	0.17
D	GRIN	300	2	0.67	0.015	-0.02	42.1	0.287	0.31
E	GRIN	300	2	0.6	0.01	-0.026	35.6	0.325	0.33
F	SCH	300	2	0.6	0.01	-0.026	30.28	0.357	0.17
G	SCH	200	2	0.6	0.01	-0.026	28.82	0.343	0.46

The inhomogeneity carrier distribution is also evidenced by the refractive index profile at bias above laser threshold. Fig. 6-17 plots the "hot" refractive index in the laser active region for the GRIN-SCH and the SCH structures, respectively. The refractive index difference indicates up to a 1/3 difference in carrier density between the two QWs.

Fig. 6-18 plots material gain as injection current for the short cavity lasers described in Table 6-3. The maximum differential material gain is achieved by the GRIN-SCH structure for the well composition of $Ga_{0.6}In_{0.4}N_{0.01}As_{0.99}$. This result supports the conclusion of the single QW calculations that QWs with more indium content give better lasing performance.

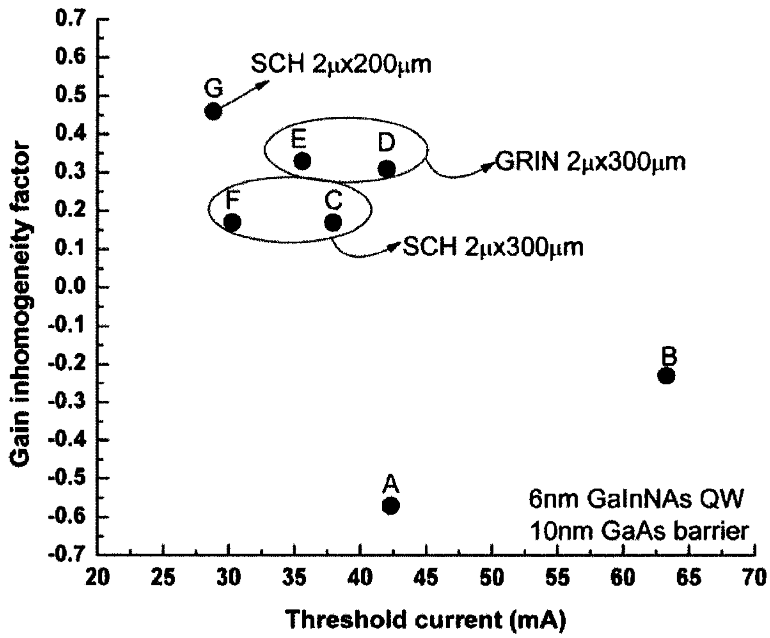

Fig. 6-16 The gain inhomogeneity as a function of threshold current for the structures described in Table 6-3. It is much influenced by the carrier density in QWs such as the cavity size and the confinement structure.

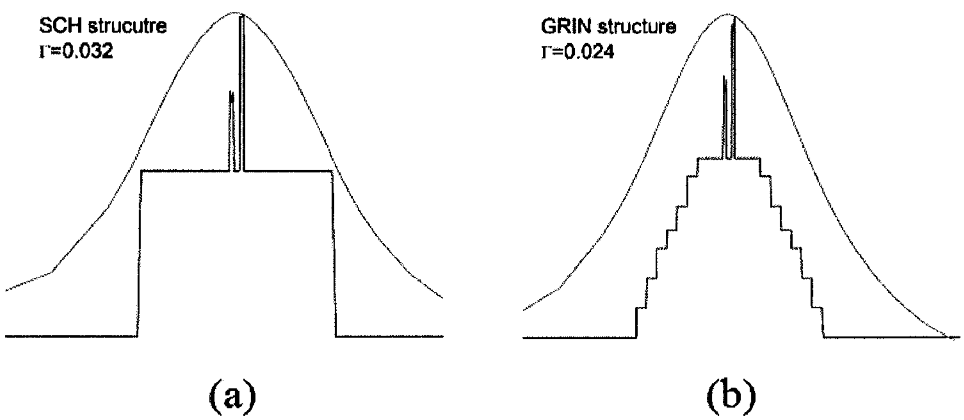

Fig. 6-17 The "hot" refractive index and optical intensity of the SCH (a) and GRIN (b) structures. The uneven refractive index between the two QWs originates from the uneven carrier population.

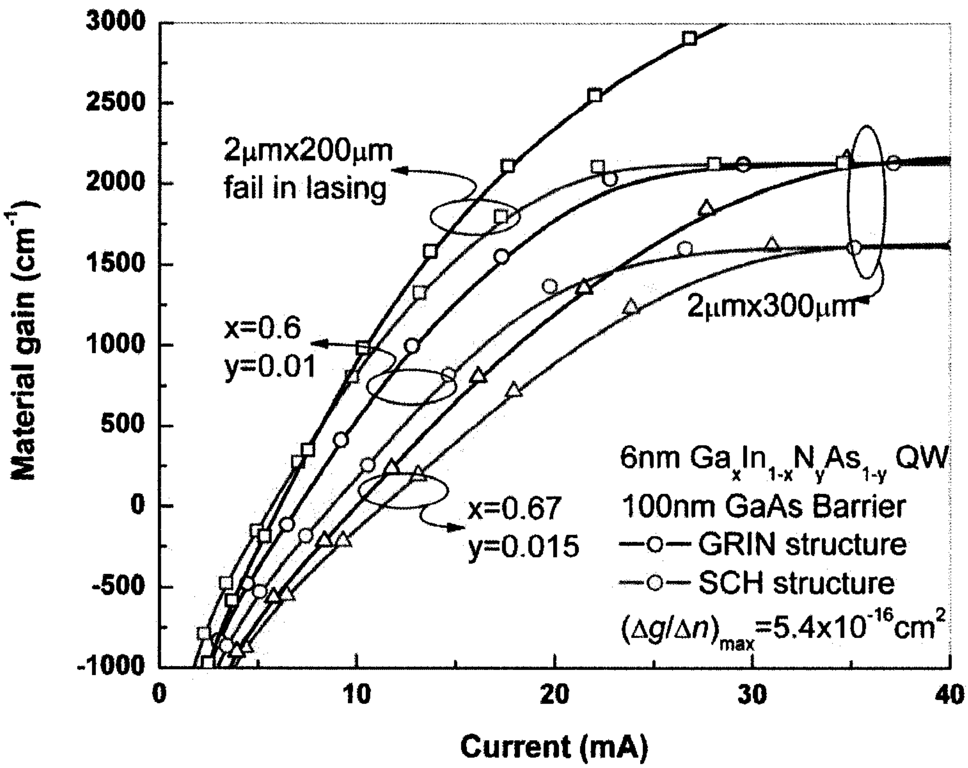

Fig. 6-18 The material gain as a function of injected current for short cavity devices in Table 6-3. The low differential gain limits the cavity length to the 300 μm range. The GRIN structure has a higher differential material gain than the SCH strucutre. And more nitrogen in the QW results in a lower differential gain.

In the above calculation, QW and barrier thicknesses are reduced from the original design, of 6.7 nm and 200 nm, to 6 nm and 10 nm. The thinner barrier helps to decrease carrier transport time without sacrificing device performance. It is necessary to further optimize the GRIN layer thickness with the help of a new version of Las2D that is equipped with small signal carrier dynamics, because the thickness of the layer has a strong influence on the optical confinement factor and the carrier transport delay. A good compromise between them can increase laser modulation band width.

6.5.4 GaInNAs Multiple QWs with GaNAs barrier.

In the development of dilute nitride lasers, either GaAs or GaNAs barriers have been used in the MQW structure. The advantages of using GaNAs barrier are as follows:

1. The small residual strain improves the crystal quality. A low threshold-current-density laser with five QWs has been demonstrated to compensate the accumulated strain of the high indium contained in the QWs [120].
2. Introducing nitrogen in the barriers effectively increases the emission wavelength of QWs due to the weaker quantum confinement. This allows QWs to emit at the required wavelength with less nitrogen in the QWs. Better crystal quality and higher differential gain is therefore easier to achieve in these QWs.
3. Incorporating nitrogen in the barrier reduces the electron barrier height. As a consequence, the laser's temperature stability and differential gain will be reduced. However, it is technically challenging to stack multi-layers with different nitrogen compositions together while still maintaining planar growth, as the overall crystal quality becomes hard to maintain. Li *et al.* made a comparison between GaAs and GaNAs barriers using single QW lasers [121]. They concluded that the GaNAs barrier does not help to improve the quality of the epitaxial material. The photoluminescence characteristics of both types of structures are similar. As a result, GaInNAs devices with GaAs barriers have dominated research activities.
4. There is no need to pursue GaNAs barriers except in the following situations:
    - The high-speed laser requires a large number of QWs for high differential gain. In this case, GaInNAs MQWs with a GaNAs barrier are essential. This is because the gain inhomogeneity prevents MQW operation in GaInNAs/GaAs well/barrier combinations. Adding a small amount of nitrogen in the barriers

largely decreases the conduction band discontinuity, and balances the gain among the QWs. The success of this type of structure depends on the maturity of the crystal growth techniques. Structures with as many as five QWs with GaNAs barriers have been reported [118].

- Long wavelength lasers with emission wavelengths longer than 1350nm: In this case, high-nitrogen-content QWs are needed to decrease the band gap. The GaNAs barrier provides the possibility of changing the barrier band gap energy in order to match the desired band gap of QWs.

Table 6-4 lists three well/barrier compositions for GaInNAs MQWs emitting in the 1.3 μm wavelength range. The N/As ratio in the barriers is chosen to be the same as it is in the QWs. Compared to the GaAs barrier devices, QWs with GaNAs barriers have a smaller net strain. The band discontinuity is well balanced at $\Delta E_c / \Delta E_g \sim 0.75$. Simulations are carried out for the well/barrier combinations in Table 6-4 with the SCH and the GRIN-SCH structures, respectively. The number of QWs is two. The thickness of QW and barrier are 6 and 10 nm, respectively. The cavity length is 300 μm and the ridge width is 2 μm.

Table 6-4 Physical properties of GaInNAs QW with GaNAs as barriers for three QW/barrier compositions using $K \cdot P$ calculation [93]. The same QW compositions with GaAs barriers are listed for comparison.

	Quantum well			Barrier		Properties					
	Ga	N	strain	N	strain	λ (e1-hh) (nm)	ΔEg_c (meV)	ΔEg_v (meV)	Net strain	$\Delta Eg_c/\Delta Eg$	m_c (m_e)
	0.6	0.12	-0.026	0	0	1281	460.3	95.5	-0.0256	0.828176	0.062
	0.67	0.015	-0.02	0	0	1238	441.2	75.2	-0.02	0.854376	0.070
	0.7	0.02	-0.017	0	0	1252	457.8	66.9	-0.0172	0.872499	0.075
A	0.6	0.012	-0.026	0.012	0.0025	1303	270	95.5	-0.000182	0.738714	0.062
B	0.67	0.015	-0.02	0.015	0.0031	1263	222.2	75.2	-0.000085	0.747142	0.070
C	0.7	0.02	-0.017	0.02	0.0041	1280	197.8	66.9	-1.4E-06	0.747261	0.075

Fig. 6-19 shows the energy band gaps of the active region for lasers with GaNAs barrier and GaAs barriers. The figure indicates the difference in conduction bands. The step-like conduction band of the GaNAs barrier laser provides a gradual energy potential for electrons. It increases the electron capture rate hence the internal quantum efficiency of the laser.

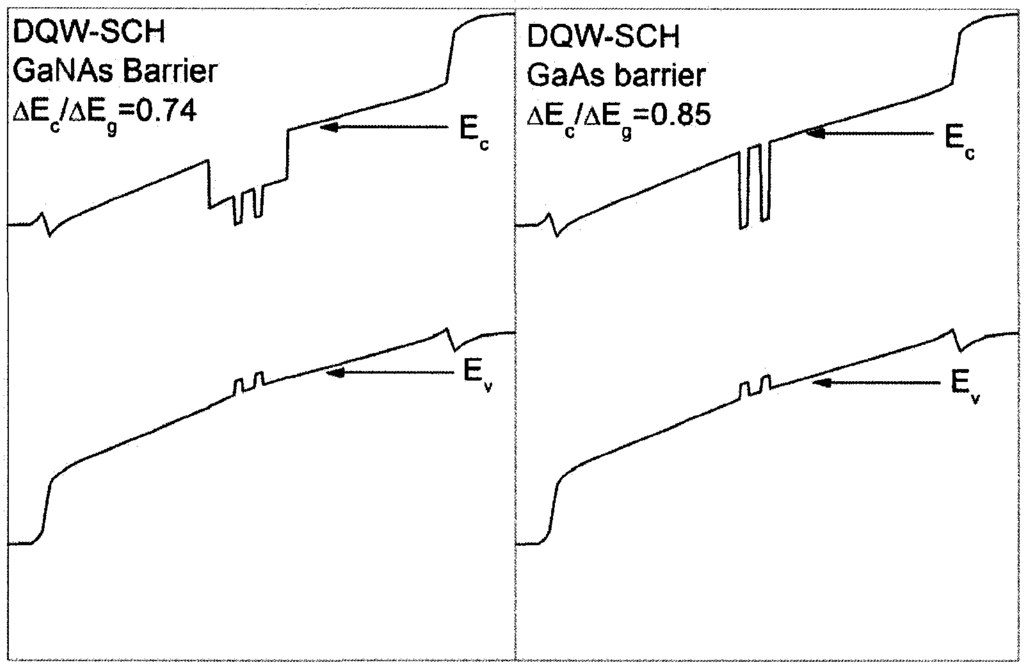

Fig. 6-19 The conduction and valence bands of GaInNAs/GaNAs and GaInNAs/GaAs DQWs at zero bias. The figure shows that the QWs in GaInNAs/GaAs heterostructure is over 2 times deeper than that in GaInNAs/GaNAs heterostructure. This makes the difference in electron confinement and electron capture. The holes are confined similarly in both structures.

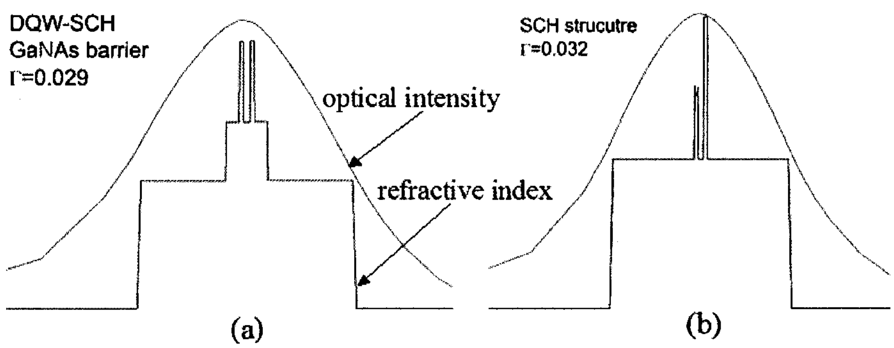

Fig. 6-20 The refractive index and optical intensity of the GaInNAs/GaNAs and GaInNAs/GaAs DQWs biased at threshold level. The QWs with GaNAs barrier shows the same refractive index in the two QWs. This indicates a uniform carrier injection.

Fig. 6-20 is the refractive index and optical intensity of the laser active region for the structures with the GaNAs barrier (a) and with the GaAs barrier (b). The GaNAs barrier laser shows a similar value for the refractive index of the two QWs. The carrier density is uniformly distributed between them. This indicates an even optical gain in each QW using GaNAs as a barrier.

Table 6-5 lists the simulation results for DQW, GaInNAs/GaNAs lasers with different well compositions. The calculations are carried out using a 2 μm x 300 μm device. Again, higher indium-content QWs have larger differential gains and smaller threshold currents. The threshold current of GaInNAs/GaNAs lasers is reduced to half of that of the threshold current of GaInNAs/GaAs lasers of the same composition and geometry. The slope efficient also increases slightly.

Table 6-5 Calculation results for GaInNAs/GaNAs DQWs listed in Table 6-4. The optimized QW composition is with 40% of indium.

	Quantum well				Properties			
	Ga	In	N	Net strain	Ith (mA)	η_s	*dg/dn (cm^2)*	λ (nm)
A	0.60	0.40	0.012	-1.80E-04	15.82	0.373	9.2×10^{-16}	1307
B	0.67	0.33	0.015	-8.50E-05	19.18	0.376	8.2×10^{-16}	1272
C	0.70	0.30	0.02	-1.40E-06	22.24	0.359	7.4×10^{-16}	1298

As gain unevenness is not a concern in GaInNAs/GaNAs QWs, multiple QWs are preferred in a high-speed laser. Beside high differential gain, a high-speed laser needs high photon density and low device parasitics. These properties can be achieved by using short cavity lasers. However, mirror losses at laser facets increase exponentially with decreasing cavity length. Once the optical gain is insufficient to overcome the total loss, the laser will fail to attain stimulated emission. For that reason, there is a low limit in laser cavity length with respect to the optical gain that the laser cavity can provide.

Fig. 6-21 is the calculated optical gain as a function of carrier density for the GaInNAs/GaNAs lasers with single, double and triple QWs. The dotted curve is the gain of a double QW laser with GaAs barriers. It is plotted here for comparison. During the simulations, the cavity length is intentionally set to such a length that lasing is prohibited. By doing this, the saturation of optical gain at high carrier density can clearly be visualized. We assume the gain equals mirror losses plus internal material loss. A reasonable value for internal loss is around 15 cm^{-1}. The values of optical gain at the crossing points of the curves correspond to the cavity lengths of 450 and 140 μm, respectively. This analysis reveals the relationship between the laser cavity length and the optimized QW number. As practical cavity lengths for lasers are between 200 and 400 μm, triple QWs provide a higher differential gain with more compatible threshold current, comparing to double QWs. For this range of cavity lengths, single QW lasers cannot guarantee lasing, while double QWs devices operate in the gain saturation region.

To confirm the above conclusion that triple QWs with GaNAs barrier give the best operating performance, simulations are carried out for composition A of Table 6-5. The laser cavity lengths are 200 and 300 μm. Fig. 6-22 shows the results in terms of threshold current and differential gain. It reinforces the conclusion from Fig. 6-21. The optimized structure is a triple QW with 200 μm in cavity length. The estimated threshold current is 12.7 mA. In terms of slope efficiency, it is more dependent on the structure of optical confinement (GRIN-SCH or SCH). It is calculated as 0.39 for the SCH structure.

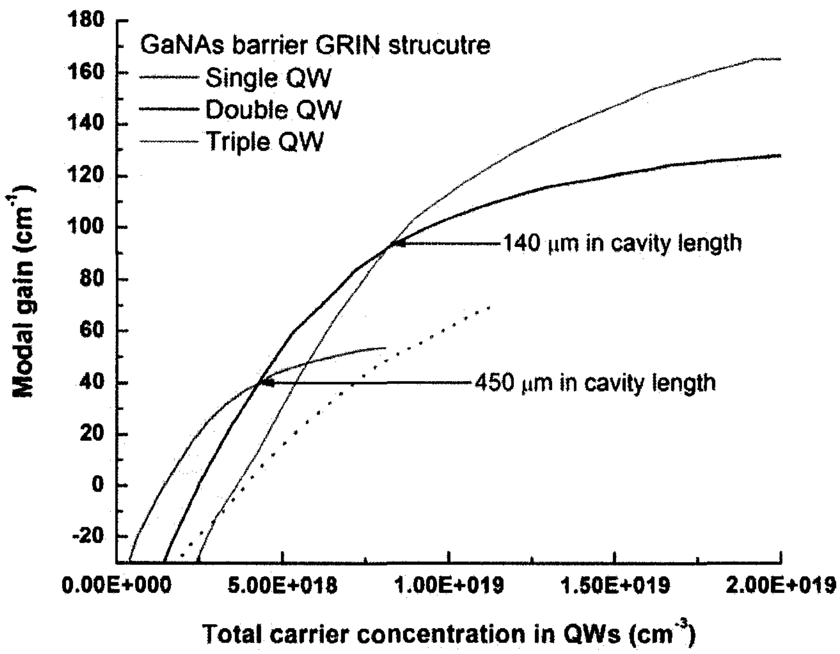

Fig. 6-21 The optical modal gain as a function of carrier density for the GaInNAs/GaNAs lasers with one, two and three QWs. The dotted line is for a GaInNAs/GaAs double QWs laser.

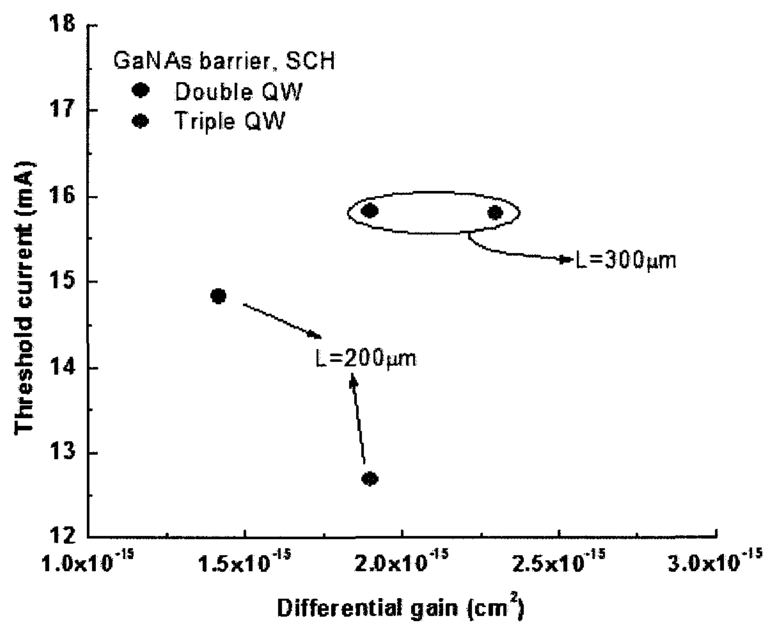

Fig. 6-22 Laser performance in terms of threshold current and differential gain for GaInNAs/GaNAs double QW and triple QW structures with the cavity length of 200 and 300 μm.

Table 6-6 lists the layer structure of this optimized design. As laser dynamics are complicated, compromises are normally required to meet certain operation specifications. This proposed design attempts to fully use the potential of GaInNAs for high-speed operation by minimizing threshold current and maximizing differential gain. The general design rules are summarized here for trade-off against other requirements:

Table 6-6 Triple $Ga_{1-x}In_xN_yAs_{1-y}$ QW with GaN_yAs_{1-y} barrier emitting in the 1.3 μm range.

	Material	Doping (cm^{-3})	Thickness (nm)	Composition	Layer description
17	GaAs:Be	1.00E+19	200		p-contact
16	$Al_xGa_{1-x}As$:Be	1.31E+18	10	x=0.12	
15	$Al_xGa_{1-x}As$:Be	1.14E+18	10	x=0.24	p-cladding
14	$Al_xGa_{1-x}As$:Be	1.00E+18	1300	x=0.33	
13	AlAs:Be	1.00E+18	10		Etch stop
12	$Al_xGa_{1-x}As$:Be	1.00E+18	200	x=0.33	p-cladding
11	GaAs	n/a	138		SCH layer
10	GaN_yAs_{1-y}	n/a	10	y=0.01	Barrier
9	$Ga_xIn_{1-x}N_yAs_{1-y}$	n/a	6	x=0.6, y=0.01	Well
8	GaN_yAs_{1-y}	n/a	10	y=0.01	Barrier
7	$Ga_xIn_{1-x}N_yAs_{1-y}$	n/a	6	x=0.6, y=0.01	Well
6	GaN_yAs_{1-y}	n/a	10	y=0.01	Barrier
5	$Ga_xIn_{1-x}N_yAs_{1-y}$	n/a	6	x=0.6, y=0.01	Well
4	GaN_yAs_{1-y}	n/a	10	y=0.01	Barrier
3	GaAs	n/a	138		SCH layer
2	$Al_xGa_{1-x}As$:Si	2.00E+18	97	x=0.33	n-cladding
	GaAs:Si	3.00E+18	3		repeat 18 time
1	GaAs:Si	2.00E+18	200		n-buffer
	(100)-GaAs:Si	2.00E+18			Substrate

1. GaInNAs QW composition: Increase indium content of QW to the strain limit. Then minimize nitrogen content with consideration of required wavelength, using QW thickness as an additional dimension to adjust lasing wavelength.
2. Temperature stable laser: Laser cavities should be longer than 400 μm. The GaInNAs double QW with GaAs barrier meets the requirements due

to the tight electron confinement and low operational carrier density. This laser demonstrates a characteristic temperature as high as 180 K. It will be an ideal light source for uncooled, 2.5Gbit/s directly modulation. However, the resonance frequency barely exceeds 10 GHz.

3. High-speed laser (beyond 10 Gbit/s modulation): Laser cavity must be shorter than 400 μm. As the result, three or more QWs are needed to overcome the large cavity loss. GaInNAs MQWs with GaNAs barriers is the only choice. There are two prominent reasons behind this requirement. The first reason is proposed by this work for the first time. That is to even the gain among QWs. The second reason is to compensate the accumulated compressive strain from wells by using tensile barriers.
4. An appropriate optical confinement plays a second order role in laser behaviors. The difference between GRIN-SCH structure and simply SCH structure is subtle. With considerations of growth and material stability over time, SCH structure is suggested.

6.6 Conclusions

This chapter reported the calibration of the laser simulator Las2D using the DQW RWG GaInNAs/GaAs lasers. The self-consistent calculation revealed that in addition to the lateral leakage, which takes about one thirds of the injection carriers, Auger recombination became another major carrier consumer. The optical modal gain calculation agreed with the experimental data. The results indicated a lower differential gain comparing to the GaInAs/GaAs 1.0μm laser. However, the gain experienced less reduction as temperature increased.

The simulation showed that a 150 nm-thick low p-doped AlGaAs cladding layer (2×10^{17} cm^{-3}) underneath the ridge reduced the laser threshold current by 35% while maintaining the laser slope efficiency. This impact-free (to process and growth) structure was suggested as the first method to improve the operational properties of the GaInNAs lasers.

An uneven carrier distribution was found due to the large conduction band discontinuity at GaInNAs-GaAs heterojunction. High indium-content QWs (40%) within compressive strain (~2.8%) favoured laser operation. The threshold current can be reduced by another 31% comparing to lasers with 37% of indium.

It was demonstarted that the use of GaNAs barrier with multiple GaInNAs QWs is an essential for equally distributed gain among QWs. The multiple QW laser with this QW/barrier combination obtained a higher differential gain than that of single and double QWs structures. A 200 μm in cavity length, triple QWs GaInNAs/GaNAs laser structure was suggested to achieve high-speed operation. The estimated threshold current was between 12 to 13 mA.

Chapter 7 Conclusions

This thesis has covered the novel dilute nitride alloys and long wavelength GaAs lasers from fundamental material modeling, through to laser structural optimization for uncooled, high-speed applications. Conclusions from each area have been made that further the scientific understanding and the manufacturability of the material. A recap of these conclusions is given below, followed by suggested future work.

The commercial success of high-speed metro (MAN) and local area networks (LAN) to deliver high-speed to the desktop relies on the realization of low cost, 1.3 μm, directly modulated, un-cooled lasers. The fundamental physics of present generation lasers prevents an easy solution to these cost and performance requirements. The experimental work of this thesis provides a solution by realization and evaluation of a temperature insensitive (T_0=155 K), edge-emitting laser using a novel dilute nitride material. With this level of temperature sensitivity, GaInNAs lasers can work uncooled in simple packages, greatly reducing the packaging costs.

The experimental work also demonstrates the possibility of high-speed operation. Package parasitism and the laser intrinsic dynamics have large influence on the 3 dB bandwidth of a directly modulated laser. For a modulation frequency above 2.5 GHz, specially designed RF matching packages must be employed to minimize the circuit parasitics. The laser intrinsic dynamics limit the laser modulation capabilities. The measurement-based RIN calculation for a relatively long cavity GaInNAs laser (448 μm cavity length) demonstrates a 9.7 GHz maximum modulation frequency. To further increase the maximum modulation bandwidth, we need to enhance the optical gain to such a level that shorter cavity devices (around 200 μm) can exhibit stimulated emission. This, as illustrated in the following text, challenges dilute nitride crystal growth and device structural design, especially the QW design.

The optical gain measurements show a low transparency current of 6 mA (with leakage correction) in a 2 μm x 450 μm laser. This indicates that the initial number of non-radiative recombination centers is of the same order of magnitude as in other active materials. However, we observed a significant difference in L-I characteristics between CW and pulsed mode operation. A strong junction self-heating occurs due to the existence of a large number of non-radiative recombination centers in the laser active region. The reasons for the existence of these centers have not been found experimentally. However, they may relate to the metastable low temperature crystal growth and the ion damage from the nitrogen plasma source during the incorporation of nitrogen. Crystal defects can migrate across the active region at high current injection. The number of non-radiative recombination center can increase and the devices fail quickly (in a few hours). The major challenge to fabricate reliable devices is to eliminate the non-radiative defects by studying the effects of the low temperature growth and the ion damage from the N plasma source. Research on growth dynamics is also required to reduce the 2-D to 3-D growth transition due to phase segregation, to precisely control composition, strain and energy band offsets at the hetero-interfaces.

The gain and photocurrent measurements provide experimental evidence for the effective electron mass enhancement and the validity of the band anti-crossing theory in dilute nitride materials. The conduction band nonparabolicity reduces the material gain as the percentage of nitrogen increases in the QWs. Therefore a MQW structure with a relatively large number of wells must be employed for the realization of high-speed lasers, since they require a high differential gain and a short resonance cavity. However, for MQWs with GaAs barriers, it is hard to achieve a high gain due to challenges in crystal growth and a strong spatial non-uniform carrier distribution. The simulations presented in the later part of this thesis offer a design alternative to GaAs barriers using GaNAs as the barrier to compensate the strain, to reduce the amount of nitrogen in the QWs, and to leverage the carrier distribution among the QWs through the more balanced conduction and valence band offsets. Therefore, further fabrication and evaluation of next generation GaInNAs/GaNAs lasers should take place.

To further extend the emission wavelength of GaAs based lasers, GaInNAs with Sb surfactant was studied in this work. The initial results are promising. The world's first 1.55 μm GaAs substrate laser was demonstrated. A room temperature, CW operation GaInNAsSb/GaNAs laser was achieved through treatment of the laser facets. Further-more, the material gain of the GaInNASb QWs was extracted for the first time using cavity loss analysis. The low material gain was due to poor crystal quality. Innovation in crystal growth is key to the realization of functional GaInNAsSb lasers.

The band anti-crossing theory described the band energy dispersion of dilute nitrides. Computation-based theory was corrected using the experimental data. The modified theory was implemented into the commercial laser simulator Las2D. Other essential physical models used in laser simulators, such as mobility models, were extended to dilute nitride materials by combining results of the experiments with those from the published literature. As the result, Las2D is now available with an additional material system. This addition to the modeling software greatly assists dilute nitride laser design and behavior prediction.

A two-dimensional simulation algorithm was developed to calibrate the Las2D simulator with the in-house fabricated GaInAs/GaAs and GaInNAs/GaAs ridge waveguide lasers. Using this algorithm, good agreement in laser behaviour was achieved between simulations and experiments. The calculation results of Las2D can therefore be trusted in laser structure design.

Using the Las2D simulator, two-dimensional simulations were carried out to optimize the dilute nitride laser structures for low threshold and high differential gain. The three major conclusions from the simulation are: (1) The threshold current can be greatly reduced by reducing the p-type doping level locally (to $2x10^{17}$ cm^{-3}) in the AlGaAs cladding layer beneath the ridge. The low threshold current will partially solve the problem of junction self-heating and improve the device efficiency. (2) There exists strong carrier density inhomogeneity among the spatially distributed GaInNAs/GaAs MQWs. As a consequence, increasing the numbers of QWs (above three) will not help in laser gain enhancement. GaInNAs/GaNAs MQWs are suggested for higher gain by trading-off against laser temperature stability. (3) The optimized QW composition is that with the highest possible indium content. The maximum amount of indium is limited by the critical condition of the strain relaxation. The practical level of strain for GaInNAs on GaAs substrates is around compressive 2.8%. This amount of strain corresponds to 40% of indium in the GaInNAs alloy.

Recently, Las2D was upgraded with small signal simulation functionality. This functionality will greatly assist high-speed laser design by evoking self-consistent calculation among optical gain and carrier transport - the essential elements of high-speed laser design. Small signal simulation and measurements should be done with next generation devices.

The effect of antimony's addition is not included in the band anti-crossing theory. The empirical solution may also be used to include this element in laser simulators.

The ultimate goal of the dilute nitride long wavelength lasers is the realization of surface emitting lasers. These lasers can be on-wafer tested. The manufacturing costs for low yield fabrication can be considerably lowered, since good die are identified immediately. Device manufactures takes two directions in designing surface emitting lasers. A structure consisting of a vertical cavity MQWs active region with an integrated Bragg mirror has been demonstrated at 2.5 Gbit/s transmission. Growing large numbers of QWs has been the solution for increasing the gain of VCSELs made from conventional material. However, as discovered in this thesis, there are significant challenges in achieving proper carrier injection in devices with large number of QWs, and consequently the output power of dilute nitride VCSELs is likely to be limited. In applications where high output power is required, dilute nitride surface emitting lasers might have to go a second design route. That is the horizontal cavity surface emitting laser (HCSELs). In HCSELs, the laser beam is redirected to the surface using a 45° mirror located at the end of the laser cavity. The large gain medium of the horizontal cavity will maintain the desired output power with the use of a small number of QWs. Manufacturability has been demonstrated by the commercial availability of InP based lasers emitting at 1310 nm.

References

[1] M. Sze, *Semiconductor Devices, Physics and Technology*, 2d Edition, S. John Wiley & Son, 2002.

[2] M.L. Cohen and J.R. Chelikowsky, *Electronic Structure and Optical Properties of Semiconductors,* Springer Series in Solid-State Sciences, Springer, Berlin, 1998.

[3] I. Vurgaftman, J.R. Meyer, and L.R. Ram-Mohan, "Band parameters for III-V compound semiconductors and their alloys," J. Appl. Phys., Vol. 89, pp. 5815-5875, 2001.

[4] J.D. Evans, J.G. Simmons, D.A. Thompson, N. Puetz, T. Makino and G. Chik, "An investigation into the temperature sensitivity of strained and unstrained multiple quantum-well, long wavelength lasers: new insight and methods of characterization," IEEE J. Sel. Top. in Quantum Electron., Vol. 1, pp. 275-284, 1995.

[5] A.F. Phillips, S.J. Sweeney, A.R. Adams, P.J.A. Thijs, "The temperature dependence of 1.3- and 1.5-μm compressively strained InGaAs(P) MQW semiconductor lasers," IEEE J. Sel. Top. in Quantum Electron., Vol. 5, pp. 401-412, 1999.

[6] T. Higashi, S.J. Sweeney, A.F. Phillips, A.R. Adams, E.P. O'Reilly, T. Uchida, and T. Fujii, "Experimental analysis of temperature dependence in 1.3-μm AlGaInAs-InP Strained MQW lasers," IEEE J. Sel. Top. in Quantum Electron., Vol. 5, pp. 413-419, 1999.

[7] S.R. Selmic, T.M. Chou, J.Sih, J.B. Kirk, A. Mantie, J.K. Butler, D. Bour, and G.A. Evans,"Design and characterization of 1.3-μm AlGaInAs-InP multiple-quantum-well lasers," IEEE J. Sel. Top. in Quantum Electron., Vol. 7, pp. 340-349, 2001.

[8] M. Kondow, T. Kitatani, S. Nakatsuka, M.C. Larson, K. Nakahara, Y. Yazawa, M. Okai, and . Uomi, "GaInNAs: A novel material for long-wavelength semiconductor lasers," IEEE J. Sel. Top. in Quantum Electron., Vol. 3, pp. 719-730, 1997.

[9] S. Tomic, E.P. O'Reilly, R. Fehse, S.J. Sweeney, A.R. Adams, A.D. Andreev, S.A. Choulis, T.J.C. Hosea, and H. Riechert, "Theoretical and experimental analysis of 1.3-μm InGaAsN/GaAs lasers," IEEE J. Sel. Top. in Quantum Electron., Vol. 5, pp. 1228-1238, 2003.

[10] J.W. Ager III, and W. Walukiewicz, "Current status of research and development of III-N-V semiconductor alloys," Semicon. Sci. Technol., Vol. 17, pp. 741-745, 2002.

[11] A. Lindsay and E.P. O'Reilly, "Theory of enhanced bandgap non-parabolicity in GaN_xAs_{1-x} and related alloys," Solid State Commun., vol. 112, pp. 443-447, 1999.

[12] E.P. O'Reilly and A. Lindsay, "K•P model of ordered GaN_xAs_{1-x}," Phys. Status Solidi. B, Vol. 216, pp. 131-134, 1999.

[13] I.A. Buyanova, W.M. Chen, B. Moneman, "Electronic properties of Ga(In)NAs alloys," MRS internet J. Nitride Semicon. Res. Vol. 6, pp. 1-19, 2001.

[14] S. A. Choulis, T. J. C. Hosea, S. Tomić, M. Kamal-Saadi, A. R. Adams, E. P. O'Reilly, B. A. Weinstein, and P. J. Klar, "Electronic structure of $In_yGa_{1-y}As_{1-x}N_x$/GaAs multiple quantum wells in the dilute-*N* regime from pressure and k•p studies," Phys. Rev. B, Vol. 66, 165321, 2002.

[15] C. Skierbiszewski, P. Perlin, P. Wisniewski, W. Knap, T. Suski, W. Walukiewicz, W. Shan, K.M. Yu, J.W. Ager, E.E. Haller, J.F. Geisz and J.M. Olson, "Large, nitrogen-induced increase of the electron effective mass in InyGa1-yNxAs1-x," Appl. Phys. Lett., Vol. 76, pp. 2409-2411, 2000.

[16] J.A. Gupta, P.J. Barrios, G.C. Aers, R.L. Williams, J. Ramsey, and Z.R. Wasilewski, "Properties of 1.3μm InGaNAs laser material grown by MBE using a N_2/Ar RF plasma," Solid-State Electron., Vol.47, pp. 399-405, 2003.

[17] S.R. Bank, M.A. Wistey, H.B. Yuen, L.L. Goddard, H. Bae, and J.S. Harris Jr, "Molecular-beam epitaxy growth of low-threshold cw GaInNAsSb lasers at 1.5μm," J. Vac. Sci. Technol. B, Vol. 23, pp1337-1340, 2005.

[18] S.M. Wang, Y.Q. Wei, X.D. Wang, Q.X. Zhao, M. Sadeghi, A. Larsson, "Very low threshold current density 1.3μm GaInNAs single quantum well lasers grown by molecular beam epitaxy," J. of Cryst. Growth, Vol. 278, pp. 734-738, 2005.

[19] Z. Niu, S. Zhang, H. Ni, D. Wu, Z. He, Z. Sun, Q. Han, and R. Wu, "1.3μm high indium content (42.5%) GaInNAs/GaAs Quantum wells grown by molecular beam epitaxy," Phys. Status Solidi. C, Vol. 3, pp. 631-634, 2006.

[20] J. S. Harris Jr, "The opportunities, successes and challenges for GaInNAsSb," J. of Cryst. Growth, Vol. 278, pp. 3-17, 2005.

[21] J.A. Gupta, P.J. Barrios, X. Zhang, J. Lapointe, D. Poitras, G. Pakulski, X. Wu and A. Delage, "Room-temperature continuous-wave operation of GaInNAsSb laser diodes at 1.55 μm," Electron. Lett., Vol. 41, pp. 1060-1061, 2005.

[22] F. Ishikawa, M. Höricke, U. Jahn, A.Trampert, K.H. Ploog, "Molecular beam epitaxial growth window for high-quality (Ga,In)(N,As) quantum wells for long wavelength emission," Appl. Phys. Lett., Vol. 88, 191115, 2006.

[23] G. Jaschke, R. Averbeck, L. Geelhaar, and H. Riechert, "Low threshold InGaAsN/GaAs lasers beyond 1500nm," J. of Cryst. Growth, Vol. 278, pp. 224-228, 2005.

[24] H.P. Xin, C.W. Tu, and M. Geva, "Annealing behavior of p-type Ga0.892In0.108NxAs1-x (0<x,0.024) grown by gas-source molecular beam epitaxy," Appl. Phys. Lett., Vol. 75, pp. 1416-1418, 1999.

[25] H. Zhao, Y.Q. Xu, H.Q. Ni, S.Y. Zhang, Q. Han, Y. Du, X.H. Yang, R.H. Wu and Z.C. Niu, "Post-growth and in situ annealing on GaInNAs(Sb) and their application on 1.55 μm lasers," Semicon. Sci. and Technol., Vol. 21, pp. 279-282, 2006.

[26] E. Tournie, M.-A. Pinault, and A. Guzman, "Mechanisms affecting the photoluminescence spectra of GaInNAs after post-growth annealing," Appl. Phys. Lett., Vol. 80, pp. 4148-4150, 2002.

[27] P.J. Klar, H. Gruning, J. Koch, S. Schafer, K. Volz, W. Stolz, W. Heimbrodt, A.M. Kamal Saadi, A. Lindsay, and E.P. O'Reilly, "(Ga, In)(N, As)-fine structure of the band gap due to nearest-neighbour configurations of the isovalent nitrogen," Phys. Rev. B, Vol. 64, pp. 121203-121206, 2001.

[28] S. Kurtz, J. Webb, L Gedvilas, D. Friedman, J. Geisz, J. Olson, R. King, D. Joslin, and N. Karam, "Structural changes during annealing of GaInAsN," Appl. Phys. Lett., Vol.78, pp. 748-750, 2001.

[29] R. Kudrawiec, G. Sek, J. Misiewicz, D. Gollub, and A. Forchel, "Explanation of annealing-induced blueshift of the optical transitions in GaInNAs/GaAs quantum wells," Appl. Phys. Lett., Vol. 83, pp. 2772-2774, 2003.

[30] N. Tansu, A. Quandt, M. Kanskar, W. Mulhearn, L.J. Mawst, "High-performance and high-temperature continuous-wave-operation 1300 nm InGaAsN quantum well lasers by organmetallic vapor phase epitaxy," Appl. Phys. Lett., Vol. 83, pp. 18-20, 2003.

[31] V. Gambin, W. Ha, M. Wistey, H. Yuen, S.R. Bank, S.M. Kim, J.S. Harris, "GaInNAsSb for 1.3-1.6 μm-long wavelength lasers grown by molecular beam epitaxy," IEEE J. Sel. Top. in Quantum Electron., Vol. 8, pp. 795-800, 2002.

[32] M. Kaminishi, S. Sato, T. Takahashi, S. Satoh, "Low threshold operation of MOCVD grown 1.3 μm range GaInNAs triple quantum-well lasers with low N content GaNAs barrier layers," 16th International

Conference on Indium Phosphide and Related Materials, pp. xiv+778, 31 May - 4 June 2004 Kagoshima, Japan

[33] W. Ha, V. Gambin, M. Wistey, S. Bank, S. Kim, J.S. Harris, "Multiple-quantum-well GaInNAs-GaNAs ridge-waveguide laser diodes operating out to 1.4 μm," IEEE Photon. Technol. Lett., Vol. 14, pp. 591-593, 2002.

[34] M.R. Gokhale, P.V. Studenkov, J. Wei, S.R. Forrest, "Low-threshold current, high-efficiency 1.3-μm wavelength aluminum-free InGaAsN-based quantum-well lasers," IEEE Photon. Technol. Lett., Vol. 12, pp. 131-133, 2000.

[35] M. Kondow, M. Kudo, S. Tanaka, S. Fujisaki, and K. Nakahara, "Impurities in GaInNAs laser diodes grown by molecular beam epitaxy," Extended abstracts of the 23rd electronic material symposium, Izu-Nagaoka, July 7 – 9, 2004, pp. 181-182.

[36] M.C. Larson, C.W. Coldren, S.G. Spruytte, H.E. Petersen, J.S. Harris, "Low-threshold oxide-confined GaInNAs long wavelength vertical cavity lasers," IEEE Photon. Technol. Lett., Vol. 12, pp. 1598-1600, 2000.

[37] N. Tansu, N.J. Kirsch, and L.J. Mawst, "Low-threshold-current-density 1300-nm dilute-nitride quantum well lasers," Appl. Phys. Lett., Vol. 81, pp. 2523-2525, 2002.

[38] M. Pessa, C.S. Peng, T. Jouhti, E.-M. Pavelescu, W. Li, S. Karirinne, H. Liu, and O. Okhotnikov, "Towards high-performance nitride lasers at 1.3μm and beyond," IEE Proc.-Optoelectron., Vol. 150, pp. 12-21, 2003.

[39] A.W. Jackson, R.L. Naone, M.J. Dalberth, J.M. Smith, K.J. Malone, D.W. Kisker, J.F. Klem, K.D. Choquette, D.K. Serkland, and K.M. Geib, "OC-48 capable InGaAsN vertical cavity lasers," Electron. Lett., vol. 37, pp. 355-356, 2001.

[40] A. Martinez, J.-G. Provost, B. Dagens, V. Sallet, D. Jahan, K. Merghem, L. Ferlazzo, J. Landreau, O. Le Gouezigou, J.-C. Harmand, and A. Ramdane, "9.7GHz small-signal bandwidth of three-quantum well GaInNAs/GaAs laser diodes operating at 1.35μm," Electron. Lett., vol. 40, pp. 425-427, 2004.

[41] D. Gollub, S. Moses, and A. Forchel, "1.3μm double quantum well GaInNAs distributed feedback laser diode with 13.8GHz small signal modulation bandwidth," Electron. Lett., vol. 40, pp. 1181-1182, 2004.

[42] J.O. Mitomo, M. Yokozeki, Y. Sato, Y. Hirano, T. Hino, and H. Narui, "1.30-μm GaInNAs laser diode with lifetime over 1000 hours grown by MOCVD," IEEE J. Sel. Top. in Quantum. Electron. Vol. 11, pp. 1099-1102, 2005.

[43] Y. Q. Wei, J. S. Gustavsson, Å. Haglund, P. Modh, M. Sadeghi, S. M. Wang, and A. Larsson, "High-frequency modulation and bandwidth limitations of GaInNAs double-quantum-well lasers," Appl. Phys. Lett., Vol. 88, 051103, 2006.

[44] S. Bonnefont, B. Messant, M. Boutillier, O. Gauthier-Lafaye, F. Lozes-Dupuy, A. Martinez, V. Sallet, K. Merghem, l. Ferlazzo, J. C. Harmand, A. Ramdane, J.G. Provost, B. Dagens, J. Landreau, O. Legouezigou, and X. Marie, "Optimization and characterization of InGaAsN/GaAs quantum-well ridge laser diodes for high frequency operation," Optical and Quantum Electronics, Vol. 38, pp. 313-324, 2006.

[45] X. Zhang, J.A. Gupta, P.J. Barrios, G. Pakulski, X. Wu, and A. Delage, "Gain spectra of 1.3um GaInNAs laser diodes," J. Vac. Sci. Technol A, vol. 24, pp. 787-790, 2006.

[46] A. Hierro, J.M. Ulloa, E. Calleja, B. Damilano, J. Barjon, J.-Y. Duboz, and J. Massies, "Room Temperature Performance of Low Threshold 1.34–1.44 μm GaInNAs–GaAs Quantum-Well Lasers Grown by Molecular Beam Epitaxy," IEEE Photon. Technol. Lett., Vol. 17, pp. 1142-1144, 2005.

[47] J.-Y. Yeh, N. Tansu and L.J. Mawst, "Long wavelength MOCVD grown InGaAsN–GaAsN quantum well lasers emitting at 1.378–1.41 μm," Electron. Lett., Vol. 40, pp. 739-741, 2004.

[48] T. Nishida, M. Takaya, S. Kakinuma, T. Kaneko, "4.2-mW GaInNAs long-wavelength VCSEL grown by metalorganic chemical vapor deposition," IEEE J. Sel. Top. Quantum Electron, Vol. 11, pp. 958-961, 2005.

[49] M. Yamada, T. Anan, H. Hatakeyama, K. Tokutome, N. Suzuki, T. Nakamura, K. Nishi, "Low-threhsold operation of 1.34-μm GaInNAs VCSEL grown by MOVPE," IEEE Photon. Technol. Lett., Vol. 17, pp. 950-952, 2005.

[50] J.A. Gupta, Z.R. Wasilewski, B.J. Riel, J. Ramsey, G.C. Aers, R.L. Williams, G.I. Sproule, A. Perovic, D.D. Provic, T. Garanzotis, A.J. Springthorpe, "Compositional control in molecular beam epitaxy growth of GaN_yAs_{1-y} on GaAs (001) using an Ar/N_2 RF plasma," J. Cryst. Growth, Vol. 242, pp. 141-154, 2002.

[51] J.Y. Duboz, J.A. Gupta, Z.R. Wasilewski, J. Ramsey, R.L. Williams, G.C. Aers, B.J. Riel, and G.I. Sproule, "Band-gap energy of $In_xGa_{1-x}N_yAs_{1-y}$ as a function of N content," Phys. Rev. B, Vol. 66, 085313, 2002.

[52] S.Y. Hu, D.B. Young, A.C. Gossard, and L.A. Coldren, "The effect of lateral leakage current on the experimental gain/current-density curve in quantum-well ridge-waveguide lasers," IEEE J. Quantum Electron, Vol. 30, pp. 2245-2250, 1994.

[53] L.A. Coldren and S.W. Corzine, "Diode Lasers and Photonic Integrated Circuits", John Wiley & Sons, 1995.

[54] T.J. Houle, J.C.L. Yong, C.M. Marinelli, S. Yu, J.M. Rorison, I.H. White, J.K. White, A.J. SpringThorpe, and B. Garrett, "Characterization of the temperature sensitivity of gain and recombination mechanisms in 1.3-μm AlGaInAs MQW lasers," IEEE J Quantum Electron, Vol. 41, pp. 132-139, 2005.

[55] A.F. Phillips, S.J. Sweeney, A.R. Adams and P.J.A. Thijs, "The temperature dependence of 1.3- and 1.5-μm compressively strained InGaAs(P) MQW semiconductor lasers," IEEE J. Sel. Top. Quantum Electron, Vol. 5, pp. 401-411, 1999.

[56] B.W. Hakki and T.L. Paoli, "CW degradation at 300°K of GaAs double-heterostructure junction lasers, II. Electronic gain," J. Appl. Phys., Vol. 44, pp. 4173-4176, 1973.

[57] D.T. Cassidy, "Technique for measurement of the gain spectra of semiconductor diode lasers," J. Appl. Phys., Vol. 56, pp. 3096-3099, 1984.

[58] H. Wang, D.T. Cassidy, "Gain measurements of Fabry-Perot semiconductor lasers using a nonlinear least-squares fitting method," IEEE J. Quantum Electron., Vol. 41, pp. 532-540, 2005.

[59] B.W. Hakki and T.L. Paoli, "Gain spectra in GaAs double-heterostructure injection lasers", J. Appl. Phys., Vol. 46, pp. 1299-1302, 1975.

[60] D.A. Ackerman, G.E. Shtengel, M.S. Hybertsen, P.A. Morton, R.F. Kazarinov, T. Tanbun-EK and R.A. Logan "Analysis of Gain in Determining T_0 in 1.3-μm Semiconductor Lasers," IEEE J. Sel. Top. in Quantum Electron. Vol. 1, pp. 250-260, 1995.

[61] S. Mogg, N. Chitica, R. Schatz and M. Hammar, "Properties of highly strained InGaAs/GaAs quantum wells for 1.2- μm laser diodes". Appl. Phys. Lett., Vol. 81, pp. 2334-2336, 2002.

[62] R. Olshansky, J. LaCourse, T. Chow, and W. Powazinik, "Measurement of radiative, Auger, and nonradiative currents in 1.3-μm InGaAsP buried heterostructure lasers," Appl. Phys. Lett., Vol. 50, pp. 310-313, 1987.

[63] C.H. Henry, "Theory of the linewidth of semiconductor lasers," IEEE J. Quantum Electron., Vol. 18, pp. 259-264, 1982.

[64] Y. Yamamoto, "AM and FM quantum noise in semiconductor lasers – Part I: Theoretical analysis," IEEE J. Quantum Electron., Vol. 19, pp. 34-46, 1983.

[65] K. Vahala and A. Yariv, "Semiclassical theory of noise in semiconductor lasers – part II," IEEE J. Quantum Electron., Vol. 19, pp. 1102-1109, 1983.

[66] P. Spano, S. Piazzolla, and M. Tamburrini, "Phase noise in semiconductor lasers: A theoretical approach," IEEE J. Quantum Electron., Vol. 19, pp. 1195-1199, 1983.

[67] G.P. Agrawal and N.K. Dutta, *Long-wavelength Semiconductor Laser,* New York: Van Nostrand Reinhold, 1986.

[68] C.H. Henry, "Phase noise in semiconductor lasers," J. Lightwave Technol., Vol. 4, pp. 298-311, 1986.

[69] R. Nagarajan, M. Ishikawa and J.E. Bowers, "Effects of carrier transport on relative intensity noise and critique of K factor prediction of modulation response," Electron. Lett., Vol. 28, pp. 846-848, 1992.

[70] M.C. Tatham, I.F. Lealman, Colin P. Seltzer, L.D. Westbrook, and D.M. Cooper, "Resonance frequency, damping, and differential gain in 1.5μm multiple quantum-well lasers," IEEE J. Quantum Electronics, Vol. 28, pp. 408-414, 1992.

[71] A. Martinez, J.-G. Provost, B. Dagens, V. Sallet, D. Jahan, K. Merghem, L. Ferlazzo, J. Landreau, O. Le Gouezigou, J.-C. Harmand, and A. Ramdane, "9.7GHz small-signal bandwidth of three-quantum well GaInNAs/GaAs laser diodes operating at 1.35μm," Electron. Lett., Vol. 40, pp. 425-427, 2004.

[72] W.H. Seo, and J.F. Donegan, "Linewidth enhancement factor of lattice-matched InGaNAs/GaAs quantum wells," Appl. Phys. Lett., Vol. 82, pp. 505-507, 2003.

[73] A. Thränhardt, I. Kuznetsova, C. Schlichenmaier, and S.W. Koch et al, "Nitrogen incorporation effects on gain properties of GaInNAs lasers: Experiment and theory," Appl. Phys. Lett., Vol. 86, 201117, 2005.

[74] L.H. Li, V. Sallet, G. Patriarche, L. Largeau, S. Bouchoule, and L. Travers, "Investigations on GaInNAsSb quinary alloy for 1.5μm laser emission on GaAs," Appl. Phys. Lett., Vol. 83, pp. 1298-1301, 2003.

[75] L.L. Goddard, S.R. Bank, M.A. Wistey, H.B. Yuen, Z. Rao, and J.S. Harris, "Recombination, gain, band structure, efficiency and reliability of 1.5-μm GaInNAsSb/GaAs lasers," J. Appl. Phys., Vol. 97, 083101, 2005.

[76] H.D. Sun, S. Calvez, M.D. Dawson, J.A. Gupta, G.I. Sproule, X. Wu and Z.R. Wasilewski, "Role of Sb in the growth and optical properties of 1.55μm GaInN(Sb)As/GaNAs quantum-well structures by molecular-beam epitaxy," Appl. Phys. Lett., Vol. 87, 181908, 2005.

[77] R. Kudrawiec, M. Gladysiewicz, H.B. Yuen, S.R. Bank, M.A. Wistey, H.P. Bae and J.S. Harris, "Photoreflectance spectroscopy of a $Ga_{0.62}In_{0.38}N_{0.026}As_{0.954}Sb_{0.02}$/GaAs single quantum well tailored at 1.5 μm," Solid State Commun., Vol. 137, pp. 138-141, 2006.

[78] H.B. Yuen, S.R. Bank, H. Bae, M.A. Wistey, and J.S. Harris, "The role of antimony on properties of widely varying GaInNAsSb compositions," J. Appl. Phys., Vol. 99, 093504, 2006.

[79] J.A. Gupta, P.J. Barrios, X. Zhang, G. Pakulski, and X. Wu, "1.53μm GaInNAsSb laser diodes grown on GaAs (100)," Electron. Lett., Vol. 41, pp. 71-72, 2005.

[80] I. Joindot and J.L. Beylat, "Intervalence band absorption coefficient measurements in bulk layer, strained and unstrained multiquantum well 1.55μm semiconductor lasers," Electron. Lett., Vol. 29, pp. 604-606, 1993.

[81] A. Champagne and R. Maciejko, *Las2D users manual*, The Optoelectronic Laboratory, Ecole Polytechnique de Montreal, pp. 2-11, 2004.

[82] Y. P. Varshni, "Temperature dependence of the energy gap in semiconductors," Physica, Vol. 34, pp. 149-154, 1967.

[83] J. Piprek, *Semiconductor Optoelectronic Devices: Introduction to Physics and Simulation*, pp. 91, San Diego, Academic Press, 2003.

[84] I. Vurgaftman and J.R. Meyer, "Band parameters fro nitrogen-containing semiconductors," J. Appl. Physics, Vol. 94, pp. 3675-3696, 2003.

[85] M. Sotoodeh, A.H. Khalid, and A.A. Rezazadeh, "Empirical low-field mobility model for III-V compounds applicable in device simulation codes," J. Appl. Phys., Vol.87, pp. 2890-2900, 2000.

[86] R. Yan, S. Corzine, L. Coldren, and I. Suemune, "Corrections to the expression of gain in GaAs," IEEE J. Quantum Electron., Vol.26, pp. 213-216, 1990.

[87] M. Asada, A. Kameyama, and Y. Suematsu, "Gain and intervalence band absorption in quantum-well lasers," IEEE J. Quantum Electron., Vol. 20, pp. 745-753, 1984.

[88] M. Asada, "Intraband relaxation time in quantum-well lasers," IEEE J. Quantum Electron., Vol. 25, pp. 2019-2026, 1993.

[89] W. Shan, W. Walukiewicz, and J.W. Ager III, "Band anticrossing in GaInNAs alloys," Phys. Rev. Lett., Vol. 82, pp. 1221-1224, 1999.

[90] P.R.C. Kent, A. Zunger, "Nitrogen pairs, triplets, and clusters in GaAs and GaP," Appl. Phys. Lett., Vol. 79, pp. 2339-2441, 2001.

[91] Y. Zhang and A. Mascarenhas, "Valence-band splitting and shear deformation potential of diluted $GaAs_{1-x}N_x$ alloys," Phys. Rev. B, Vol. 61, pp. 4433-4436, 2000.

[92] J. Wu, W. Shan and W. Walukiewicz, "Band anticrossing in highly mismatched III-V semiconductor alloys," Semicon. Sci. Technol., Vol. 17, pp. 860-869, 2002.

[93] http://athens.phy.nrc.ca/ims/qp/codes/inganas/inganas.help.html

[94] J.A. Gupta, Z.R. Wasilewski, B.J. Riel, J. Ramsey, G.C. Aers, R.L. Williams, G.I. Sproule, A. Perovic, D.D. Perovic, T. Garanzotis, and A.J. SpringThorpe, "Compositional control in molecular beam epitaxy growth of GaNyAs1-y on GaAs (001) using an Ar/N-2 RF plasma," J. of Cryst. Growth, Vol. 242, pp. 141-154, 2002.

[95] W. Zawadzki, "Electron transport phenomena in small gap semiconductors," Adv. Phys. Vol. 23, pp. 435-522, 1974.

96 P.J. Klar, H. Gruning, W. Heimbrodt, G. Weiser, J. Koch, K. Volz, W. Stolz, S.W. Koch, S. Tomic, S.A. Choulis, T.J.C. Hosea, E.P. O'Reilly, M. Hofmann, J. Hader, and J.V. Moloney, "Interband transitions of quantum wells and device structures containing Ga(N,As) and (Ga, In)(N,As)," Semicond. Sci. Technol. Vol. 17 , pp. 830–842, 2002.

[97] B.Q. Sun, D.S. Jiang, X.D. Luo, Z. Y. Xu, Z. Pan, L.H. Li, and R.H. Wu, "Interband luminescence and absorption of GaNAs/GaAs single-quantum-well structures," Appl. Phys. Lett., Vol. 76, pp. 2862-2864, 2000.

[98] http://www.ioffe.rssi.ru/SVA/NSM/Semicond/GaInAs/basic.html

[99] S. Fahy and E.P. O'Reilly, "Theory of electron mobility in dilute nitride semiconductors," Physica E, Vol. 21, pp. 881-885, 2004.

[100] K. Volz, J. Koch, B. Kunert, and W. Stolz, "Doping behavior of Si, Te, Zn and Mg in lattice-matched (GaIn)(NAs)/GaAs bulk films," J. of Cryst. Growth, Vol. 248, pp. 451-456, 2003.

[101] J. Piprek, *Semiconductor Optoelectronic Devices: Introduction to Physics and Simulation*, pp. 91, San Diego, Academic Press, 2003.

[102] D. Ban, E.H. Sargent, K. Hinzer, St. J. Dixon-Warren, I. Calder, A.J. SpringThorpe, and J.K. White, "Direct observation of lateral current spreading in ridge-waveguide lasers using scanning voltage microscopy," Appl. Phys. Lett. Vol. 82, pp. 4166-4168, 2003.

[103] G.E. Shtengel, D.A. Ackerman, P.A. Morton, E.J. Flynn, and M.S. Hybertsen, "Impedance-corrected carrier lifetime measurements in semiconductor lasers," Appl. Phys. Lett., Vol. 67, pp. 1506-1508, 1995.

[104] Y.Zou, J.S. Osinski, P.Grodzinski, P. Daniel, W.C. Rideout, W.F. Sharfin, J. Schlafer, and F.D. Crawford, "Experimental study of Auger recombination, gain, and temperature sensitivity of 1.5um compressively strained semiconductor lasers," IEEE J. Quantum Electron., Vol. 29, pp. 1565-1574, 1993.

[105] G.J. Letal, J.G. Simmons, J.D. Evans, and G.P. Li, "Determination of active-region leakage currents in ridge-waveguide strained-layer quantum-well lasers by varying the ridge width," IEEE J. Quantum Electron., Vol. 34, pp. 512-518, 1998.

[106] Y. Suematsu and A.R. Adams, *Handbook of Semiconductor Lasers and Photonic Integrated Circuits*, London, Chapman & Hall, 1994.

[107] G. Fuchs, J. Hoerer, A. Hangleiter, V. Haerle, F. Scholz, R.W. Glew, and L. Goldstein, "Intervalence band absorption in strained and unstrained InGaAs multiple quantum well structures," Appl. Phys. Lett., Vol. 60, pp. 231-233, 1992.

[108] G.C. Aers, Institute of Microstructural Science, National Research Council of Canada, Private communication to the author of [91].

[109] G. Morthier and P. Vankwikelberge, *Hand book of distributed feedback laser diode*, Artech House Publishers, 1997.

[110] K. Hinzer, Centre for Research in Photonics, University of Ottawa, Ottawa, Canada, Private communications.

[111] N. Tessler and G. Eisenstein, "On carrier injection and gain dynamics in quantum well lasers," IEEE J. Quantum Electron. Vol. 29, pp. 1586-1595, 1993.

[112] N. Tessler and G. Eisenstein, "Distributed nature of quantum well lasers," Appl. Phys. Lett., Vol. 63, pp. 10-12, 1993.

[113] A. Hangleiter, A. Grabmaier, and G. Fuchs, "Damping of the relaxation resonance in multiple-quantum-well lasers by slow interwell transport," Appl. Phys. Lett., Vol. 62, pp. 2316-2318, 1993.

[114] M. Hamp and D.T. Cassidy, "Experimental and theoretical analysis of the carrier distribution in asymmetric multiple quantum-well InGaAsP lasers," IEEE J. Quantum Electron., Vol. 37, pp. 92-99, 2001.

[115] M. Hamp, D.T. Cassidy, B.J. Robinson, Q.C. Zhao, and D.A. Thompson, "Nonuniform carrier distribution in asymmetric multiple-quantum-well InGaAsP laser structures with different numbers of quantum wells," Appl. Phys. Lett., Vol. 74, pp. 744-746, 1999.

[116] D. Tauber and J.E. Bowers, "Dynamics of wide bandwidth semiconductor lasers", *High Speed Diode Lasers*, Editor: S.A. Gurevich, World Scientific, Singapore, 1998.

[117] P.M. Smowton, G.M. Lewis, A. Sobiesierski, P. Blood, J. Lutti, and S. Osbourne, "Non-uniform carrier distribution in multi-quantum-well lasers," Appl. Phys. Lett., Vol. 83, pp. 419-421, 2003.

[118] D. Gollub, S. Moses, and A. Forchel, "Comparison of GaInNAs laser diodes based on two to five quantum wells," IEEE J. Quantum Electron., Vol. 40, pp. 337-342, 2004.

[119] Y.Q. Wei, M. Sadeghi, S.M. Wang, P. Modh, and A. Larsson, "High performance 1.28μm GaInNAs double quantum well lasers," Electron. Lett., Vol. 41, pp. 1328-1329, 2005.

[120] C. Setiagung, H. Shimizu, Y. Ikenaga, K. Kumada, and A. Kasukawa, "Very low threshold current density of 1.3-μm-ridge GaInNAsSb-GaNAs 3 and 5 QWs lasers," IEEE J. Sel. Top. In Quantum Electron., Vol. 9, pp. 1209-1213, 2003.

---

121 L.H. Li, G. Patriarche, A. Lemaitre, L. Largeau, L. Travers, and J.C. Harmand, "Comparison of GaInNAs/GaAs and GaInNAs/GaNAs/GaAs quantum wells emitting over 1.3μm wavelength," J. of Cryst. Growth, Vol. 251, pp. 403-407, 2003.